# Ordered and chaotic behavior of the accretion flow in X-ray binary pulsars

**Dmitry Klochkov**

Institut für Astronomie und Astrophysik
Kepler Center for Astro and Particle Physics
Mathematisch-Naturwissenschaftliche Fakultät

Eberhard Karls Universität Tübingen

Summary to Cumulative Habilitation
for Receiving the *venia legendi*
for Astronomy and Astrophysics

Tübingen                                             June 2015

# Table of contents

# Chapter 1

# Introduction

## 1.1   X-ray binary pulsars. General picture

X-ray binary pulsars (or accreting pulsars) are among brightest sources of X-ray emission in our Galaxy, with luminosities reaching $10^{38}$–$10^{39}$ erg s$^{-1}$. These objects are close binary systems consisting of a "normal" (main sequence or giant) star and a very compact *neutron star* (NS). The latter has a mass of about 1.5 $M_\odot$ and a radius of only $\sim$12-13 km. Supported against gravitational collapse by the pressure of degenerate nucleons (mostly neutrons), NSs are the densest macroscopic objects made of ordinary matter. They represent the final points of stellar evolution for the stars with a mass in the range between $\sim$8 and 20 $M_\odot$. X-ray binary pulsars are powered by the gravitational energy of matter supplied by the binary companion star and accreted by the magnetized NS. The magnetic field of the latter is believed to have a roughly dipole configuration, with a field strength at the stellar surface of $B \sim 10^{12} - 10^{13}$ G. Such a strong magnetic field makes NSs the strongest magnets in the universe. In the vicinity of a magnetized NS, the accretion flow consisting of heated ionized gas is channeled by the magnetic field lines toward the polar caps of the star. In these regions, matter impacts the stellar surface at a velocity of $\sim$0.5$c$. As a result of an abrupt deceleration, the plasma is heated to $10^7$–$10^8$ K and radiates primarily in hard X-rays. Rotation of the NS causes a periodic modulation of the observed flux – X-ray pulsations.

The configuration of the accretion flow depends on the donor star. In Low Mass X-ray Binaries (LMXB), where the binary companion is a late type star of a mass close to or below one solar mass, the most common mode of accretion is via Roche lobe overflow and an accretion disk (Shakura, 1972; Shakura & Sunyaev, 1973). As *Roche lobe* one refers to the equipotential surface which contains the point $L_1$ on the straight line connecting the two stars where the vector sum of the centrifugal force
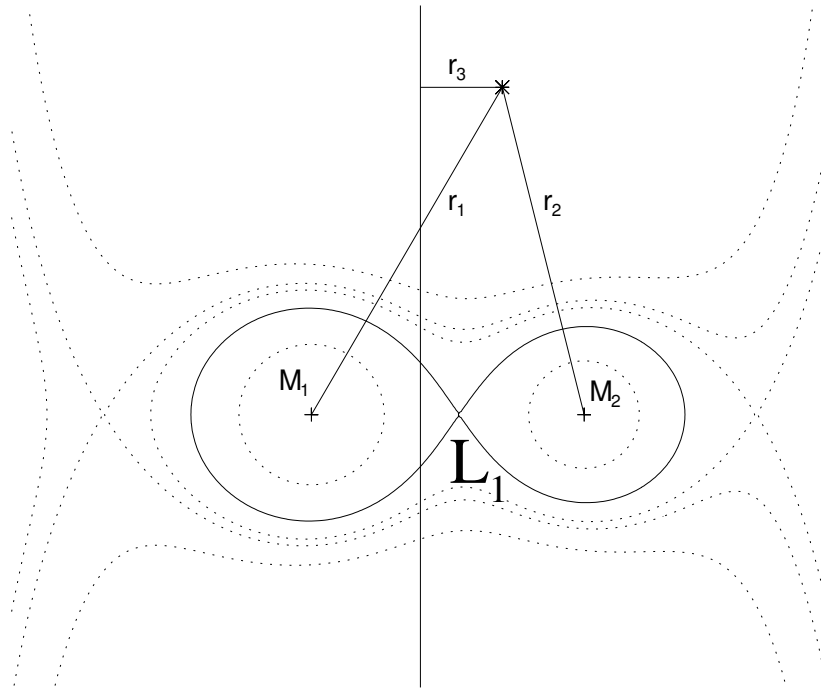
Fig. 1.1 Equipotential surfaces in a binary system consisting of stars with masses $M_1$ and $M_2$ in the reference frame rotating with the binary. If the stars are approximated by point-like masses, the potential can be calculated as $\phi = -GM_1/r_1 - GM_2/r_2 - \omega^2 r_3^2/2$, where $\omega$ is the orbital frequency of the binary. The Roche lobe is shown by the solid curve. In the Lagrange point $L_1$, the vector sum of the centrifugal force and the gravitational attraction forces of the two stars vanish.

and the gravitational attraction forces of the stars vanish (Fig. 1.1). If the "normal" companion fills the Roche lobe, matter from its surface begins to flow through the $L_1$ point towards the NS ("Roche lobe overflow") and forms a disk-like structure around the latter – an accretion disk.

In High Mass X-ray Binaries (HMXB), the donor star has a mass above a few solar masses. Such systems are relatively wide and the donor star usually does not fill its Roche lobe. The compact star captures matter either from the donor's strong stellar wind or from the circumstellar disk around the donor star. Such circumstellar disks are formed around fast rotating giant stars of spectral types Be or Oe. Binary systems containing such a star and an accreting pulsar are dubbed *Be X-ray binaries* (BeXRB). X-ray emission of accreting pulsars in HMXBs is usually transient, i.e., characterized by irregular or periodic outbursts separated by episodes of quiescence. The variability is attributed either to the orbital motion of the NS in the spatially inhomogeneous outflow of the donor star or to the time variability of the outflow. In HMXBs, an accretion disk only forms under certain conditions. Depending on the
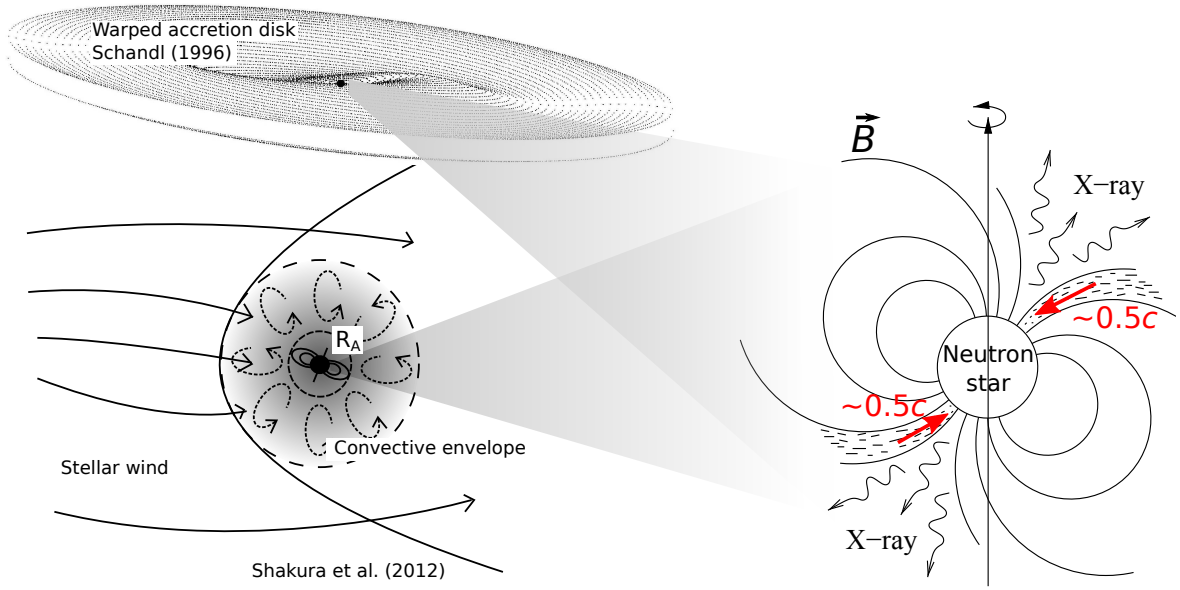
Fig. 1.2 The structure of the accretion flow in an X-ray binary pulsar (accreting magnetized neutron star).

presence of the accretion disk, accreting binary pulsars are therefore divided into "disk-fed" and "wind-fed" accretors.

The radius around the NS where the accretion flow is disrupted by the magnetic field and matter attaches to the field lines is usually referred to as the *magnetospheric boundary* or the *Alfvén surface*. The radius of the Alfvén surface (Alfvén radius) is defined as the radius $R_A$ where magnetic stresses would balance the ram pressure of a spherically symmetrical accretion flow (see e.g. Pringle & Rees, 1972):

$$R_A = \left( \frac{\mu^2}{2\dot{M}\sqrt{2GM}} \right)^{2/7},$$

(1.1)

where $M$ is the NS mass, $\mu$ is its magnetic dipole moment, and $\dot{M}$ is the mass accretion rate. For a typical accreting pulsar, the Alfvén radius is around 1000 km, i.e., a hundred NS radii. It should be noted that Eq 1.1 is a rough measure. The actual radius if the magnetospheric boundary depends on the geometry of the accretion flow and on the detailed physics of its interaction with the magnetic field. Obviously, $R_A$ should be greater than the NS radius to show the phenomenon of accreting pulsar. This condition is satisfied for the NS surface field $B \gtrsim 10^8$ G.

Inside the magnetospheric boundary, the accreted matter couples to a subset of the *B*-field lines in a configuration which in the case of a dipole field is roughly azimuthally symmetric about the magnetic pole of the NS (Fig. 1.2). This region is expected to have an approximately column-like shape and is therefore often referred to as an "accretion column" (Davidson & Ostriker, 1973; Mészáros, 1992, and references therein). In the accretion column, the accreted matter is decelerated from $\sim 0.5c$ to zero. Because of the large amount of liberated kinetic energy, there can be significant interaction between the radiated photons and the accreted material, and therefore the structure of the accretion column strongly depends on the X-ray luminosity (and thus the column's $\dot{M}$). In the deceleration region the bulk kinetic energy of the plasma is converted to heat and radiation. The region can have a substantial vertical extension (a fraction of the neutron star's radius).

Due to the strong *B*-field in the column, quantum electrodynamical effects become important. While electrons can move freely parallel to the field lines, their motion perpendicular to the field is quantized into discrete energy levels, the Landau levels. For typical $10^{12}$ G *B*-fields, these levels are separated approximately by $\Delta E = E_{\mathrm{cyc}} \simeq 12 \, \mathrm{keV} \cdot (B/10^{12} \, \mathrm{G})$. The cross section for the scattering of photons off these quantized electrons shows strong resonances at $E_{\mathrm{cyc}}$ and its integer multiples (Daugherty & Harding, 1986, and references therein). As a result, absorption line-like Cyclotron Resonant Scattering Features (CRSFs or *cyclotron lines*) appear in the X-ray continuum of the sources. Observations of cyclotron lines (measurements of their centroid energies $E_{\mathrm{cyc}}$) provide the only *direct* way to determine the *B*-field strength of NSs.

## 1.2   Open questions and motivation

Beyond the basic description of the magnetosperic boundary in the previous section, there is no consensus on how or where exactly the matter attaches to the field lines and flows to the NS surface, or on the interaction of the field with the accretion disk outside the magnetospheric radius. As already mentioned, the magnetospheric radius may differ substantially from $R_{\mathrm{A}}$, depending on the detailed physics of plasma penetrating the magnetosphere. In many studies dealing with disk-fed pulsars, matter is assumed to leave the accretion disk in a narrow transition zone at the inner disk edge, thereafter flowing along magnetic field lines (see e.g. Anzer & Boerner, 1983; Ghosh & Lamb, 1979; Wang, 1987). However, detailed numerical magnetohydrodynamical simulations have so far been performed only for low-magnetized
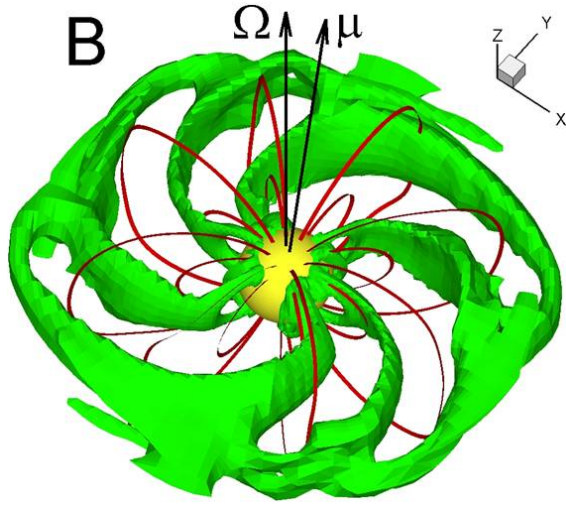
Fig. 1.3 The accretion flow onto a low-magnetized neutron star from the MHD simulations by Romanova et al. (2008). A constant-density surface and sample magnetic field lines are shown.
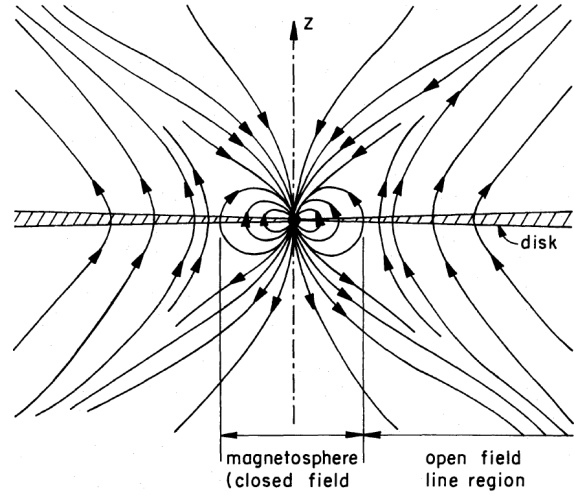


Fig. 1.4 A schematic representation of the magnetic field configuration around a magnetized neutron star considered by Lovelace et al. (1995).

NSs ($B \sim 10^8$ G). They indicate a complicated geometry of the Alfvén surface. An example of such simulations by Romanova et al. (2008) is shown in Fig. 1.3.

The configuration of the accretor's magnetic field at/around the magnetospheric boundary, which is still uncertain, is essential for the dynamical interaction of the compact star with matter in the accretion disk. It might determine the possibility of matter outflows from the inner disk regions along the open (going to infinity) magnetic field lines. Such open field lines are believed to exist at the regions outside the magnetospheric boundary where the angular frequency of the accretion disk is much lower than that of the magnetosphere rotating with the angular frequency of the NS (Lovelace et al., 1995). Figure 1.4 shows the magnetic field configuration around the magnetospheric boundary of an accreting pulsar adopted in Lovelace et al. (1995) which I considered to be the most realistic in my research.

Also for the polar emitting regions (accretion columns), there is no agreement on the dimensions and shape of the emitting column or on the physical conditions inside the X-ray emitting region such as the vertical velocity and temperature profiles. Both are expected to depend on $\dot{M}$ and on the $B$-field strength and configuration. While in many models the vertical extension of the emitting region is assumed or derived to be small compared to the NS radius (e.g., Kraus, 2001; Mészáros, 1992), alternative models assume the height of the column comparable or even exceeding the radius of the star (Doroshenko et al., 2010; Leahy, 2003). The shape of the column is also highly debated in the literature. A possibility of a "hollow column" or a "hollow

cone" was suggested, e.g, by Lyubarskii & Syunyaev (1988), Leahy (2003), and Kraus (2001). A luminous halo might form around the accretion column (Davidson & Ostriker, 1973; Lyubarskii & Syunyaev, 1988) and the radiation from the polar cap and the halo can be scattered in the upper accretion stream (Brainerd & Meszaros, 1991; Soffel et al., 1985). Finally, Poutanen et al. (2013) recently suggested that cyclotron responance features in the spectra of accreting pulsars are formed in the radiation *reflected* off the NS surface.

Observations of accreting NSs are the ultimate way to test the models for the physics of the magnetospheric boundary and of the accretion column. The tremendous progress of the observational techniques has been achieved in the field of X-ray astronomy over the recent years driven by the operation of modern orbital X- and gamma-ray observatories such as *Rossi* XTE, INTEGRAL, *Swift, Suzaku, Chandra, XMM-Newton, and NuSTAR*. The delivered observational data of unprecedented quality (high spatial, energy, and timing resolution, broad spectral coverage, high photon statistics) allowed the new analysis technuques to be applied which revealed the previously unknown properties of accreting pulsars which require further developments of the theoretical models describing these objects. As a result, the interest in X-ray binary pulsars was renewed in the recent years, especially because of mounting evidences for deviations of the observed properties from the basic picture. I am involved in the research, which addresses the detailed physics of the most intriguing regions of accreting pulsars, the polar emitting structures (accretion columns) and the magnetospheric boundary, which are responsible for the majority of the observational properties of these sources.

# Chapter 2

# Magnetospheric boundary

## 2.1 Angular momentum exchange between the accretion disk and the neutron star

Under a simplified assumption that the plasma at the inner edge of the accretion disk immediately acquires the angular velocity of of the neutron star while attaching to the field lines, the evolution of the star's angular frequency $\omega_{NS}$ is determined by the flux of the angular momentum at the inner disk radius assumed to be of the order of $R_A$ (Pringle & Rees, 1972):

$$\frac{d}{dt} I \omega_{NS} = \dot{M}(GMR_A)^{\frac{1}{2}}, \tag{2.1}$$

where $M$ and $I$ are the neutron star's mass and moment of inertia. The Alfvén radius $R_A$ depends on the mass accretion rate $\dot{M}$ (see Eq. 1.1) which is proportional to the X-ray flux (Sect. 1.1). One, therefore, expects the following dependence of the pulse period derivative $\dot{P}$ of an accreting pulsar (spin-up rate) on its X-ray luminosity $L_X$ in this simple model:

$$-\dot{P} = L_X^{6/7}. \tag{2.2}$$

In this picture, accretion can only take place if the Keplerian angular frequency of matter at the inner disk rim $\omega_K(R_A)$ is lower than that of the NS, $\omega_{NS}$. In this case, the co-rotation radius $R_C$, where the Keplerian angular frequency is equal to that of the magnetosphere ($R_C = [GM/\omega_{NS}]^{1/3}$), stays outside $R_A$. In the opposite case, when $\omega_K(R_A) < \omega_{NS}$, accretion is inhibited by centrifugal forces. Such a regime is often referred to as "propeller" (Illarionov & Sunyaev, 1975).

In the equations above, only the spin-up torque due to inflow of angular momentum at $R_A$ is considered. A more realistic description should take into account spin-down torques resulting from the interaction of the parts of the accretion disk outside $R_C$
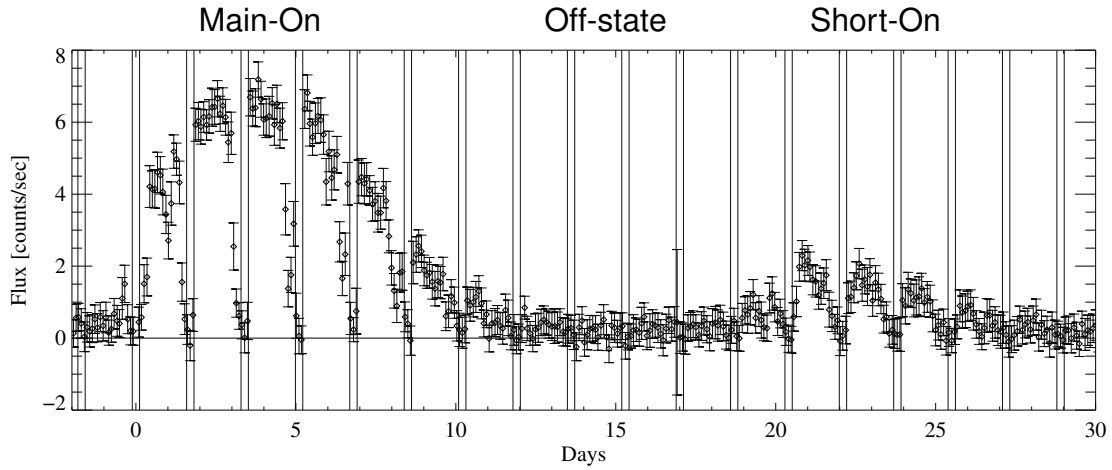
Fig. 2.1 The averaged 35 d profile of Her X-1 obtained by stacking of a large number of RXTE/ASM light curves from individual 35 d cycles (Klochkov et al., 2006).

with the NS magnetosphere. If the spin-down torque exceeds the spin-up torque, the NS spins down and the co-rotation radius moves further beyond $R_A$. This leads to a decrease of the spin-down torque because the parts of the disk rotating slower than the NS turn out to be further away from the magnetosphere. If the spin-up torque is dominating, $\omega_{NS}$ increases shifting $R_C$ inwards. The pulsar is approaching the centrifugal barrier where the spin-down torque increases. The considerations above imply the existence of an equilibrium frequency $\omega_{eq}$ of the accreting NS where the spin-up and spin-down torques exactly balance. From these considerations, $\omega_{eq}$ should be reached when the co-rotation radius is close to the Alfvén radius.

I have investigated the evolution of the pulse period in the persistent accreting pulsar Her X-1 over the the time period of more than five years. I used the publicly available data from the BAT hard X-ray detector onboard the *Swift* satellite. The BAT instrument has a huge field of view of 1.4 steradian and is designed to provide triggers and accurate positions for gamma-ray bursts. While searching for bursts and other transient sources, *BAT* points at different locations in the sky, thus performing an all-sky monitoring in hard X-rays (see, e.g., Krimm et al., 2013). After an appropriate processing, the data from BAT can be used to search for a periodic signal from sources in its field of view.

The X-ray flux of Her X-1 shows a regular alternation of *on* and *off* states repeating with a period of ∼35 d. One 35 d cycle includes two *on* states: the *main-on* characterized by a peak flux of up to 300 mCrab and the *short-on* when the flux is ∼five times lower (Fig. 2.1). The 35 d periodicity is believed to be caused by the tilted and twisted accretion disk precessing with a period of ∼35 d (e.g., Klochkov et al., 2006, and references therein). In my work, I measured the pulse period *P* and its
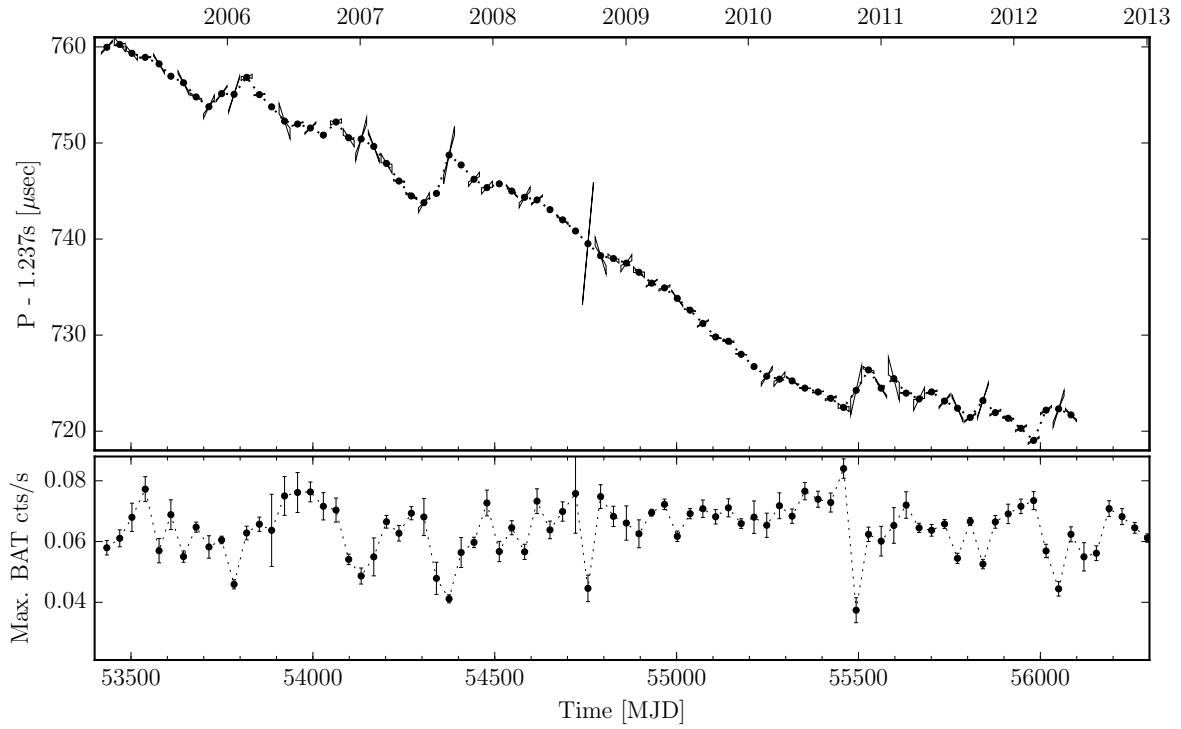
Fig. 2.2 *Top:* Pulse period $P$ of Her X-1 measured with *Swift*/BAT as a function of time. The cones around each point indicate the allowed range of the slope corresponding to the measured $\dot{P}$ and its uncertainties. *Bottom:* The X-ray flux of the source measured with RXTE/ASM during the maximum of the main-on state (it is believed to reflect the luminosity of Her X-1).

time derivative $\dot{P}$ for each pulsar's main-on between 2005 (start of the *Swift* mission) and 2009 (time of the publication). In the meanwhile, this work has been continued as a student project under my coordination. The resulting $P$ and $\dot{P}$ measurements are presented in the top panel of Fig. 2.2. One can clearly see that the spin-down episodes (were $P$ goes up with time) are associated with drops in the source's luminosity (bottom panel of the figure). Such a correlation is expected in the basic accretion theory since both the luminosity and spin-down rate $(-\dot{P})$ are proportional to the mass accretion rate $\dot{M}$ (see the beginning of the chapter).

In our work Klochkov et al. 2009 presented in Appendix A, we associated the spin-down episodes in Her X-1 with increased mass outflows from the inner parts of the accretion disk. During such episodes, a substantial fraction of matter can escape the system in the form of a coronal wind ejection along the open field lines. The escaping material effectively carries away angular momentum leading to the observed spin-down episodes. An indirect evidence for such a coronal mass ejection comes from the observed secular change of the system's orbital period (Staubert et al., 2009). We have demonstrated that the spin-down power of the neutron star

$I\omega\dot{\omega}$ during the observed spin-down episodes is indeed roughly equal to the angular momentum carried away by the coronal outflow per unit time for for the mass loss rate $M_{ej}$ derived from the secular decay of the orbital period:

$$I\omega\dot{\omega} \sim \dot{M}_{ej}\frac{GM}{R_C}\,.\qquad\qquad(2.3)$$

## 2.2   Flaring activity and oscillations of the magnetospheric boundary

At the mass accretion rate below $\sim 10^{18}$ g s$^{-1}$ ($L_X \lesssim 10^{37}$ erg s$^{-1}$), many pulsar exhibit flaring behavior or flux oscillation on a time scale of several hours. The most famous example is probably the series of roughly equidistant flares observed in 1985 with the EXOSAT satellite in the 42 s pulsar EXO 2030+375 (Fig. 2.3). The source belongs to the class of BeXRBs showing sporadic and/or regular X-ray outbursts (see Section 1.1). The flares observed with EXOSAT followed the decay of a major outburst of EXO 2030+375 (Parmar et al., 1989). Other well-known "flaring" X-ray binary pulsars are LMC X-4 (e.g., Moon et al., 2003b), SMC X-1 (e.g., Moon et al., 2003a), Vela X-1 (Fürst et al., 2010; Kreykenbohm et al., 2008). Flaring behavior is also the main characteristic of Super Giant Fast X-ray transients (SFXTs), a new class of HMXBs discovered with the INTEGRAL observatory (see e.g. Sidoli, 2011).

I have studied the data on EXO 2030+375 taken with the INTEGRAL X-/$\gamma$-ray orbital observatory (Winkler et al., 2003) granted in response to an accepted Data Right proposal under my PIship. The source showed quasi-periodic flares on top of the rising phase of an outburst in 2010-2011 (Klochkov et al., 2010). In our work Klochkov et al. 2011a presented in Appendix B, we explained the the observed flaring behavior by oscillations in the mass flow rate towards the polar caps of the NS due to matter piling up at the inner radius of the accretion disk. When the gas pressure at the inner disk edge exceeds the magnetic pressure, the reservoir of accumulated gas is accreted by the NS and the new pile up cycle begins. The period of the resulting oscillations is expected to be close to the local viscous time scale $\tau_c$ at the inner disk radius (which is close to the co-rotation radius). We have demonstrated that for the parameters of EXO 2030+375 during the observations, $\tau_c$ at the inner disk radius is around $\sim$7 hr which is very close to the observed time separation of the flares.

We also noticed an indication of a shortening of the time intervals between the flares over the rise of the outburst. Such a decrease is naturally expected because the increased mass transfer rate through the disk results in a shorter re-fill time of the reservoir. The dependence of the separation time between the flares on the averaged
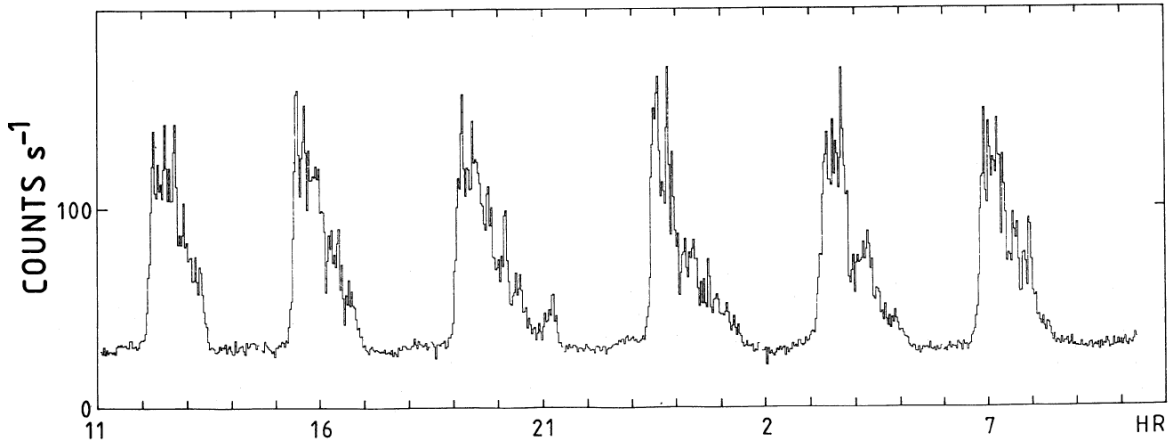
Fig. 2.3 A series of flares observed with EXOSAT in EXO 2030+375 a few month after its major outburst in 1985 (Parmar et al., 1989).

mass transfer rate through the disk is most probably the reason of the difference in the oscillation periods between the 1985 EXOSAT observations and our INTEGRAL 2011 observations, ~7 vs. ~4 hr, respectively.

We have found strong difference in the spectrum-luminosity dependence between the rising phase of the outburst accompanied by flares and its decay where no flares were observed. In the proposed mechanism of flares, such a difference is indeed expected. If the flares are caused by the oscillating inner edge of the accretion disk, matter from the oscillating disk rim would couple to different dipole field lines of the NS (and follow them forming a slightly different emitting region on the stellar surface) compared to the decay part of the outburst where the configuration of the inner disk rim is presumably stable.

It is interesting to note the rarity of the detected flaring episodes (even considering the relatively sparse observational coverage). Such a rarity means that the range of physical conditions needed to initiate the oscillations is very narrow leading to the serendipitous character of the phenomenon.

# Chapter 3

# Polar emitting regions

## 3.1 Luminosity dependence of the emitting region

The most important "outer" parameter of an accreting neutron star is its *mass accretion rate* $\dot{M}$. It determines the energy budget available for radiation ($L_X \simeq 0.1\dot{M}c^2$ for a 10 km NS) and can thus be straightforwardly assessed from the observed X-ray flux. Soon after discovery of the first X-ray binary pulsars, it was realized that $\dot{M}$ governs the structure and physics of the NS polar emitting regions (Basko & Sunyaev, 1976). It is very advantageous that $\dot{M}$ varies substantially in most of accreting pulsars, allowing one to study the "reaction" of the emitting structure on the varying rate of the mass inflow. Especially intriguing is the observed variation of the CRSF energy $E_{\rm cyc}$ (reflecting the strength of the $B$-field at the emission site, see Sect. 1.1) with luminosity observed in several X-ray binary pulsars (e.g., Mihara et al., 2004; Staubert et al., 2007; Tsygankov et al., 2010). Such a variation most probably reflects a *displacement* of the emitting region in the inhomogeneous magnetic field of the NS. This channel of information about the emitting structure is being actively explored leading to a number of proposed theoretical models (e.g., Becker et al., 2012; Mushtukov et al., 2014; Poutanen et al., 2013). Two examples where the variability of the X-ray spectrum with luminosity can be seen "by eye" are shown in Fig. 3.1.

The most intriguing property of the observed CRSF–luminosity dependences in X-ray binary pulsars is their apparent bimodality. A strong *negative* $E_{\rm cyc} - L_X$ correlation has been reported for V 0332+53 (Tsygankov et al., 2010). An opposite behavior, i.e. a *positive* $E_{\rm cyc} - L_X$ correlation, has been observed in Her X-1 (Klochkov et al., 2011b; Staubert et al., 2007), in A 0535+26 (Klochkov et al., 2011b; Müller et al., 2013; Sartore et al., 2015), and for GX 304−1 (Klochkov et al., 2012). Also the sign of the correlation between the hardness of the spectral continuum (reflected by the photon index $\Gamma$ characterizing the power-law part of the spectrum, $F \propto E^{-\Gamma}$) and
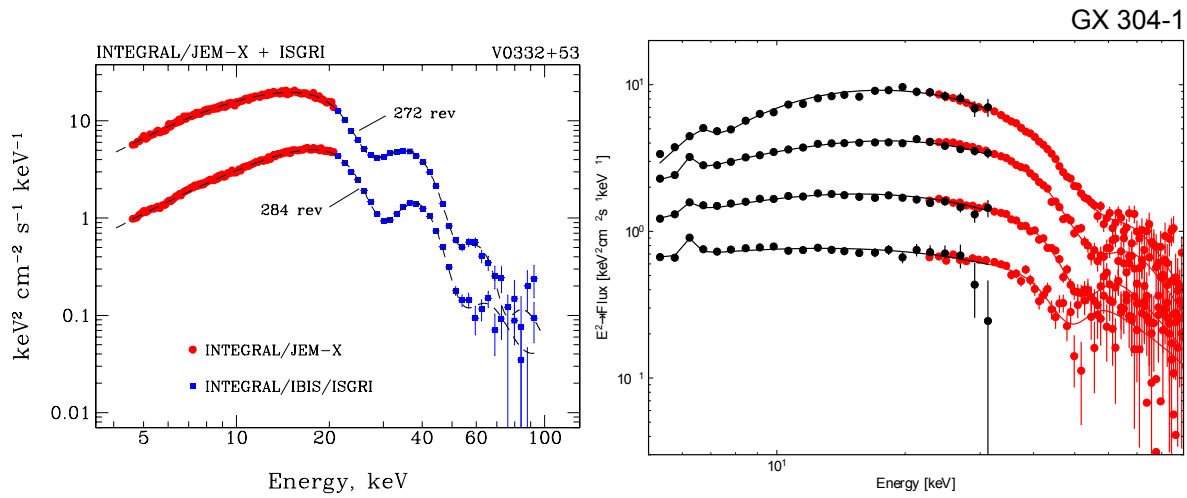
Fig. 3.1 The X-ray spectra of two accreting pulsars, V 0332+53 (Tsygankov et al., 2006) and GX 304−1 (Klochkov et al., 2012), taken at different luminosities of the sources. The difference of the spectral shape between the spectra corresponding to different luminosities can be seen.

$L_X$ is opposite in the two groups of sources. Figure 3.2 shows examples of the found spectrum–flux correlations in a few accreting pulsars.

The apparent bimodality in the spectral–flux dependence must reflect different regimes of accretion. A particular regime is realized in a source depending most probably on whether its X-ray luminosity $L_X$ is above or below a certain critical value $L_{crit} \sim$ (a few) $\times 10^{37}$ erg s$^{-1}$. In accreting pulsars radiating above $L_{crit}$ ("super-critical" sources), the observed negative $E_{cyc} - L_X$ correlation can be explained either by an increase of the height of the emitting region above the NS surface with $L_X$ (Becker et al., 2012) or by a varying illumination of the NS surface by the accretion column assuming that the line is produced in the continuum reflected by the surface (Poutanen et al., 2013). Below $L_{crit}$ ("sub-critical" sources), the height of the emitting region probably *decreases* with increasing $L_X$ due to a different mechanism of matter deceleration (Staubert et al., 2007). Such a behavior would explain the positive $E_X - L_X$ correlation in "sub-critical" sources. My research contributed both to the observational study of the spectrum–luminosity dependences in accreting pulsars (Klochkov et al., 2012, 2011b; Müller et al., 2013) and to their theoretical modeling (Becker et al., 2012, and the next section).

The flux of most accreting pulsars varies by a factor of 1.5–2 from one pulsation cycle (i.e., the NS rotation cycle) to the next while the flux averaged over many pulsation cycles remains constant or varies slowly. In our work Klochkov et al. (2012) presented in Appendix C, I utilized such a "pulse-to-pulse" variability to explore for the first time the spectrum–luminosity dependences in accreting pulsars on the time
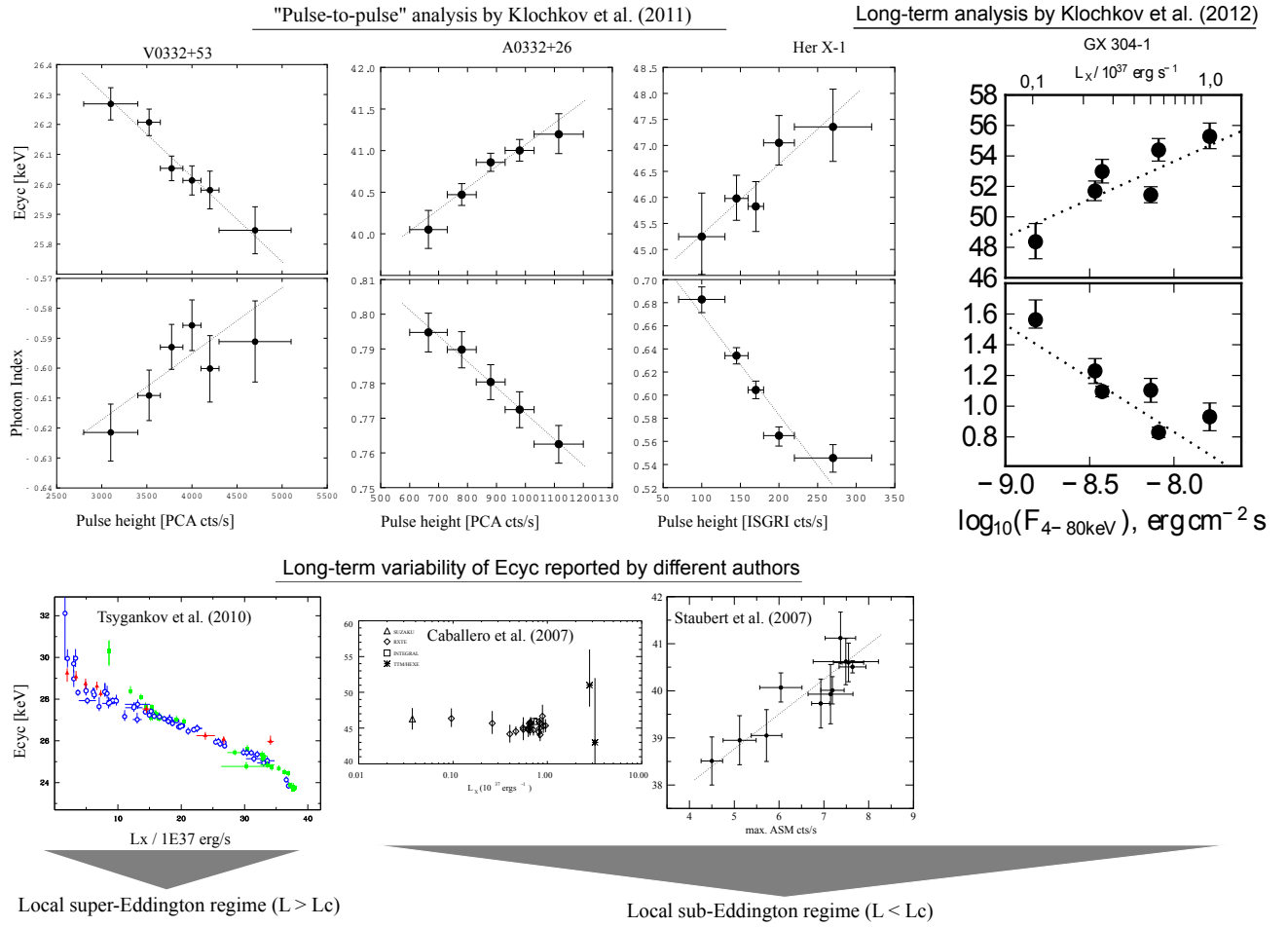
Fig. 3.2 The dependences of the cyclotron line energy $E_{cyc}$ and of the photon index $\Gamma$ (vertical axes) on flux/luminosity (horizontal axes) derived from the pulse-to-pulse analysis and from the long-term variability for four accreting pulsars (four columns)

scales from a fraction of a second to a few second. Some of the dependences shown in Fig. 3.2 have been revealed in such a pulse-to-pulse analysis. The new technique allows one to explore the spectrum–luminosity relation in persistent sources whose luminosity does not change substantially on longer time scales (like, e.g., in Her X-1) or in short pointed observations during which the averaged flux remained roughly constant. The pulse-to-pulse method also appears to be more sensitive to the $E_{cyc} - L_X$ correlations than the traditional analysis where the spectra are averaged over longer time intervals. In the long-term analysis, the spectral variability on the short time scale is averaged out leading to an additional smearing of the cyclotron lines and of other spectral features. Indeed, our analysis revealed a positive $E_{cyc} - L_X$ correlation in the transient X-ray binary pulsar A 0535+26 where the CRSF was previously claimed to be constant (second column of Fig. 3.2). The correlation in A 0535+26 has recently been confirmed by Sartore et al. (2015) based on the data

from INTEGRAL/SPI. A positive $E_{cyc} - L_X$ correlation is indeed expected in A 0535+26 because its luminosity during most of its outbursts barely reaches the threshold value $L_{crit}$.

The differences in the structure of the NS polar emitting regions for the luminosities above and below the critical luminosity are also reflected by the differences in the pulse profile – the X-ray light curve folded with the spin period of the NS. The shape of the pulse profile depends on the emission diagram of the emitting regions and on the orientation of the rotation and magnetic axes of the star with respect to each other and to the observer. The gravitational light bending in the vicinity of the compact NS is also important. The dependence of the X-ray spectrum on the NS rotation phase (pulse-phase resolved spectroscopy) can be used to connect a particular pulse phase to a certain orientation of the polar emitting region with respect to the observer. In our work Klochkov et al. (2008) presented in Appendix E, we investigated both the pulse profile and the pulse-phase resolved spectra of the transient accreting pulsar EXO 2030+375 at different luminosity levels. The pulse-phase dependences of the continuum parameters close to the maximum of the outburst, as well as the evolution of the pulse profiles from the maximum to the end of the outburst, were found to be consistent with a picture where the pulsar's emission diagram changes from the fan-beam configuration close to the maximum of the outburst (above $L_{crit}$) to a combination of pencil and fan beams at the end of the decay phase (below $L_{crit}$). Such a transition in the emission diagram is indeed expected when a pulsar switches from the super-critical to sub-critical accretion mode.

## 3.2 The "critical" luminosity

The critical luminosity $L_{crit}$ separating the two accretion modes discussed in the previous section can be estimated from the parameters of the accreting NS. It should correspond to the minimal mass accretion rate $\dot{M}$ at which the photon field at the polar emitting regions is capable of decelerating infalling plasma to rest. Below this luminosity, other deceleration mechanisms should play a significant role (Coulomb interaction, collective plasma effects) leading to a different structure of the emitting region compared to that at higher luminosities. Above $L_{crit}$, infalling plasma is decelerated via interactions with photons at a certain region above the NS surface. The deceleration region is often referred to as *radiative shock wave* (Basko & Sunyaev, 1976) although it most probably has a substantial vertical extention (e.g., numerical calculations by Wang & Frank, 1981).

In our work Becker et al. (2012) presented in Appendix F, we introduced a theoretical calculation of the critical luminosity. Our calculations take into account the energy dependent scattering cross section of photons off electrons in the magnetic field of the pulsar. The value of the critical luminosity depends, therefore, on the magnetic field of the NS. As a result, the following expression for $L_{crit}$ has been obtained:

$$L_{crit} = 1.49 \times 10^{37} \text{erg s}^{-1} \left( \frac{\Lambda}{0.1} \right)^{-\frac{7}{5}} w^{-\frac{28}{15}} \left( \frac{M_{NS}}{1.4 M_{\odot}} \right)^{\frac{29}{30}} \left( \frac{R_{NS}}{10\,\text{km}} \right)^{\frac{1}{10}} \left( \frac{B}{10^{12}\,\text{G}} \right)^{\frac{16}{15}},$$
(3.1)

where $\Lambda$ and $w$ are dimensionless coefficients characterizing the geometry of the pulsar's magnetospheric boundary (see Appendix F for details). In all accreting pulsars showing correlations of the cyclotron line energy $E_{cyc}$ with luminosity $L_X$, the critical luminosity calculated using Eq. (3.1) is consistent with the sign of the observed correlation. Namely, the pulsars whose luminosity is below $L_{crit}$ show a positive $E_{cyc} - L_X$ correlation while in the pulsars radiating above $L_{crit}$, the $E_{cyc} - L_X$ correlation is negative (see also the previous section) as it is expected in the described picture of two accretion modes.

In our work Becker et al. (2012), we also investigated the possibility of another accretion regime expected at lower mass accretion rates where infalling plasma is stopped by a hydrodynamical gas shock. The corresponding transition from the Coulomb stopping accretion regime to the gas shock is expected to take place at a luminosity below $\sim 10^{37}$ erg s$^{-1}$. Observational evidences for the existence this second critical luminosity are still to be found.

## 3.3 Long-term evolution of the local magnetic field at the polar regions

The magnetic field of accreting NS is generally expected to decay on a time scale of $\gtrsim 10^6$ yr (e.g., Bhattacharya et al., 1992). The decay is believed to cause the observed difference of the $B$-field strength between young accreting pulsars ($10^{11} - 10^{13}$ G) and the accreting NSs in old low-mass X-ray binaries ($10^8 - 10^9$ G). The corresponding change of the field strength on the human life timescale is, however, negligible and is not expected to be revealed by observations. Surprisingly, we have discovered a clear long-term variability of the CRSF centroid energy (which is proportional to the magnetic field strength at the emitting region) in one of the best studied accreting pulsars Her X-1 (Staubert et al. 2014, Appendix G). The discovery has been made
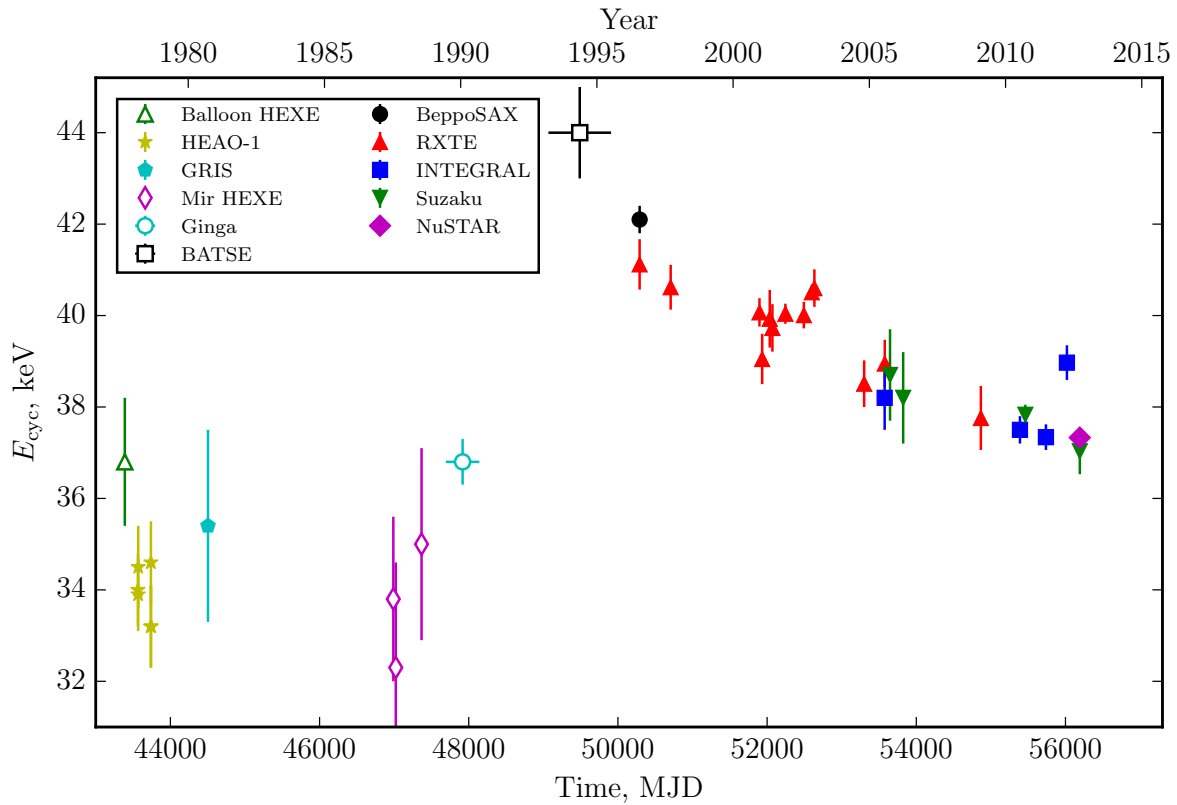
Fig. 3.3 The centroid energy of the cyclotron resonance line feature $E_{cyc}$ measured in Her X-1 with different instruments as a function of time since the discovery of the source.

by a comparison of the CRSF measurements by different instruments over the $\sim$35 yr history of the source observations and taking into account other effects such as the dependence of the cyclotron line energy on luminosity (Section 3.1) and on the 35 d super-orbital phase of the source. Figure 3.3 shows the CRSF energy $E_{cyc}$ in Her X-1 as a function of time measured with different instruments since the discovery of the pulsar.

In addition to and independently of the $E_{cyc} - L_X$ relation discussed in the previous sections, the line centroid energy has been significantly evolving since the beginning of the observations. Specifically, $E_{cyc}$ has been systematically decreasing since $\sim$1995 from $\sim$41 to $\sim$37 keV, that is, by $\sim$10% in total. To take the $E_{cyc} - L_X$ dependence into account, we modeled the measured CRSF energy by a linear function of both time and luminosity $E_{cyc} = F(t, L_X)$. The time dependence of the line energy was found to be characterized by the time derivative $dE_{cyc}/dt = -0.26 \pm 0.01$ keV/yr, indicating a significant trend. Even more intriguing, the measured evolution of $E_{cyc}$ includes a jump occurred in the early 1990s which was not accompanied by any other

noticeable changes in the source properties such as X-ray flux or timing characteristics.

In our work, we argue that the observed secular $E_{cyc}$ variation reflects a *local* evolution in the magnetic field configuration at the polar regions of the NS. Such local changes of the magnetic field, that are due to accumulation and spreading of accreted matter in the magnetically confined accretion mound, can indeed occur on timescales that are much shorter than the time scale for the global decay of the NS magnetic field. For instance, the time scale for the Ohmic decay $\tau_{Ohmic} = 4\pi R^2 \sigma/c^2$ for a small region like an NS polar cap with $R \lesssim 1\,km$ can be as short as $\sim 10^2\,yr$. A relatively short timescale of 100–1000 yr for the *B*-field evolution depending on the equation of state of the NS crust has also been obtained by Priymak et al. (2014). Another possible cause of the observed variability discussed in Staubert (2014) is a slight imbalance between the rate on which matter is accreted (gained) and the rate at which it is lost from the accretion mound – either by leaking to larger areas of the NS surface or by incorporation into the NS crust.

If the observed temporal evolution of the CRSF energy is indeed associated with local effects in the vicinity of the polar cap, it is expected that the decrease of $E_{cyc}$ should stop after some time, probably with an abrupt jump of the local magnetic field back to the unperturbed value. As mentioned above, such a jump might have indeed been observed in the early 1990s. However, the relatively sparse time coverage of Her X-1 by X-ray observations did not allow following the event in detail. Currently, $E_{cyc}$ is roughly approaching the level it had before the jump in 1990s. Therefore, a new jump may be expected in the coming years! In this respect, it is interesting to note an "outlier" – the latest INTEGRAL data point in Fig. 3.3 (the rightmost filled blue square) located significantly higher than the rest of the neighboring measurements. Although we cannot rule an unknown instrumental effect (however, we performed a deep investigation of this data point, see Appendix G), the measurement can indicate a physical short-term variability of the local *B*-field configuration which can be a precursor of a larger jump. It is, therefore, crucially important to continue the $E_{cyc}$ monitoring in Her X-1.

# Chapter 4

# Conclusions and future plans

In the presented studies of accreting binary pulsars, physics of the magnetospheric boundary and of the NS polar emitting regions has been addressed. The two regions are responsible for the majority of the pulsars' observational properties. The main channel of information used in our study is the reaction of the magnetospheric boundary and of the emitting region to the changes of the mass supply rate in the accretion flow. Specifically, we studied the dependences of the sources' X-ray spectra, NS spin period, and quasi-periodic flux oscillations (flaring) on the mass accretion rate $\dot{M}$ reflected by the source X-ray luminosity $L_X$. In addition, our studies for the first time revealed long-term variations of the observed magnetic field strength in an accreting X-ray pulsar. The presented research led to the following conclusions about the physics of accreting magnetized neutron stars.

**Magnetospheric boundary.** The existence of strong outflows from the inner regions of the accretion disk has been established. The ejected matter carries away substantial amount of angular momentum which causes episodes of strong NS spin-down. In Her X-1 and most probably in other similar Roche-lobe overflowing X-ray binary pulsars, the outflows must be responsible for a substantial fraction of the orbital period decay $\dot{P}_{orb}$ of the binary system. The oscillations of the magnetospheric radius at a low accretion rate have been observed. Such oscillations cause flaring activity in transient accreting pulsars at low accretion rates when the mass transfer rate through the accretion disk starts to increase (e.g., at the beginning of an outburst in BeXRBs).

**Polar emitting region.** The two modes of accretion in X-ray binary pulsars have been established which are characterized by different types of the spectrum–luminosity dependences. The mode of accretion depends on the configuration of the emitting region (accretion column/mound) which is different at luminosities above and below a "critical" luminosity of a few times $10^{37}$ erg s$^{-1}$. The configuration is

determined by the deceleration mechanism of infalling matter. At higher luminosity / mass accretion rate, the infalling plasma is decelerated by the dense photon field produced in the accretion column. At lower mass accretion rate the matter is most probably decelerated by Coulomb interactions and collective plasma effects.

**Long-term evolution of the NS magnetic field.** The decay of the $B$-field strength reflected by the energy of the cyclotron absorption feature $E_{cyc}$ firmly established in Her X-1, a single example of such a behavior. The variability most probably reflects local variations of the magnetic field configuration at the magnetic poles of the NS driven by the accumulation and spreading of the accreted plasma which is coupled to the magnetic field.

In the future, we plan to develop a two-dimensional numerical model of the accretion column in collaboration with the groups in Dr. Karl Remeis-Sternwarte (Bamberg) and at Moscow State University. The model should include the temperature, density, emissivity and velocity distributions over the column such that the X-ray spectrum and the emitting diagram could be calculated as a function of the mass accretion rate and compared with the observed dependences. A preliminary version of such a model is already available and shows a good agreement with the observed behavior of the pulsars' X-ray spectra.

On the observational side, we plan to increase the sample of accreting pulsars showing a clear luminosity-dependences of the X-ray spectrum. Currently, we have a running student project (by E. Laplace) focused on the study of the spectral hardness in accreting pulsars as a function of $L_X$ based on the publicly available data from all sky monitors (RXTE/ASM, MAXI, *Swift*/BAT). The first results clearly indicate the existence of two modes in the hardness–luminosity dependences separated by the aforementioned critical luminosity.

We plan to follow the evolution of the observed $B$-field strength in Her X-1 in the next years. The new observations of the source with INTEGRAL and *NuSTAR* orbital observatories in response to our observing proposals are scheduled. In parallel, we plan to search for a similar phenomenon in other accreting pulsars showing cyclotron lines.

# References

Anzer, U. & Boerner, G. 1983, A&A, 122, 73

Basko, M. M. & Sunyaev, R. A. 1976, MNRAS, 175, 395

Becker, P. A., Klochkov, D., Schönherr, G., et al. 2012, A&A, 544, A123

Bhattacharya, D., Wijers, R. A. M. J., Hartman, J. W., & Verbunt, F. 1992, A&A, 254, 198

Brainerd, J. J. & Meszaros, P. 1991, ApJ, 369, 179

Daugherty, J. K. & Harding, A. K. 1986, ApJ, 309, 362

Davidson, K. & Ostriker, J. P. 1973, ApJ, 179, 585

Doroshenko, V., Santangelo, A., Suleimanov, V., et al. 2010, A&A, 515, A10

Fürst, F., Kreykenbohm, I., Pottschmidt, K., et al. 2010, A&A, 519, A37

Ghosh, P. & Lamb, F. K. 1979, ApJ, 234, 296

Illarionov, A. F. & Sunyaev, R. A. 1975, A&A, 39, 185

Klochkov, D., Doroshenko, V., Santangelo, A., et al. 2012, A&A, 542, L28

Klochkov, D., Ferrigno, C., Santangelo, A., et al. 2011a, A&A, 536, L8

Klochkov, D., Santangelo, A., Staubert, R., & Ferrigno, C. 2008, A&A, 491, 833

Klochkov, D., Santangelo, A., Turler, M., et al. 2010, The Astronomer's Telegram, 3052, 1

Klochkov, D., Staubert, R., Postnov, K., Shakura, N., & Santangelo, A. 2009, A&A, 506, 1261

Klochkov, D., Staubert, R., Santangelo, A., Rothschild, R. E., & Ferrigno, C. 2011b, A&A, 532, A126

Klochkov, D. K., Shakura, N. I., Postnov, K. A., et al. 2006, Astronomy Letters, 32, 804

Kraus, U. 2001, ApJ, 563, 289

Kreykenbohm, I., Wilms, J., Kretschmar, P., et al. 2008, A&A, 492, 511

Krimm, H. A., Holland, S. T., Corbet, R. H. D., et al. 2013, ApJS, 209, 14

Leahy, D. A. 2003, ApJ, 596, 1131

Lovelace, R. V. E., Romanova, M. M., & Bisnovatyi-Kogan, G. S. 1995, MNRAS, 275, 244

Lyubarskii, Y. E. & Syunyaev, R. A. 1988, Soviet Astronomy Letters, 14, 390

Mészáros, P. 1992, High-energy radiation from magnetized neutron stars (Chicago: Chicago Univ. Press)

Mihara, T., Makishima, K., & Nagase, F. 2004, ApJ, 610, 390

Moon, D.-S., Eikenberry, S. S., & Wasserman, I. M. 2003a, ApJL, 582, L91

Moon, D.-S., Eikenberry, S. S., & Wasserman, I. M. 2003b, ApJ, 586, 1280

Müller, D., Klochkov, D., Caballero, I., & Santangelo, A. 2013, A&A, 552, A81

Mushtukov, A. A., Suleimanov, V. F., Tsygankov, S. S., & Poutanen, J. 2014, ArXiv e-prints

Parmar, A. N., White, N. E., Stella, L., Izzo, C., & Ferri, P. 1989, ApJ, 338, 359

Poutanen, J., Mushtukov, A. A., Suleimanov, V. F., et al. 2013, ArXiv e-prints

Pringle, J. E. & Rees, M. J. 1972, A&A, 21, 1

Priymak, M., Melatos, A., & Lasky, P. D. 2014, MNRAS, 445, 2710

Romanova, M. M., Kulkarni, A. K., & Lovelace, R. V. E. 2008, ApJL, 673, L171

Sartore, N., Jourdain, E., & Roques, J.-P. 2015, ArXiv e-prints

Shakura, N. I. 1972, Astronomicheskii Zhurnal, 49, 921

Shakura, N. I. & Sunyaev, R. A. 1973, A&A, 24, 337

Sidoli, L. 2011, Advances in Space Research, 48, 88

Soffel, M., Herold, H., Ruder, H., & Ventura, J. 1985, A&A, 144, 485

Staubert, R. 2014, in proceedings of 10th INTEGRAL Workshop: "A Synergistic View of the High Energy Sky", 15-19 September 2014, Annapolis, MD, USA, PoS(INTEGRAL2014)024

Staubert, R., Klochkov, D., & Wilms, J. 2009, A&A, 500, 883

Staubert, R., Klochkov, D., Wilms, J., et al. 2014, ArXiv e-prints

Staubert, R., Shakura, N. I., Postnov, K., et al. 2007, A&A, 465, L25

Tsygankov, S. S., Lutovinov, A. A., Churazov, E. M., & Sunyaev, R. A. 2006, MNRAS, 371, 19

Tsygankov, S. S., Lutovinov, A. A., & Serber, A. V. 2010, MNRAS, 401, 1628

Wang, Y.-M. 1987, A&A, 183, 257

Wang, Y.-M. & Frank, J. 1981, A&A, 93, 255

Winkler, C., Courvoisier, T. J.-L., Di Cocco, G., et al. 2003, A&A, 411, L1

# Appendix A

# Continuous monitoring of pulse period variations in Hercules X-1 using *Swift*/BAT

# Continuous monitoring of pulse period variations in Hercules X-1 using *Swift/BAT*

D. Klochkov[1], R. Staubert[1], K. Postnov[2], N. Shakura[2], and A. Santangelo[1]

[1] Institut für Astronomie und Astrophysik, Universität Tübingen (IAAT), Sand 1, 72076 Tübingen, Germany
e-mail: klochkov@astro.uni-tuebingen.de
[2] Sternberg Astronomical Institute, Moscow University, 119992 Moscow, Russia

## ABSTRACT

*Context.* Monitoring of pulse period variations in accreting binary pulsars is an important tool to study the interaction between the magnetosphere of the neutron star and the accretion disk. While the X-ray flux of the brightest X-ray pulsars have been successfully monitored over many years (e.g. with *RXTE/ASM, CGRO/BATSE, Swift/BAT*), the possibility to monitor their pulse timing properties continuously has so far been very limited.
*Aims.* In our work we show that the *Swift/BAT* observations can be used to monitor coherent pulsations of bright X-ray sources and use *Swift* archival data to study one of the most enigmatic X-ray pulsars, Hercules X-1. A quasi-continuous monitoring of the pulse period and the pulse period derivative of an X-ray pulsar, here Her X-1, is achieved over a long time ($\gtrsim$4 yr). We compare our observational results with predictions of accretion theory and use them to test different aspects of the physical model of the system.
*Methods.* In our analysis we use the data accumulated with *Swift/BAT* starting from the beginning of 2005 (shortly after launch) until the present time. To search for pulsations and for their subsequent analysis we used the count rate measured by the *BAT* detector in the entire field of view.
*Results.* The slope of the correlation between the locally determined spin-up rate and the X-ray luminosity is measured for Her X-1 and found to be in agreement with predictions of basic accretion torque theory. The observed behaviour of the pulse period together with the previously measured secular decrease of the system's orbital period is discussed in the framework of a model assuming ejection of matter close to the inner boundary of the accretion disk.

**Key words.** X-rays: binaries – stars: neutron – accretion, accretion disks

## 1. Introduction

The persistent accreting pulsar Hercules X-1 was one of the first X-ray sources discovered by the *Uhuru* satellite in 1972 (Tananbaum et al. 1972; Giacconi et al. 1973) and since then it remains one of the most intensively studied X-ray pulsars. The basic phenomenological picture of Her X-1 was established soon after its discovery: a close binary system consisting of an accreting magnetized neutron star with a 1.24 s spin period and a stellar companion HZ Her (first suggested by Liller 1972) – a main sequence star of the spectral type A/F (Crampton 1974). The mass of the optical companion is $\sim$2 $M_\odot$ which places the system between high and low mass X-ray binaries. Other main parameters of the binary system are the following: orbital period $P_{\rm orb} \simeq 1.7$ days, X-ray luminosity of the source $L_{\rm X} \sim 2 \times 10^{37}$ erg s$^{-1}$ for a distance of $\sim$7 kpc (Reynolds et al. 1997). The binary orbit is almost circular (Staubert et al. 2009b) and has an inclination $i \sim 85-88°$ (Gerend & Boynton 1976). The magnetic field strength on the surface of the neutron star is believed to be around $3 \times 10^{12}$ G, as estimated from the energy of the cyclotron resonant scattering feature (Trümper et al. 1978).

Like many other X-ray pulsars, Her X-1 exhibits significant variation of the pulsation period (i.e. spin rate of the neutron star). Alternation of spin-up and spin-down episodes on timescales of several months in this system is superimposed on a background of systematic spin-up (Sheffer et al. 1992; Staubert et al. 2006; Klochkov 2007). The behaviour of the pulsar's spin period on shorter time scales is not very well studied because such a study would require a continuous monitoring of Her X-1

with a sensitive X-ray detector. Only between 1991 and 2000 did the *BATSE* instrument onboard *CGRO* (Fishman et al. 1989) provide information about the source's pulse period on a regular basis. These data allowed Staubert et al. (2006) to reveal an anticorrelation between the pulse period and times of X-ray *turn-ons*, i.e. switching from an *off*-state with low X-ray flux to the so-called *main-on* state with high flux (such turn-ons regularly occur in Her X-1 with a period of $\sim$35 days and are believed to be caused by a precessing tilted accretion disk around the neutron star, see e.g. Gerend & Boynton 1976).

In this work we present a continuous monitoring of the Her X-1 pulse period $P$ and its local (measured at the time of the observation) time derivative $\dot{P}$ using the *Swift/BAT* instrument starting from 2005 (begin of scientific operation) to 2009. We compare the observed pulse period development with that measured previously with *CGRO/BATSE*. The data of the monitoring allowed us to explore for the first time the correlation between the *locally* measured $\dot{P}$ and the X-ray flux of the pulsar and compare the results with predictions of accretion theory. The observed strong spin-down episodes are discussed in the framework of a model assuming ejection of matter from the inner part of the accretion disk along the open magnetic field lines.

## 2. Observations

For our analysis, we used the public archival data obtained with the Burst Alert Telescope (*BAT*, 15–150 keV, Barthelmy et al. 2005) onboard the *Swift* observatory (Gehrels et al. 2004). With

its large field of view (1.4 sterad), the *BAT* instrument was originally designed to provide fast triggers for gamma-ray bursts and their accurate positions in the sky (∼4 arcsec). Following such a trigger, the observatory points in the direction of the burst, which can be then observed with the X-ray and UV/optical telescopes onboard the satellite. While searching for bursts, *BAT* points at different locations of the sky, thus performing an all-sky monitoring in hard X-rays (measurements of the X-ray flux are provided by the *Swift/BAT* team in the form of X-ray light curves for the several hundred bright persistent and transient sources[1]).

Most of the *BAT* observations are stored in the form of detector plane maps (histograms) accumulated over the 5-min exposure time, which limits the possibilities of timing analysis. In addition to the detector plane histograms, however, the stored data contain 64-ms count rates corresponding to the total flux detected by *BAT*. If a bright pulsating source with a known period falls into the field of view of the instrument, the total count rate can be used to search for coherent pulsations of that source. We have used this strategy to measure the 1.24 s pulsations of Her X-1 during its main-on states (when the X-ray flux of the source is high), repeating every ∼35 days.

## 3. Timing analysis of BAT data

To determine the pulse period, we used a method similar to that described by Staubert et al. (2009b). The method includes two techniques for the determination of the period: *epoch folding* with a $\chi^2$ search (e.g. Leahy et al. 1983) and *pulse phase connection* (e.g. Deeter et al. 1981). The first one is used to establish the presence of the periodic signal from Her X-1 in the *BAT* data, determine the approximate period, and construct pulse profiles (by folding the data with the found period), while the second is subsequently applied to the pulse profiles to determine the precise value of the period and its time derivative.

As already mentioned, for our analysis we used the total count rates measured by *BAT* with a time resolution of 64 ms. All times of the count rates were translated to the solar system barycenter and corrected for binary motion (using our newest orbital ephemeris presented in Staubert et al. 2009b). We then performed a period search using *epoch folding* in a narrow period interval around the expected pulse period (∼1.237 s). If a strong periodic signal was present, we determined the period and used it to construct X-ray pulse profiles for subsequent *pulse phase connection*. The integration time in each case was chosen to be large enough to obtain a pulse profile with sufficient statistics (normally ∼1 ks). A typical profile used in our phase-connection analysis is shown in Fig. 1.

To obtain pulse arrival times for the subsequent phase connection analysis we have fit all individual pulse profiles with a template profile constructed by superposing the individual profiles from the same main-on state. In many cases we ignored the data at the start and the end of a main-on where the profiles deviate noticeably from those obtained in the middle of the main-on. Thus, within one main-on, we restricted our analysis to the time intervals where the shape of the pulse profile does not change appreciably. Nevertheless, we cannot completely exclude possible systematic effects which might affect our results due the variation of the profile shape (see also the Discussion). If the interval between the adjacent pulse arrival times is short enough (or if the uncertainty of the assumed pulse period is sufficiently small),
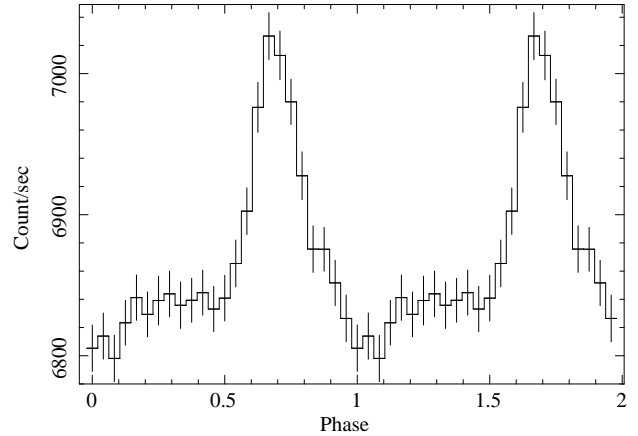
**Fig. 1.** An example of a *Swift/BAT* pulse profile used to study pulse shifts for the precise measurement of the pulse period variations in Her X-1. The profile is taken at MJD 54516.083 with ∼1200 s integration time.

one can reconstruct the number of pulsation cycles passed in between, excluding any mis-counting. In this case, the estimated pulse arrival times can be analytically modelled. For example, if the pulse period $P$ is constant, the expected arrival time of pulse number $n$ is

$$t_n = t_0 + nP, \tag{1}$$

where $t_0$ is the arrival time of the "zero"-th pulse. In the case of non-zero first and second derivatives of the pulse period, the arrival times are given by (see e.g. Staubert et al. 2009b)

$$t_n = t_0 + nP_0 + \frac{1}{2}n^2 P \dot{P}_0 + \frac{1}{6}n^2 P_0^2 \ddot{P}_0 + ..., \tag{2}$$

where $P_0$, $\dot{P}_0$, and $\ddot{P}_0$ are the pulse period and its time derivatives at the time $t_0$ respectively.

A convenient way to explore the variation of the pulse period, often used in the phase connection technique, is to construct a so-called (O–C) diagram showing the estimated (observed) pulse arrival time minus the calculated one assuming a constant period (i.e. using Eq. (1)). An example of such a diagram measured with *BAT* during one of the Her X-1 main-on states is shown in Fig. 2. A straight line in the graph would correspond to a constant period defined by the slope of the line. The solid curve indicates a parabolic fit to the data corresponding to a constant positive $\dot{P}$ according to Eq. (2) (in the shown case the best-fit $\dot{P} \simeq 1.4 \times 10^{-12}$ s/s).

## 4. Pulse period variability

Using the method described in the previous section we determined the pulse period $P$ and its time derivative $\dot{P}$ for most of the Her X-1 main-on cycles observed with *BAT* (for other parts of the 35 d cycle the flux was too low for such determinations). At the time of writing this paper the data are available for the time period from March 2005 to May 2009 that covers 45 35d cycles (main-on states) of the pulsar. For several cycles the *BAT* observations have relatively poor statistics due to gaps in the data. For such cycles, only $P$, but no $\dot{P}$, could be determined. For the cycle with the turn-on at MJD ∼ 54339.68, even the pulse period could not be found due to a gap in the data. However, during
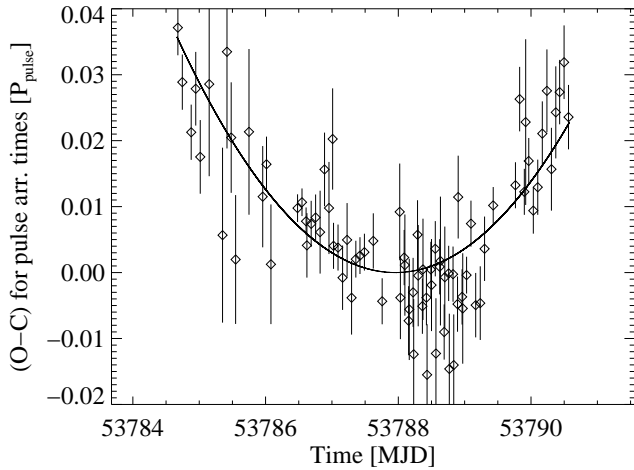
**Fig. 2.** Estimated (observed) minus calculated (assuming a constant period) pulse arrival times of Her X-1 in units of its pulse period during one of its main-on states observed with *Swift/BAT*. A parabolic fit to the data shown with the solid line corresponds to a constant positive $\dot{P} \simeq 1.4 \times 10^{-12}$ s/s (according to Eq. (2)).
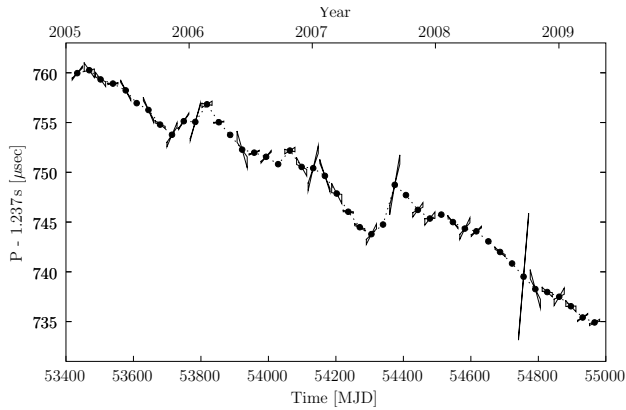


**Fig. 3.** Pulse period $P$ of Her X-1 measured with *Swift/BAT* as a function of time. The cones around each point indicate the allowed range of the slope corresponding to the measured $\dot{P}$ and its uncertainties. Measurement errors of the period itself are smaller than the symbol sizes.

this cycle Her X-1 was observed with the *INTEGRAL* satellite (Staubert et al. 2009b). So, we included the value of $P$ measured with *INTEGRAL* in our data set (since the *INTEGRAL* observations caught only the end of the main-on, $\dot{P}$ could not be measured).

For the main-on starting at MJD ~ 53577.14 only the pulse period $P$ could be measured with *BAT* (no $\dot{P}$). But the main-on was simultaneously observed with the *INTEGRAL* and *RXTE* observatories (Klochkov et al. 2008; Staubert et al. 2009b). The value of $P$ measured during these pointings is consistent (within $1\sigma$ uncertainty) with the value found from the *BAT* data. We consider this agreement as a successful cross-check between the *Swift*, *RXTE*, and *INTEGRAL* observations.

The time evolution of the measured pulse period for the main-ons of Her X-1 is shown in Fig. 3. Where a corresponding value of $\dot{P}$ was measured, the $1\sigma$-uncertainty range is indicated by the cones, the orientation of which reproduce the measured $\dot{P}$ value.

A close quantitative inspection of all measured values of $P$ and $\dot{P}$ leads to the following list of statements about their evolution with time.

– The pulse period evolution shown in Fig. 3 resembles a sawtooth where one can distinguish five spin-down and five spin-up episodes (from comparing adjacent measurements). The overall mean spin-up rate is $\langle\dot{P}\rangle = -1.8203(3) \times 10^{-13}$ s s$^{-1}$ or $-15.728(2)$ ns d$^{-1}$. We note that this is slightly steeper than the general mean spin-up of $-9$ ns d$^{-1}$ observed from the discovery of the source to the dramatic spin-down event during the *Anomalous Low* of 1999/2000 (Klochkov 2007).
– The spin-down episodes (with mean spin-down rates between $0.95 \times 10^{-13}$ and $4.5 \times 10^{-13}$ s s$^{-1}$), lasting from 1 to 3 35 d cycles, are generally shorter than the spin-up episodes (with mean spin-up rates from $2.9 \times 10^{-13}$ to $4.4 \times 10^{-13}$ s s$^{-1}$) which last from 3 to 13 35 d cycles.
– Locally measured $\dot{P}$ values, ranging from $-11 \times 10^{-13}$ s s$^{-1}$ to $+48 \times 10^{-13}$ s s$^{-1}$, show stronger modulation than $\dot{P}$ values found from comparing the pulse period of adjacent 35 d cycles which range from $-6.0 \times 10^{-13}$ s s$^{-1}$ to $+14 \times 10^{-13}$ s s$^{-1}$.
– Generally, the locally measured $\dot{P}$ values and the "cycle-to-cycle" $\dot{P}$ values show a similar behavior (with the former having the larger amplitude). For many points, however, the locally measured $\dot{P}$ is substantially different from the one derived from $P$ values of adjacent measurements (that is, from the slope of the pulse period development).

From the last two statements one can conclude that strong pulse period variations in Her X-1 occur on shorter time scales than the 35 d super-orbital period of the system.

We will discuss the pulse period variations again in Sect. 6.

## 5. Correlation between spin-up rate and X-ray flux

A positive correlation between the spin-up rate of a neutron star and its X-ray luminosity is generally expected from accretion theory (see e.g. Pringle & Rees 1972), where an increase of the mass accretion rate $\dot{M}$ leads to an increase in the rate of change of the neutron star's angular momentum. Such a correlation has been observed in many accreting pulsars (see e.g. Bildsten et al. 1997, for a review). In Her X-1, however, the correlation was so far questionable (see however Wilson et al. 1994; Klochkov 2007). One of the difficulties is the relatively low amplitude of the $\dot{M}$ variation in the system (reflected by the maximum main-on flux, see below), of a factor ~2. Another problem is the lack of local spin-up measurements (so far $\dot{P}$ in Her X-1 was locally measured only in a few cases). For the rest of the existing data $\dot{P}$ was estimated by taking differences of the pulse periods between adjacent main-on states which gives an averaged value over two or more 35 d cycles (see e.g. Klochkov 2007, where data from *CGRO/BATSE* were used). The X-ray luminosity $L_X$ which we assume to be proportional to the mass accretion rate $\dot{M}$ is usually estimated from the maximum X-ray flux during the main-on coincident with the observation (Staubert et al. 2007). Such an estimate is supposed to be very close to the local value of $L_X$.

In this work we have used the values of $\dot{P}$ locally measured with *BAT* to explore the correlation between the spin-up rate and the X-ray luminosity. Following Staubert et al. (2007) we have used the maximum main-on flux detected with *BAT*[2] as a measure of $L_X$. In Fig. 4 we plot the measured pulse period derivative

[2] We used the *Swift/BAT* transient monitor results provided by the *Swift/BAT* team (http://heasarc.gsfc.nasa.gov/docs/swift/results/transients/).
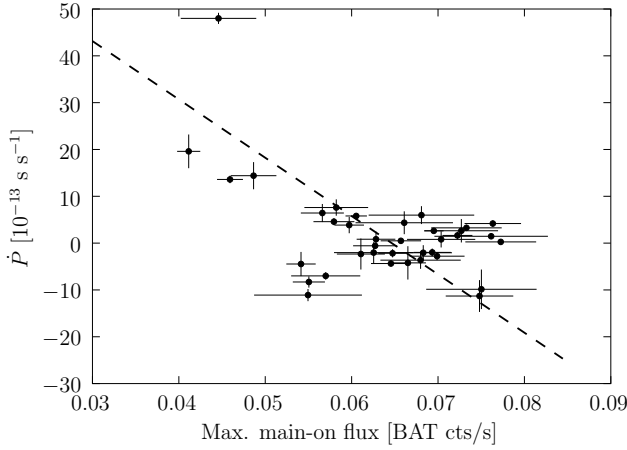
**Fig. 4.** The locally measured time derivative of the pulse period, $\dot{P}$, in Her X-1 versus the maximum X-ray flux during the main-on state as determined from the *Swift/BAT* data. A linear fit (taking uncertainties of both variables into account) is shown with the dashed line.



**Fig. 5.** Pulse period $P$ of Her X-1 measured with *CGRO/BATSE* as a function of time. The values are derived from the publicly available pulse search data (Wilson, priv. comm.). The solid lines indicate the exponential fit to the pulse period during the "relaxation" time after two "glitch"-like episodes.

versus the maximum main-on flux. The dashed line indicates a linear fit to the data that takes uncertainties of both variables into account (using the orthogonal regression method, Boggs et al. 1989). The data indicate an anticorrelation as predicted by the basic accretion theory. Inspection of the linear Pearson's correlation coefficient gives a probability of $\sim 4 \times 10^{-4}$ to find the measured correlation by chance. We note, however, that such a high significance appears mainly due to the group of four points with high spin-down rate and low flux (in the upper left part of the graph in Fig. 4). The rest of the points form an uncorrelated "cloud" around $\dot{P} = 0$. On the other hand, the data contain no points with large spin-down ($\dot{P} > 10^{12}$ s/s) and large luminosity (in the upper right part of the graph) that could destroy the correlation.

The best-fit slope of the $\dot{P}(L_X)$ dependence assuming a linear relation is found to be $\Delta \dot{P}_{-13}/\Delta F_{BAT} = -(1.2 \pm 0.2) \times 10^3$, where $\dot{P}_{-13} = \dot{P}/(10^{-13}$ s/s$)$ and $F_{BAT}$ is the count rate measured with *BAT*. Assuming a distance of 7 kpc (see Introduction) one can find that 0.05 *BAT* cts s$^{-1}$ approximately corresponds to $2 \times 10^{37}$ erg s$^{-1}$. Thus, we can rewrite the found value of the slope as $\Delta \dot{P}_{-13}/\Delta L_{37} = -30 \pm 5$ where $L_{37} = L_X/(10^{37})$ erg s$^{-1}$. At a first approximation the value of the slope can be calculated using the equation:

$$\frac{dI\omega}{dt} = \dot{M}_x \sqrt{GMR_d} - \kappa_0 \frac{\mu^2}{R_c^3} + \kappa_1 \mu^2 \left( \frac{1}{R_d^3} - \frac{1}{R_c^3} \right), \quad (3)$$

where the first term stands for the spin-up from the inner disk radius $R_d$, the second term describes spin-down due to magnetic coupling beyond the corotation radius $R_c$, and the last term takes into account angular momentum exchange due to magnetic coupling in the region between $R_c$ and $R_d$; $\kappa_0$ and $\kappa_1$ are numerical coefficients. The inner disk radius is about the Alfvén radius of the magnetosphere $R_A$, which is determined in the standard way (e.g. Pringle & Rees 1972):

$$R_A = \left( \frac{\mu^2}{2\dot{M}\sqrt{2GM}} \right)^{2/7}. \quad (4)$$

At the corotational regime when $R_d \sim R_c$, the last term in Eq. (3) can be rewritten in the form $\kappa_1 \mu^2 3(R_c - R_d)/R_d^4$ and is much
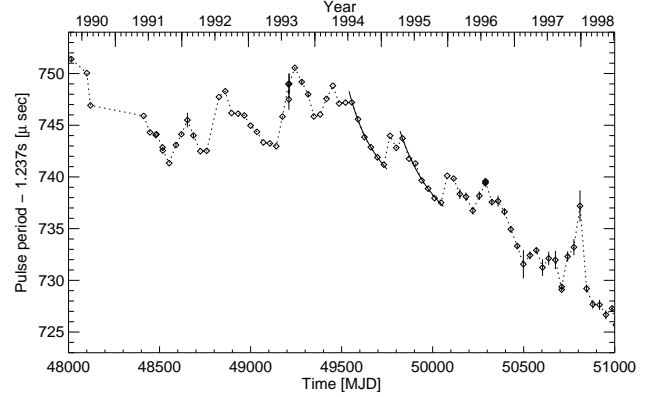
smaller than the first two terms separately, but can be comparable to their difference at the point of equilibrium, where $R_d \simeq R_c$. Indeed, from Eq. (3) one can find that the spin-up and spin-down torques separately would give $\dot{P} \sim +$ or $-10^{-11}$ s s$^{-1}$, whereas on average we observe $< \dot{P} > \sim 10^{-13}$ s s$^{-1}$. Eq. (3) can be rewritten as

$$\dot{P} = -\frac{P^2}{2\pi I} \left( \dot{M} \sqrt{GMR_c} - \kappa_0 \frac{\mu^2}{R_c^3} \right) \quad (5)$$

and used to calculate the theoretical slope of the $\dot{P}(L_X)$ dependence. Here we did not include the third term in Eq. (3), which is by $(R_c - R_d)/R_d$ times smaller than the spin-up term, and can be ignored when calculating the expected slope of $\dot{P} - L_X$ relation. Assuming a radiative efficiency of accretion of $\sim 10\%$ ($L_X = 0.1 \dot{M}c^2$) we can obtain $\partial \dot{P}_{-13}/\partial L_{37} \simeq -50$ which is close to the value of $\Delta \dot{P}_{-13}/\Delta L_{37}$ found from the fit of the *BAT* data ($-30 \pm 5$). A detailed discussion of the observed correlation will be given in Sects. 6.2 and 6.3.

## 6. Discussion

### 6.1. Pulse period variations. Comparison with BATSE data

The general behaviour of the pulse period in Her X-1 measured with *Swift/BAT* (Fig. 3) is similar to that observed previously in this source. The long-term spin-up trend is occasionally interrupted by short (a few 35 d cycles) spin-down episodes. In Fig. 5 we plot for comparison the historical development of the Her X-1 pulse period measured with *CGRO/BATSE*. We have made use of the publicly distributed pulsar data as well as lists kindly provided by Wilson (see also Staubert et al. 2006).

In both the *BATSE* and *BAT* data, the spin-down episodes are generally shorter than the spin-up episodes. One also sees that in most cases the averaged absolute value of $\dot{P}$ is larger during the spin-down intervals than during spin-ups. Such an asymmetry is difficult to explain within the basic accretion theory (i.e. using Eq. (3)) assuming that the spin period reflects stochastic variations of $\dot{M}$. In some cases spin-down episodes with subsequent spin-ups are reminiscent of glitch-like behaviour observed

in some radio-pulsars where a rapid change of the pulse period is followed by a slower "relaxation" to the long-term trend. However, compared to radio pulsars, the "glitches" in Her X-1 appear with an opposite sign: an initial rapid increase of the period is followed by a slower decrease (as it should be if in both radio pulsars and Her X-1 the glitches are caused by a sudden decrease/increase of the moment of inertia of the star's crust). Two such glitch-like episodes are indicated in Fig. 5 by solid lines which show the fit of the "relaxation" intervals by an exponential function on top of the linear decrease of the period (see e.g. Shemar & Lyne 1996). The characteristic relaxation times, $\tau$, for the two cases are around 100 days which is similar to the values observed in radio pulsars (Shemar & Lyne 1996). Some of the other spin-up/spin-down transitions also resemble glitches, even though their decay is less clearly exponential. One should note, however, than in radio pulsars the glitch-like variations of the spin period are predominantly observed in cases of young neutron stars, with characteristic ages ($\tau = P/2\dot{P}$) less than 1 Myr. The neutron star in Her X-1 is believed to be much older.

### 6.2. Correlation $\dot{P} - L_X$

As we have shown, the *BAT* data indicate a correlation between the spin-up rate ($-\dot{P}$) and the X-ray flux $L_X$ with the slope of the correlation consistent with the prediction of the basic accretion theory. However, even for the relatively narrow range of $L_X$ observed in Her X-1 the correlation appears to be surprisingly loose. There are several *physical* and *observational* factors that might introduce dispersion in the observed $\dot{P} - L_X$ relation. The observational factors include the systematics that affects our measurements of the spin-up rate and the X-ray flux. As it was already mentioned in Sect. 3, the pattern-matching technique requires a stable shape of the pulse profiles. Even though we tried to restrict our analysis to the intervals where the pulse profile does not change significantly, we cannot exclude that the variability of the profile shape contributes to the measured value of $\dot{P}$. We believe, however, that this systematic effect, if present, does not exceed the statistical errors. On the other hand, the X-ray luminosity $L_X$ might not be unambiguously related to the maximum main-on flux if the latter is subject to variable absorption by a hot corona even in the middle of a main-on where the angle between the plane of the accretion disk and observer's line of sight reaches a maximum.

A physical reason for the scattering in the correlation is the possible bimodal behaviour of the pulsar where it switches between the spin-up and spin-down regimes at the same level of X-ray luminosity. Such a possibility appears e.g. in the accretion torque theory presented by Lovelace et al. (1995) where spin-up/spin-down transitions occur if the corotation radius is close to the Alfvén radius (or, more precisely, to the turnover radius $r_{to}$ introduced by Lovelace et al. 1995), i.e. if the pulsar is close to the so-called corotational regime when the spin-up and spin-down torques are nearly balanced.

The "uncorrelated" cloud of data points around $\dot{P} = 0$ in Fig. 4 might indicate an area of the spin-up/spin-down transitions (bimodal behaviour) where different values of $\dot{P}$ are observed at the same level of $L_X$.

Another factor that might increase the dispersion of data points in the correlation relates to the idea of a freely processing neutron star in Her X-1 (Trümper et al. 1978). While having a number of difficulties from the theoretical point of view (Shaham 1977; Sedrakian et al. 1999), this hypothesis, however, can explain the systematic variation of X-ray pulse profiles exhibited by the system (Staubert et al. 2009a, and references

therein). Free precession results in systematic variations of the observed spin period of the neutron star (Shakura 1988; Postnov et al. 1991; Bisnovatyj-Kogan & Kahabka 1993). With the geometrical parameters of free precession that can be assumed for Her X-1 on the basis of modelling of its pulse profiles (Postnov, priv. comm., paper in preparation), the amplitude of $\dot{P}$ variation due to free precession might be as high as $10^{-12}$ s/s which is comparable to the variations that we observe with *BAT* (Fig. 4). Since the precessional phase might be different in different observations, the described effect might introduce additional scattering in the $\dot{P}-L_X$ correlation if the free precession indeed takes place in Her X-1.

### 6.3. Evidence for the coronal mass ejection

As mentioned in Sect. 5, in Her X-1, spin-up and spin-down torques are very well balanced, so that the averaged $\dot{P}$ is relatively close to zero. However, from the points in the upper left part of the graph in Fig. 4, one can conclude that there occur extremely large spin-down torques (at small fluxes), which are up to 5 times as strong as spin-up ones. So, the key feature to explain is why do we observe such strong spin-down episodes?

One possibility is to assume that the accretion disk carries some magnetic field which can interact via reconnection with the neutron star's magnetosphere beyond the corotation radius $R_c$. This might imply that beyond $R_c$ the field lines can sometimes inflate to become open (see also discussion in Lovelace et al. 1995). During such episodes, a substantial fraction of matter in the inner part of the accretion disk can escape the system in the form of a coronal wind ejection along the open field lines.

Such an ejection of matter should be reflected in a secular change of the system's orbital period which is indeed observed in Her X-1 (Deeter et al. 1991; Staubert et al. 2009b). To assess the importance of coronal mass ejections for the orbital period evolution, we invoke general considerations of the non-conservative treatment of binary orbital parameters (see e.g. Grishchuk et al. 2001). We shall assume a circular binary orbit. Let $M_o$ be the mass of the optical star and $M_x$ – that of the neutron star, $q = M_x/M_o$ is the binary mass ratio. The total angular momentum of the binary is mostly stored in the orbital motion of the binary components: $J = J_{orb} = M_x M_o/(M_x + M_o)\omega_{orb}a^2$, where $\omega_{orb} = 2\pi/P_{orb}$ is the orbital angular frequency, $P_{orb}$ is the orbital period, and $a = a_x + a_o$ is the binary's semimajor axis. Let us define the non-conservativeness parameter in the standard way (e.g. Ritter & Kolb 1992):

$$\eta = -\frac{\dot{M}_x}{\dot{M}_o} \le 1, \quad \dot{M}_o < 0. \tag{6}$$

Next we assume that the ejected mass carries away the specific angular momentum of the neutron star $j_x = \omega_{orb}a_x^2 = \omega_{orb}a^2(M_o/(M_x + M_o))^2$. (This assumption is justified by the small inner radius of the disk $R_d \ll a_x$.) Then using the Kepler's 3rd law and the total angular momentum balance, $\dot{J} = j_x(\dot{M}_x + \dot{M}_o)$, we can express the fractional change of the orbital period through $\dot{M}_x/M_x$, $q$ and $\eta$:

$$\frac{1}{3}\frac{\dot{P}_{orb}}{P_{orb}} = -\frac{\dot{M}_x}{M_x}\left[1 - \frac{q}{\eta} - \left(1 - \frac{1}{\eta}\right)\frac{q/3 + 1}{q + 1}\right]. \tag{7}$$

For $\eta = 1$ the familiar expression for the conservative mass exchange is obtained. It is convenient to normalize the mass accretion rate onto the neutron star $\dot{M}_x$ to the value that can be derived

from the observed fractional change of the orbital period in the conservative case:

$$\frac{(\dot{M}_x)_{\text{cons}}}{M_x} = \frac{1}{3}\frac{\dot{P}_{\text{orb}}}{P_{\text{orb}}}\frac{1}{q-1}\,,\tag{8}$$

so that $\dot{m} \equiv \dot{M}_x/(\dot{M}_x)_{\text{cons}}$. In Her X-1 $q \simeq 0.63$ and one finds $(\dot{M}_x)_{\text{cons}} \simeq 8 \times 10^{17}\,\text{g s}^{-1}$ for the measured $\dot{P}_{\text{orb}} = -4.85 \times 10^{-11}\,\text{s s}^{-1}$ (Staubert et al. 2009b). Then we can eliminate $\dot{P}_{\text{orb}}/P_{\text{orb}}$ from the left hand side of Eq. (7) to obtain the equation for $\eta$ at a given $\dot{m}$:

$$\eta = \frac{q^2 + \frac{2}{3}q - 1}{\frac{q^2-1}{\dot{m}} + \frac{2}{3}q}\,.\tag{9}$$

From here we see that $\dot{m} < 1$ leads to $\eta < 1$, i.e. if one wants to decrease the mass accretion rate onto the neutron star to get a smaller X-ray luminosity (as is the case of Her X-1, where the mean observed $L_x \sim 2 \times 10^{37}\,\text{erg s}^{-1}$ is 4 times smaller than the one following from the conservative mass exchange analysis, Staubert et al. 2009b), a non-conservative mass exchange is required. Specifically, if we want to bring into accordance the observed $\dot{P}_{\text{orb}}$ and $L_X$ in Her X-1, we would need $\dot{m} \simeq 1/4$ and (from Eq. (9)) $\eta \sim 0.1$, a fairly high non-conservative mass exchange.

The binary mass ratio $q$ in Her X-1, however, may be uncertain. Indeed, recent analysis of non-LTE effects in the formation of the $H_\gamma$ absorption line allows two solutions: $q = 0.45$ and $q = 0.72$ (Abubekerov et al. 2008). Equation (8) implies that the critical $(\dot{M}_x)_{\text{cons}}$ decreases for smaller $q$: for $q = 0.45$ we obtain $(\dot{M}_x)_{\text{cons}} \simeq 5.4 \times 10^{17}\,\text{g s}^{-1}$. For this mass ratio the appropriate value of the dimensionless parameter $\dot{m}$ is $1/2$, for which from Eq. (9) we find $\eta \simeq 0.38$. This value implies that on average about half of the matter transferred through the disk should escape from the system to provide the observed decrease of the system's orbital period. Note, however, that such a small mass ratio suggests an unusually small mass of the neutron star of about $0.85\,M_\odot$.

It is very likely that an accretion disk corona is present in Her X-1 (see the recent analysis of *Chandra* X-ray observations by Ji et al. 2009). This suggests that there might be a permanent coronal accretion disk wind which carries away some angular momentum from the system. Episodic ejection of matter in Her X-1 has sporadically been invoked in the literature to explain some properties of the system. Crosa & Boynton (1980) found that the average mass transfer rate to the outer rim of the accretion disk is somewhat larger than that required to maintain the observed X-ray luminosity. In the model of Schandl & Meyer (1994), the disk wind results from irradiation of the disk by the central source. Vrtilek et al. (2001) and Boroson et al. (2001) found signatures of outflowing gas in the UV spectrum of the system. In the framework of our model, the mass ejection from the system through the open magnetic field lines occurs most efficiently during strong spin-down episodes which are associated with low X-ray luminosity. Indeed, as we see in Fig. 4, the observed X-ray flux is decreased by a factor of two during strong spin-down. From Eq. (9) it is easy to find that at a given $q$ a fractional decrease in $\dot{m}$ leads to a comparable fractional decrease in $\eta$, i.e. accretion indeed becomes more non-conservative during strong mass ejection episodes. During such episodes, the neutron star spin-down power $I\omega\dot{\omega}$ is spent to expel accreting matter from the inner disk radius $R_d \sim R_c$:

$$I\omega\dot{\omega} \sim \dot{M}_{\text{ej}}\frac{GM}{R_c}\,.\tag{10}$$

This equation is satisfied for the observed parameters of Her X-1: the ejected mass rate during strong spin-downs $\dot{M}_{\text{ej}} \sim 0.5\dot{M}_x \simeq 10^{17}\,\text{g s}^{-1}$, $\dot{P} \simeq 10^{-12}\,\text{s s}^{-1}$, and $R_c \simeq 1.3 \times 10^8\,\text{cm}$.

## 7. Summary

We have used the publicly available *Swift/BAT* data to study the long-term behaviour of the pulsar's spin period in Her X-1. The measured pulse period variations were compared with those observed previously with *CGRO/BATSE*.

For the first time, the pulse period derivative was measured for a long series of observed main-on states of the source. This allowed us for the first time to test the correlation between the X-ray luminosity and the locally measured spin-up rate of the neutron star in Her X-1. We argue that the data indeed show such a correlation with the slope consistent with the prediction of the basic accretion theory for the parameters of Her X-1. The relatively large scattering of the data points in the vicinity of $\dot{P} \sim 0$ can be caused by the bimodal behaviour of the accretion flow configuration at the magnetospheric boundary which results in switching of the pulsar between spin-up and spin-down branches when it stays close to the corotational regime. In addition, free precession of the neutron star, if it takes place in the system, can significantly affect the measured values of $\dot{P}$ and, therefore, contribute to the scattering.

We argue that together with the long-term decrease of the orbital period in Her X-1 the measured pulse period behaviour requires the presence of mass ejection from the inner parts of the accretion disk along the open magnetic field lines. The mass ejection episodes probably take place during strong spin-down episodes which are associated with the low X-ray luminosity.

The described technique allows one to use the *BAT* instrument as a long-term monitor of spin periods in other bright accreting pulsars (see also Camero-Arranz et al. 2009).

## References

Abubekerov, M. K., Antokhina, E. A., Cherepashchuk, A. M., et al. 2008, Astron. Rep., 52, 379
Barthelmy, S. D., Barbier, L. M., Cummings, J. R., et al. 2005, Space Sci. Rev., 120, 143
Bildsten, L., Chakrabarty, D., Chiu, J., et al. 1997, ApJS, 113, 367
Bisnovatyj-Kogan, G. S., & Kahabka, P. 1993, A&A, 267, L43
Boggs, P. T., Donaldson, J. R., Byrd, R. H., et al. 1989, ACM Trans. Math. Softw., 15, 348
Boroson, B., Kallman, T., & Vrtilek, S. D. 2001, ApJ, 562, 925
Camero-Arranz, A., Finger, M. H., Ikhsanov, N. R., Wilson-Hodge, C. A., & Beklen, E. 2009, ArXiv e-prints
Crampton, D. 1974, ApJ, 187, 345
Crosa, L., & Boynton, P. E. 1980, ApJ, 235, 999
Deeter, J. E., Boynton, P. E., & Pravdo, S. H. 1981, ApJ, 247, 1003
Deeter, J. E., Boynton, P. E., Miyamoto, S., et al. 1991, ApJ, 383, 324
Fishman, G. J., Meegan, C. A., Wilson, R. B., et al. 1989, in BAAS, 21, 860
Gehrels, N., Chincarini, G., Giommi, P., et al. 2004, ApJ, 611, 1005
Gerend, D., & Boynton, P. E. 1976, ApJ, 209, 562
Giacconi, R., Gursky, H., Kellogg, E., et al. 1973, ApJ, 184, 227
Grishchuk, L. P., Lipunov, V. M., Postnov, K. A., Prokhorov, M. E., & Sathyaprakash, B. S. 2001, Physics Uspekhi, 44, 1

Ji, L., Schulz, N., Nowak, M., Marshall, H. L., & Kallman, T. 2009, ArXiv e-prints

Klochkov, D. 2007, Ph.D. Thesis, University of Tübingen, Germany, http://w210.ub.uni-tuebingen.de/volltexte/2007/3181/pdf/disser.pdf

Klochkov, D., Staubert, R., Postnov, K., et al. 2008, A&A, 482, 907

Leahy, D. A., Elsner, R. F., & Weisskopf, M. C. 1983, ApJ, 272, 256

Liller, W. 1972, IAU Circ., 2415

Lovelace, R. V. E., Romanova, M. M., & Bisnovatyi-Kogan, G. S. 1995, MNRAS, 275, 244

Postnov, K. A., Prokhorov, M. E., & Shakura, N. I. 1991, in High-Energy Astrophysics. American and Soviet Perspectives, ed. W. H. G. Lewin, G. W. Clark, R. A. Sunyaev, K. K. Trivers, & D. M. Abramson, 307

Pringle, J. E., & Rees, M. J. 1972, A&A, 21, 1

Reynolds, A. P., Quaintrell, H., Still, M. D., et al. 1997, MNRAS, 288, 43

Ritter, H., & Kolb, U. 1992, A&A, 259, 159

Schandl, S., & Meyer, F. 1994, A&A, 289, 149

Sedrakian, A., Wasserman, I., & Cordes, J. M. 1999, ApJ, 524, 341

Shaham, J. 1977, ApJ, 214, 251

Shakura, N. I. 1988, in Proc. "Physics of Neutron Stars", Leningrad, 2, english translation: Physics of Neutron Stars, ed. A. M. Kaminker, Nova, Sci. Publ., Inc., 55, 1995

Sheffer, E. K., Kopaeva, I. F., Averintsev, M. B., et al. 1992, Sov. Astron., 36, 41

Shemar, S. L., & Lyne, A. G. 1996, MNRAS, 282, 677

Staubert, R., Schandl, S., Klochkov, D., et al. 2006, in The Transient Milky Way: A Perspective for MIRAX, ed. F. D'Amico, J. Braga, & R. E. Rothschild, AIP Conf. Ser., 840, 65

Staubert, R., Shakura, N. I., Postnov, K., et al. 2007, A&A, 465, L25

Staubert, R., Klochkov, D., Postnov, K., et al. 2009a, A&A, 494, 1025

Staubert, R., Klochkov, D., & Wilms, J. 2009b, A&A [arXiv:0904.2307], Accepted

Tananbaum, H., Gursky, H., Kellogg, E. M., et al. 1972, ApJ, 174, L143

Trümper, J., Pietsch, W., Reppin, C., et al. 1978, ApJ, 219, L105

Vrtilek, S. D., Quaintrell, H., Boroson, B., et al. 2001, ApJ, 549, 522

Wilson, R. B., Finger, M. H., Pendleton, G. N., Briggs, M., & Bildsten, L. 1994, in The Evolution of X-ray Binariese, ed. S. Holt, & C. S. Day, AIP Conf. Ser., 308475

# Appendix B

# Quasi-periodic flares in EXO 2030+375 observed with INTEGRAL

**Astronomy & Astrophysics**

L        E

# Quasi-periodic flares in EXO 2030+375 observed with INTEGRAL

D. Klochkov[1], C. Ferrigno[2], A. Santangelo[1], R. Staubert[1], P. Kretschmar[3], I. Caballero[4],
K. Postnov[5], and C. A. Wilson-Hodge[6]

[1] Institut für Astronomie und Astrophysik, Universität Tübingen (IAAT), Sand 1, 72076 Tübingen, Germany
   e-mail: klochkov@astro.uni-tuebingen.de
[2] ISDC Data Center for Astrophysics of the University of Geneva, chemin d'Écogia 16, 1290 Versoix, Switzerland
[3] European Space Astronomy Centre (ESA/ESAC), Science Operations Department, Villanueva de la Cañada (Madrid), Spain
[4] CEA Saclay, DSM/IRFU/SAp-UMR AIM (7158) CNRS/CEA/Université Paris Diderot, 91191 Gif-sur-Yvette, France
[5] Sternberg Astronomical Institute, Universitetski pr. 13, 119991 Moscow, Russia
[6] NASA Marshall Space Flight Center, Huntsville, AL 35812, USA

Received 30 September 2011 / Accepted 6 November 2011

**ABSTRACT**

*Context.* Episodic flaring activity is a common feature of X-ray pulsars in HMXBs. In some Be/X-ray binaries flares were observed in quiescence or prior to outbursts. EXO 2030+375 is a Be/X-ray binary showing "normal" outbursts almost every ~46 days, near periastron passage of the orbital revolution. Some of these outbursts were occasionally monitored with the INTEGRAL observatory.
*Aims.* The INTEGRAL data revealed strong quasi-periodic flaring activity during the rising part of one of the system's outburst. Such activity has previously been observed in EXO 2030+375 only once, in 1985 with EXOSAT. (Some indications of single flares have also been observed with other satellites.)
*Methods.* We present the analysis of the flaring behavior of the source based on INTEGRAL data and compare it with the flares observed in EXO 2030+375 in 1985.
*Results.* Based on the observational properties of the flares, we argue that the instability at the inner edge of the accretion disk is the most probable cause of the flaring activity.

**Key words.** stars: neutron – accretion, accretion disks – X-rays: binaries

## 1. Introduction

Accreting X-ray pulsars, mostly residing in high-mass X-ray binaries (HMXBs), often show abrupt increases in their X-ray luminosity lasting from a few tens of seconds to several hours – X-ray flares. Flaring activity is often observed on top of a slower flux variation related to X-ray outbursts or super-orbital modulation. Among the best-known "flaring" X-ray pulsars are LMC X-4 (e.g. Moon et al. 2003b, end references therein), SMC X-1 (Angelini et al. 1991; Moon et al. 2003a), Vela X-1 (Kreykenbohm et al. 2008; Fürst et al. 2010). X-ray binaries with a donor star of Be (or Oe) spectral type (Be/X-ray binaries or BeXRB) are currently the most numerous class of HMXBs with X-ray pulsars (Liu et al. 2006), although another class of HMXB pulsars, the supergiant fast X-ray transients (SFXT), is rapidly growing (e.g. Sidoli 2011). BeXRBs are characterized by periodic or sporadic X-ray outbursts lasting from several days to several weeks when the neutron star accretes matter from the equatorial disk around the donor star (see e.g. Reig 2011, for a recent review). These systems are also known to show occasional X-ray flares (Finger et al. 1999; Reig et al. 2008; Caballero et al. 2008; Postnov et al. 2008).

Probably the most remarkable flaring activity among BeXRBs was exhibited by the 42 s pulsar EXO 2030+375. A series of six roughly equidistant flares with a mean period of ~four hours was observed with the EXOSAT satellite a few months after the giant outburst of the source in 1985 (Parmar et al. 1989). EXO 2030+375 is one of the most regularly monitored BeXRBs. In addition to two "major" outbursts in 1985 and 2006 with a peak X-ray luminosity of $L_X \gtrsim 10^{38}$ erg s$^{-1}$, assuming a distance

of 7 kpc (Wilson et al. 2002), the source exhibited less powerful "normal" outbursts with $L_X \sim 10^{37}$ erg s$^{-1}$ almost every orbit. The orbital period of the system is ~46 d (Wilson et al. 2008).

Some flaring of EXO 2030+375 has been reported since the EXOSAT observations, but it has generally appeared to be a single flare during the rise of normal outbursts (Reig & Coe 1998; Camero Arranz et al. 2005). Flares were also apparently present during and between the normal outbursts shortly after the 2006 major outburst (Fig. 3 in Wilson et al. 2008). But the short duration and broad spacing of the observations make it unclear whether this is the same quasi-periodic phenomenon that was seen with EXOSAT. In this Letter we present the INTEGRAL observations of the source that, for the first time since the EXOSAT observations, reveal strong quasi-periodic flaring behavior.

## 2. Observations and data processing

Since its major outburst in 2006, EXO 2030+375 has repeatedly appeared in the field of view of INTErnational Gamma Ray Astrophysics Laboratory (INTEGRAL, Winkler et al. 2003) during the observational program concentrated on the "Cygnus Region". The INTEGRAL observatory has three main X-ray instruments: (i) the imager IBIS sensitive from ~20 keV to a few MeV with high spatial and moderate spectral resolution (Ubertini et al. 2003); (ii) the spectrometer SPI, which is sensitive in the roughly same energy range as IBIS, but with much higher spectral resolution and substantially lower imaging capability (Vedrenne et al. 2003); and (iii) the X-ray monitor
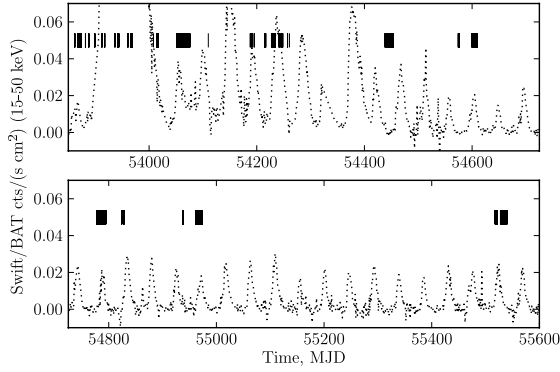
JEM-X with moderate spectral and spatial resolution, operating between ~3 and ~35 keV (Lund et al. 2003). INTEGRAL observations normally consist of a series of pointings called Science Windows, 2 to 4 ks each.

Because the times of the observations were not optimized for EXO 2030+375, the INTEGRAL coverage of the source's normal outbursts is rather sparse. The *Swift*/BAT light curve of the pulsar[1] with the indicated INTEGRAL observations is shown in Fig. 1.

For our analysis we used the ISGRI detector layer of IBIS sensitive in the 20–300 keV energy range (Lebrun et al. 2003) and JEM-X. Owing to limited count-rate statistics, no additional information could be gained from SPI data. The standard data processing was performed with version 9 of the Offline Science Analysis (OSA) software provided by the INTEGRAL Science Data Centre (ISDC, Courvoisier et al. 2003). We performed an additional gain correction of the ISGRI energy scale based on the background Tungsten spectral lines.

To search for the flaring activity, we examined the entire IBIS/ISGRI light curve by combining the publicly available ISGRI data products in the HEAVENS data base[2] with the results of our own analysis. We did not find any clear evidence of flares in all the data except for the latest INTEGRAL observations of the source in November and December 2010 (MJD ~55 520–55 540), partially covering a normal outburst. The rising part of the outburst is shown in Fig. 2. The upper panel of Fig. 3 shows the entire outburst as observed with INTEGRAL. In this work we concentrate on the analysis of the source's flaring behavior during this outburst.

## 3. Timing analysis

As can be seen in Fig. 2, the flux in the rising part of the outburst experiences quasi-periodic oscillations/flares that cease as the averaged flux increases. One can identify at least five subsequent flares with a mean period of ~0.3 days (~7 h).

To characterize the level of the flux variability during the outburst we calculated the normalized excess variance in the light curve in relatively broad time intervals. We defined four equal adjacent intervals in the rising part and five equal adjacent intervals in the decay. The normalized excess variance is often used
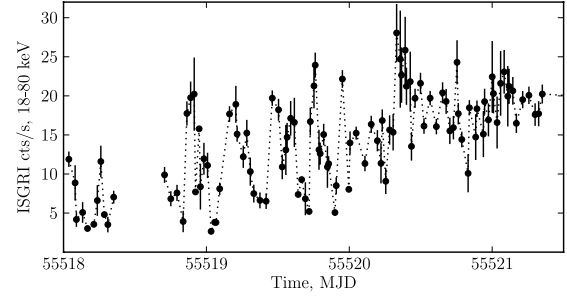
---

[1] We used the *Swift*/BAT transient monitor results provided by the *Swift*/BAT team

[2] http://www.isdc.unige.ch/heavens/heavens

**Fig. 2.** INTEGRAL/ISGRI light curve of EXO 2030+375 during the rise of its normal outburst in Nov.–Dec. 2010. The flaring activity is clearly seen. The light curve of the entire outburst is shown in Fig. 3. One Crab corresponds to ~260 cts/s in the specified energy range.
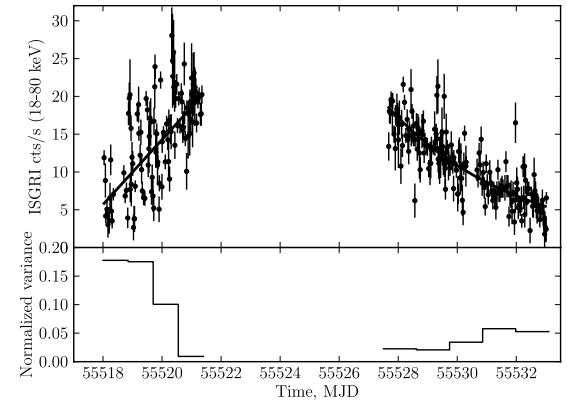


**Fig. 3.** *Top*: ISGRI light curve of the EXO 2030+375 outburst approximated with a polynomial function (solid curve) which represents the averaged evolution of the flux. *Bottom:* normalized excess variance of the source flux with respect to the polynomial function.

as a simple measure of the intrinsic variability amplitude in light curves, (see e.g. Nandra et al. 1997):

$$\sigma^2_{\text{NXS}} = \frac{1}{N\langle f\rangle^2}\Sigma^N_{i=1}[(f_i - f_i^{\text{aver}})^2 - \sigma_i^2]. \tag{1}$$

Here $N$ is the number of data points in the corresponding time interval, $f_i$ is the flux of the individual data points, $\sigma_i$ – their uncertainty, $f_i^{\text{aver}}$ is the smoothed evolution of the flux obtained by a polynomial fit to the light curve (upper panel of Fig. 3), and $\langle f\rangle$ is the mean value of the flux within the interval. The normalized variance $\sigma^2_{\text{NXS}}$ in our case represents the amplitude of intrinsic flux variations superimposed on the smoothed flux development. The term $\sigma_i$ under the summation ($\Sigma$) eliminates the contribution of the Poisson noise. The bottom panel of Fig. 3 represents the normalized variance as a function of time during the outburst of EXO 2030+375. It can be seen that the amplitude of the variability is high at the rising phase (corresponding to the flaring episode). Then it decreases towards the maximum of the outburst and remains low during the decay.

To study periodicity of the flares, we performed a formal period search in the rising part of the outburst (between MJD 55 518.5 and 55 521.5) using the Lomb-Scargle periodogram. The results are presented in Fig. 4. The periodogram shown in the top panel indicates a clear peak around ~0.3 days (~7 h). The averaged profile obtained by folding the light curve with this period is shown in the bottom panel. The profile shape is asymmetric and characterized by a steep rise and a slower decay.
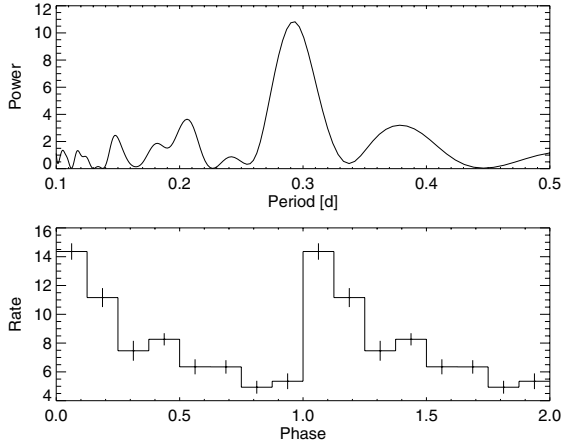
**Fig. 4.** *Top*: Lomb-Scargle periodogram of the "flaring" part of EXO 2030+375 light curve (between MJD 55 518.5 and 55 521.5). The peak around ~0.3 d is clearly seen. *Bottom:* "Flaring" part of the light curve folded with best period found from the periodogram (0.293 d).
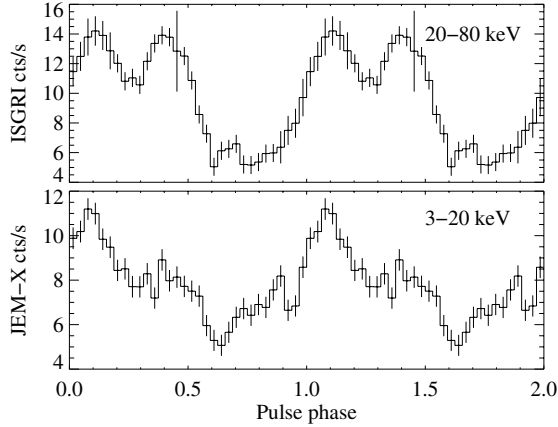


**Fig. 5.** Pulse profiles of EXO 2030+375 obtained with ISGRI (*top*) and JEM-X (*bottom*) instruments during the outburst (MJD 55 518.5-55 533.0).

We used the INTEGRAL data to study the pulse period behavior and pulse profiles during the outburst. The photon arrival times were converted to the reference frame of the solar system barycenter and corrected for the binary orbital motion using the ephemeris by Wilson et al. (2008). Using the pulse-phase-connection technique (e.g. Staubert et al. 2009), we found the pulse period $P = 41.31516(2)$ s at the epoch $T_0$(MJD) = 55 526.056994 and the period derivative $\dot{P} = -1.9(1) \times 10^{-9}$ s/s, that indicates significant spin-up. We used the measured pulse ephemeris to construct and study the pulse profiles of the source. We could not find any difference between the profiles obtained during the rise and decay of the outburst. Figure 5 shows the profiles accumulated during the entire outburst.

## 4. Spectral analysis

For the spectral analysis we used JEM-X data between 3.5 and 35 keV, and ISGRI data between 20 and 80 keV. We added systematic uncertainties at the level of 2% to the *JEM-X* spectra and 1% to the *ISGRI* spectra based on the recommendations of the instrument teams and the Crab observations. The spectrum of the source during the outburst (accumulated between MJD
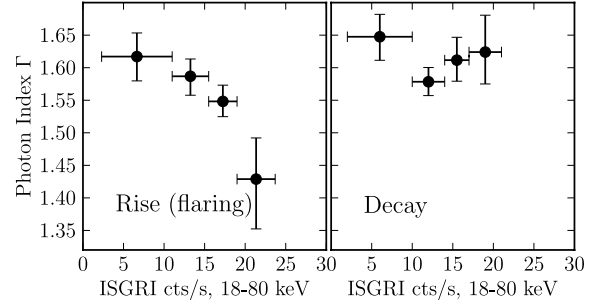


**Fig. 6.** Photon index $\Gamma$ as a function of flux during the rising (flaring) part of the outburst *(left)* and the decay phase *(right)*. One Crab corresponds to ~260 cts/s in the specified energy range.

55 518.5 and 55 533.0) was modeled with the cutoff-powerlaw model ($F(E) \propto E^{-\Gamma} \times \exp [E/E_{\text{fold}}]$, where $E$ is the photon energy, $\Gamma$ and $E_{\text{fold}}$ are the photon index and the folding energy, respectively) modified at lower energies by photoelectric absorption.

The best-fit parameters are $\Gamma = 1.6(1)$, $E_{\text{fold}} = 30(2)$ keV, the absorption column density $n_{\text{H}} = 11(1) \times 10^{22}$ hydrogen atoms per cm$^2$. The uncertainties in parentheses refer to the last digit and are at the 90% confidence level. The value of $n_{\text{H}}$ is substantially higher than measured in previous observations of the source, including older INTEGRAL measurements ($1-3 \times 10^{22}$ cm$^{-2}$, e.g. Klochkov et al. 2007; Wilson et al. 2008). We note, however, that studying $n_{\text{H}}$ with JEM-X is generally problematic as the data below ~3 keV are not available. The significance of the measured increase in absorption is therefore questionable.

The data quality does not permit spectroscopy of individual flares. To characterize the spectral behavior of EXO 2030+375 during the flaring episode and compare it with the rest of the outburst, we explored the luminosity-dependence of the source spectrum during the rising (flaring) part and the decay of the outburst. We grouped the individual INTEGRAL pointings according to the measured flux in the 20–80 keV range. For each group we extracted and analyzed the X-ray spectrum using the spectral model described above. The statistics did not allow us to explore the dependence of each individual spectral parameter on flux. We therefore fixed $n_{\text{H}}$ and $E_{\text{fold}}$ to their averaged values ($11 \times 10^{22}$ cm$^{-2}$ and 30 keV, respectively) and explored the photon index $\Gamma$ as a function of flux.

The resulting dependence is shown in Fig. 6 for the rise (left) and decay (right) of the outburst. Higher values of $\Gamma$ correspond to a softer spectrum (see the model description above). The horizontal error bars represent the width of the flux bins. The vertical error bars indicate $1\sigma$-uncertainties. While the spectrum apparently tends to get harder with increasing flux during the rising part of the outburst, it remains roughly constant during the decay. To quantify this behavior, we performed linear fits to the data points and calculated the slopes with the corresponding uncertainties. The slope is $(-9.0 \pm 3.7) \times 10^{-3}$ (cts/s)$^{-1}$ in the rising part and $(2.8 \pm 4.2) \times 10^{-3}$ (cts/s)$^{-1}$ in the decay of the outburst (uncertainties at $1\sigma$ confidence level).

## 5. Discussion

A direct comparison of the flares presented here with those observed with EXOSAT in 1985 revealed significant similarity. The peak fluxes and the relative amplitude of the flares are roughly the same in both episodes. Also the average shape – fast rise/slow decay – is similar in the two cases. The mean period

is, however, different: ~4 h for the EXOSAT flares and ~7 h for the INTEGRAL ones. The location of the EXOSAT flares with respect to the nearest "normal" outburst is difficult to reconstruct because no monitoring of the source flux (apart from the EXOSAT data themselves) was performed at the time. Since the orbital phase of "normal" outbursts varies significantly with time (Wilson et al. 2002), the extrapolation of the orbital phase ephemeris back to the EXOSAT observations would not resolve the problem.

X-ray flares in accreting pulsars are usually attributed to one of the following mechanisms: (1) instabilities of the accretion flow around/within the magnetospheric boundary (e.g. Moon et al. 2003b; Postnov et al. 2008); (2) highly inhomogeneous stellar wind of the donor star (e.g. Taam et al. 1988; Walter & Zurita Heras 2007); and (3) nuclear burning at the neutron star surface (e.g. Levine et al. 2000; Brown & Bildsten 1998). The nuclear burning scenario is, however, difficult to reconcile with a relatively high accretion rate before and after a flare, which would suppress the thermonuclear instability (Bildsten & Brown 1997). In the case of EXO 2030+375, inhomogeneities of the companion's stellar wind are also unlikely to be a direct cause of the flares for the following reasons. First, the viscous time of the accretion disk that is believed to be present in EXO 2030+375 during normal outbursts (Wilson et al. 2002) and to even survive during quiescence (Hayasaki & Okazaki 2006), is at least several days, which would smooth out any variations in the mass accretion rate $\dot{M}$ caused by inhomogeneity of the wind shorter than this time. Second, nonuniform stellar wind cannot explain the observed quasi-periodic appearance of the flares. On the other hand, various kinds of magneto-hydrodynamic instabilities at the inner edge of the accretion disk may easily lead to oscillations in the mass flow towards the polar caps of the neutron star (Apparao 1991; Postnov et al. 2008; D'Angelo & Spruit 2010), leading to the observed flaring activity. For example, D'Angelo & Spruit (2010) have illustrated that when the magnetospheric radius $r_m$ (where magnetic field of the neutron star truncates the accretion disk) is larger but close to the corotation radius $r_c$ (where the Keplerian frequency is equal to the accretor's spin frequency), matter in the inner regions of the disk will pile up leading to an increase in the local gas pressure and, therefore, a decrease in $r_m$. When $r_m$ crosses $r_c$, the accumulated reservoir of gas is accreted by the neutron star and the cycle repeats.

To assess the applicability of this scenario to the flares observed in EXO 2030+375, we estimated the expected characteristic time scale of $\dot{M}$-oscillations. Without going into physical details of the disk-field coupling at $r_m$ one would generally expect that the oscillations in $\dot{M}$ take place on the time scale close to the local viscous time at $r_m \sim r_c$. Following the standard $\alpha$-viscosity prescription (Shakura & Sunyaev 1973), this time can be estimated as $\tau_c \sim r_c^2/\nu(r_c) \sim 1/[\Omega\alpha(H/R)^2]$, where $\nu(r_c)$ is the viscosity at $r_c$, $\Omega$ is the spin frequency of the neutron star, and $(H/R)$ the semithickness of the accretion disk. Using "standard" values of $\alpha = 0.1$, $H/R = 0.05$, and the known pulse period $P \simeq 40$ s, one gets $\tau_c \sim 7$ h, i.e. of several hours, as was observed.

The averaged profile of the flares is characterized by a steep rise and a slower decay (Fig. 4), which is very similar to the flares observed with EXOSAT in 1985 (Fig. 2 of Parmar et al. 1989). According to the authors, such a shape suggests a "draining reservoir" that is in line with the picture described above (matter piling up on the inner edge of the disk).

The observed difference in the spectral behavior between the flaring part and the rest of the outburst (Sect. 4) suggests different configurations of the region where matter couples to the

field lines. Such a difference is indeed expected if the flares are caused by the oscillating inner edge of the accretion disk. In this case, matter from the oscillating inner disk rim would couple to different dipole field lines of the neutron star (and follow them) compared to the decay part of the outburst where the configuration of the inner disk rim is presumably stable.

The difference in the mean period of flares in the INTEGRAL and EXOSAT observations can also be understood in the described picture. The period must depend on the mass transfer rate through the accretion disk, i.e. time needed to refill the reservoir. This rate could be different between the EXOSAT and INTEGRAL observations due to, e.g., changes in the state of the Be-disk. In Fig. 2 one might also notice some shortening of the the flare separation time as the flux increases (although this behavior is difficult to quantify with the available statistics). Such behavior, if real, might reflect shortening of the reservoir refill time as the mass transfer rate increases towards the maximum of the outburst.

Thus, we argue that the observational appearance of the flares in EXO 2030+375 suggests that the instability of the inner disk edge (pile-up/draining of matter) is the most probable cause of the flares.

It is important to note that the rarity of the detected flaring episodes (even considering the relatively sparse observational coverage) means that the range of physical conditions needed to initiate flares could be very narrow, which would lead to the serendipitous character of the phenomenon.

## References

Angelini, L., White, N. E., & Stella, L. 1991, ApJ, 371, 332
Apparao, K. M. V. 1991, ApJ, 375, 701
Bildsten, L., & Brown, E. F. 1997, ApJ, 477, 897
Brown, E. F., & Bildsten, L. 1998, ApJ, 496, 915
Caballero, I., Santangelo, A., Kretschmar, P., et al. 2008, A&A, 480, L17
Camero Arranz, A., Wilson, C. A., Connell, P., et al. 2005, A&A, 441, 261
Courvoisier, T. J.-L., Walter, R., Beckmann, V., et al. 2003, A&A, 411, L53
D'Angelo, C. R., & Spruit, H. C. 2010, MNRAS, 406, 1208
Finger, M. H., Bildsten, L., Chakrabarty, D., et al. 1999, ApJ, 517, 449
Fürst, F., Kreykenbohm, I., Pottschmidt, K., et al. 2010, A&A, 519, A37
Hayasaki, K., & Okazaki, A. T. 2006, MNRAS, 372, 1140
Klochkov, D., Horns, D., Santangelo, A., et al. 2007, A&A, 464, L45
Kreykenbohm, I., Wilms, J., Kretschmar, P., et al. 2008, A&A, 492, 511
Lebrun, F., Leray, J. P., Lavocat, P., et al. 2003, A&A, 411, L141
Levine, A. M., Rappaport, S. A., & Zojcheski, G. 2000, ApJ, 541, 194
Liu, Q. Z., van Paradijs, J., & van den Heuvel, E. P. J. 2006, A&A, 455, 1165
Lund, N., Budtz-Jørgensen, C., Westergaard, N. J., et al. 2003, A&A, 411, L231
Moon, D.-S., Eikenberry, S. S., & Wasserman, I. M. 2003a, ApJ, 582, L91
Moon, D.-S., Eikenberry, S. S., & Wasserman, I. M. 2003b, ApJ, 586, 1280
Nandra, K., George, I. M., Mushotzky, R. F., et al. 1997, ApJ, 476, 70
Parmar, A. N., White, N. E., Stella, L., Izzo, C., & Ferri, P. 1989, ApJ, 338, 359
Postnov, K., Staubert, R., Santangelo, A., et al. 2008, A&A, 480, L21
Reig, P. 2011, Ap&SS, 332, 1
Reig, P., & Coe, M. J. 1998, MNRAS, 294, 118
Reig, P., Belloni, T., Israel, G. L., et al. 2008, A&A, 485, 797
Shakura, N. I., & Sunyaev, R. A. 1973, A&A, 24, 337
Sidoli, L. 2011, Adv. Space Res., 48, 88
Staubert, R., Klochkov, D., & Wilms, J. 2009, A&A, 500, 883
Taam, R. E., Brown, D. A., & Fryxell, B. A. 1988, ApJ, 331, L117
Ubertini, P., Lebrun, F., Di Cocco, G., et al. 2003, A&A, 411, L131
Vedrenne, G., Roques, J.-P., Schönfelder, V., et al. 2003, A&A, 411, L63
Walter, R., & Zurita Heras, J. 2007, A&A, 476, 335
Wilson, C. A., Finger, M. H., Coe, M. J., et al. 2002, ApJ, 570, 287
Wilson, C. A., Finger, M. H., & Camero-Arranz, A. 2008, ApJ, 678, 1263
Winkler, C., Courvoisier, T. J.-L., Di Cocco, G., et al. 2003, A&A, 411, L1

# Appendix C

# Pulse-amplitude-resolved spectroscopy of bright accreting pulsars: indication of two accretion regimes

**Astronomy & Astrophysics**

# Pulse-amplitude-resolved spectroscopy of bright accreting pulsars: indication of two accretion regimes

D. Klochkov[1], R. Staubert[1], A. Santangelo[1], R. E. Rothschild[2], and C. Ferrigno[3]

[1] Institut für Astronomie und Astrophysik, Universität Tübingen (IAAT), Sand 1, 72076 Tübingen, Germany
e-mail: klochkov@astro.uni-tuebingen.de
[2] Center for Astrophysics and Space Sciences, University of California, San Diego, La Jolla, CA, USA
[3] ISDC Data Center for Astrophysics of the University of Geneva chemin d'Écogia, 16 1290 Versoix, Switzerland

## ABSTRACT

*Context.* In addition to coherent pulsation, many accreting neutron stars exhibit flaring activity and strong aperiodic variability on time scales comparable to or shorter than their pulsation period. This behavior shows that the accretion flow in the vicinity of the accretor must be highly non-stationary. Observational study of this phenomenon is often problematic because it requires very high statistics of X-ray data and a specific analysis technique.
*Aims.* In our research we used high-resolution data taken with RXTE and INTEGRAL on a sample of bright transient and persistent pulsars to perform an in-depth study of their variability on time scales comparable to the pulsation period – "pulse-to-pulse variability".
*Methods.* The high-quality data allowed us to collect individual pulses of different amplitude and explore their X-ray spectrum as a function of pulse amplitude. The described approach allowed us for the first time to study the luminosity dependence of pulsars' X-ray spectra in observations where the averaged (over many pulse cycles) luminosity of the source remains constant.
*Results.* In all studied pulsars we reveal significant spectral changes as a function of the pulse height both in the continuum and in the cyclotron absorption features. The sources appear to form two groups that show different dependencies of the spectrum on pulse height. We interpret this division as a manifestation of two distinct accretion regimes that are at work in different pulsars.

**Key words.** X-rays: binaries – stars: neutron – accretion, accretion disks

## 1. Introduction

Strong aperiodic variability of the X-ray flux is a well known characteristic of many X-ray binary systems. First discovered in black hole candidates (with Cyg X-1 being the most remarkable case), it was later shown to be a common feature also among accreting neutron stars (see e.g. Belloni & Hasinger 1990, for a review). Although *homogeneity* and *stationarity* of the accretion flow is often assumed in calculations dealing with physics inside the X-ray emitting structure on a neutron star (because it greatly simplifies the mathematical treatment of the problem), the observed variability clearly indicates that the accretion flow in the close vicinity of the accretor must be highly non-stationary. On the other hand, the penetration of matter into the magnetosphere of the neutron star around the stopping radius is believed to be governed by various kinds of instabilities that plasma supported by magnetic field is subject to (see e.g. Ghosh & Lamb 1979; Kulkarni & Romanova 2008; Bozzo et al. 2008). The instabilities will naturally lead to fragmentation of a continuous flow into more or less isolated blobs or filaments. More focused theoretical studies of the non-stationary accretion problem have been performed e.g. by Morfill et al. (1984); Demmel et al. (1990), and Orlandini & Boldt (1993), who have explicitly shown that the inhomogeneity of the flow is generally expected in accreting pulsars and that it does not only arise from the original inhomogeneity of the accreted matter (e.g. "clumps" in the stellar wind or variations of matter supply from the donor star) but can naturally be produced by instabilities close to the magnetospheric boundary of the neutron star.

So far, the aperiodic variability of accreting pulsars has mostly been studied by means of power spectra of their high time-resolution light curves (e.g. Belloni & Hasinger 1990; Pottschmidt et al. 1998; Revnivtsev et al. 2009). In our work, however, we concentrate on the variability of individual X-ray pulses often referred to as *pulse-to-pulse variability*. This kind of variability seems to be a common phenomenon among accreting pulsars and has been reported by several authors for bright outbursts of some transient or strongly variable sources: Frontera et al. (1985) for A 0535+26, Staubert et al. (1980); Kretschmar et al. (2000) for Vela X-1, Tsygankov et al. (2007) for 4U 0115+63. However, a detailed study of the pulse-to-pulse variability is usually limited by the photon statistics, especially for relatively fast pulsars (with a spin period of a few seconds or less). In the present work, we used the publicly available archival data from high-sensitivity X-ray detectors onboard RXTE and INTEGRAL taken on a set of four bright accreting pulsars – V 0332+53, 4U 0115+63, A 0535+26, and Her X-1.

The four accreting pulsars are well established cyclotron line sources, i.e. their spectra contain cyclotron resonant scattering features (CRSFs). These features appear as absorption lines caused by resonant scattering of photons off the relativistic plasma electrons at Landau levels (see e.g. Trümper et al. 1978; Isenberg et al. 1998; Araya-Góchez & Harding 2000). The CRSFs, if detected, provide a direct way to measure the magnetic field strength at the site of X-ray emission as the energy of the fundamental line and the spacing between the harmonics are proportional to the *B*-field strength. In some sources

the cyclotron line energy was found to change with luminosity. In V 0332+53 and 4U 0115+63 a negative correlation of the line energy with luminosity was observed (Tsygankov et al. 2007, 2010; Mowlavi et al. 2006; Mihara et al. 2004), while for Her X-1 Staubert et al. (2007) reported a positive correlation of the line energy with luminosity.

A description of the observational data is provided in Sect. 2. Using a special analysis technique (described in Sect. 3), we collected individual pulses of different amplitudes and studied the differences in their X-ray spectra. As a result, we reveal significant correlations of different spectral parameters with pulse amplitude (Sect. 4). Based on the sign of the correlations, the explored pulsars can be divided into two groups. We argue that the two groups correspond to two distinct regimes of accretion that are at work in different sources: local sub- and super-Eddington regime (see discussion in Sect. 5). The summary and conclusions are provided in Sect. 6.

## 2. Observations

For our analysis we used the data taken with the RXTE satellite (Bradt et al. 1993) during the intense outbursts of the transient high-mass X-ray binaries (HMXB) V 0332+53, 4U 0115+63, and A 0535+26 and during a *main-on* state of the persistent intermediate mass X-ray binary Her X-1 (these states of high X-ray flux occur in the system about every 35 days, most probably reflecting periodic obscuration of the source by a precessing tilted accretion disk, see e.g. Klochkov et al. 2006, and references therein). In the case of A 0535+26 we also used data taken with the INTEGRAL observatory (Winkler et al. 2003) simultaneously with the RXTE observations. The main X-ray instruments onboard the two satellites provide a broad-band coverage of the sources' X-ray spectra: RXTE/PCA (Jahoda et al. 1996) and INTEGRAL/JEM-X (Lund et al. 2003) are sensitive from a few keV to ~35 keV, while RXTE/HEXTE (Rothschild et al. 1998) and INTEGRAL/IBIS(ISGRI) (Ubertini et al. 2003) – from ~20 keV to a few hundred keV.

Our main criterion for the selection of the observations and instruments was a sufficiently dense timing coverage of the sources during their high flux states, which provides best statistics. Additionally, for RXTE/PCA we searched for the data taken in an appropriate data mode that allows one to achieve simultaneously high time- and energy-resolution in the entire PCA energy range. Specifically, we used the data taken in *GoodXenon* and certain *generic event* modes (with sufficient energy- and time-resolution). Where possible, we selected the RXTE observations with both HEXTE clusters switched on to maximize the photon statistics. INTEGRAL data were only used for of A 0535+26, which has a long (~100 s) pulse period. For the other three pulsars with much shorter pulse periods (a few seconds), individual pulsations cannot be distinguished in the INTEGRAL (IBIS/ISGRI) light curves, which prevents pulse-to-pulse study.

For each of the three transient sources we used a short continuous set of pointings covering ~1 day or less of the brightest part of an outburst (close to its maximum) so that the average flux level within the observations did not change significantly. The observed flux variability is therefore related to X-ray pulsations and pulse-to-pulse variations. For the persistent pulsar Her X-1 we used the data from the main-on state of the source corresponding to the 35 d cycle No. 323 (according to the numbering convention adopted in Staubert et al. 1983), which is best covered by RXTE observations. We selected the data from the middle part of the main-on where the flux does not change

**Table 1.** Observations used for the pulse-amplitude-resolved analysis.

| Source name | Instrument | Mid MJD | Exposure (ks) |
|---|---|---|---|
| V 0332+53 | RXTE | 53 354[a] | 23.7 |
| 4U 0115+63 | RXTE | 51 249[b] | 32.8 |
| A 0535+26 | RXTE | 53 615[c] | 30.8 |
| | INTEGRAL | 53 615[c] | 104.7 |
| Her X-1 | RXTE | 52 600[d] | 98.7 |

**Notes.** [a] Giant outburst in 2004; [b] giant outburst in 1999; [c] normal outburst in 2005; [d] main-on state.
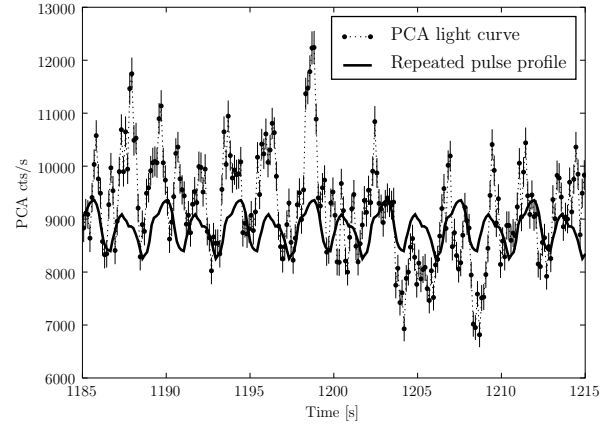


**Fig. 1.** Sample light curve of V 0332+53 during its 2005 giant outburst obtained with RXTE/PCA and summed over all energy channels (2−80 keV). The solid curve shows the repeated pulse profile obtained by folding a longer data sample. Dramatic pulse-to-pulse variability is clearly seen.

significantly, i.e. where the obscuration by the accretion flow is minimal. The chosen observations of Her X-1 are spread over ~5 d. A summary of the observational data on all sources is provided in Table 1.

## 3. Analysis technique

The standard data reduction has been performed with the software packages and calibration data provided by the instrument teams. For RXTE we used HEASoft 6.9[1], for INTEGRAL – OSA 9.0[2].

To analyze the pulse-to-pulse variability, for each source we extracted a high-resolution light curve where single pulses are clearly distinguishable. An example of such a light curve obtained with RXTE/PCA in 2−80 keV range (this is the entire PCA range, although the effective area of the instrument drops above 30−35 keV) on V 0332+53 is shown in Fig. 1 where the strong variability of the profile shape from one pulse to the next is visible. We then selected a pulse-phase interval containing the brightest part of the pulse profile, referred to as *pulse*. The chosen pulse-phase intervals for each source are shown in Fig. 2 by the shaded areas. For each pulse we calculated its mean count rate (in all PCA channels for the RXTE data and in 20−100 keV for the INTEGRAL data), that is the average count rate within the selected pulse-phase interval, which we call the *amplitude* or *height* of the pulse. As can be seen in Fig. 1, the amplitude of individual pulses varies over a broad range. This allows one

---

[1] http://heasarc.nasa.gov/lheasoft/

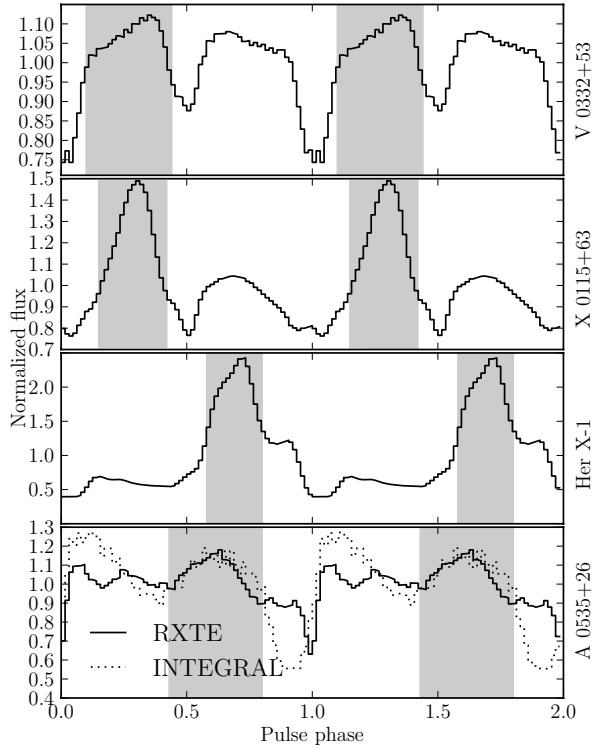[2] http://www.isdc.unige.ch/integral/analysis#Software

**Fig. 2.** Averaged (over many pulsation cycles) pulse profiles of the pulsars in our sample obtained with RXTE/PCA in 2–80 keV range (solid curve) and (in case of A 0535+26) with INTEGRAL/ISGRI in 20–100 keV range (dotted curve on *the bottom panel*). The shaded areas mark the pulse-phase intervals used for our pulse-amplitude-resolved analysis (see text).

to explore the variation of the X-ray spectrum as a function of pulse amplitude, which is the central point of our research.

The photon statistics does not allow us to extract meaningful spectra of single pulses. Therefore, we grouped together pulses of similar amplitude. For this purpose we explored the distribution of pulse amplitudes for each source and split the entire range of amplitudes into five to six bins, keeping approximately the same statistics within each bin. Then, for each amplitude bin we constructed a list of good time intervals (GTIs) to select the pulses (i.e. the data inside the selected pulse-phase intervals) whose amplitude falls into the bin. Providing the data-processing pipeline with the produced GTIs we extracted the broad-band X-ray spectra for the selected bins, i.e. as a function of pulse height. We note again that the extracted spectra correspond to a fixed pulse-phase interval. This minimizes possible influence of pulse-phase dependence of the spectrum.

To maximize the photon statistics in our spectra, where possible we used PCA data up to 60 keV. Even though the effective area of the instrument at this energy drops dramatically along with an increase of the relative background contribution, the photon statistics is still competitive with that of HEXTE (which suffers from larger dead time). For the spectral analysis of the PCA data we used the updated response v11.7 (2009 May 11) and background estimation files *Sky_VLE*. According to the instrument team, the new calibration files in combination with the updated HEASoft package (starting from version 6.7) provide significant improvements to spectral analysis and allow one to use PCA data up to ~50 keV with systematic uncertainties

of 0.5%[3]. Our analysis of pulse-averaged spectra between 40 and 60 keV has shown that the PCA spectrum extracted with the new calibration is in complete accord with the HEXTE spectrum for which the background is directly measured during the observations (using the off-set pointings of the collimator). The agreement between the two detectors is also claimed by Rothschild et al. (2011), who also used PCA data up to 60 keV in their analysis of the RXTE observations of Cen A. Following Rothschild et al. (2011), the background model counts histogram was included in the spectral fitting as a correction file to account for small deviations of the background and dead-time models from reality (`recorn` model in *XSPEC 12.6.0*). We added systematic uncertainties at the level of 1.0% to our PCA spectra, which are somewhat larger than the recommended 0.5% (see above) but allow us to obtain more conservative estimates of the spectral parameter errors. No systematic errors have been added to HEXTE because it is not recommended by the instrument team (the uncertainties of this instrument are dominated by statistical fluctuations).

For the INTEGRAL instruments we used the standard method of background evaluation from the deconvolution of the detector images provided by the OSA software[4]. We added systematic uncertainties at the level of 2% to the JEM-X spectra and 1% to the IBIS/ISGRI spectra based on the recommendations of the instrument teams and the Crab observations closest to our observations.

It is known that inaccuracy in the absolute calibration of the X-ray instruments onboard INTEGRAL and RXTE might lead to systematic differences in the observed spectral shape of a source between the two satellites (see e.g. Tsujimoto et al. 2011). In our research, however, we focus on *relative* variations of the spectral parameters as a function of pulse amplitude rather than their absolute values. Therefore, the cross-calibration accuracy is not critical for our study. We also note that the pulse-averaged cyclotron line energies measured simultaneously with INTEGRAL and RXTE in A 0535+26 (Caballero et al. 2007) and Her X-1 (Klochkov et al. 2008a; Staubert et al. 2007) agree within ~1 keV between the two satellites.

## 4. Results

For each pulsar in our sample we obtained a series of broad-band (~3–80 keV) X-ray spectra corresponding to different pulse amplitudes. The spectral continua are modeled using the powerlaw-cutoff function. The fluorescent $K_\alpha$ emission at 6.4 keV has been modeled by an additive Gaussian. The absorption cyclotron features are clearly seen in our pulse-amplitude-resolved spectra and are modeled using multiplicative absorption lines with a Gaussian optical depth profile. A more detailed description of the spectral models is provided below, in the subsections devoted to the individual sources. Since the analysis procedures are very similar for all sources in our sample, we provide a full description of our spectral fitting (including a list of spectral parameters, $\chi^2$ values etc.) only for the first pulsar, V 0332+53 (Sect. 4.1). For the other the sources we skip the detailed information and concentrate on final results – variations of the spectral parameters with pulse amplitude.

All our spectral fits were checked for possible intrinsic dependencies/degeneracies of different parameter pairs using error contour plots. No significant correlations were found except the

**Table 2.** Best-fit spectral parameters of V 0332+53 for different pulse-amplitude bins. The indicated uncertainties are at $1\sigma$ (68%) confidence level.

| Pulse amplitude bin [PCA cts/s] | 2800–3400 | 3400–3650 | 3650–3900 | 3900–4100 | 4100–4300 | 4300–5100 |
|---|---|---|---|---|---|---|
| $\Gamma$ | $-0.621^{+0.009}_{-0.010}$ | $-0.609^{+0.009}_{-0.008}$ | $-0.593^{+0.008}_{-0.007}$ | $-0.586^{+0.008}_{-0.008}$ | $-0.600^{+0.011}_{-0.011}$ | $-0.591^{+0.014}_{-0.013}$ |
| $E_{\rm fold}$ [keV] | 5.79 (fixed) | 5.79 (fixed) | 5.79 (fixed) | 5.79 (fixed) | 5.79 (fixed) | 5.79 (fixed) |
| $E_{\rm bump}$ [keV] | $11.64^{+0.29}_{-0.26}$ | $11.39^{+0.25}_{-0.23}$ | $11.12^{+0.26}_{-0.23}$ | $10.97^{+0.27}_{-0.24}$ | $10.99^{+0.41}_{-0.39}$ | $10.34^{+0.51}_{-0.55}$ |
| $\sigma_{\rm bump}$ [keV] | 2.65 (fixed) | 2.65 (fixed) | 2.65 (fixed) | 2.65 (fixed) | 2.65 (fixed) | 2.65 (fixed) |
| $E_{\rm Fe}$ [keV] | 6.4 (fixed) | 6.4 (fixed) | 6.4 (fixed) | 6.4 (fixed) | 6.4 (fixed) | 6.4 (fixed) |
| $\sigma_{\rm Fe}$ [$keV$] | 0.01 (fixed) | 0.01 (fixed) | 0.01 (fixed) | 0.01 (fixed) | 0.01 (fixed) | 0.01 (fixed) |
| $E_{\rm cyc}$ [keV] | $26.27^{+0.05}_{-0.05}$ | $26.21^{+0.04}_{-0.04}$ | $26.05^{+0.04}_{-0.04}$ | $26.01^{+0.05}_{-0.06}$ | $25.98^{+0.06}_{-0.06}$ | $25.85^{+0.08}_{-0.08}$ |
| $\sigma_{\rm cyc}$ [keV] | $3.65^{+0.08}_{-0.07}$ | $3.61^{+0.07}_{-0.07}$ | $3.64^{+0.06}_{-0.06}$ | $3.74^{+0.07}_{-0.07}$ | $3.97^{+0.10}_{-0.10}$ | $4.04^{+0.13}_{-0.12}$ |
| $\tau_{\rm cyc}$ | $11.54^{+0.32}_{-0.31}$ | $11.11^{+0.28}_{-0.27}$ | $10.83^{+0.25}_{-0.24}$ | $10.84^{+0.27}_{-0.28}$ | $11.41^{+0.40}_{-0.38}$ | $11.23^{+0.50}_{-0.47}$ |
| $E_{\rm cyc,1}$ [keV] | $48.96^{+0.95}_{-0.92}$ | $47.71^{+0.65}_{-0.62}$ | $48.56^{+1.08}_{-0.68}$ | $48.98^{+0.71}_{-1.02}$ | $48.15^{+0.83}_{-0.80}$ | $47.76^{+0.97}_{-0.90}$ |
| $\sigma_{\rm cyc,1}$ [keV] | 3 (fixed) | 3 (fixed) | 3 (fixed) | 3 (fixed) | 3 (fixed) | 3 (fixed) |
| $\tau_{\rm cyc,1}$ | $4.7^{+1.6}_{-1.2}$ | $4.9^{+1.0}_{-0.9}$ | $4.3^{+1.0}_{-0.8}$ | $3.3^{+1.1}_{-0.9}$ | $5.1^{+1.4}_{-1.1}$ | $6.0^{+1.9}_{-1.5}$ |
| $\chi^2_{\rm red}$/d.o.f. | 1.2/96 | 1.5/96 | 1.5/96 | 1.3/96 | 0.8/96 | 1.5/96 |

one between the photon index and the cutoff energy, which was eliminated by fixing the cutoff energy (see below). The presented results are also found to be stable with respect to the choice of different spectral functions, both for the continuum and the cyclotron absorption lines. We are, therefore, confident that the variability reported below arises from the sources' behavior and reflects real physics.

### 4.1. V 0332+53

V 0332+53 belongs to the category of Be/X-ray binaries (BeXRB) – currently the most numerous class of HMXBs. The neutron star in these systems periodically or sporadically accretes mass from the equatorial disk around the Be- or Oe-type optical companion. The episodes of accretion give rise to powerful X-ray outbursts, while in quiescence the X-ray flux often falls below the detection limit of most instruments. The neutron star in V 0332+53 has a spin period of ~4.3 s (Stella et al. 1985). For this source we used the RXTE data close to the maximum of its giant (type II) outburst in 2004 (see e.g. Coe 2000, for the nomenclature of outburst types in BeXRBs), when the bolometric luminosity reached a few times $10^{38}$ erg s$^{-1}$ for a distance of 7 kpc (Tsygankov et al. 2010). Up to three cyclotron features have been detected in the source: the fundamental line at ~26 keV and two harmonics, at ~50 and ~70 keV respectively. As mentioned in the introduction, during the outbursts the fundamental line exhibits a strong negative correlation with the X-ray flux (e.g. Tsygankov et al. 2010; Mowlavi et al. 2006).

In the short set of RXTE observations that we have analyzed (where the source luminosity did not change significantly, see Sect. 2), the dynamical range of the pulse amplitude variations reached a factor of ~1.5. For this range we defined six amplitude bins and extracted six spectra, one for each bin. The X-ray continuum was modeled using a powerlaw function with an exponential decay toward higher energies – the *XSPEC* `cutoffpl` model: $I(E) \propto E^{-\Gamma} \exp(-E/E_{\rm fold})$, where $E$ is the photon energy, $\Gamma$ – photon index, and $E_{\rm fold}$ – exponential folding energy. To account for a bump-like feature appearing in the residuals between 10 and 20 keV, we added a broad Gaussian with the centroid energy $E_{\rm bump} \sim 11$ keV and a width of $\sigma_{\rm bump} \sim 3$ keV.

The spectra revealed two absorption features, the fundamental cyclotron line and its first harmonic, which we modeled using Gaussian absorption lines as stated above (the *XSPEC* `gabs` multiplicative model: $M(E) \propto \exp[-\tau_{\rm cyc}/(\sqrt{2\pi}\sigma_{\rm cyc}) \cdot \exp(-0.5(E - E_{\rm cyc})^2/\sigma_{\rm cyc}^2)]$, where $E_{\rm cyc}$, $\sigma_{\rm cyc}$, and $\tau_{\rm cyc}$ are the centroid energy, width, and optical depth of the line, respectively). To account for uncertainties in the absolute normalization of the flux in different instruments, we introduced in our model a multiplicative factor $F$ which was fixed to 1.0 for PCA and left free for HEXTE. In all pulse-amplitude bins the best-fit value of $F$ for HEXTE was around 0.90(1), indicating a 10% difference in the absolute flux normalization between the two instruments. Similar differences (from 10 to 14%) were found for all other RXTE observations analyzed in this work. The energy range of the spectra was set to 3.5–60 keV for PCA (see Sect. 3 about the usage of PCA at high energies) and to 17–75 keV for HEXTE. The best-fit spectral parameters for each pulse-phase amplitude bin together with the $1\sigma$-uncertainties and the corresponding reduced $\chi^2$ values are summarized in Table 2. The parameters of the first cyclotron line harmonic are denoted with "1" in the subscript. Figure 4 shows one of our pulse-amplitude-resolved spectra of V 0332+53 modeled with the described function.

Some spectral parameters that did not show any significant variation with pulse-amplitude were fixed to their averaged (over pulse-amplitude bins) values, as indicated in Table 2. The photon index $\Gamma$ and the exponential folding energy $E_{\rm fold}$ were found to be strongly coupled (showing intrinsic positive correlation with each other), i.e. the quality of the data did not allow us to determine their variation independently. $E_{\rm fold}$ showed weaker variability with pulse amplitude compared to $\Gamma$ and was fixed to its average value. Thus, we only explored the variation of $\Gamma$ as a function of the pulse amplitude.

The data revealed significant changes of the photon index and the energy of the fundamental cyclotron line $E_{\rm cyc}$ with pulse amplitude as can be seen in Fig. 3 (left column). The horizontal axis of the plots represents the pulse amplitude (determined in the way described in Sect. 3) measured in PCA count rate summed over all energy channels (2–80 keV, see above) and normalized to one PCU. The horizontal error-bars indicate the
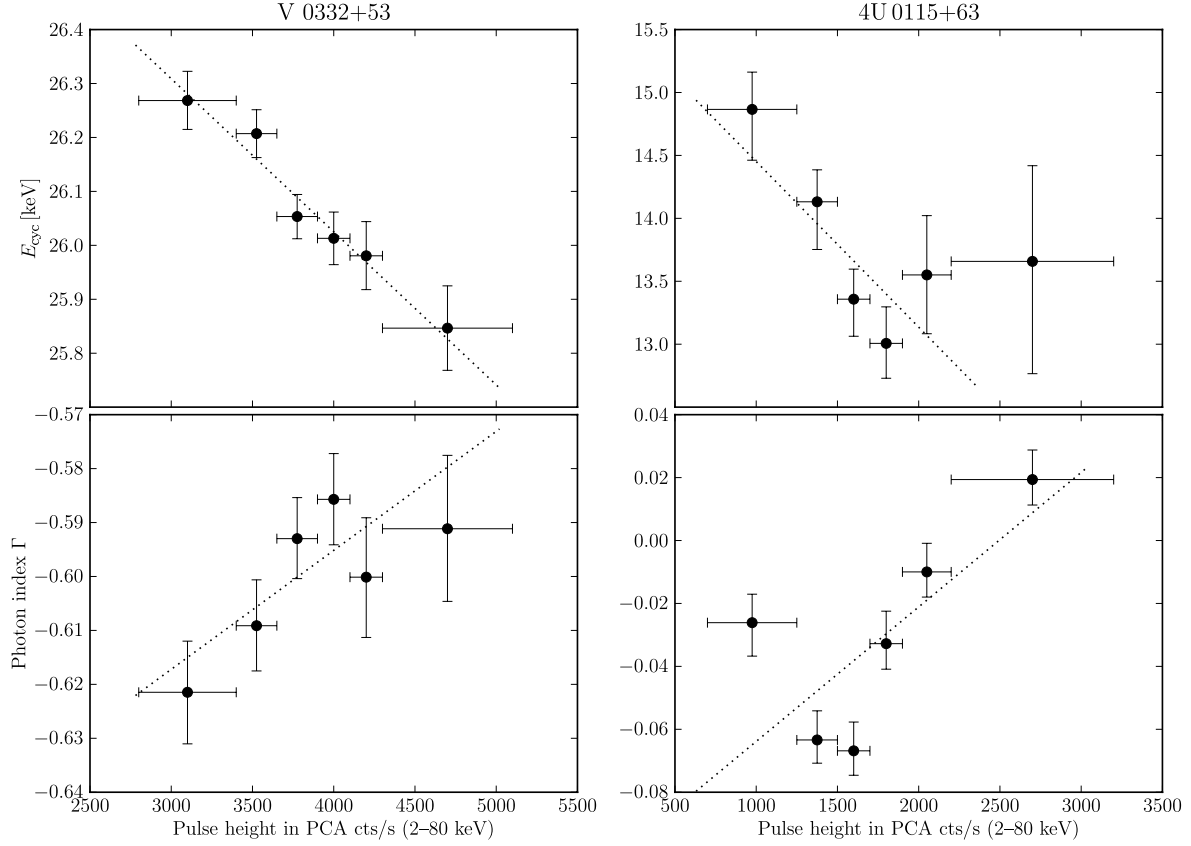
**Fig. 3.** Variation of the fundamental cyclotron line centroid energy $E_{\rm cyc}$ (*top*) and the photon index $\Gamma$ (*bottom*) with pulse amplitude measured in V 0332+53 (*left*) and in 4U 0115+63 (*right*) using the RXTE data. The vertical bars indicate uncertainties at $1\sigma$ (68%) confidence level.
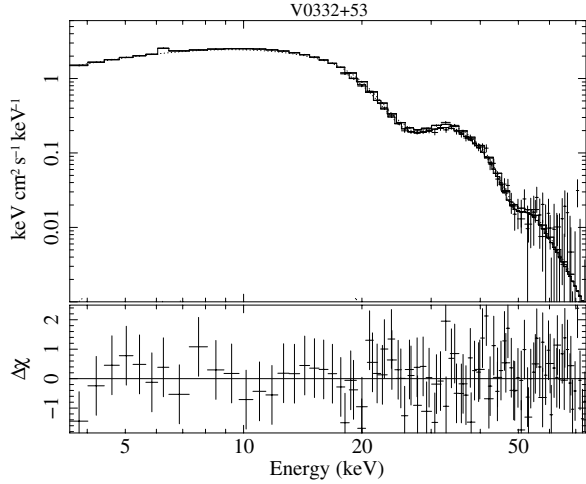


**Fig. 4.** Example of the pulse-amplitude-resolved spectrum of V 0332+53 obtained with PCA and HEXTE (from the pulse-amplitude bin 3650−3900 cts/s). *The top panel* shows the unfolded spectrum modeled with a cutoff-powerlaw function with two absorption lines (see text). *The bottom panel* shows the corresponding residual plot.

width of the corresponding pulse amplitude bins. An almost linear decrease of $E_{\rm cyc}$ with pulse height is clearly seen as well as a somewhat less significant softening of the spectrum (reflected

by an increase of the photon index $\Gamma$). The dotted lines represent linear fits to the data. The measured slope of the $E_{\rm cyc}$ − pulse-height dependence is $(-2.84 \pm 0.50) \times 10^{-4}$ keV/(cts/s). The Pearson linear correlation coefficient is $-0.98$ with the corresponding two-sided null-hypothesis probability (the probability to find the correlation by chance in a non-correlated data sample) $\sim 4 \times 10^{-4}$, indicating a highly significant anti-correlation. The slope of the $\Gamma$ − pulse-height dependence is $(2.21 \pm 0.88) \times 10^{-5}$ (cts/s)$^{-1}$. The Pearson linear correlation coefficient with the associated two-sided null-hypothesis probability are in this case $\sim 0.77$ and $\sim 0.07$, respectively. The (positive) correlation in this case is not very significant, but still might indicate a possible physical relation between the parameters.

To check the reliability of the shown dependencies, we performed spectral fits with alternative spectral functions for the continuum and cyclotron features: `powerlaw×highecut` ($I(E) \propto E^{-\Gamma}$ below $E_{\rm cutoff}$ and $E^{-\Gamma} \exp\left[-(E - E_{\rm cutoff})/E_{\rm fold}\right]$ above $E_{\rm cutoff}$) instead of `cutoffpl` and `cyclabs` (Lorenzian absorption line) instead of `gabs`. For all combinations of the continuum and line models the variations of $\Gamma$ and $E_{\rm cyc}$ with pulse amplitude emerge with similar significance.

As mentioned above, we checked our fits for any possible statistical (model-dependent) correlations of parameters using $\chi^2$-contour plots for different parameter pairs. All free parameters were found to be well decoupled (i.e. showing no or only a weak statistical dependence). In all cases the $\chi^2$ minimum and the corresponding confidence range are well defined. Examples of the $\chi^2$-contour plots for some parameters are shown in Fig. 5.
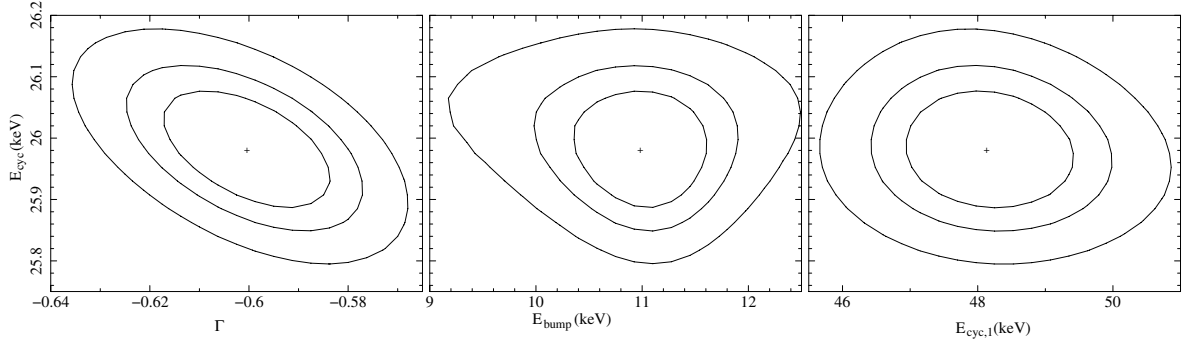
**Fig. 5.** $\chi^2$-contour plots for some pairs of spectral parameters of V 0332+53. The $\chi^2$-minima are well defined and the parameters show no degeneracy. To generate the plots we used the spectrum from the pulse-amplitude bin 3650−3900 cts/s.

The averaged pulse profile of the source shows two almost equally strong peaks (Fig. 2). As described in Sect. 3, we selected for our study a phase interval that includes the first (the highest) peak. However, we repeated our analysis also for the second peak and found very similar dependencies of the spectral parameters on pulse amplitude.

The revealed variation of $E_{cyc}$ agrees with the negative correlation of the line energy with the *averaged* (over many pulse cycles) flux level during the rise and decay of the strong outbursts reported for this source (see above). We stress, however, that in our analysis the correlation with pulse height appears in a short (less than one day) set of pointings where the average flux stays roughly constant. The positive correlation of $\Gamma$ with pulse height, if it is real, is also consistent with the gradual decrease of the averaged photon index observed during the decay of the outburst, which can be derived from Table 2 of Mowlavi et al. (2006).

### 4.2. 4U 0115+63

Another member of the BeXRB class, 4U 0115+63 has a pulsation period of ∼3.6 s (Cominsky et al. 1978). Up to five cyclotron line harmonics have been detected in the X-ray spectrum of the source with the fundamental line at ∼11−16 keV having the lowest energy among accreting pulsars (Heindl et al. 1999; Santangelo et al. 1999; Ferrigno et al. 2009, and references therein). Like in V 0332+53, the fundamental line in 4U 0115+63 was found to increase during the decay phase of the giant outbursts (Mihara et al. 2004; Tsygankov et al. 2007). For our analysis we used the RXTE observations of the intense giant outburst of the source in 1999 when the bolometric luminosity exceeded $10^{38}$ erg s$^{-1}$, assuming a distance of 7 kpc (Tsygankov et al. 2007). The data cover roughly 0.5 day of the outburst close to its maximum. In our pulse-amplitude resolved spectra we detected (and modeled using the `gabs` *XSPEC* model, see above) the fundamental line and its three harmonics. Following Tsygankov et al. (2007) and Ferrigno et al. (2009), we used the `powerlaw×highecut` model for the spectral continuum.

The amplitude of variations in the pulse height exhibited by 4U 0115+63 in our data sample reached a factor of ∼2.5. As for V 0332+53, the data quality allowed us to divide the pulse-height distribution into six bins and explore the variations in the centroid energy of the fundamental cyclotron line $E_{cyc}$ and the photon index $\Gamma$ with pulse height (Fig. 3, right column). The exponential folding energy $E_{fold}$ was again found to be coupled with $\Gamma$. As for V 0332+53, we fixed $E_{fold}$ to its mean (over

pulse-height bins) value, 8.2 keV, so that the softening/hardening of the spectral continuum is described by the changes in $\Gamma$ and the cutoff energy $E_{cutoff}$ (the latter, however, did not show any significant dependence on pulse amplitude). Parameters of the cyclotron line harmonics showed no significant variation with pulse amplitude.

As can be seen in the top right plot of Fig. 3, the energy of the fundamental cyclotron line decreases with increasing pulse amplitude (probably showing some saturation at highest amplitudes, see below), similarly to V 0332+53. The source also shows softening of the spectrum (increase of the photon index) with increasing pulse height (bottom right plot in Fig. 3), which is also similar to V 0332+53.

As before, the dotted lines represent linear fits to the data points. The measured slopes are $(-1.32 \pm 0.38) \times 10^{-4}$ keV/(cts/s) for the $E_{cyc}$ − pulse-height dependence and $(4.27 \pm 0.68) \times 10^{-5}$ (cts/s)$^{-1}$ for the $\Gamma$ − pulse-height dependence, indicating a significant variation. The Pearson correlation coefficient and the associated two-sided null-hypothesis probability are ∼−0.58 and ∼0.22 respectively for $E_{cyc}$, and ∼0.70 and ∼0.12 for $\Gamma$. As can be seen, the linear correlation inspection indicate only sparse correlations of the parameters. We note, however, that the formal linear correlation analysis does not take into account the uncertainties of the parameters (which are known in our case) and is not very reliable in case of a limited sample (a few points). The formal linear fits taking into account the uncertainties, nevertheless, indicate significant variations (see the slope values above). The two rightmost points in the $E_{cyc}$ − pulse-height plot (Fig. 3, top right) might indicate some saturation of the downward trend in the cyclotron line energy. However, since the uncertainties associated with the points are larger compared to the other points, the apparent "flattening" might result from poor statistics. The leftmost data point on the $\Gamma$ − pulse-height plot (Fig. 3, bottom right) significantly deviates from a linear upward trend formed by the other data points. Considering the relatively small uncertainties of the data values, this might indicate a more complicated (than the linear) relation between $\Gamma$ and the pulse amplitude in this source.

Like in V 0332+53, the decrease of the line energy with the pulse amplitude (which we see on the time scale of single X-ray pulsations) is in line with the negative correlation of $E_{cyc}$ with the average flux measured on a much longer time scale during the decay of the source's outbursts.

For 4U 0115+63 we did not find any alternative spectral function that would provide an acceptable fit of the spectral continuum. However, we checked our spectral fits using Lorentzian absorption lines to model CRSFs instead of the Gaussian lines.
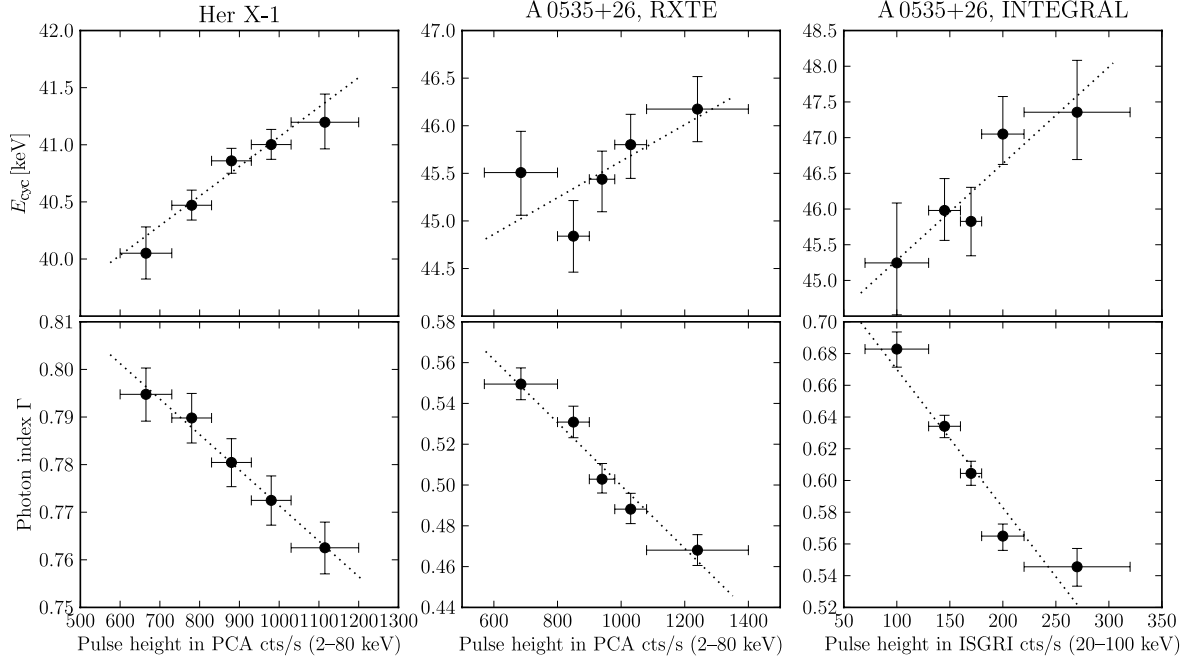
**Fig. 6.** Variation of the fundamental cyclotron line centroid energy $E_{cyc}$ (*top*) and the photon index $\Gamma$ (*bottom*) with pulse amplitude measured in Her X-1 using the RXTE (*left column*) and in A 0535+26 using RXTE (*middle column*), and using INTEGRAL (*right column*). The vertical bars indicate uncertainties at a $1\sigma$ (68%) confidence level. The dotted lines represent linear fits to the data points.

The reported effects (variations of $E_{cyc}$ and $\Gamma$) appear equally significant in the spectral fits with both types of absorption lines.

### 4.3. Her X-1

Unlike the V 0332+53 and 4U 0115+63, Her X-1 is a persistent X-ray source. As stated in Sect. 2, the observed regular changes of the source flux are related to the periodic obscuration by matter in the accretion flow, whereas the intrinsic luminosity of the source (estimated to be $\sim 2 \times 10^{37}$ erg s$^{-1}$ for a distance of 7 kpc, Reynolds et al. 1997) remains roughly constant (possibly exhibiting, however, long-term changes, see below). The pulsation period of Her X-1 is $\sim 1.24$ s, which is the shortest period in our sample. Being historically the first source where a cyclotron feature was detected (Trümper et al. 1978), Her X-1 has the most regular and continuous records of the line energy among all accreting neutron stars (e.g. Staubert et al. 2007; Klochkov et al. 2008b). Analyzing the RXTE observations of the source spread over $\sim 10$ years, Staubert et al. (2007) found that the cyclotron line centroid energy is *positively* correlated with the X-ray luminosity, which apparently slowly varies with the amplitude of a factor of two between different main-on states (the authors used the maximum main-on flux as a measure of the source luminosity). This behavior is opposite to that observed in the outbursts of the transient sources V 0332+53 and 4U 0115+63 (see above), making Her X-1 particularly interesting for our pulse-amplitude-resolved study.

We found that the amplitude of the single pulses during the selected observation (covering a large part of a main-on, see Sect. 2) varies by a factor of $\sim 2$. For spectral extraction, we selected five pulse-amplitude bins. The spectrum was modeled with the function used by Staubert et al. (2007) (and in most previous spectral studies of Her X-1) – `powerlaw×highecut` with

a Gaussian absorption line to model the CRSF. The exponential cutoff energy $E_{cutoff}$ was found to be strongly coupled with the photon index $\Gamma$ and, therefore, was fixed to its average (over all pulse-amplitude bins) value, 21.4 keV. As a result of our analysis, we were able to detect a strong *positive correlation* between $E_{cyc}$ and the pulse amplitude during a *single* main-on state (Fig. 6, top left panel). The slope of the best-fit linear relation (dotted line) is $(2.59 \pm 0.58) \times 10^{-3}$ keV/(cts/s). The Pearson linear correlation coefficient is $\sim 0.97$, corresponding to the probability to find the correlation by chance (two-sided) of only $\sim 6 \times 10^{-3}$ – highly significant positive correlation. This confirms the dependence found by Staubert et al. (2007) using a completely different approach. Additionally, we detected a *negative* correlation between the photon index $\Gamma$ and the pulse amplitude (Fig. 6, bottom left panel), which is contrary to V 0332+53 and 4U 0115+63 (see Fig. 6 and the previous subsections). The slopes of the best-fit linear relation (dotted line) between $\Gamma$ and the pulse height is $(-7.46 \pm 1.56) \times 10^{-5}$ (cts/s)$^{-1}$. The Pearson linear correlation coefficient and the corresponding two-sided null-hypothesis probability are $\sim -0.99$ and $\sim 4 \times 10^{-4}$ respectively – again, a highly significant (negative) correlation.

As for 4U 0115+63, the `powerlaw×highecut` function was the only suitable continuum model. Thus, we checked stability of our results only relative to the choice of the cyclotron model: `gabs` vs. `cyclabs`. The found correlations are well visible in both models.

### 4.4. A 0535+26

A 0535+26 is another BeXRB that sporadically shows intense outbursts. It has, however, a much longer pulsation period compared to V 0332+53 and 4U 0115+63 – around 103 s (Finger et al. 1994). Two absorption features, interpreted as cyclotron

lines (fundamental and first harmonic), have been observed in the source X-ray spectrum at ~45 keV and ~100 keV (Caballero et al. 2008, and references therein). Contrary to the sources described above, no clear variations of the cyclotron line energy with flux have so far been reported (Caballero et al. 2008).

For A 0535+26 we used the data obtained simultaneously with RXTE and INTEGRAL covering ~1 day around the maximum of the normal outburst in 2005 when the source luminosity reached roughly ~$10^{38}$ erg s$^{-1}$ (Caballero et al. 2007). Following Caballero et al. (2007, 2008), we used the *XSPEC* cutoffpl model (see Sect. 4.1) to describe the spectral continuum and a Gaussian absorption line to model the fundamental CRSF (the first harmonic was not detected in our pulse-amplitude resolved spectra). In case of INTEGRAL we set the energy range to 4−30 keV for JEM-X and to 18−90 keV for IBIS/ISGRI. As for RXTE, we introduced in our spectral model a multiplicative factor $F$ that was fixed to 1.0 for ISGRI and left free for JEM-X to account for uncertainties in the absolute flux normalization in the two instruments. In all pulse-amplitude bins the best-fit value of $F$ for ISGRI was around 0.96(2), indicating a 4% difference in the absolute flux normalization between the two instruments. Because of the strong intrinsic coupling between the photon index $\Gamma$ and the exponential folding energy $E_{\mathrm{fold}}$ (both in the RXTE and INTEGRAL data), we fixed the latter to its mean value (15.8 keV for RXTE and 16.3 keV for INTEGRAL) and explored only the variation of $\Gamma$.

As can be seen in Fig. 6, the data from both satellites independently show a strong indication of a *positive* correlation between the fundamental cyclotron line energy and the pulse height. The horizontal axis of the plots showing the INTEGRAL data represents the pulse amplitude measured in units of IBIS/ISGRI count rate in the 20−100 keV range. The slopes of linear fits to the data (as before, indicated with the dotted lines) are $(1.92 \pm 0.92) \times 10^{-3}$ keV/(PCA cts/s) for the RXTE observations (Fig. 6, top middle) and $(1.36 \pm 0.53) \times 10^{-2}$ keV/(ISGRI cts/s) for the INTEGRAL observations (Fig. 6, top right). The Pearson correlation coefficients with the associated two-sided null-hypotheses probability values are ~0.70 and ~0.19 respectively for the RXTE data (sparse correlation) and ~0.94 and ~0.02 for the INTEGRAL data. We repeat, however, that the similar relations are found by the two satellites independently, which supports the correlation. Our finding is particularly interesting because no corresponding "long time-scale correlation" of $E_{\mathrm{cyc}}$ with flux has been reported (see above). Our results make A 0535+26 only the second source (after Her X-1) that shows positive correlation of the cyclotron line energy with flux.

Additionally, the data from both satellites show hardening of the spectrum (decrease in $\Gamma$) with increasing pulse height, as shown in the bottom panels of the middle and the right column in Fig. 6. The slopes of linear fits to the data (dotted lines) are $(-1.54 \pm 0.19) \times 10^{-4}$ keV/(PCA cts/s) for the RXTE observations (Fig. 6, bottom middle) and $(-8.71 \pm 0.86) \times 10^{-2}$ keV/(ISGRI cts/s) for the INTEGRAL observations (Fig. 6, bottom right). The Pearson correlation coefficients with the associated two-sided null-hypotheses probability values are ~−0.98 and ~4 × $10^{-3}$ respectively for the RXTE data and ~−0.96 and ~0.01 for the INTEGRAL data − a significant correlation in both cases. This (anti-)correlation is contrary to the one observed in V 0332+53 and 4U 0115+63 but similar to the one found in Her X-1, which also shows a positive correlation between $E_{\mathrm{cyc}}$ and pulse amplitude. The negative correlation of $\Gamma$ with pulse height in A 0535+26 is also in line with Fig. 4 of Caballero et al. (2008) that shows higher values of the photon index at lower luminosities (at the beginning and the end of the outburst).

We note that it is not possible to compare directly the variations of the spectral parameters measured with INTEGRAL and RXTE as a function of pulse amplitude with each other. The high-resolution light curves used for the pulse selection were obtained with INTEGRAL/IBIS/ISGRI and RXTE/PCA in different energy bands (PCA is mostly sensitive below ~35 keV, while IBIS/ISGRI – above 20 keV, see Sect. 2), which leads to systematically different pulse-height distributions. Additionally, as we mentioned in Sect. 3, insufficient intercalibration accuracy of the two observatories might lead to systematic uncertainties in the absolute values of $E_{\mathrm{cyc}}$ and $\Gamma$ measured with the two instruments. Nevertheless, the *relative* variations of the spectral parameters with pulse amplitude can still be determined with the two satellites regardless of cross-calibration problems. Thus, the similarity of the parameters behavior found independently with RXTE and INTEGRAL suggests that the obtained effects indicate real physics.

As with other sources, we checked the found correlations using the Lorentzian line profile instead of the Gaussian one and found them to be independent with respect to the choice of the line model.

## 5. Discussion

The revealed dependencies of the spectral parameters on pulse amplitude in our sample of bright X-ray pulsars are mostly consistent with the long-term spectral changes related to the variability of the averaged luminosity of the sources (e.g. during the outbursts) reported previously, i.e. the correlations between the spectral parameters and flux have the same sign. We note, however, that it is generally impossible to compare our correlations directly with those found on the basis of the long-term flux variations. Our pulse amplitude reflects the flux in a narrow pulse-phase interval, consequently its value and variability range differ substantially from those of the pulse-averaged flux. Therefore, the individual pulse heights cannot easily be converted to the source luminosity as was done for the pulse-averaged flux in the previous works. The spectral parameters in our analysis were also extracted from the narrow pulse-phase interval and are, therefore, different from the pulse-averaged values. The variability of the average (over many pulse cycles) pulse profile along the outbursts in the previously reported "long-term" analyses would additionally complicate the comparison.

It has been argued by several authors that the long-term spectral variability of the cyclotron line energy reflects the changes in the accretion column structure, namely the variable height of the X-ray emitting region above the neutron star surface as a function of the mass accretion rate $\dot{M}$ (Mihara et al. 1998; Mowlavi et al. 2006; Staubert et al. 2007). Because the variability revealed in our work apparently takes place on the time scale of single X-ray pulsations, we have to conclude that the characteristic time scale of the changes in the emitting structure (in response to variable $\dot{M}$ reflected by the pulse height) are on the order of a few seconds or shorter. Any X-ray spectra accumulated over many subsequent pulsation cycles of a source therefore provide only an average characterization of the accretion structure over a range of its states corresponding to different local accretion rates.

### 5.1. Two regimes of accretion

Two of the four accreting pulsars studied in this work exhibit a negative correlation of the fundamental cyclotron line energy and a positive correlation of the photon index with pulse amplitude. In the other two sources the correlations are in the opposite

**Table 3.** Correlations of spectral parameters with pulse height.

| Source name | $E_{cyc}$ vs. pulse height | | | $\Gamma$ vs. pulse height | | |
|---|---|---|---|---|---|---|
| | slope [keV/(cts/s)] | Pearson cor. coeff. | 2-sided $P$-value | slope [(cts/s)$^{-1}$] | Pearson cor. coeff. | 2-sided $P$-value |
| V 0332+53 | $(-2.84 \pm 0.50) \times 10^{-4}$ | $-0.98$ | $4 \times 10^{-4}$ | $(2.21 \pm 0.88) \times 10^{-5}$ | $+0.77$ | 0.07 |
| 4U 0115+63 | $(-1.32 \pm 0.38) \times 10^{-4}$ | $-0.58$ | 0.22 | $(4.27 \pm 0.68) \times 10^{-5}$ | $+0.70$ | 0.12 |
| Her X-1 | $(2.59 \pm 0.58) \times 10^{-3}$ | $+0.97$ | $6 \times 10^{-3}$ | $(-7.46 \pm 1.56) \times 10^{-5}$ | $-0.99$ | $4 \times 10^{-4}$ |
| A 0535+26, XTE | $(1.92 \pm 0.92) \times 10^{-3}$ | $+0.70$ | 0.19 | $(-1.54 \pm 0.19) \times 10^{-4}$ | $-0.98$ | $4 \times 10^{-3}$ |
| A 0535+26, INT. | $(1.36 \pm 0.53) \times 10^{-2}$ | $+0.94$ | 0.02 | $(-8.71 \pm 0.86) \times 10^{-2}$ | $-0.96$ | 0.01 |

direction: a positive correlation of $E_{cyc}$ and a negative correlation of $\Gamma$ with pulse height. The correlations quantified by the values of the linear slope and the linear correlation coefficients (see the previous section) are summarized in Table 3. The two groups of pulsars apparently have different physical conditions inside their X-ray emitting structure leading to the different behavior of the spectral parameters.

The "long-term" negative correlation of the cyclotron line energy with the X-ray flux during the rises and decays of the outbursts of V 0332+53 and 4U 0115+63 has been attributed to the variable height of the radiative shock above the accretor surface where a substantial part of the kinetic energy possessed by inflowing matter transforms into radiation (Mihara et al. 1998, 2004; Mowlavi et al. 2006; Tsygankov et al. 2007). The height of the shock in these pulsars is believed to be directly proportional to the local mass accretion rate $\dot{M}$ (Basko & Sunyaev 1976). We argue that the negative correlation of $E_{cyc}$ with pulse amplitude reflects the same physical effect (changing of the shock height with $\dot{M}$) but on much shorter time scales. Indeed, the pulse height most probably reflects the local $\dot{M}$, which is highly variable on short time-scales, leading to the observed pulse-to-pulse variability. On the other hand, the "reaction time" of the emitting structure determined by the characteristic time scales at which the kinetic energy of infalling matter is converted into radiation and the latter diffuses through the column has been shown to be short enough – less than $10^{-6}$–$10^{-7}$ s (Orlandini & Boldt 1993; Morfill et al. 1984). The softening of the spectral index with pulse amplitude can also be qualitatively understood in this framework. According to the basic model of the accretion column in Basko & Sunyaev (1976), the plasma temperature in the column monotonically decreases with height (up to the the radiative shock). Thus, at higher $\dot{M}$ (i.e. at larger pulse amplitudes) one would expect more soft photons to be produced by the lateral walls of a taller column, which would naturally lead to a softer X-ray spectrum, as is observed.

Generally, the negative $E_{cyc} - \dot{M}$ correlation is only expected if the mass accretion rate is high enough for the radiative shock to form, i.e. if it is above some critical luminosity $L_c$, roughly corresponding to the local Eddington limit at the polar caps (Basko & Sunyaev 1976; Nelson et al. 1993). If the luminosity is below $L_c$, a different accretion regime is expected. So far, only one pulsar, Her X-1, has been reported to have a statistically significant positive $E_{cyc} - \dot{M}$ correlation (Staubert et al. 2007). The authors argued that this correlation is indeed expected at the luminosities below $L_c$, when infalling matter is stopped by the Coulomb drag and collective plasma effects rather than in a radiative shock. Our pulse-amplitude-resolved analysis showed that the positive $E_{cyc} - \dot{M}$ correlation found by Staubert et al. (2007) on the time scale of months to years is also present on the time scale of individual pulses and, consequently, supports the idea that in Her X-1 accretion proceeds in the local sub-Eddington regime (contrary to V 0332+53 and 4U 0115+63).

A positive correlation of $E_{cyc}$ with pulse height in A 0535+26, which we found here for the first time, apparently reveals the second (after Her X-1) case of a positive $E_{cyc} - \dot{M}$ correlation in an accreting pulsar. A similar to Her X-1 dependence of $\Gamma$ on pulse amplitude (see Table 3) additionally supports the idea that a different (compared to V 0332+53 and 4U 0115+63) accretion regime is realized in the two sources. We note here that the value of the critical luminosity $L_c$ is expected to vary from one pulsar to another because it generally depends on the $B$-field strength at the neutron star surface and the area of the polar cap (which might depend on the local magnetic field configuration, i.e. presence of higher multipole components etc.). Thus, it is well possible that the pulsars at a similar luminosity level (as e.g. A 0535+26 and 4U 0115+63) exhibit different accretion regimes.

We note that the small number of sources in our sample does not allow us to extend the obtained results (existence of the two accretion modes described above) to the entire population of accreting pulsars. Further observations of known cyclotron line sources together with discoveries of new X-ray pulsars showing cyclotron line variations would allow one to test our finding on a larger sample of pulsars.

## 6. Summary and conclusions

We studied the pulse-amplitude-resolved spectral variability in a sample of four bright accreting pulsars using the high-resolution X-ray data taken with RXTE and INTEGRAL. Our analysis revealed for the first time the spectral differences between X-ray pulses of different amplitudes, both in the spectral continuum and in the resonant cyclotron feature.

For the pulsars in which a negative correlation of the cyclotron line energy with flux on longer time scales has been reported previously, we found a similar (negative) correlation on the time scale of singe pulse cycles. In Her X-1 we found a positive correlation of the line energy with pulse height that is consistent with the long-term correlation of the CRSF energy and the maximum main-on flux reported by Staubert et al. (2007). Our analysis revealed a positive correlation of the cyclotron line energy with pulse amplitude in A 0535+26 where no correlation of the CRSF energy with flux has so far been reported.

The pulsars in our sample show two different types of spectral dependencies on pulse amplitude. We argue that the different behaviors reflect two distinct accretion regimes (local sub- and super-Eddington) realized in different pulsars, which was previously proposed to explain the peculiarity of Her X-1 compared to higher-luminosity pulsars.

# References

Araya-Góchez, R. A., & Harding, A. K. 2000, ApJ, 544, 1067
Basko, M. M., & Sunyaev, R. A. 1976, MNRAS, 175, 395
Belloni, T., & Hasinger, G. 1990, A&A, 230, 103
Bozzo, E., Falanga, M., & Stella, L. 2008, ApJ, 683, 1031
Bradt, H. V., Rothschild, R. E., & Swank, J. H. 1993, A&AS, 97, 355
Caballero, I., Kretschmar, P., Santangelo, A., et al. 2007, A&A, 465, L21
Caballero, I., Santangelo, A., Kretschmar, P., et al. 2008, A&A, 480, L17
Coe, M. J. 2000, in The Be Phenomenon in Early-Type Stars, ed. M. A. Smith, H. F. Henrichs, & J. Fabregat, IAU Colloq., 175, ASP Conf. Ser., 214, 656
Cominsky, L., Clark, G. W., Li, F., Mayer, W., & Rappaport, S. 1978, Nature, 273, 367
Demmel, V., Morfill, G., & Atmanspacher, H. 1990, ApJ, 354, 616
Ferrigno, C., Becker, P. A., Segreto, A., Mineo, T., & Santangelo, A. 2009, A&A, 498, 825
Finger, M. H., Wilson, R. B., & Hagedon, K. S. 1994, IAU Circ., 5931, 1
Frontera, F., dal Fiume, D., Morelli, E., & Spada, G. 1985, ApJ, 298, 585
Ghosh, P., & Lamb, F. K. 1979, ApJ, 232, 259
Heindl, W. A., Coburn, W., Gruber, D. E., et al. 1999, ApJ, 521, L49
Isenberg, M., Lamb, D. Q., & Wang, J. C. L. 1998, ApJ, 493, 154
Jahoda, K., Swank, J. H., Giles, A. B., et al. 1996, in SPIE Conf. Ser. 2808, ed. O. H. Siegmund, & M. A. Gummin, 59
Klochkov, D. K., Shakura, N. I., Postnov, K. A., et al. 2006, Astron. Lett., 32, 804
Klochkov, D., Staubert, R., Postnov, K., et al. 2008a, A&A, 482, 907
Klochkov, D., Staubert, R., Postnov, K., et al. 2008b, in Proceedings of the 7th INTEGRAL Workshop

Kretschmar, P., Kreykenbohm, I., Wilms, J., et al. 2000, in AIP Conf. Ser. 510, ed. M. L. McConnell, & J. M. Ryan, 163
Kulkarni, A. K., & Romanova, M. M. 2008, MNRAS, 386, 673
Lund, N., Budtz-Jørgensen, C., Westergaard, N. J., et al. 2003, A&A, 411, L231
Mihara, T., Makishima, K., & Nagase, F. 1998, Adv. Space Res., 22, 987
Mihara, T., Makishima, K., & Nagase, F. 2004, ApJ, 610, 390
Morfill, G. E., Truemper, J., Tenorio-Tagle, G., & Bodenheimer, P. 1984, A&A, 139, 7
Mowlavi, N., Kreykenbohm, I., Shaw, S. E., et al. 2006, A&A, 451, 187
Nelson, R. W., Salpeter, E. E., & Wasserman, I. 1993, ApJ, 418, 874
Orlandini, M., & Boldt, E. 1993, ApJ, 419, 776
Pottschmidt, K., Koenig, M., Wilms, J., & Staubert, R. 1998, A&A, 334, 201
Revnivtsev, M., Churazov, E., Postnov, K., & Tsygankov, S. 2009, A&A, 507, 1211
Reynolds, A. P., Quaintrell, H., Still, M. D., et al. 1997, MNRAS, 288, 43
Rothschild, R. E., Blanco, P. R., Gruber, D. E., et al. 1998, ApJ, 496, 538
Rothschild, R. E., Markowitz, A., Rivers, E., et al. 2011, ApJ, 733, 23
Santangelo, A., Segreto, A., Giarrusso, S., et al. 1999, ApJ, 523, L85
Staubert, R., Kendziorra, E., Pietsch, W., et al. 1980, ApJ, 239, 1010
Staubert, R., Bezler, M., & Kendziorra, E. 1983, A&A, 117, 215
Staubert, R., Shakura, N. I., Postnov, K., et al. 2007, A&A, 465, L25
Stella, L., White, N. E., Davelaar, J., et al. 1985, ApJ, 288, L45
Trümper, J., Pietsch, W., Reppin, C., et al. 1978, ApJ, 219, L105
Tsujimoto, M., Guainazzi, M., Plucinsky, P. P., et al. 2011, A&A, 525, A25
Tsygankov, S. S., Lutovinov, A. A., Churazov, E. M., & Sunyaev, R. A. 2007, Astron. Lett., 33, 368
Tsygankov, S. S., Lutovinov, A. A., & Serber, A. V. 2010, MNRAS, 401, 1628
Ubertini, P., Lebrun, F., Di Cocco, G., et al. 2003, A&A, 411, L131
Winkler, C., Gehrels, N., Schönfelder, V., et al. 2003, A&A, 411, L349

# Appendix D

# Outburst of GX 304-1 monitored with INTEGRAL: positive correlation between the cyclotron line energy and flux

**Astronomy & Astrophysics**

# Outburst of GX 304–1 monitored with INTEGRAL: positive correlation between the cyclotron line energy and flux

D. Klochkov[1], V. Doroshenko[1], A. Santangelo[1], R. Staubert[1], C. Ferrigno[2], P. Kretschmar[3], I. Caballero[4], J. Wilms[5], I. Kreykenbohm[5], K. Pottschmidt[6,9], R. E. Rothschild[7], C. A. Wilson-Hodge[8], and G. Pühlhofer[1]

[1] Institut für Astronomie und Astrophysik, Universität Tübingen (IAAT), Sand 1, 72076 Tübingen, Germany
e-mail: klochkov@astro.uni-tuebingen.de
[2] ISDC Data Center for Astrophysics, University of Geneva, chemin d'Écogia 16, 1290 Versoix, Switzerland
[3] European Space Astronomy Centre (ESA/ESAC), Science Operations Department, Villanueva de la Canãda, Madrid, Spain
[4] CEA Saclay, DSM/IRFU/SAp – UMR AIM (7158) CNRS/CEA/Université P. Diderot, Orme des Merisiers, Bât. 709, 91191 Gif-sur-Yvette, France
[5] Dr. Karl Remeis Sternwarte & Erlangen Centre for Astroparticle Physics, Sternwartstr. 7, 96049 Bamberg, Germany
[6] Center for Space Science and Technology, University of Maryland Baltimore County, 1000 Hilltop Circle, Baltimore, MD 21250, USA
[7] Center for Astrophysics and Space Sciences, University of California, San Diego, 9500 Gilman Dr., La Jolla, CA 92093-0424, USA
[8] NASA Marshall Space Flight Center, Huntsville, AL 35812, USA
[9] CRESST & NASA Goddard Space Flight Center, Astrophysics Science Division, Code 661, Greenbelt, MD 20771, USA

**ABSTRACT**

*Context.* X-ray spectra of many accreting pulsars exhibit significant variations as a function of flux and thus of mass accretion rate. In some of these pulsars, the centroid energy of the cyclotron line(s), which characterizes the magnetic field strength at the site of the X-ray emission, has been found to vary systematically with flux.
*Aims.* GX 304−1 is a recently established cyclotron line source with a line energy around 50 keV. Since 2009, the pulsar shows regular outbursts with the peak flux exceeding one Crab. We analyze the INTEGRAL observations of the source during its outburst in January–February 2012.
*Methods.* The observations covered almost the entire outburst, allowing us to measure the source's broad-band X-ray spectrum at different flux levels. We report on the variations in the spectral parameters with luminosity and focus on the variations in the cyclotron line.
*Results.* The centroid energy of the line is found to be positively correlated with the luminosity. We interpret this result as a manifestation of the local sub-Eddington (sub-critical) accretion regime operating in the source.

**Key words.** X-rays: binaries – stars: neutron – accretion, accretion disks

## 1. Introduction

In accreting binary pulsars, matter from the normal stellar companion is transferred to a highly magnetized ($B \gtrsim 10^{12}$ G) neutron star. In the vicinity of the accretor, the gas flow is disrupted by the neutron star's magnetic field and channeled towards the magnetic poles, where most of the X-rays originate. The physics and the structure of the X-ray emitting region(s) above the neutron star surface are still highly debated (see, e.g., Becker & Wolff 2007; Farinelli et al. 2012). Since the matter hitting the accretor's surface is highly ionized, the magnetic field strength is a crucial parameter determining the physical processes inside the emitting region and the formation of the observed X-ray spectrum. A direct way to assess the *B*-field strength at the site of X-ray emission is the measurement of the cyclotron resonant scattering features (CRSF or *cyclotron lines*) in the X-ray spectrum of a pulsar. These features appear as absorption lines, caused by the resonant scattering of photons off the electrons in Landau levels (see, e.g., Trümper et al. 1978; Isenberg et al. 1998). The energy of the fundamental line and the spacing between the harmonics are directly proportional to the field strength.

In some accreting pulsars, the energy of the cyclotron line has been found to vary with luminosity, apparently due to a displacement of the line formation region. Such variations of the line energy have been reported for V 0332+53 (e.g., Tsygankov et al. 2010), 4U 0115+63 (e.g., Tsygankov et al. 2010), Her X-1 (Staubert et al. 2007; Klochkov et al. 2011), and A 0535+26 (Klochkov et al. 2011). The luminosity-dependence of the cyclotron feature has strong implications for the physics of the X-ray emitting region as discussed, e.g., by Staubert et al. (2007), Klochkov et al. (2011), and Becker & Wolff (2007).

GX 304−1 is a recently established cyclotron line source (Yamamoto et al. 2011). It was discovered in a balloon experiment in 1967 and subsequently identified as an X-ray pulsar with a period of ∼272 s (McClintock et al. 1977). The system contains a Be-type optical companion (Mason et al. 1978) and is located at a distance of ∼2.4 kpc (Parkes et al. 1980). Since 1980, GX 304−1 has remained in a quiescent state, showing no outbursts. Starting from 2008, when the source was detected with INTEGRAL (Manousakis et al. 2008), GX 304−1 "resumed" its activity exhibiting outbursts with a period of ∼132.5 d.

The energy of the cyclotron line in GX 304−1 was measured with *Suzaku* and RXTE to be around 52 keV by

**Table 1.** INTEGRAL observations of the GX 304−1 outburst in January–February 2012.

| Rev. | Obs. ID | Mid. MJD | Exposure [ks] | | |
| | | | JEM-X | IBIS | SPI |
|------|---------|----------|-------|------|-----|
| 1131 | 09400230006 | 55 944.0 | 64.6 | 42.7 | 68.6 |
| 1132 | 09400230007 | 55 947.0 | 42.4 | 31.9 | 36.6 |
| 1133 | 09400230008 | 55 950.0 | – | – | 10.7 |
| 1134 | 09400230009 | 55 952.8 | 7.3 | 25.4 | 37.8 |
| 1135 | 09400230010 | 55 955.7 | – | 6.7 | 25.1 |
| 1136 | 09400230011 | 55 958.7 | 36.9 | 28.1 | 32.9 |
| 1137 | 09400230012 | 55 962.0 | 78.1 | 59.7 | 78.4 |
| 1138 | 09400230013 | 55 965.0 | 60.7 | 45.2 | 52.3 |

Yamamoto et al. (2011). These authors demonstrate that the data taken at different flux levels show an indication of a positive correlation between the line energy and the X-ray flux, although at a low significance level. This made GX 304−1 a good target for a luminosity-dependent study of the cyclotron feature. In this work, we present the analysis of INTEGRAL data (see next section for the mission description) taken during the January 2012 outburst of the source. The data reveal a positive correlation between the cyclotron line energy and the source flux, as well as the variation in other spectral parameters during the outburst. We discuss our finding in the context of a model assuming that different accretion regimes can operate in a particular pulsar depending on its X-ray luminosity.

## 2. Observations and data reduction

At the beginning of January 2012, GX 304−1 entered an outburst as reported by Yamamoto et al. (2012). The outburst was monitored by the International Gamma-Ray Astrophysics Laboratory – INTEGRAL (Winkler et al. 2003), starting at MJD ∼ 55 943.5, when the source flux in the ∼20−80 keV range was ∼250 mCrab, through the maximum of the outburst, when the source flux exceeded one Crab, to MJD ∼ 55 965.5, when the flux dropped to ∼100 mCrab. INTEGRAL performed one observation every satellite orbit (about three days), with a typical exposure of a few tens of kiloseconds each. In total, eight observations were performed. The INTEGRAL scientific payload contains three X-ray instruments: (i) the imager IBIS sensitive from ∼20 keV to a few MeV (Ubertini et al. 2003; Lebrun et al. 2003); (ii) the spectrometer SPI sensitive in roughly the same energy range as IBIS (Vedrenne et al. 2003); and (iii) the X-ray monitor JEM-X operating between ∼3 and ∼35 keV (Lund et al. 2003). Table 1 summarizes the INTEGRAL observations of GX 304−1. The increased solar activity during the observations led to the reduction in the exposure time and availability of the instruments as can be seen from the exposure columns of Table 1.

The INTEGRAL observations are indicated in Fig. 1, which shows the *Swift*/BAT light curve of GX 304−1[1]. The INTEGRAL monitoring has an excellent coverage of the entire outburst, providing a rare opportunity to follow the evolution of the outburst from the early rising phase to the late decay phase.

For our analysis, we used data from the ISGRI detector of IBIS, which is sensitive in the 20−300 keV energy range, JEM-X, and SPI. Standard data processing was performed with version 9 of the Offline Science Analysis (OSA) software. We performed an additional gain correction of the

---

[1] We used the *Swift*/BAT transient monitor results provided by the *Swift*/BAT team.
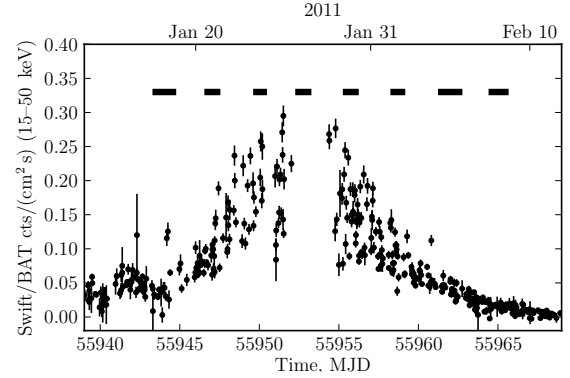
**Fig. 1.** INTEGRAL observations of GX 304−1 (horizontal bars) superposed on the *Swift*/BAT light curve of the source during its outburst in January−February 2012 (∼0.22 units of the vertical axis corresponds to one Crab).

ISGRI energy scale based on the background spectral lines of Tungsten (the modified response files based on the nearest Crab observations were used).

## 3. Spectral analysis

Figure 1 shows that the X-ray flux of GX 304−1 during the observed part of the outburst changed by an order of magnitude. This allowed a detailed study of the luminosity dependence of the source's broad-band X-ray spectrum. X-ray pulsations with a period of ∼274.9 s were detected in all INTEGRAL observations. This value is roughly consistent with the known pulse period. A detailed timing analysis is not part of the present work and will be presented elsewhere.

In all observations, the X-ray continuum could be closely modeled by a standard power-law/cutoff function (flux $\propto E^{-\Gamma} \exp[E/E_{\rm fold}]$, where $E$ is the photon energy, $\Gamma$ is the photon index, and $E_{\rm fold}$ is the exponential roll-off parameter) modified by photo-electric absorption at low energies. In addition, the spectra showed a cyclotron resonant scattering feature around ∼50 keV in absorption, which was modeled with a multiplicative absorption line with a Gaussian optical depth profile $I(E) = I_{\rm cont}(E) \cdot {\rm e}^{-G(E)}$, where $G(E) = -\tau_{\rm cyc}/(\sqrt{2\pi}\sigma_{\rm cyc}) \cdot \exp[-0.5(E - E_{\rm cyc})^2/\sigma_{\rm cyc}^2]$, $I_{\rm cont}(E)$ is the continuum function, $E_{\rm cyc}$, $\sigma_{\rm cyc}$, and $\tau_{\rm cyc}$ are the centroid energy, width, and optical depth of the line, respectively. The line is clearly detected in ISGRI and SPI data separately, as shown by the residual plots in Fig. 2. The inclusion of the absorption line in the model leads to an improvement in the reduced $\chi^2$ from 3.10 for 145 d.o.f. (with the corresponding null-hypothesis probability of only ∼$10^{-32}$) to 0.75 for 142 d.o.f. (null-hypothesis probability >0.9). The energy of the line is consistent with that reported by Yamamoto et al. (2011) based on the RXTE and *Suzaku* observations. We also included an additive Gaussian component to model the Fe $K_\alpha$ fluorescence emission line around 6.4 keV. The inclusion of the line reduces the residuals around 6 keV. The corresponding improvement of the reduced $\chi^2$ is, however, marginal: from 0.80 (143 d.o.f.) to 0.75 (142 d.o.f.). The presence of the Fe line is, therefore, questionable.

Both the continuum and cyclotron line parameters vary systematically during the outburst. Here, we focus on the evolution of the cyclotron line energy $E_{\rm cyc}$, to establish a possible correlation of $E_{\rm cyc}$ with flux, similar to that found by Yamamoto et al. (2011). To characterize this variability, we used

**Table 2.** Best-fit spectral parameters with the corresponding $1\sigma$-uncertainties for the INTEGRAL observations used in this work.

| Revolution | 1131 | 1132 | 1134 | 1136 | 1137 | 1138 |
|---|---|---|---|---|---|---|
| $\Gamma$ | $1.10^{+0.03}_{-0.03}$ | $0.83^{+0.03}_{-0.03}$ | $0.93^{+0.09}_{-0.09}$ | $1.10^{+0.08}_{-0.08}$ | $1.23^{+0.08}_{-0.08}$ | $1.56^{+0.13}_{-0.05}$ |
| $E_{\rm fold}$, keV | $19.1^{+0.7}_{-0.6}$ | $15.5^{+0.4}_{-0.4}$ | $14.5^{+0.6}_{-0.6}$ | $16.9^{+0.8}_{-0.7}$ | $19.5^{+1.1}_{-1.0}$ | $28.6^{+3.8}_{-2.2}$ |
| $E_{\rm cyc}$, keV | $52.98^{+0.80}_{-0.75}$ | $54.39^{+0.75}_{-0.73}$ | $55.28^{+0.87}_{-0.81}$ | $51.44^{+0.54}_{-0.52}$ | $51.70^{+0.66}_{-0.63}$ | $48.37^{+1.19}_{-1.12}$ |
| $\sigma_{\rm cyc}$, keV | $6.45^{+0.62}_{-0.58}$ | $7.56^{+0.59}_{-0.57}$ | $8.45^{+0.83}_{-0.75}$ | $5.60^{+0.48}_{-0.46}$ | $5.44^{+0.56}_{-0.55}$ | $4.80^{+0.91}_{-0.89}$ |
| $\tau_{\rm cyc}$ | $9.4^{+1.3}_{-1.2}$ | $12.1^{+1.4}_{-1.3}$ | $13.3^{+2.4}_{-2.0}$ | $8.8^{+0.9}_{-0.9}$ | $8.9^{+1.2}_{-1.1}$ | $5.7^{+1.3}_{-1.3}$ |
| Flux/$10^{-8}$ erg s$^{-1}$ cm$^{-2}$ | $0.375^{+0.002}_{-0.002}$ | $0.811^{+0.004}_{-0.004}$ | $1.630^{+0.011}_{-0.011}$ | $0.729^{+0.005}_{-0.005}$ | $0.340^{+0.002}_{-0.003}$ | $0.151^{+0.002}_{-0.002}$ |
| $L_{\rm X}/10^{37}$ erg s$^{-1}$ | 0.26 | 0.56 | 1.12 | 0.50 | 0.23 | 0.10 |
| $\chi^2_{\rm red}$/d.o.f. | 1.1/164 | 0.7/164 | 1.3/164 | 1.1/164 | 0.9/164 | 1.0/164 |

**Notes.** The luminosity is provided assuming a distance of 2.4 kpc and an isotropic emission diagram.
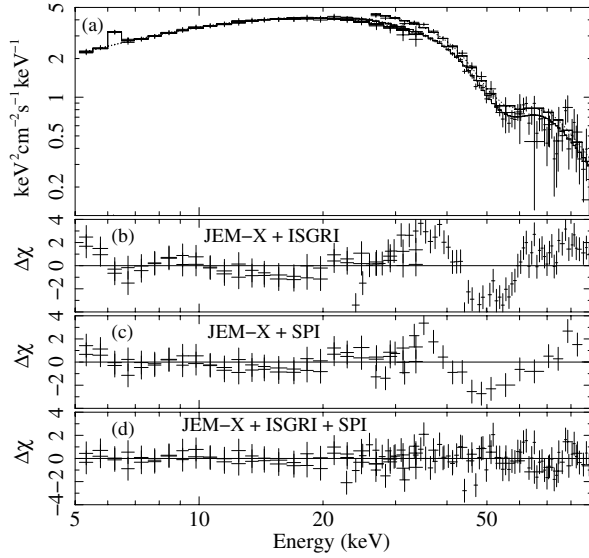


**Fig. 2.** Example of the INTEGRAL spectrum of GX 304−1 (revolution 1132) with a simultaneous fit of data from JEM-X, ISGRI, and SPI with a power-law/cutoff model including a cyclotron absorption line (see text) **a)**; the residuals for a fit with the model without the cyclotron line for JEM-X + ISGRI **b)**; and JEM-X + SPI **c)**; and with the model where the line is included for data from all instruments **d)**.

only observations where data from all three INTEGRAL X-ray instruments were available. This filtering allowed us to obtain a homogeneous set of data and, hence minimize possible systematic effects. Following this selection, data from the orbits 1133 and 1135 were excluded. The JEM-X data collected during the orbit 1134 (peak of the outburst) have been flagged as "bad" by the instrument team owing to the impossibility to provide a precise energy calibration. In our analysis, however, we use the JEM-X data to restrict the low-energy part of the broadband X-ray continuum of the source, for which a precise energy scale is not very critical. Therefore, after consulting the JEM-X team, we re-introduced the JEM-X data from the revolution 1134 in our analysis. We checked, however, that inclusion of the JEM-X data of rev. 1134 to the corresponding spectral fit does not significantly influence the measured energy of the cyclotron line (the focus of this work), but only affects its uncertainty. Table 2 summarizes the best-fit spectral parameters achieved in each observations.

A clear systematic variation in the line energy over the outburst is evident in Fig. 3, which shows that $E_{\rm cyc}$ generally follows
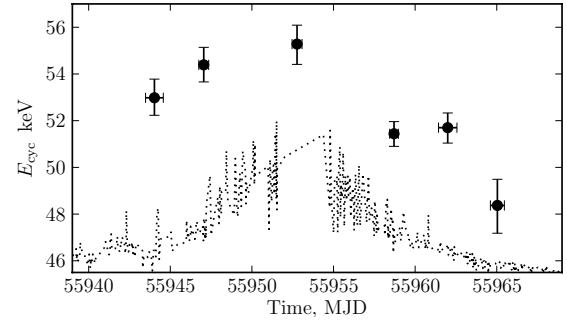


**Fig. 3.** Evolution of the cyclotron line centroid energy $E_{\rm cyc}$ throughout the outburst of GX 304−1 as measured with INTEGRAL. The vertical error bars indicate $1\sigma$-uncertainties. The horizontal error bars indicate the time intervals of the observations. The dotted line represents the re-scaled *Swift*/BAT light curve.
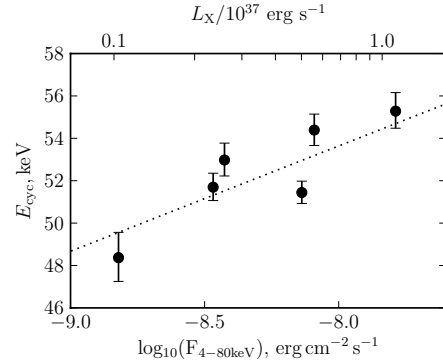


**Fig. 4.** Cyclotron line centroid energy $E_{\rm cyc}$ as a function of the logarithm of flux in the 4−80 keV range. The error bars indicate $1\sigma$-uncertainties (the flux uncertainties are smaller than the symbol size). The top X-axis represents the corresponding isotropic source luminosity assuming a distance of 2.4 kpc. The dotted line shows a linear fit to the $E_{\rm cyc}$–$\log_{10}$(Flux) dependence.

the X-ray flux. To assess the interdependence of the two parameters, we plotted $E_{\rm cyc}$ as a function of the X-ray flux in the 4−80 keV range measured with INTEGRAL in the respective observations (Fig. 4). The plot shows a positive correlation between the two values. A linear fit to the dependence of $E_{\rm cyc}$ on the logarithm of flux (dotted line in the plot) reveals a slope of $4.97 \pm 1.12$ keV/$\log_{10}$(erg cm$^{-2}$ s$^{-1}$). The standard linear correlation analysis of the $E_{\rm cyc} - \log_{10}$(Flux) dependence yields a

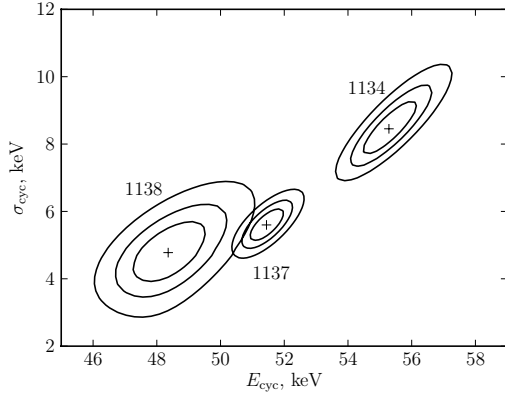**Fig. 5.** $\chi^2$-contour plots of the parameter pair $E_{cyc}/\sigma_{cyc}$ for a few selected observations. The contours correspond to $\chi^2_{min} + 1.0$ (the projections of this contour to the parameter axes correspond to the 68%-uncertainty for one parameter of interest), $\chi^2_{min} + 2.3$ (68%-uncertainty for two parameters of interest), and $\chi^2_{min} + 4.61$ (90%-uncertainty for two parameters of interest). The respective orbit numbers are indicated.

Pearson's correlation coefficient of 0.88 with a probability of obtaining the correlation by chance of ~0.01 (one-sided).

We verified whether our spectral fits contain artificial (model-driven) dependences of the cyclotron line energy $E_{cyc}$ and other model parameters using $\chi^2$-contour plots. No significant model-driven dependences between $E_{cyc}$ and any of the continuum parameters were found. The line energy was, however, found to be somewhat coupled to the line width $\sigma_{cyc}$ and its central optical depth $\tau_{cyc}$. Nevertheless, the $\chi^2$-minima and the confidence intervals could be clearly identified and are separated for the different observations as shown in Fig. 5. The plot shows the contours for the $E_{cyc}/\sigma_{cyc}$ pair. The $E_{cyc}/\tau_{cyc}$ contours look similar.

To check whether the $E_{cyc}$/flux correlation is related to instrumental effects, we performed spectral fits using only the JEM-X and SPI data (excluding ISGRI). To verify whether the correlation depends on the choice of the spectral model, we fit the data using a Lorentzian line profile instead of a Gaussian one. We also tried two alternative continuum functions: XSPEC `powerlaw×highecut` and `compTT` models. In the former model, the `highecut` component controls the exponential roll-off. In addition to $E_{fold}$, this component has an additional parameter – the cutoff energy $E_{cutoff}$, above which the spectrum is affected by the roll-off. In our fits, $E_{cutoff}$ stays between a few and ~10 keV. In all cases, the positive $E_{cyc}$/flux correlation was reproduced. We conclude, therefore, that the reported correlation arises from the source's behavior and reflects real physics.

## 4. Discussion and conclusions

The positive correlation between the cyclotron line centroid energy and the flux found with INTEGRAL confirms the claim of this correlation by Yamamoto et al. (2011). The revealed dependence establishes GX 304−1 as the third member of a slowly emerging class of accreting pulsars showing a positive $E_{cyc}$/flux correlation with the other members being Her X-1 (Staubert et al. 2007) and possibly A 0535+26 (Klochkov et al. 2011), for which the positive correlation has so far been only established in the pulse-to-pulse analysis. The opposite (negative) correlation between the line energy and the flux was found in V 0332+53 and 4U 0115+63 (e.g., Tsygankov et al. 2007, 2010). According to

discussions in Staubert et al. (2007), Klochkov et al. (2011), and Becker et al. (2012), these two types of dependences reflect two different regimes of accretion. A particular regime is realized in a source depending on whether its X-ray luminosity $L$ is above or below a critical luminosity $L_c$, which corresponds to the local Eddington luminosity at the X-ray emitting structure(s) on/above the neutron star surface. In accreting pulsars radiating above $L_c$ ("super-critical" sources), infalling matter is decelerated in a radiative shock, whose height is believed to increase with $L$, i.e., drift towards an area with a lower $B$-field strength. The opposite behavior probably occurs in sources radiating below or close to $L_c$ ("sub-critical" sources), where infalling matter is stopped by the Coulomb drag and collective plasma effects rather than in a radiative shock. As discussed in Staubert et al. (2007) and Becker et al. (2012), the height of the emitting region decreases with increasing luminosity owing to a corresponding increase in ram pressure of the infalling material, leading to a positive $E_{cyc}$/flux correlation. The critical luminosity $L_c$ depends on the parameters of the accreting neutron star, but is generally around a few times ~$10^{37}$ erg s$^{-1}$ (Basko & Sunyaev 1976; Staubert et al. 2007; Becker et al. 2012). Assuming a distance of 2.4 kpc (Parkes et al. 1980), the X-ray luminosity of GX 304−1 in the 4−80 keV range during the reported INTEGRAL observations varies between ~$1.1 \times 10^{36}$ erg s$^{-1}$ and ~$1.13 \times 10^{37}$ erg s$^{-1}$. Thus, according to the described picture, the source should belong to the class of "sub-critical" sources, for which a positive $E_{cyc}$/flux correlation is expected. The reported observations are, therefore, in agreement with the idea of two accretion regimes and increases the yet very small sample of accreting pulsars with established $E_{cyc}$/flux correlations.

## References

Basko, M. M., & Sunyaev, R. A. 1976, MNRAS, 175, 395
Becker, P. A., & Wolff, M. T. 2007, ApJ, 654, 435
Becker, P., Klochkov, D., Schoenherr, G., et al. 2012, A&A, in press, DOI: 10.1051/0004-6361/201219065
Farinelli, R., Ceccobello, C., Romano, P., & Titarchuk, L. 2012, A&A, 538, A67
Isenberg, M., Lamb, D. Q., & Wang, J. C. L. 1998, ApJ, 493, 154
Klochkov, D., Staubert, R., Santangelo, A., Rothschild, R. E., & Ferrigno, C. 2011, A&A, 532, A126
Lebrun, F., Leray, J. P., Lavocat, P., et al. 2003, A&A, 411, L141
Lund, N., Budtz-Jørgensen, C., Westergaard, N. J., et al. 2003, A&A, 411, L231
Manousakis, A., Beckmann, V., Bianchin, V., et al. 2008, ATEL, 1613
Mason, K. O., Murdin, P. G., Parkes, G. E., & Visvanathan, N. 1978, MNRAS, 184, 45
McClintock, J. E., Nugent, J. J., Li, F. K., & Rappaport, S. A. 1977, ApJ, 216, L15
Parkes, G. E., Murdin, P. G., & Mason, K. O. 1980, MNRAS, 190, 537
Priedhorsky, W. C., & Terrell, J. 1983, ApJ, 273, 709
Protassov, R., van Dyk, D. A., Connors, A., Kashyap, V. L., & Siemiginowska, A. 2002, ApJ, 571, 545
Staubert, R., Shakura, N. I., Postnov, K., et al. 2007, A&A, 465, L25
Trümper, J., Pietsch, W., Reppin, C., et al. 1978, ApJ, 219, L105
Tsygankov, S. S., Lutovinov, A. A., Churazov, E. M., & Sunyaev, R. A. 2007, Astron. Lett., 33, 368
Tsygankov, S. S., Lutovinov, A. A., & Serber, A. V. 2010, MNRAS, 401, 1628
Ubertini, P., Lebrun, F., Di Cocco, G., et al. 2003, A&A, 411, L131
Vedrenne, G., Roques, J.-P., Schönfelder, V., et al. 2003, A&A, 411, L63
Winkler, C., Courvoisier, T. J.-L., Di Cocco, G., et al. 2003, A&A, 411, L1
Yamamoto, T., Sugizaki, M., Mihara, T., et al. 2011, PASJ, 63, 751
Yamamoto, T., Tomida, H., Mihara, T., et al. 2012, ATEL, 3856

# Appendix E

# Giant outburst of EXO 2030+375: pulse-phase resolved analysis of INTEGRAL data

**Astronomy**
**&**
**Astrophysics**

# Giant outburst of EXO 2030+375: pulse-phase resolved analysis of *INTEGRAL* data

D. Klochkov[1], A. Santangelo[1], R. Staubert[1], and C. Ferrigno[2]

[1] Institut für Astronomie und Astrophysik, Universität Tübingen (IAAT), Sand 1, 72076 Tübingen, Germany
e-mail: klochkov@astro.uni-tuebingen.de
[2] INAF IFC-Pa, via U. La Malfa 153, 90146 Palermo, Italy

## ABSTRACT

In June–September 2006 the Be/X-ray binary EXO 2030+375 experienced the second giant outburst since its discovery. The source was shown to have a complicated pulse-averaged X-ray spectral continuum with possible evidence of cyclotron absorption features. In this paper we present the first pulse-phase resolved analysis of the broad band X-ray spectra of EXO 2030+375 obtained with the *INTEGRAL* observatory close to the maximum and during the decay phase of the giant outburst. We report a strong variability of the spectrum with pulse phase. Alternative spectral continuum models are discussed. The dependence of the spectral parameters on pulse phase during the maximum of the outburst and the evolution of the pulse profiles with time are qualitatively consistent with the pulsar's emission diagram changing from the fan-beam geometry close to the maximum of the outburst to a combination of pencil and fan beams (of comparable intesities) at the end of the decay phase. Evidence of a cyclotron absorption line around 63 keV at the pulse phase interval preceeding the main peak of the pulse profile is present in the spectrum obtained close to the maximum of the outburst.

**Key words.** stars: neutron – X-rays: binaries – accretion, accretion disks

## 1. Introduction

The transient accreting pulsar EXO 2030+375 belongs to the most common type of X-ray pulsar systems – the Be/X-ray binaries. Such systems form a subclass of high mass X-ray binaries. They consist of a pulsar and a Be (or Oe) companion, a main-sequence star of spectral type B (or O) that shows Balmer emission lines (see e.g. Slettebak 1988, for a review). The line emission is believed to be associated with an equatorial outflow of material expelled from the rapidly rotating Be star that probably forms a quasi-Keplerian disk around its equator (Hanuschik 1996; Quirrenbach et al. 1997). If the disk reaches a radius comparable to the periastron separation, then disk gas accreted by the neutron star can power a significant (and usually transient) X-ray source.

Be/X-ray binaries typically show two types of outburst behavior:

1. normal (or type I) outbursts. They are characterized by relatively low X-ray luminosities $L_X \sim 10^{36}$–$10^{37}$ erg s$^{-1}$, low spin-up rates (if any), and recurrence at the orbital period (or its multiples). Such outbursts last from days to weeks and are associated with the periastron passages of the neutron star;
2. giant (or type II) outbursts. They are characterized by higher X-ray luminosities $L_X \gtrsim 10^{37}$ erg s$^{-1}$ and high spin-up rates. Such outbursts occur irregularly. They last several weeks and are not correlated with any particular orbital phase. The typical time between outbursts is around several years. Giant outbursts are thought to stem from a dramatic expansion of the disk surrounding the Be star, leading to the formation of an accretion disk around the compact object.

EXO 2030+375 is one of the best-studied Be/X-ray binaries. It was discovered with the *EXOSAT* satellite during a giant outburst in 1985 (Parmar et al. 1989b). The optical companion of the pulsar is a B0 Ve star identified by optical and infrared observations of the *EXOSAT* error circle (Motch & Janot-Pacheco 1987; Janot-Pacheco et al. 1988; Coe et al. 1988). The orbital period and eccentricity of the system are ~46 d and ~0.42, respectively (Wilson et al. 2002). The period of X-ray pulsations is ~42 s. There were two giant outbursts in the history of observations of EXO 2030+375. During the first one in 1985 (when the pulsar was discovered), the X-ray luminosity of the source reached a value of $L_{1-20 \text{ keV}} \sim 2 \times 10^{38}$ erg s$^{-1}$ (assuming a distance of 7.1 kpc, Wilson et al. 2002). The spin frequency of the pulsar changed dramatically, with a spin-up timescale $-P/\dot{P} \sim 30$ yr indicating the formation of an accretion disk around the neutron star. The second giant outburst took place in June–September 2006 (Corbet & Levine 2006; Klochkov et al. 2007) and was again accompanied by a strong spin-up of the neutron star. The X-ray luminosity at the maximum of the outburst was slightly lower than during the 1985 giant outburst: $L_{1-20 \text{ keV}} \sim 1.2 \times 10^{38}$ erg s$^{-1}$ (Wilson & Finger 2006).

During the 2006 giant outburst the source was observed several times with the *INTEGRAL* satellite. A preliminary pulse-averaged spectral analysis of some of these observations are presented in Klochkov et al. (2007). A detailed analysis of pulse-averaged *RXTE* spectra obtained during the outburst was performed by Wilson et al. (2008). It has been shown that the pulse averaged X-ray continuum of the source has a complicated shape and cannot be modeled by a simple power law/cutoff model. Wilson et al. (2008) include an absorption line at ~10 keV (which they interpreted as a cyclotron line) in their spectral model, whereas Klochkov et al. (2007) have shown that the spectrum can be fitted equally well without the absorption line, but including a broad emission "bump" at ~15 keV.
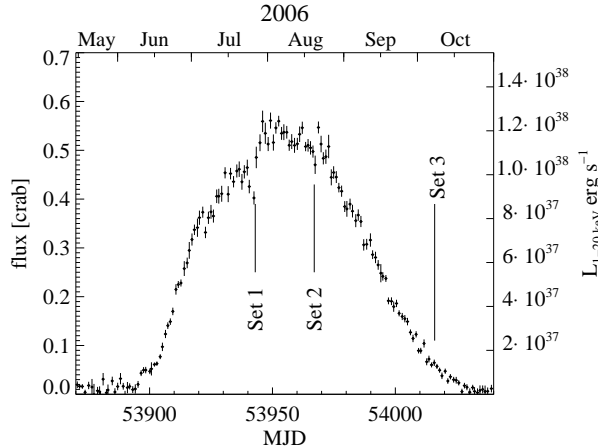
**Fig. 1.** The *RXTE/ASM* light curve of EXO 2030+375 showing the 2006 giant outburst. Times of *INTEGRAL* observations analyzed in this work are marked with vertical lines. The observations are referred to as Set 1, Set 2, and Set 3 in the text.

Here we present for the first time pulse-phase resolved broad band (3–150 keV) spectra of EXO 2030+375 during a giant outburst. For our analysis we used all the available *INTEGRAL* data taken during the 2006 outburst. The X-ray continuum of the source shows strong variability with pulse phase, with some features present only at particular pulse-phase intervals. The description of observations that we used is provided in Sect. 2. Details of data processing are described in Sect. 3. Sections 4 and 5 are devoted to the analysis of the data close to the maximum and during the decay of the outburst, respectively. The results are discussed in Sect. 6 and briefly summarized in Sect. 7.

## 2. Observations

The **INTE**rnational **G**amma **R**ay **A**strophysics **L**aboratory (*INTEGRAL*, Winkler et al. 2003) performed three pointed observations of EXO 2030+375 during its giant outburst in June–September 2006. Two observations (on 19–20 August and 23–25 September) were done close to the maximum of the outburst. The third one (on 6–8 October) was performed at the end of the decay phase, when the X-ray luminosity dropped by a factor of ~10 with respect to the maximum of the outburst. A part of the *RXTE/ASM* light curve[1] including the giant outburst is shown in Fig. 1. The times of the *INTEGRAL* observations are indicated and referred to as Set 1, Set 2, and Set 3 throughout the paper.

Observations corresponding to Sets 1 and 2 were done when the source was at similar luminosity levels ($L_{1-20\,\text{keV}} \sim 10^{38}$ erg s$^{-1}$) before and after the maximum of the outburst. A preliminary analysis of the two data sets was presented by Klochkov et al. (2007) who showed that spectral and timing characteristics of the source during the two observations were similar. Due to the high X-ray flux, the data allowed us to perform a detailed pulse-phase resolved spectral analysis of EXO 2030+375 using twelve phase bins. During the observations corresponding to Set 3, the X-ray luminosity of the source was at a level typical of normal (Type I) outbursts by this system ($L_{1-20\,\text{keV}} \sim 10^{37}$ erg s$^{-1}$). Spectra and pulse profiles of the source during these observations were considerably different with respect to those in Sets 1 and 2. In spite of a poorer

**Table 1.** Summary of observations.

| Obs. | Obs.time (ks) | Mean MJD | Mean ASM flux (mCrab) |
|------|------|------|------|
| Set 1 | 62 | 53 942.9 | 450 |
| Set 2 | 140 | 53 967.6 | 500 |
| Set 3 | 122 | 54 015.2 | 60 |

statistics, the data taken in Set 3 still allowed us to perform pulse-phase resolved spectral analysis, although with a coarser binning (four bins) in pulse phase. Table 1 contains the summary of the observations analyzed in this work.

## 3. Data processing

For our analysis we used the data obtained with the instruments *IBIS/ISGRI* (20–300 keV, Ubertini et al. 2003) and *JEM-X* (3–30 keV, Lund et al. 2003) onboard *INTEGRAL*. To perform the standard data reduction, the Off-line Science Analysis (OSA) software (version 6) was used (Courvoisier et al. 2003). To construct energy-resolved pulse profiles we used the software developed at IASF, Palermo (Mineo et al. 2006). While extracting spectra and pulse profiles of EXO 2030+375, two other bright sources in the field of view of the *INTEGRAL* instruments, Cyg X-1 and Cyg X-3, were included to the extraction catalog used by the analysis software, which removes the contamination of EXO 2030+375. All other sources in the field of view are much weaker than EXO 2030+375 and therefore do not provide any noticeable contamination. The spectral analysis of the observations was performed using the XSPEC v.11.3.2l spectral fitting package (Arnaud 1996). Following the OSA User Manuals[2], we added a systematic error to the final count rates at a level of 1% for *ISGRI* and 2% for *JEM-X* to account for small-scale uncertainties in the response matrices of the respective instruments.

To extract X-ray pulse profiles and to define pulse phase intervals for pulse phase resolved spectra, all photon arrival times were translated into the solar system barycenter and corrected for orbital motion in the binary. The orbital parameters were taken from Wilson et al. (2005): $P_{\text{orb}} = 46.0202(2)$ d, $T_{\text{peri}} = \text{MJD } 51\,099.43(2)$, $a \sin i = 238(2)$ lt-sec, $e = 0.416(1)$, $\omega = 210^\circ.8(4)$. The pulse periods and associated derivatives were determined for each of the three observational sets individually by employing initial epoch-folding and a subsequent phase-connection analysis similar to Ferrigno et al. (2007) and Deeter et al. (1981). To perform phase-connection, we used a pattern-matching technique applied to well-defined pulse profiles from a sufficient number of pulses. Any variation in the pulse shape inside each observation is marginal and does not affect our method. The determined periods and period derivatives are summarized in Table 2. Values corresponding to Sets 1 and 2 are slightly improved with respect to those reported in Klochkov et al. (2007).

## 4. Maximum of the outburst

Observations corresponding to Sets 1 and 2 were performed close to the maximum of the outburst (Fig. 1). During Set 1, which is roughly half as long as Set 2 (see Table 1), the main target of observations was Cyg X-3 located 4° away from EXO 2030+375. Therefore, the statistics of the EXO 2030+375 data obtained during Set 1 is noticeably worse than during Set 2.

---

[1] We used the results provided by the ASM/RXTE team.

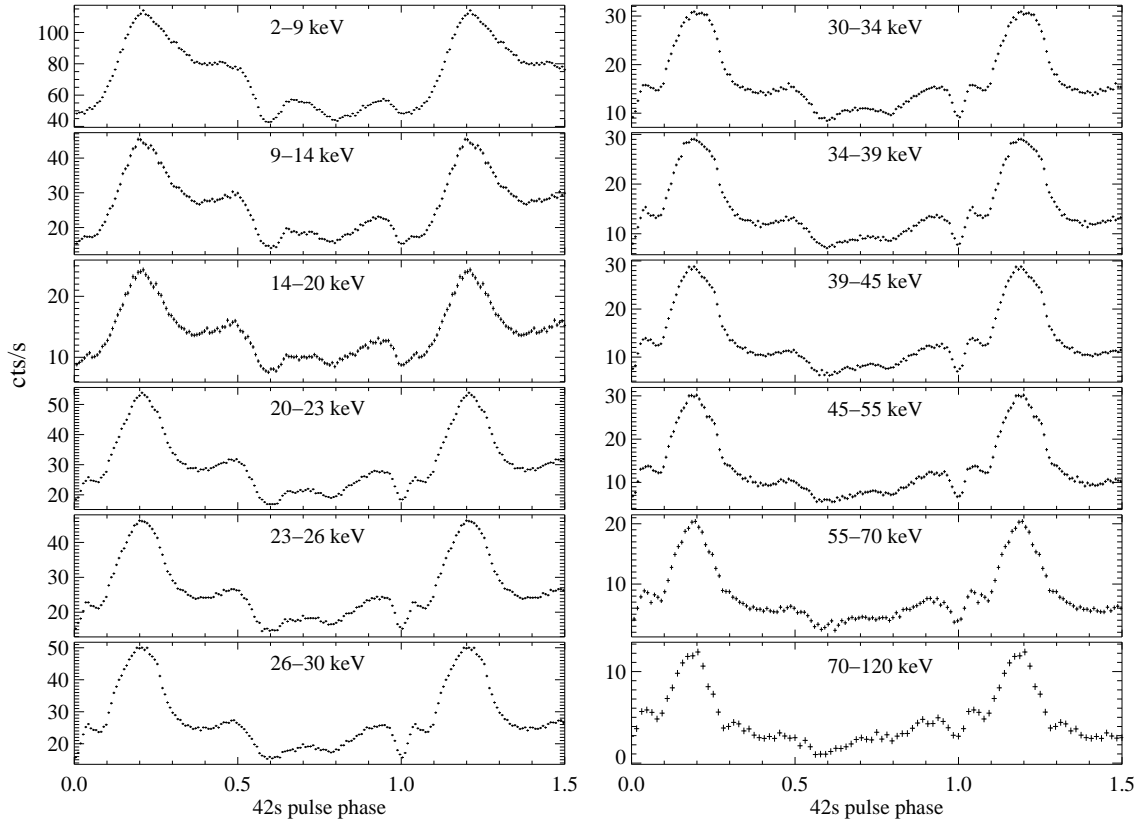[2] `http://isdc.unige.ch/index.cgi?Support+documents`

**Fig. 2.** Energy-resolved pulse profiles of EXO 2030+375 obtained with *JEM-X* (below 20 keV) and *IBIS/ISGRI* (above 20 keV) in Set 2 (where the data have the best statistics).

**Table 2.** The pulse periods and associated derivatives for three sets of observations analyzed in this work.

| Observation | Reference epoch (MJD) | $P$ [s] | $-\mathrm{d}P/\mathrm{d}t$ [$10^{-8}$ s/s] |
|---|---|---|---|
| Set 1 | 53 942.240864 | 41.58084(3) | 2.96(21) |
| Set 2 | 53 966.392169 | 41.519270(5) | 2.758(20) |
| Set 3 | 54 014.010200 | 41.45425(6) | 0.22(23) |

Note. Uncertainties in parentheses (68%) refer to the last digit(s).

As a result, our pulse-phase resolved analysis of the maximum of the outburst is mainly driven by the data taken in Set 2.

To explore spectral changes with pulse phase, we constructed pulse-phase resolved spectra and energy-resolved pulse profiles. While the former allow detailed study of spectral parameters as a function of pulse phase, the latter can be used to explore the intensity of different pulse-profile components (peaks, dips, etc.) in different energy ranges without relying on any particular spectral function.

### 4.1. Energy-resolved pulse profiles

Figure 2 presents energy-resolved background-subtracted pulse profiles of the source obtained during the observations corresponding to Set 2. The corresponding pulse period and its derivative, as well as the zero epoch, are provided in Table 2. The pulse profiles in the energy bands below 20 keV were obtained

from the *JEM-X* data, while the *IBIS/ISGRI* data were used for energies above 20 keV. Several components can be distinguished in the profiles: the main peak at phase ~0.2 followed by a fainter component at phase ~0.5 (which we will refer to as the "trailing shoulder") and two smaller peaks in the interpulse interval 0.6–1.0. The sharpest detail of the profile is a narrow dip preceding the main peak. Phase 0.0 was arbitrarily chosen to coincide with the dip in the average *ISGRI* pulse profile. As one can see, the shape of the profile changes smoothly with energy indicating variations in the X-ray spectrum with pulse phase. The pulse fraction of the source determined as $(F_{max} - F_{min})/(F_{max} + F_{min})$ (where $F_{max}$ and $F_{min}$ are fluxes in the maximum and minimum of the pulse profile, respectively) as a function of energy is shown in Fig. 3. One can see a bump-like structure around ~10–20 keV that is probably related to the continuum feature in this energy range (the "bump" or the absorption line, see Sects. 1 and 4.2). Above ~20 keV, the pulse fraction seeply increases.

### 4.2. Pulse-resolved spectra

As one can conclude from the dependence of the pulse profile shape on energy, the X-ray spectrum of EXO 2030+375 clearly varies with pulse phase. We have therefore performed a separate analysis of the spectra accumulated in different pulse phase intervals. Phase binning was chosen to provide similar statistics of spectra in each bin and to have better phase resolution around the main peak where the most rapid spectral changes are expected. The binning was chosen a priori based solely on the shape of the pulse profile. No further adjustments were made after the
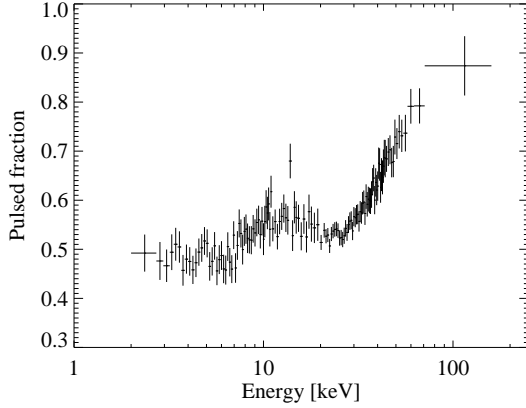
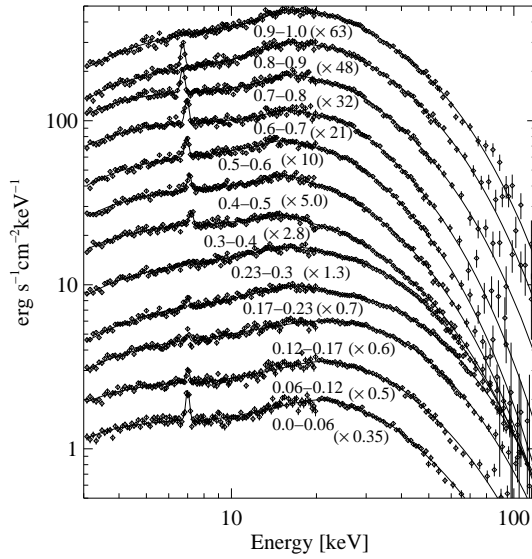**Fig. 3.** The pulse fraction of EXO 2030+375 as a function of energy.



**Fig. 4.** Pulse-resolved broad band X-ray spectra of EXO 2030+375 obtained in Set 2. Phase bins are indicated (phase zero is the same as in Fig. 2). Values in parenthesis indicate the multiplicative factor applied to the flux in each spectrum to avoid overlaps. The solid line represents the fit of the spectra using Model I (see text for the model details).

spectra had been obtained. Figure 4 shows unfolded pulse phase-resolved spectra of the source (shifted vertically with respect to each other to avoid overlaps). The pulse phase is defined in the same way as in the previous section. Variability of the spectral continuum is clearly seen.

As pointed out in Sect. 1, the pulse-averaged spectral continuum of the source is rather complicated and cannot be modeled by any of the simple spectral functions (a power law modified at higher energies by an exponential cutoff), which are usually used to fit spectra of accreting pulsars. In an attempt to model the spectrum Wilson et al. (2008) modified a power law/cutoff model by a Gaussian absorption line at ∼10 keV, while Klochkov et al. (2007) included a broad Gaussian emission component at ∼15 keV instead. In this work we tried to use both models to fit the pulse-resolved spectra. The reduced $\chi^2$ in all phase bins is very similar for the two models. This does not allow one to ultimately choose between the two spectral functions. The two models are referred to as Model I (with a "bump") and Model II (with an absorption line at 10 keV) throughout the paper.

Below we describe the spectral functions corresponding to the two models. The common part of Models I and II is the power law/cutoff continuum smoothed at the cutoff energy by a third-order polynomial:

$$I_{\text{cont}} = K \cdot \begin{cases} E^{-\Gamma}, & \text{if } E \leq E_{\text{cutoff}} - \Delta E \\ E^{-\Gamma} \cdot \exp\left(-\frac{E - E_{\text{cutoff}}}{E_{\text{fold}}}\right), & \text{if } E > E_{\text{cutoff}} + \Delta E \\ AE^3 + BE^2 + CE + D, & \text{if } E_{\text{cutoff}} - \Delta E < E < \\ & \quad E_{\text{cutoff}} + \Delta E, \end{cases} \quad (1)$$

where $K$ is the normalization coefficient, $E$ the photon energy; $\Gamma$, $E_{\text{cutoff}}$, $E_{\text{fold}}$, and $\Delta E$ are model parameters. Numerical coefficients $A$, $B$, $C$, and $D$ are chosen to obey the condition of continuity for the function and its first derivative at the points $(E_{\text{cutoff}} - \Delta E)$ and $(E_{\text{cutoff}} + \Delta E)$. Model I includes a broad Gaussian emission component (a "bump") around 15 keV:

$$I_{\text{Model I}} = I_{\text{cont}} + K_{\text{bump}} \exp\left\{-\frac{(E - E_{\text{bump}})^2}{2\sigma_{\text{bump}}^2}\right\}, \quad (2)$$

where $E_{\text{bump}}$ and $\sigma_{\text{bump}}$ are the energy and width of the "bump", and $K_{\text{bump}}$ is the numerical constant describing the intensity of the component. In Model II, the power law/cutoff continuum $I_{\text{cont}}$ is modified by a multiplicative absorption line with a Gaussian optical depth profile:

$$I_{\text{Model II}} = I_{\text{cont}} \cdot \exp\left\{-\tau_{\text{line}} \exp\left(-\frac{(E - E_{\text{line}})^2}{2\sigma_{\text{line}}^2}\right)\right\}, \quad (3)$$

where $E_{\text{line}}$, $\sigma_{\text{line}}$, and $\tau_{\text{line}}$ are the centroid energy, width, and the central depth of the line, respectively. Additionally, we multiplied the functions $I_{\text{Model I}}$ and $I_{\text{Model II}}$ by the factor $\exp[-N_{\text{H}} \sigma_{\text{bf}}(E)]$ describing the low-energy absorption by cold matter in the line of sight. Here, $\sigma_{\text{bf}}(E)$ is the photoabsorption cross-section per hydrogen atom for matter of cosmic abundances (Bałucińska-Church & McCammon 1992) used in the phabs model of XSPEC, and $N_{\text{H}}$ is the equivalent hydrogen column density. We also added a Gaussian emission line to model the iron fluorescence line at ∼6.4 keV. The latter, however, improves the fit only slightly. For all pulse-phase resolved spectra the value of $N_{\text{H}}$ was fixed to $2 \times 10^{22}$ cm$^{-2}$ (the average of the best-fit values found in all phase bins). It was also found that the energy of the "bump" in Model I does not change significantly with pulse phase being close to 15 keV. It was, therefore, fixed to this value for all phase bins.

Figures 5 and 6 show the most important spectral parameters obtained using the two models as a function of pulse phase. The data correspond to the observations performed in Set 2, which have the best statistics. Vertical error bars correspond to 90%-uncertainties. Note that the pulse phase range shown in the figures is from 0.0 to 1.5 so that some data points are repeated (the same is true for Fig. 10).

The same kind of analysis was performed using the observations corresponding to Set 1 (slightly before the maximum of the outburst). Due to poorer statistics, we had to use a coarser binning compared to Set 2. The spectral parameters of the pulse-resolved spectra were less constrained in this case. However, the behavior of the parameters agrees with what is found in Set 2. We also notice that the best-fit parameters of the pulse-averaged spectra taken in Sets 1 and 2 are also consistent with each other (see Table 3 in Klochkov et al. 2007).

Residuals left after fitting the spectrum by Models I and II from phase bin 0.06–0.12 obtained in Set 2 reveal an absorption feature at ∼63 keV (see Fig. 7). Inclusion of a Gaussian absorption line at this energy flattens the residuals. The best-fit energy of the line is $63.6^{+3.7}_{-2.9}$ keV for Model I and $63.3^{+4.0}_{-2.9}$ keV for
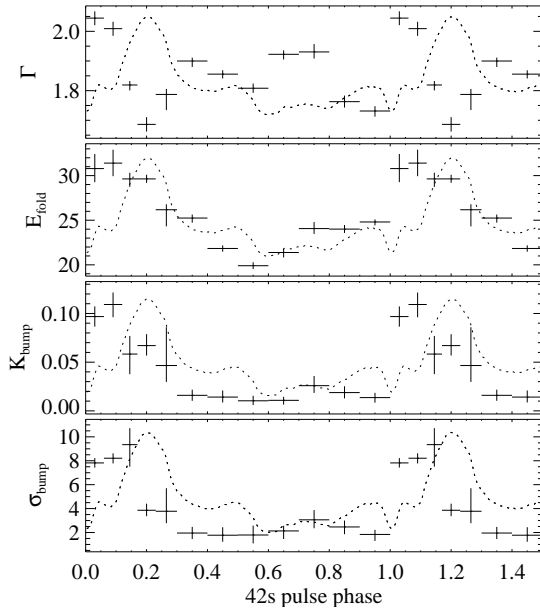
**Fig. 5.** Best-fit parameters of Model I (see text) as a function of pulse phase obtained by fitting the spectra from Set 2. The dotted curve shows the averaged *ISGRI* (20–120 keV) pulse profile scaled and shifted vertically to match the plot. Vertical error bars correspond to 90%-uncertainties.
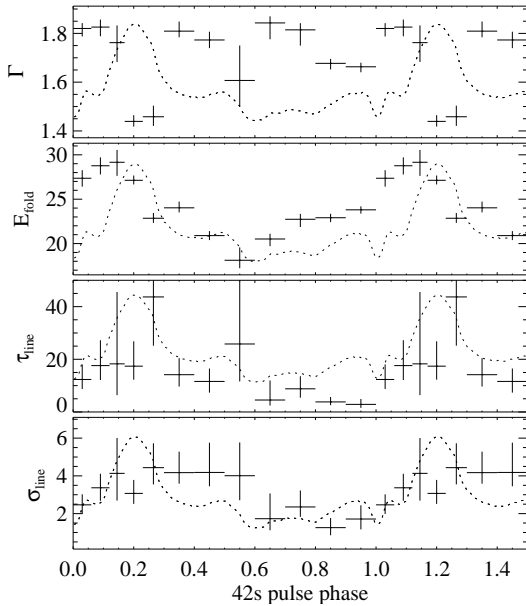


**Fig. 6.** Best-fit parameters of Model II (see text) as a function of pulse phase obtained by fitting the spectra from Set 2. As in Fig. 5, the dotted curve shows the *ISGRI* pulse profile. Vertical error bars correspond to 90%-uncertainties.

Model II. We checked the presence and the energy of the feature using other possible continuum models, such as Fermi-Dirac cutoff (Tanaka 1986) and the so-called negative and positive power-law times EXponential model (NPEX, Makishima et al. 1999), including a "bump" or an absorption line at 10 keV to match the continuum. It was found that the presence and the energy of the feature are independent of the choice of the spectral
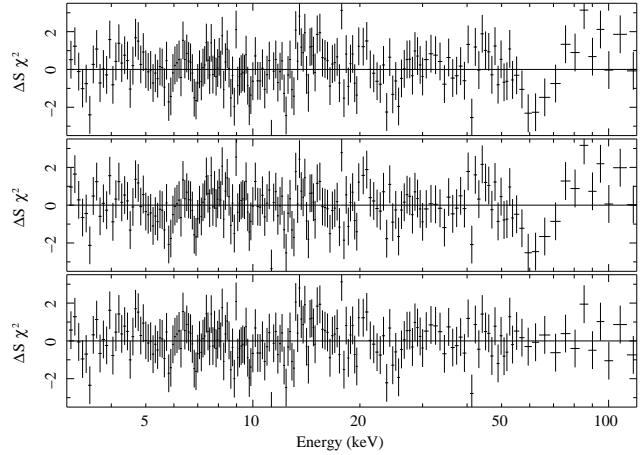


**Fig. 7.** Residuals of the spectrum from the phase bin 0.06–0.12 fitted with Model I *(top)* and Model II *(middle)*. *The bottom panel* shows the residuals after fitting the spectrum with Model I where a Gaussian absorption line at ~63.6 keV is included (the corresponding fit with Model II looks very similar).

function. The F-test probability that the line is due to statistical fluctuations is $\sim 3 \times 10^{-5}$ (see however Protassov et al. 2002, about non-applicability of the F-test to line-like features).

## 5. Decay of the outburst

### 5.1. Energy-resolved pulse profiles

As mentioned in Sect. 2, during Set 3, *INTEGRAL* caught the source at the end of the outburst's decay phase when the X-ray luminosity was ~10 times lower than the maximum of the outburst (Fig. 1). Due to lower statistics we used much coarser binning in energy (for pulse profiles) and pulse phase (for pulse-phase resolved spectra) than in Set 2 (4 instead of 12 in both cases). The resulting pulse profiles are shown in Fig. 8. As before, the corresponding pulse period, its derivative, and the epoch zero can be found in Table 2. To choose the time of phase zero in accordance with the one used for Set 2 we used the dependence of the pulse profiles shape on the X-ray luminosity presented in Fig. 1 of Parmar et al. (1989a). The dependence allows one to identify features in the profiles (e.g. the dip around pulse phase 0.6) in both observations (Sets 1 and 2) and choose the zero epoch for both observations consistently.

The dependence of the pulse profile on energy in Set 3 (Fig. 8) is mainly characterized by a decreasing relative amplitude of the peak at phase ~0.9 with respect to the main peak (phase ~0.2) with energy. The sharp dip seen in the 2–10 keV at phase ~0.6 almost disappears at higher energies. Generally, one can see that the shape of the pulse profiles is substantially different as compared to the profiles obtained close to the maximum of the outburst at similar energies. In Sect. 6 we show that the changes could be qualitatively explained if assuming that a pencil beam component appears at the end of the outburst.

### 5.2. Pulse-phase resolved spectra

To produce pulse-phase resolved spectra from the data obtained in Set 3, we used four phase bins. They cover each of the two peaks and two phase intervals of the interpulse. The spectral continuum can be modeled well by the power law/cutoff function
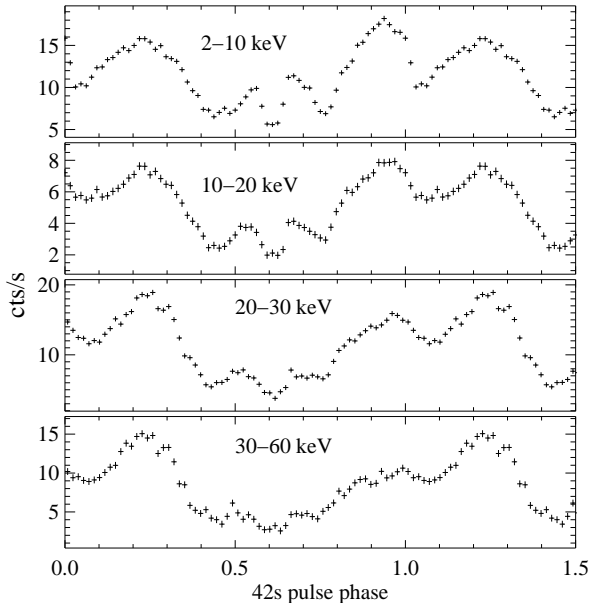
**Fig. 8.** Energy-resolved pulse profiles of EXO 2030+375 obtained with *JEM-X* (below 20 keV) and *IBIS/ISGRI* (above 20 keV) in Set 3 (at the end of the outburst).
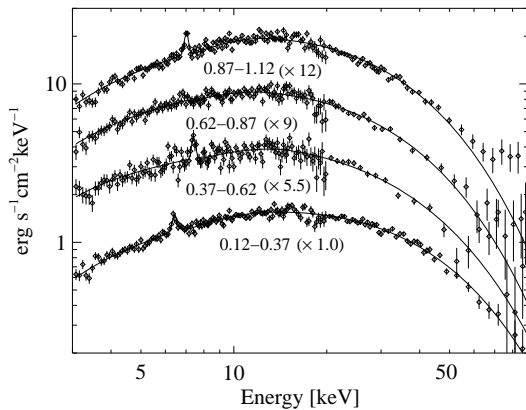


**Fig. 9.** Pulse-phase resolved broad band X-ray spectra of EXO 2030+375 obtained in Set 3. Phase bins are indicated (phase zero is the same as in Figs. 8). Values in parentheses indicate the multiplicative factor applied to the flux in each spectrum to avoid overlaps. The solid line represents the fit of the spectra using the power law/cutoff model (see text for the model details).

provided by Eq. (1) without inclusion of the "bump" or the 10 keV absorption line. Like in Sect. 4.2, we modified the model at lower energies by photoabsorption (with $N_H \sim 2 \times 10^{22}$ cm$^{-2}$) and added a Gaussian line to model the iron fluorescence emission at ~6.4 keV. Figure 9 represents the unfolded pulse-phase resolved spectra fitted with the described model and shifted vertically with respect to each other in order to avoid overlaps. (This was done multiplying the flux in each spectrum by a numerical factor indicated in parentheses.) Significant variation in the continuum is clearly seen. The pulse phase is defined in the same way as in Fig. 8.

Figure 10 shows the photon index $\Gamma$ and the folding energy $E_{fold}$ as a function of pulse phase during Set 3. Vertical error bars correspond to 90%-uncertainties.
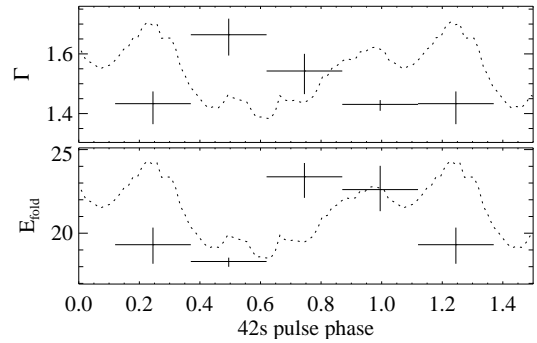


**Fig. 10.** Best-fit spectral parameters of EXO 2030+375 obtained in Set 3 as a function of pulse phase. The dotted curve shows the averaged *ISGRI* (20–120 keV) pulse profile. Vertical error bars correspond to 90%-uncertainties.

## 6. Interpretation and discussion

### 6.1. Pulse-period derivatives

The values of pulse-period derivatives measured close to the maximum and at the end of the outburst (Table 2) basically confirm the statement in Klochkov et al. (2007) that the spin-up rate of the pulsar is proportional to its X-ray flux as expected in the simple accretion torque theory (e.g. Pringle & Rees 1972). The observed dependence is similar to what was measured by *EXOSAT* during the 1985 giant outburst of EXO 2030+375 (Parmar et al. 1989b). However, with only a few points, it is not possible to explore the correlation using more complicated accretion torque models.

### 6.2. Variation in the spectral continuum with pulse phase

The *INTEGRAL* observations have shown that the spectral continuum of EXO 2030+375 is strongly pulse-phase dependent. Observations of the source close to the maximum of the outburst allowed us to perform a detailed study of this dependence. A harder main peak and softer interpulse region observed in the source is a common property of accreting pulsars (see e.g. Tsygankov et al. 2007, and references therein). It is usually explained by assuming that, during the peak, we mostly see the comptonized photons coming from a hot region close to the footstep of the accretion column while in the interpulse softer radiation scattered by the upper parts of the column is observed (Basko & Sunyaev 1976). A closer look at Fig. 2, however, reveals a more complicated picture. Both the main peak and its left flank increase in relative amplitude with energy, leading to a slight shift of the profile maximum towards an earlier pulse phase. This shows that the spectral continuum changes asymmetrically with respect to the main peak. The variation in spectral parameters with pulse phase (Figs. 5 and 6) demonstrates the corresponding complex pulse-phase dependence of the spectrum. The photon index $\Gamma$ reaches a minimum (the hardest spectrum) in the middle of the main peak (top panel in Figs. 5 and 6), while the maximum of the exponential folding energy $E_{fold}$ is shifted with respect to the peak towards earlier pulse phases. This contrasts to e.g. Her X-1, where both the maximum of $E_{fold}$ and the minimum of $\Gamma$ are coincident with the main pulse (Klochkov et al. 2008).

A possible qualitative explanation for the observed asymmetry of the spectral variation with pulse phase in EXO 2030+375 can be the following. Since the luminosity of the source close to the maximum of the outburst, $\sim 10^{38}$ erg s$^{-1}$, is well above the local Eddington limit (so-called critical luminosity, $L_c \sim 10^{37}$ erg s$^{-1}$, Basko & Sunyaev 1976; Staubert et al. 2007), it is expected that accreted matter is decelerated by radiation pressure leading to the formation of an optically thick accretion column. The bulk of the emission in this case is expected to occur as a fan beam (see also the modeling of the source's pulse profiles performed by Parmar et al. 1989a). Therefore, during the maximum of the profile (main peak) the angle between the column axis and the observer's line of sight has the highest value (the column is seen from the side). The observer is looking almost along the beam, seeing the photons coming from a Compton scattering region with large optical depth. This leads to the observed hard power law during the peak. Before the peak, when $E_{\rm fold}$ reaches a maximum, the direction of the line of sight might be closer to that of the column axis and, thus, of the magnetic field lines. Due to the dependence of the scattering cross-section on the angle between the photon direction and the magnetic field lines (Harding & Daugherty 1991), one expects that the photons, whose direction in this case is closer to that of the field lines, have experienced less scatterings and, therefore, originated deeper inside the accretion column where the temperature is higher. The X-ray spectrum of these photons is expected to have larger $E_{\rm fold}$ reflecting higher electron temperature but a softer power-law index due to lower Compton scattering optical depth (see e.g. Rybicki & Lightman 1979), as observed. This explanation, however, requires that in the latter case the angle between the observer's line of sight and the column axis was not too small. Otherwise, depending on the geometry of the accretion flow, the column density along the line of sight will be very high, resulting in a higher optical depth.

The changing of the pulse profile towards the end of the outburst seems to confirm this picture. In the pulse profiles corresponding to the outburst's decay (Fig. 8), one can see a new peak that appears at the phase interval preceeding the main pulse, i.e. where, according to our view, the observer's line of sight is closest to the magnetic field lines. At this pulse phase one expects to see a pencil beam if the luminosity decreases (Reig & Coe 1998; Parmar et al. 1989a). The observed peak, therefore, may correspond to the pencil beam component of the emission diagram, whose intensity is comaparable to that of the fan beam component at lower luminosity. Thus, both the pulse phase variation of the spectral continuum during the maximum of the outburst and the evolution of the pulse profile with luminosity fit the described picture where the emission diagram changes from a fan beam geometry close to the maximum of the outburst to a combination of a fan and a pencil beam at the end of the decay phase.

The behavior of the spectral parameters with pulse phase in Set 3 is less clear due to lower statistics (only four phase bins are used). As in the maximum of the outburst, during the main peak of the profile, the spectrum is characterized by a hard $\Gamma$ and a relatively low $E_{\rm fold}$ (Fig. 10). During the peak around phase 0.0 (pencil beam), $E_{\rm fold}$ is higher. As before, this can be explained by photons from the pencil beam moving along the magnetic field lines originating deeper in the accretion column where the electron temperature is higher. On the other hand, the emission region is believed to move closer to the star surface as the luminosity decreases (Basko & Sunyaev 1976). This means that the column density of gas above the emission region will be higher, leading to greater optical depth for Compton scattering. This can explain the hard photon index at this pulse phase.

### 6.3. "Bump" versus absorption line at 10 keV

As discussed in Sect. 4.2, to model the spectral continuum of EXO 2030+375 in the maximum of the outburst, one has to modify the standard power law/cutoff model either by a "bump" at $\sim 15$ keV or by an absorption line at $\sim 10$ keV. Both models provide equally good fits of the pulse-phase resolved spectra. If interpreted as a cyclotron absorption feature (Wilson et al. 2008), the absorption line at 10 keV is observed at rather unusual energy that is much smaller than the exponential cutoff energy $E_{\rm cutoff}$. This contrasts with all other know cyclotron line sources (see e.g. Fig. 9 in Coburn et al. 2002). We point out here that a feature around 8–15 keV (a "wiggle" or a "bump") is observed in many accreting pulsars (e.g., 4U 1907, Her X-1, Coburn et al. 2002), including those that do not otherwise exhibit a cyclotron line (e.g. GS 1843+00, Coburn 2001). Thus, the interpretation of the absorption line at 10 keV in EXO 2030+375 as the cyclotron resonant scattering feature might be hasty. On the other hand, the nature of the feature in this and other sources is still unclear. Most probably it arises from modeling the spectral continuum with a simple empirical function. For a proper modeling of the spectrum in the considered energy range (including the feature) one would need a proper theoretical model accounting for all relevant processes at the site of the X-ray emission.

### 6.4. Evidence of a cyclotron line at ~63 keV

The X-ray spectrum of EXO 2030+375 taken close to the maximum of the outburst in the narrow pulse-phase interval (0.06–0.12) preceeding the main peak shows evidence of an absorption line around $\sim 63$ keV (Fig. 7). If interpreted as a fundamental cyclotron line, the corresponding magnetic field strength is $B \simeq 5 \times 10^{12}$ G ($E_{\rm cyc} \sim 11.6 \times (B/10^{12}\,{\rm G})$ keV), which is one of the highest values among accreting pulsars. However, evidence of a cyclotron line at $\sim 36$ keV has previously been reported for EXO 2030+375 by Reig & Coe (1999) during a normal outburst, so the line at $\sim 63$ keV might well be the first harmonic rather than the fundamental line. It is known that the relative strength of the fundamental line and harmonics might vary significantly, sometimes making the fundamental line more difficult to detect than the harmonic (a good example is A 0535+26, see e.g. Kendziorra et al. 1994).

## 7. Summary and conclusions

We used *INTEGRAL* observations to study the pulse-phase dependence of the broad band X-ray spectrum of EXO 2030+375 close to the maximum and during the decay of its 2006 giant outburst. This is the first pulse-phase resolved spectral study of the source. In all observations, significant pulse phase variability of the X-ray continuum was observed.

Alternative spectral continuum models are discussed. We argue that the interpretation of the feature at $\sim 10$ keV as a cyclotron absorption line proposed previously is questionable.

Pulse-phase dependencies of the continuum parameters close to the maximum of the outburst, as well as the evolution of the pulse profiles from the maximum to the end of the outburst, is qualitatively consistent with the picture where the pulsar's emission diagram changes from the fan-beam configuration close to the maximum of the outburst to a combination of pencil and fan beams (whose amplitudes are comparable) at the end of the decay phase.

Evidence of an absorption line at $\sim 63$ keV is found during the maximum of the outburst at a narrow phase interval

preceeding the main peak of the pulse profile. This feature can be interpreted as the first harmonic of the previously reported cyclotron line at ~36 keV.

# References

Arnaud, K. A. 1996, in Astronomical Data Analysis Software and Systems V, ed. G. H. Jacoby & J. Barnes, ASP Conf. Ser., 101, 17
Bałucińska-Church, M., & McCammon, D. 1992, ApJ, 400, 699
Basko, M. M., & Sunyaev, R. A. 1976, MNRAS, 175, 395
Coburn, W. 2001, Ph.D. Thesis, University of California, San Diego
Coburn, W., Heindl, W. A., Rothschild, R. E., et al. 2002, ApJ, 580, 394
Coe, M. J., Payne, B. J., Longmore, A., & Hanson, C. G. 1988, MNRAS, 232, 865
Corbet, R. H. D., & Levine, A. M. 2006, The Astronomer's Telegram, 843
Courvoisier, T. J.-L., Walter, R., Beckmann, V., et al. 2003, A&A, 411, L53
Deeter, J. E., Pravdo, S. H., & Boynton, P. E. 1981, ApJ, 247, 1003
Ferrigno, C., Segreto, A., Santangelo, A., et al. 2007, A&A, 462, 995
Hanuschik, R. W. 1996, A&A, 308, 170
Harding, A. K., & Daugherty, J. K. 1991, ApJ, 374, 687

Janot-Pacheco, E., Motch, C., & Pakull, M. W. 1988, A&A, 202, 81
Kendziorra, E., Kretschmar, P., Pan, H. C., et al. 1994, A&A, 291, L31
Klochkov, D., Horns, D., Santangelo, A., et al. 2007, A&A, 464, L45
Klochkov, D., Staubert, R., Postnov, K., et al. 2008, A&A, 482, 907
Lund, N., Budtz-Jørgensen, C., Westergaard, N. J., et al. 2003, A&A, 411, L231
Makishima, K., Mihara, T., Nagase, F., & Tanaka, Y. 1999, ApJ, 525, 978
Mineo, T., Ferrigno, C., Foschini, L., et al. 2006, A&A, 450, 617
Motch, C., & Janot-Pacheco, E. 1987, A&A, 182, L55
Parmar, A. N., White, N. E., & Stella, L. 1989a, ApJ, 338, 373
Parmar, A. N., White, N. E., Stella, L., Izzo, C., & Ferri, P. 1989b, ApJ, 338, 359
Pringle, J. E., & Rees, M. J. 1972, A&A, 21, 1
Protassov, R., van Dyk, D. A., Connors, A., Kashyap, V. L., & Siemiginowska, A. 2002, ApJ, 571, 545
Quirrenbach, A., Bjorkman, K. S., Bjorkman, J. E., et al. 1997, ApJ, 479, 477
Reig, P., & Coe, M. J. 1998, MNRAS, 294, 118
Reig, P., & Coe, M. J. 1999, MNRAS, 302, 700
Rybicki, G. B., & Lightman, A. P. 1979, Radiative processes in astrophysics (New York: Wiley-Interscience), 393
Slettebak, A. 1988, PASP, 100, 770
Staubert, R., Shakura, N. I., Postnov, K., et al. 2007, A&A, 465, L25
Tanaka, Y. 1986, in Radiation Hydrodynamics in Stars and Compact Objects, Proc. IAU Colloq. 89, ed. D. Mihalas & K.-H. A. Winkler (Berlin: Springer Verlag), Lect. Notes Phys., 255, 198
Tsygankov, S. S., Lutovinov, A. A., Churazov, E. M., & Sunyaev, R. A. 2007, ArXiv e-prints, 704
Ubertini, P., Lebrun, F., Di Cocco, G., et al. 2003, A&A, 411, L131
Wilson, C. A., & Finger, M. H. 2006, The Astronomer's Telegram, 877
Wilson, C. A., Finger, M. H., Coe, M. J., Laycock, S., & Fabregat, J. 2002, ApJ, 570, 287
Wilson, C. A., Fabregat, J., & Coburn, W. 2005, ApJ, 620, L99
Wilson, C. A., Finger, M. H., & Camero-Arranz, A. 2008, ApJ, 678, 1263
Winkler, C., Courvoisier, T. J.-L., Di Cocco, G., et al. 2003, A&A, 411, L1

## Appendix F

## Spectral formation in accreting X-ray pulsars: bimodal variation of the cyclotron energy with luminosity

# Spectral formation in accreting X-ray pulsars: bimodal variation of the cyclotron energy with luminosity

P. A. Becker[1], D. Klochkov[2], G. Schönherr[3], O. Nishimura[4], C. Ferrigno[5], I. Caballero[6], P. Kretschmar[7], M. T. Wolff[8], J. Wilms[9], and R. Staubert[2]

[1] School of Physics, Astronomy, and Computational Sciences, MS 5C3, George Mason University, 4400 University Drive, Fairfax, VA, USA
   e-mail: pbecker@gmu.edu
[2] Institut für Astronomie und Astrophysik, Abt. Astronomie, Universität Tübingen, Sand 1, 72076 Tübingen, Germany
[3] Leibniz-Institut für Astrophysik Potsdam, An der Sternwarte 16, 14482 Potsdam, Germany
[4] Department of Electronics and Computer Science, Nagano National College of Technology, 716 Tokuma, 381-8550 Nagano, Japan
[5] ISDC Data Center for Astrophysics, Université de Genève, Chemin d'Ecogia 16, 1290 Versoix, Switzerland
[6] AIM (UMR 7158 CEA/DSM – CNRS – Université Paris Diderot) Irfu/Service d'Astrophysique, 91191 Gif-sur-Yvette, France
[7] European Space Agency, European Space Astronomy Centre, PO Box 78, 28691 Villanueva de la Cañada, Madrid, Spain
[8] Space Science Division, Naval Research Laboratory, Washington, DC, USA
[9] Dr. Karl Remeis-Observatory and Erlangen Centre for Astroparticle Physics, Sternwartstr. 7, 96049 Bamberg, Germany

## ABSTRACT

*Context.* Accretion-powered X-ray pulsars exhibit significant variability of the cyclotron resonance scattering feature (CRSF) centroid energy on pulse-to-pulse timescales, and also on much longer timescales. Two types of spectral variability are observed. For sources in group 1, the CRSF energy is negatively correlated with the variable source luminosity, and for sources in group 2, the opposite behavior is observed. The physical basis for this bimodal behavior is currently not well understood.
*Aims.* We explore the hypothesis that the accretion dynamics in the group 1 sources is dominated by radiation pressure near the stellar surface, and that Coulomb interactions decelerate the gas to rest in the group 2 sources.
*Methods.* We derive a new expression for the critical luminosity, $L_{crit}$, such that radiation pressure decelerates the matter to rest in sources with X-ray luminosity $L_X > L_{crit}$. The formula for $L_{crit}$ is based on a simple physical model for the structure of the accretion column in luminous X-ray pulsars that takes into account radiative deceleration, the energy dependence of the cyclotron cross section, the thermodynamics of the accreting gas, the dipole structure of the pulsar magnetosphere, and the diffusive escape of radiation through the column walls. We show that for typical neutron star parameters, $L_{crit} = 1.5 \times 10^{37} B_{12}^{16/15}$ erg s$^{-1}$, where $B_{12}$ is the surface magnetic field strength in units of $10^{12}$ G.
*Results.* The formula for the critical luminosity is evaluated for five sources, using the maximum value of the CRSF centroid energy to estimate the surface magnetic field strength $B_{12}$. The results confirm that the group 1 sources are supercritical ($L_X > L_{crit}$) and the group 2 sources are subcritical ($L_X < L_{crit}$), although the situation is less clear for those highly variable sources that cross over the line $L_X = L_{crit}$. We also explain the variation of the CRSF energy with luminosity as a consequence of the variation of the characteristic emission height. The sign of this dependence is opposite in the supercritical and subcritical cases, hence creating the observed bimodal behavior.
*Conclusions.* We have developed a new model for the critical luminosity in accretion-powered X-ray pulsars that explains the bimodal dependence of the CRSF centroid energy on the X-ray luminosity $L_X$. Our model provides a physical basis for the observed variation of the CRSF energy as a function of $L_X$ for both the group 1 (supercritical) and the group 2 (subcritical) sources as a result of the variation of the emission height in the column.

**Key words.** stars: neutron – pulsars: general – radiative transfer – accretion, accretion disks

## 1. Introduction

X-ray binary pulsars (XRBPs) were first observed by Giacconi et al. (1971) and Tananbaum et al. (1972), and now include many of the brightest sources in the X-ray sky. In XRBPs, the main sequence companion star transfers matter to the neutron star via Roche lobe overflow, or via a strong stellar wind (Frank et al. 2002). The gas forms an accretion disk around the neutron star, and the material spirals inward until the pressure of the star's dipole magnetic field becomes comparable to the ram pressure of the matter in the disk. This occurs at the Alfvén radius, located several thousand kilometers out in the accretion disk.

The fully-ionized accreting plasma is entrained by the magnetic field at the Alfvén radius, and from there the matter is guided through the magnetosphere, forming accretion columns at one or both of the magnetic poles of the star. As the star spins, the inclination angle between the star's magnetic axis and the axis of the accretion disk changes, and therefore the Alfvén radius varies with the spin period of the star.

The observed X-ray emission is powered by the conversion of gravitational potential energy into kinetic energy, which is then transferred to the radiation field via electron scattering, and ultimately escapes through the walls of the column. The structure of the accretion column is maintained by the
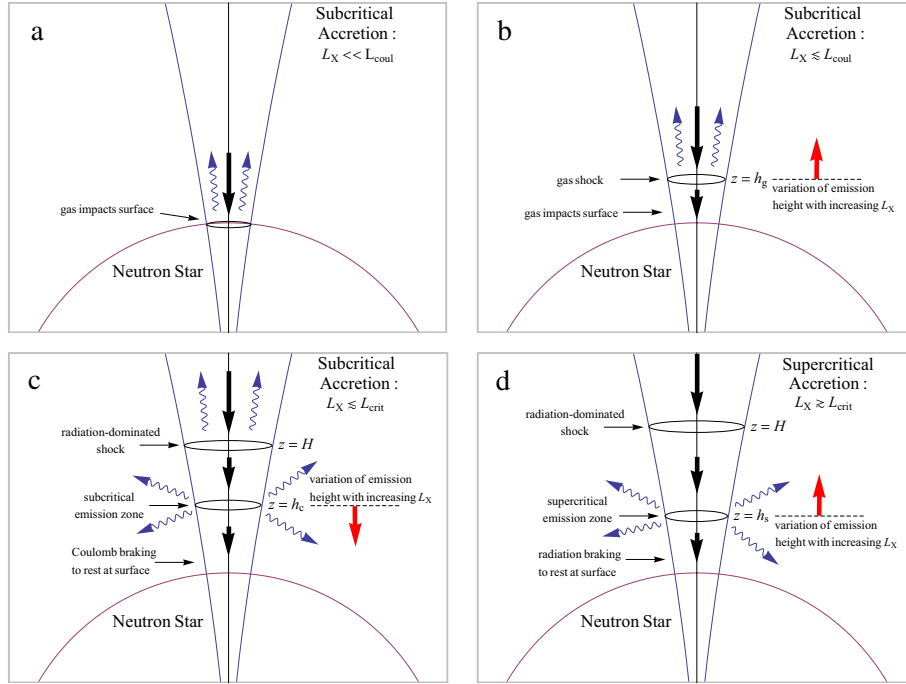
**Fig. 1.** Schematic illustration of the geometry of the accretion column and the variation of the characteristic emission height and emission beam pattern with increasing luminosity $L_X$: **a)** subcritical, $L_X < L_{coul} < L_{crit}$, pencil beam; **b)** subcritical, $L_X \lesssim L_{coul} < L_{crit}$, pencil beam; **c)** subcritical, $L_{coul} < L_X \lesssim L_{crit}$, intermediate beam pattern; **d)** supercritical, $L_X \gtrsim L_{crit}$, fan beam.

strong magnetic field, with a surface strength $B_* \gtrsim 10^{12}$ G, which results in a magnetic pressure far exceeding that of either the gas or the radiation field. The high incident speed of the freely-falling plasma, $\sim 0.6\,c$, creates very high temperatures, $T \sim 10^8$ K. However, the observed X-ray pulsar spectra are highly nonthermal, indicating that the accreting gas is unable to equilibrate during the accretion timescale. In this situation, bulk and thermal Comptonization play key roles in establishing the shape of the observed spectra (Becker & Wolff 2007).

The X-ray spectra of many XRBPs contain cyclotron resonant scattering features (CRSFs) appearing as absorption lines. The features are caused by resonant scattering of photons off plasma electrons whose energy is quantized according to their Landau level (see e.g. Trümper et al. 1978; Isenberg et al. 1998; Araya-Góchez & Harding 2000). The CRSFs, when detected, provide a direct measurement of the magnetic field strength at the characteristic altitude of the X-ray emission. The energy of the fundamental line and the spacing between the harmonics are approximately proportional to the $B$-field strength.

Many XRBPs display X-ray spectra that vary significantly with luminosity on timescales much longer than the pulsation period. In particular, variations in the energy of CRSFs as a function of luminosity on timescales of days to months have been detected in V 0332+53 (Mowlavi et al. 2006; Tsygankov et al. 2010), 4U 0115+63 (Mihara et al. 2004; Tsygankov et al. 2007), and Her X-1 (Staubert et al. 2007; Vasco et al. 2011). In addition to the longer-term variability, there is also mounting evidence for pulse-to-pulse variability, in which the spectral hardness, the centroid energy of the CRSF, and the luminosity vary in a correlated way (Klochkov et al. 2011). This short-timescale variability is likely related to the non-stationarity of the accretion flow, perhaps indicating that the entrainment of matter from the disk onto the magnetic field lines results in filaments and

blobs of accreting gas which are then channeled onto the star in a non-uniform way.

The data from both long-term and short-term (pulse-to-pulse) observations point to the existence of two types/modes of spectral variability (see discussion by Klochkov et al. 2011). For sources in group 1 (e.g., V 0332+53), the centroid energy of the CRSF is negatively correlated with luminosity. For sources in group 2 (e.g., Her X-1), the opposite behavior is observed. The type of spectral variability is likely driven by the mode of accretion, which in turn is determined by the luminosity (see discussion in Staubert et al. 2007). Staubert et al. (2007) and Klochkov et al. (2011) have proposed that for sources in group 1, the deceleration of the flow to rest at the stellar surface is accomplished by the pressure of the radiation field, and in the group 2 sources the deceleration occurs via Coulomb interactions. In this interpretation, a given source falls in one group or the other depending on the value of its X-ray luminosity, $L_X$, relative to the critical luminosity, $L_{crit}$. The hypothesis is that the group 1 sources are supercritical, with X-ray luminosity $L_X > L_{crit}$, and the group 2 sources are subcritical ($L_X < L_{crit}$).

The theory predicts that sources in their supercritical state should display a negative correlation between the luminosity and the cyclotron energy, while sources in the subcritical state should display the reverse behavior. Geometrically, the variation of the CRSF energy with luminosity is connected with variation of the characteristic emission height, which is the altitude in the accretion column where the cyclotron absorption feature is imprinted on the observed spectrum. The variation of the emission height as a function of luminosity in the subcritical and supercritical cases is indicated schematically in Fig. 1.

The general picture described above provides a qualitative basis for the interpretation of the observed correlated variation of the CRSF centroid energy with X-ray luminosity in

some XRBPs. However, in order to obtain a quantitative understanding of these observations, one must develop a more detailed physical model for the critical luminosity, and for the dependence of the CRSF energy on the luminosity in the subcritical and supercritical regimes. The first goal of this paper is to derive a new expression for the critical luminosity, taking into account the magnetospheric connection between the radius of the accretion column and the Alfvén radius in the disk, and the energy and angle dependence of the cyclotron scattering cross section. The second goal is to examine the dependence of the CRSF centroid energy on the luminosity in the subcritical and supercritical sources.

The remainder of the paper is organized as follows. In Sect. 2, we obtain a fundamental expression for the critical luminosity that depends on the stellar mass, radius, and surface magnetic field strength. In Sect. 3 we develop simple physical models for the variation of the characteristic emission height as a function of the luminosity for subcritical and supercritical sources. In Sect. 4, we evaluate the critical luminosity based on measurements of the CRSF centroid energy for several XRBPs. We use our subcritical and supercritical models for the variation of the emission height to predict the variation of the CRSF energy as a function of luminosity. The predicted spectral variability is compared with the observational data for each source. We discuss our results and draw conclusions in Sect. 5.

## 2. Critical luminosity

### 2.1. Eddington luminosity and radiative deceleration

First we recall the definition of the standard Eddington luminosity, $L_{Edd}$, for spherically symmetric accretion onto a central mass $M_*$. If the accreting gas is fully-ionized hydrogen, we obtain

$$L_{Edd} = \frac{4\pi GM_* m_p c}{\sigma_T},\tag{1}$$

where $\sigma_T$ is the Thomson cross section, $m_p$ is the proton mass, $c$ is the speed of light, and $G$ is the gravitational constant. When the X-ray luminosity $L_X = L_{Edd}$, the rate at which momentum is transferred to the gas via Compton scattering balances the gravitational force. Hence if $L_X > L_{Edd}$, the net force is in the outward direction and the gas decelerates as it falls toward the central mass.

We need to make two adjustments to Eq. (1) in order to compute the effective Eddington limit, $L_{Edd}^*$, appropriate for treating X-ray pulsar accretion columns. The first adjustment is to replace the Thomson cross section $\sigma_T$ with $\sigma_\parallel$, which represents the mean scattering cross section for photons propagating parallel to the magnetic field axis. The second adjustment is to take the geometry of the accretion flow into account by reducing the luminosity by the ratio of the column cross-sectional area divided by the surface area of the star. Employing these corrections yields for the effective Eddington limit

$$L_{Edd}^* = L_{Edd}\,\frac{\sigma_T}{\sigma_\parallel}\,\frac{\pi r_0^2}{4\pi R_*^2} = \frac{GM_* m_p c}{\sigma_\parallel}\,\frac{\pi r_0^2}{R_*^2},\tag{2}$$

where $R_*$ is the stellar radius and $r_0$ denotes the radius of the accretion column, which we assume to have an approximately cylindrical geometry.

Based on Eq. (2), Basko & Sunyaev (1976) concluded that for X-ray luminosities $L_X \gtrsim 10^{36}$ erg s$^{-1}$, the incident, freely-falling gas is decelerated by a vertical flux of radiation that is locally super-Eddington. The scattering of the incident radiation removes kinetic energy from the electrons (and from the protons via Coulomb coupling), thereby decelerating the gas. Although the radiation flux seen by the gas inside the column is propagating upward, the X-rays that ultimately carry away the kinetic energy actually escape through the walls of the column, rather than the top, unless the luminosity $L_X \lesssim 10^{36}$ erg s$^{-1}$.

The deceleration of the gas begins when the freely-falling material encounters a radiation-dominated shock whose height above the star increases with increasing luminosity, reaching an altitude of several kilometers for $L_X \sim 10^{37-38}$ erg s$^{-1}$. As the gas passes through the shock, the accretion velocity is reduced by a factor of ~7. Even though the radiation flux inside the column is super-Eddington, the height of the radiation-dominated shock is stable. This reflects the fact that the shock is a wave structure, and is not composed of a fixed population of particles. Matter moves through the shock and decelerates, but the shock height remains fixed, unless the luminosity changes. Unlike a classical gas-mediated shock, the radiation-dominated shock is not discontinuous, and instead has a thickness that is a few times larger than the mean-free path for radiation scattering.

Below the radiation-dominated shock, the matter is further decelerated in the hydrostatic "sinking regime", in which the remaining momentum is transferred to the radiation field and radiated away through the column walls (Basko & Sunyaev 1976). The specific mechanism accomplishing the final deceleration to rest at the stellar surface in the sinking region depends on the luminosity of the accretion flow (see Fig. 1). At the highest luminosities, $L_X \sim 10^{37-38}$ erg s$^{-1}$, the radiation field accomplishes the deceleration all the way down to the stellar surface (Basko & Sunyaev 1976). At intermediate luminosities $L_X \sim 10^{36-37}$ erg s$^{-1}$, the final phase of deceleration may occur via Coulomb breaking in a plasma cloud just above the stellar surface (Nelson et al. 1993). It is expected that at very low luminosities, $L_X \lesssim 10^{34-35}$ erg s$^{-1}$, there is no radiation-dominated shock at all, and the material passes through a conventional gas-mediated shock at altitude $z = h_g$ before striking the stellar surface (Langer & Rappaport 1982).

The angular pattern of the emitted radiation also depends on the luminosity (see Fig. 1). In high-luminosity sources ($L_X \sim 10^{37-38}$ erg s$^{-1}$), the emitted radiation primarily escapes through the column walls in the sinking region, forming a "fan beam" (Davidson 1973). For low-luminosity sources ($L_X \lesssim 10^{35}$ erg s$^{-1}$), the emission escapes from the top of the column, forming a "pencil beam" (Burnard et al. 1991; Nelson et al. 1993). In the intermediate range, $L_X \lesssim 10^{35-37}$ erg s$^{-1}$, the emission pattern may be a hybrid combination of these two types (Blum & Kraus 2000).

Focusing on the high-luminosity case for now, we can estimate the luminosity required to decelerate the gas to rest at the stellar surface by considering the physical processes occurring in the sinking region below the radiation-dominated shock. The accreting matter approaches the top of the shock with the incident free-fall velocity, which we approximate using the value at the stellar surface,

$$v_{ff} = \left(\frac{2GM_*}{R_*}\right)^{1/2}.\tag{3}$$

Advection is dominant over diffusion in the shock, and therefore very little radiation energy escapes through the walls of the accretion column in the vicinity of the shock (Burnard et al. 1991). Hence the shock jump conditions are well approximated by the standard Rankine-Hugoniot relations for a gas with adiabatic

index $\gamma = 4/3$ (Basko & Sunyaev 1976). In this case, the matter leaves the shock with the post-shock velocity

$$v_{\rm ps} = \frac{1}{7} v_{\rm ff} = \frac{1}{7} \left( \frac{2GM_*}{R_*} \right)^{1/2}, \tag{4}$$

where we have assumed that the shock is strong, which is reasonable in the luminous sources (Becker 1998). If the altitude of the radiation-dominated shock above the stellar surface is $H$, and the gas decelerates at a constant rate $a$ from the post-shock velocity $v_{\rm ff}/7$ to rest at the stellar surface in the dynamical time $t_{\rm dyn}$, then we can write the simple kinematical relations

$$H = \frac{1}{2} a t_{\rm dyn}^2, \qquad v_{\rm ps} = a t_{\rm dyn}. \tag{5}$$

Upon elimination of $t_{\rm dyn}$, we obtain for the required upward acceleration

$$a = \frac{v_{\rm ps}^2}{2H} = \frac{GM_*}{49R_*H}. \tag{6}$$

Since the effective gravity is reduced by the pressure of the radiation field, the net acceleration can also be related to the luminosity $L_{\rm X}$ via

$$a = \left( \frac{L_{\rm X}}{L_{\rm Edd}^*} - 1 \right) \frac{GM_*}{R_*^2}. \tag{7}$$

Setting Eqs. (6) and (7) equal and solving for $L_{\rm X}$ yields

$$L_{\rm X} = L_{\rm crit} \equiv L_{\rm Edd}^* \left( \frac{R_*}{49H} + 1 \right). \tag{8}$$

Substituting for $L_{\rm Edd}^*$ using Eq. (2), we obtain for the critical luminosity

$$L_{\rm crit} = \frac{GM_* m_{\rm p} c}{\sigma_\parallel} \frac{\pi r_0^2}{R_*^2} \left( \frac{R_*}{49H} + 1 \right). \tag{9}$$

Our goal is to express the parameters $r_0$, $\sigma_\parallel$, and $H$ appearing on the right-hand side of Eq. (9) in terms of observable quantities.

## 2.2. Radiation-dominated shock height

The altitude, $H$, of the radiation-dominated shock can be estimated by considering the relationship between the dynamical timescale for deceleration, $t_{\rm dyn}$, and the photon escape timescale, $t_{\rm diff}$, which is the mean time it takes the photons to diffuse through the walls of the accretion column. In order for the gas to come to rest at the stellar surface, these two timescales must be comparable in the sinking region below the shock, which is a general property of accretion flows onto white dwarf stars and neutron stars (e.g., Imamura et al. 1987). Combining Eqs. (4) and (5), we obtain for the dynamical time

$$t_{\rm dyn} = \frac{2H}{v_{\rm ps}} = 14H \left( \frac{R_*}{2GM_*} \right)^{1/2}. \tag{10}$$

The escape timescale for the photons to diffuse through the column walls is estimated by writing

$$t_{\rm esc} = \frac{r_0}{v_\perp^{\rm diff}}, \qquad v_\perp^{\rm diff} = \frac{c}{\tau_\perp}, \qquad \tau_\perp = r_0 n_{\rm e} \sigma_{\rm T}, \tag{11}$$

where $n_{\rm e}$ is the electron number density, $v_\perp^{\rm diff}$ is the photon diffusion velocity perpendicular to the column axis, and $\tau_\perp$ is the

perpendicular optical thickness. The Thomson cross section $\sigma_{\rm T}$ is appropriate for photons propagating perpendicular to the column axis (Wang & Frank 1981). The electron number density $n_{\rm e}$ appearing in Eq. (11) can be eliminated using the mass conservation relation,

$$\dot{M} = \pi r_0^2 n_{\rm e} m_{\rm p} v, \tag{12}$$

where $\dot{M}$ is the accretion rate and $v$ is the inflow velocity, defined to be positive. Combining relations, we can express the escape time through the walls as

$$t_{\rm esc} = \frac{\dot{M} \sigma_{\rm T}}{\pi m_{\rm p} v c}. \tag{13}$$

The deceleration in the sinking region begins on the downstream side of the shock, and therefore we set $v = v_{\rm ps}$ in Eq. (13) and equate $t_{\rm dyn}$ and $t_{\rm esc}$ to obtain

$$H = \frac{\dot{M} \sigma_{\rm T}}{2\pi m_{\rm p} c}, \tag{14}$$

which is essentially the same result obtained by Burnard et al. (1991). Expressing the accretion rate in terms of the luminosity using the relation

$$L_{\rm X} = \frac{GM_* \dot{M}}{R_*} \tag{15}$$

yields the equivalent expression

$$H = 1.14 \times 10^5 \, {\rm cm} \left( \frac{M_*}{1.4 \, M_\odot} \right)^{-1} \left( \frac{R_*}{10 \, {\rm km}} \right) \left( \frac{L_{\rm X}}{10^{37} \, {\rm erg \, s^{-1}}} \right). \tag{16}$$

This confirms that the shock is located a few kilometers above the stellar surface in the luminous sources with $L_{\rm X} \sim 10^{37-38}$ erg s$^{-1}$ (Basko & Sunyaev 1976). It follows that $R_*/(49H) \ll 1$ for sources close to or above the critical luminosity, and therefore Eq. (9) reduces to

$$L_{\rm crit} = \frac{GM_* m_{\rm p} c}{\sigma_\parallel} \frac{\pi r_0^2}{R_*^2}, \tag{17}$$

in agreement with Burnard et al. (1991). Note that in this limit, the critical luminosity simply reduces to the effective Eddington value given by Eq. (2).

## 2.3. Connection between column radius and Alfvén radius

In this section, we wish to relate the critical luminosity $L_{\rm crit}$ in Eq. (17) to the magnetic field strength at the stellar surface, $B_*$, by utilizing the connection between the radius of the accretion column, $r_0$, and the Alfvén radius in the disk, $R_{\rm A}$. The inclination angle between the axis of the accretion disk and the star's magnetic axis varies with a period equal to the pulsar's spin period, and this causes an associated variation of the Alfvén radius. However, for our purposes here, an adequate approximation is obtained by using Eq. (13) from Lamb et al. (1973), which yields

$$R_{\rm A} = 2.73 \times 10^7 \, {\rm cm} \left( \frac{\Lambda}{0.1} \right) \left( \frac{M_*}{1.4 \, M_\odot} \right)^{1/7} \left( \frac{R_*}{10 \, {\rm km}} \right)^{10/7}$$

$$\times \left( \frac{B_*}{10^{12} \, {\rm G}} \right)^{4/7} \left( \frac{L_{\rm X}}{10^{37} \, {\rm erg \, s^{-1}}} \right)^{-2/7}, \tag{18}$$

where the constant $\Lambda = 1$ for spherical accretion and $\Lambda < 1$ for disk accretion. A variety of uncertainties are folded into $\Lambda$,

such as the spin-averaging of $R_A$ and the possible role of plasma shielding and other magnetospheric effects. Based on Eq. (2) from Harding et al. (1984), $\Lambda$ can be approximated in the disk application using

$$\Lambda \approx 0.22 \, \alpha^{18/69}, \tag{19}$$

where $\alpha < 1$ denotes the Shakura-Sunyaev parameter (Shakura & Sunyaev 1973). Although it is difficult to estimate $\alpha$ with any certainty, we generally expect to find $\alpha \sim 0.01-0.1$. We therefore set $\Lambda = 0.1$ in our numerical applications.

The Alfvén radius in the disk is connected with the outer surface of the accretion column through the dipole shape of the pulsar magnetosphere. The equation for the shape of the critical field line as a function of the polar angle $\theta$ is given by the standard dipole formula

$$R = R_A \sin^2 \theta. \tag{20}$$

Setting the radius $R$ equal to the stellar radius $R_*$ yields for the critical angle at the outer edge of the accretion column

$$\sin^2 \theta_c = \frac{R_*}{R_A}. \tag{21}$$

Using the small-angle relation $\theta_c \approx \sin \theta_c$, we obtain for the column radius

$$r_0 = R_* \theta_c = R_* \left( \frac{R_*}{R_A} \right)^{1/2}. \tag{22}$$

By substituting for the Alfvén radius in Eq. (22) using Eq. (18), we find that the expression for the column radius $r_0$ can be rewritten in cgs units as

$$r_0 = 1.93 \times 10^5 \text{ cm} \left( \frac{\Lambda}{0.1} \right)^{-1/2} \left( \frac{M_*}{1.4 \, M_\odot} \right)^{-1/14} \left( \frac{R_*}{10 \text{ km}} \right)^{11/14}$$
$$\times \left( \frac{B_*}{10^{12} \text{ G}} \right)^{-2/7} \left( \frac{L_X}{10^{37} \text{ erg s}^{-1}} \right)^{1/7}. \tag{23}$$

Using Eq. (23) to substitute for $r_0$ in Eq. (17), and setting $L_X = L_{crit}$, we obtain for the critical luminosity the new expression

$$L_{crit} = 7.79 \times 10^{35} \text{ erg s}^{-1} \left( \frac{\Lambda}{0.1} \right)^{-7/5} \left( \frac{\sigma_\parallel}{\sigma_T} \right)^{-7/5}$$
$$\times \left( \frac{M_*}{1.4 \, M_\odot} \right)^{6/5} \left( \frac{R_*}{10 \text{ km}} \right)^{-3/5} \left( \frac{B_*}{10^{12} \text{ G}} \right)^{-4/5}, \tag{24}$$

where we have also introduced the Thomson cross section $\sigma_T$ as a convenient scaling for the parallel scattering cross section $\sigma_\parallel$. The next step is to evaluate the cross section ratio $\sigma_\parallel/\sigma_T$ in terms of observable source parameters.

### 2.4. Electron scattering cross section for parallel propagation

In typical X-ray pulsars, most of the observed radiation is emitted at energies below the cyclotron energy, $E_{cyc}$. Hence the cross-section ratio $\sigma_\parallel/\sigma_T$ can be roughly approximated using (e.g., Arons et al. 1987).

$$\frac{\sigma_\parallel}{\sigma_T} = \left( \frac{\bar{E}}{E_{cyc}} \right)^2, \tag{25}$$

where $\bar{E}$ is a measure of the mean energy of the photons propagating parallel to the magnetic field, and the cyclotron energy $E_{cyc}$ is given by

$$E_{cyc} = 11.58 \text{ keV} \left( \frac{B}{10^{12} \text{ G}} \right). \tag{26}$$

The mean photon energy $\bar{E}$ in Eq. (25) can be estimated observationally by integrating the spectrum for a given source. However, in luminous X-ray pulsars, most of the observed radiation escapes through the walls of the accretion column, perpendicular to the magnetic field, and therefore the observed spectrum may not be representative of the distribution of photons propagating along the column axis. As an alternative, we can estimate $\bar{E}$ based on the thermal structure of the accreting gas. Specifically, we assume that

$$\bar{E} = wkT_{eff}, \tag{27}$$

where $T_{eff}$ is the effective temperature of the radiation in the post-shock region, $k$ is Boltzmann's constant, and the constant $w$ depends on the shape of the spectrum inside the column. We expect that $w \sim 1-3$, with the lower value corresponding to bremsstrahlung and the upper value to a Planck spectrum. Detailed models suggest that the spectrum inside the column is dominated by bremsstrahlung emission (Becker & Wolff 2007), and therefore we will set $w = 1$ in the numerical results presented later.

The effective temperature is related to the post-shock radiation pressure, $P_r$, via

$$aT_{eff}^4 = 3P_r. \tag{28}$$

The value of $P_r$ can be estimated using the momentum balance relation

$$P_r = \rho_{ff} v_{ff}^2 = \frac{\dot{M} v_{ff}}{\pi r_0^2}, \tag{29}$$

where $\rho_{ff}$ and $v_{ff}$ (Eq. (3)) denote the upstream mass density and velocity, respectively, just above the shock. Eliminating $P_r$ between Eqs. (28) and (29), and substituting for $\dot{M}$ and $r_0$ using Eqs. (15) and (23), we find that

$$T_{eff} = 4.35 \times 10^7 \text{ K} \left( \frac{\Lambda}{0.1} \right)^{1/4} \left( \frac{M_*}{1.4 \, M_\odot} \right)^{-5/56} \left( \frac{R_*}{10 \text{ km}} \right)^{-15/56}$$
$$\times \left( \frac{B_*}{10^{12} \text{ G}} \right)^{1/7} \left( \frac{L_X}{10^{37} \text{ erg s}^{-1}} \right)^{5/28}. \tag{30}$$

Combining Eqs. (25)−(27), and (30), we obtain for the required cross section ratio the result

$$\frac{\sigma_\parallel}{\sigma_T} = 0.106 \left( \frac{\Lambda}{0.1} \right)^{1/2} w^2 \left( \frac{M_*}{1.4 \, M_\odot} \right)^{-5/28} \left( \frac{R_*}{10 \text{ km}} \right)^{-15/28}$$
$$\times \left( \frac{B_*}{10^{12} \text{ G}} \right)^{-12/7} \left( \frac{L_X}{10^{37} \text{ erg s}^{-1}} \right)^{5/14}. \tag{31}$$

Using this result to substitute for $\sigma_\parallel/\sigma_T$ in Eq. (24) yields the final expression for the critical luminosity as a function of the surface magnetic field strength,

$$L_{crit} = 1.49 \times 10^{37} \text{ erg s}^{-1} \left( \frac{\Lambda}{0.1} \right)^{-7/5} w^{-28/15}$$
$$\times \left( \frac{M_*}{1.4 \, M_\odot} \right)^{29/30} \left( \frac{R_*}{10 \text{ km}} \right)^{1/10} \left( \frac{B_*}{10^{12} \text{ G}} \right)^{16/15}. \tag{32}$$

For typical neutron star parameters, with $M_* = 1.4\,M_\odot$, $R_* = 10$ km, $\Lambda = 0.1$, and $w = 1$, we obtain $L_{\rm crit} = 1.49 \times 10^{37}$ erg s$^{-1}\,B_{12}^{16/15}$, where $B_{12}$ is the surface magnetic field strength in units of $10^{12}$ G. In Sect. 4 we plot the critical luminosity and compare it with the variability data for several XRBPs.

## 3. Variation of emission height

The new expression for the critical luminosity given by Eq. (32) allows us to separate accretion-powered X-ray pulsars into sub-critical and supercritical categories. Our hypothesis is that in the subcritical sources with variable luminosity $L_X$, the cyclotron energy $E_{\rm cyc}$ will exhibit a positive correlation with $L_X$, and in the supercritical sources the reverse behavior will be observed. The observed CRSF is imprinted on the spectrum at the altitude where most of the emitted radiation escapes from the accretion column. In order to quantify the expected behaviors in the sub-critical and supercritical regimes, we must therefore explore the expected variation of the emission height as a function of luminosity for both types of sources. The geometry of the super- and subcritical sources is depicted schematically in Fig. 1.

### 3.1. Supercritical sources

In the supercritical sources (luminosity $L_X \gtrsim L_{\rm crit}$), radiation pressure dominates the flow dynamics all the way to the stellar surface. Inside the radiation-dominated shock, the infalling matter begins to decelerate as it first encounters the "cushion" of radiation hovering at the shock altitude (Davidson 1973). At this altitude, there is a local balance between downward advection and upward diffusion of radiation, and therefore the photon distribution is roughly static. Most of the kinetic energy of the accretion flow is carried away by the scattered radiation, which is likely to be beamed in the downward direction due to special-relativistic aberration (e.g., Ferrigno et al. 2009). Below the shock altitude, the photons are trapped by advection, although they eventually manage to escape by diffusing through the walls of the column. Hence the observed radiation does not escape from the shock altitude $H$, but rather from a lower altitude.

Our goal here is to estimate the typical altitude, denoted by $h_s$, at which the photons diffuse through the column walls to form the observed X-ray spectrum in the supercritical case. We assume that the observed CRSF is imprinted at this altitude, because at higher altitudes the photons have not had enough time to diffuse through the column and escape through the walls. Conversely, at lower altitudes, the increasing density of the gas in the column inhibits the escape of radiation. We therefore expect that the CRSF energy will reflect the cyclotron energy at the altitude $z = h_s$ where the final deceleration phase begins.

We can estimate the emission height $h_s$ in the supercritical sources by ensuring that all of the kinetic energy is radiated through the walls by the escaping photons in the altitude range $0 < z < h_s$ (Basko & Sunyaev 1976). Working in the frame co-moving with the mean vertical velocity of the radiation in the accretion column, we note that the fraction of the radiation escaping through the walls in the comoving time interval d$t'$ is equal to d$t'/t_{\rm esc}$, where $t_{\rm esc}$ is the escape time given by Eq. (13). The requirement that all of the radiation escapes by the time the matter reaches the stellar surface is therefore expressed by the integral condition

$$\int_0^{h_s} \left|\frac{{\rm d}t'}{{\rm d}z'}\right| \frac{{\rm d}z'}{t_{\rm esc}\,(z')} = 1. \tag{33}$$

Using Eq. (13) to substitute for $t_{\rm esc}$ yields

$$\int_0^{h_s} \frac{\pi m_{\rm p} v c}{\dot{M}\sigma_{\rm T}} \frac{{\rm d}z'}{v_{\rm eff}} = 1, \tag{34}$$

where the effective velocity for the photon transport is defined by

$$v_{\rm eff} \equiv \left|\frac{{\rm d}z'}{{\rm d}t'}\right|. \tag{35}$$

The flow is expected to be almost perfectly "trapped" in the region below $z' = h_s$, meaning that advection and diffusion are nearly balanced, leaving very little net flux of radiation (Becker 1998). This implies that the effective velocity $v_{\rm eff}$ is much smaller than the flow velocity $v$. We define the parameter $\xi$ as the ratio of these two velocities,

$$\xi \equiv \frac{v_{\rm eff}}{v}. \tag{36}$$

We demonstrate in Appendix A that the value of $\xi$ can be estimated using

$$\xi = \frac{1}{\mathcal{M}_\infty^2}, \tag{37}$$

where $\mathcal{M}_\infty$ denotes the incident (upstream) Mach number of the flow with respect to the radiation sound speed. In the sinking region below the shock, the effective velocity approaches zero as the gas settles onto the stellar surface. The relationship between the upstream Mach number $\mathcal{M}_\infty$ and the X-ray luminosity $L_X$ is plotted in Fig. 12 from Becker (1998). For the parameter range of interest here, it is sufficient to adopt a constant value for $\xi$ in the range $\xi \sim 10^{-2}$–$10^{-3}$. The low value for the effective velocity tends to make the emission region more compact in the supercritical sources.

Combining relations, we find that

$$\int_0^{h_s} \frac{\pi m_{\rm p} c}{\dot{M}\sigma_{\rm T}\xi} {\rm d}z' = 1, \tag{38}$$

and therefore the altitude of the emission region is given by

$$h_s = \frac{\dot{M}\sigma_{\rm T}\xi}{\pi m_{\rm p} c} = \frac{L_X R_* \sigma_{\rm T}\xi}{\pi m_{\rm p} c G M_*}, \tag{39}$$

where the final result follows from Eq. (15). We can also express $h_s$ in cgs units using

$$h_s = 2.28 \times 10^3 \text{ cm} \left(\frac{\xi}{0.01}\right)\left(\frac{M_*}{1.4\,M_\odot}\right)^{-1}$$
$$\times \left(\frac{R_*}{10 \text{ km}}\right)\left(\frac{L_X}{10^{37} \text{ erg s}^{-1}}\right). \tag{40}$$

Note that the emission height in the supercritical sources varies in proportion to the luminosity $L_X$ (see Fig. 1).

Based on Eqs. (16) and (40), we conclude that

$$\frac{h_s}{H} = 2.0\,\xi \ll 1, \tag{41}$$

and therefore the characteristic height of emission in the super-critical sources is located far below the altitude of the radiation-dominated shock. Eq. (40) indicates that the height of the emission region $h_s$ scales in proportion to the luminosity $L_X$ in the supercritical sources, which is consistent with the observed behavior in the group 1 sources (Klochkov et al. 2011).

## 3.2. Subcritical sources

In the subcritical sources (luminosity $L_X \lesssim L_{crit}$), the matter still passes through a radiation-dominated shock, which accomplishes the initial deceleration, but the pressure of the radiation is insufficient to bring the matter to rest at the stellar surface (Basko & Sunyaev 1976). In this case, the final stopping occurs via direct Coulomb interactions close to the base of the accretion column (Burnard et al. 1991). Our goal in this section is to estimate the characteristic emission height for the subcritical sources, denoted by $h_c$, which is the altitude at which Coulomb interactions begin to decelerate the plasma to rest. The emission is expected to be concentrated in this region because this is essentially the first opportunity that the radiation inside the column has to diffuse through the walls. At higher altitudes, the radiation is swept along by advection, and there is not enough time for the photons to escape. At lower altitudes, the radiation is trapped in the column due to the increasing density, and therefore the emission through the walls tapers off as $z \rightarrow 0$. Hence we expect that in the subcritical case, the CRSF energy is imprinted at the altitude $z = h_c$ where the strong Coulomb deceleration begins.

The Thomson optical depth, $\tau_*$, required to stop the flow via Coulomb interactions can be estimated in the typical pulsar magnetic field regime using Eq. (3.34) from Nelson et al. (1993) to write

$$\tau_* = 51.4 \left(\frac{M_*}{1.4\, M_\odot}\right)^2 \left(\frac{R_*}{10\text{ km}}\right)^{-2} \frac{1}{\ln(2n_{max})}, \tag{42}$$

where the maximum excited Landau level, $n_{max}$, is given by

$$n_{max} = \frac{m_e v_{ff}^2}{2E_{cyc}}. \tag{43}$$

A summary of the derivation leading up to Eq. (42) is provided in Appendix B. Adopting typical X-ray pulsar parameters, we find that $\tau_* \sim 20$, which is the value utilized in our numerical examples.

We can use Eq. (42) to estimate the emission height in the subcritical sources, $h_c$, as follows. The Thomson depth $\tau$ as a function of the altitude $z$ measured from the stellar surface is computed using

$$\tau(z) = \int_0^z \frac{\rho(z')\sigma_T}{m_p}\, dz', \tag{44}$$

where $\rho = n_e m_p$ is the mass density, given by (see Eq. (12))

$$\rho(z) = \frac{\dot{M}}{\pi r_0^2 v(z)}. \tag{45}$$

Assuming that the gas decelerates uniformly in the Coulomb stopping region (starting at altitude $h_c$) from the post-shock velocity $v_{ps}$, we find that the required deceleration is given by $a = v_{ps}^2/(2\,h_c)$ (cf. Eq. (6)). The velocity profile $v(z)$ associated with the constant deceleration $a$ is computed using the standard kinematical relations

$$a = -\frac{dv}{dt} = v\frac{dv}{dz} = \frac{1}{2}\frac{dv^2}{dz}, \tag{46}$$

where the negative sign appears because we have defined $v$ and $a$ to be positive. Setting $v_{ps} = v_{ff}/7$ (see Eq. (4)), we obtain for the deceleration $a = v_{ff}^2/(98\,h_c)$. Upon integration of Eq. (46), we therefore find that the velocity profile in the Coulomb stopping region is given by

$$v(z) = \frac{v_{ff}}{7}\sqrt{\frac{z}{h_c}}, \tag{47}$$

where $v_{ff}$ is evaluated using Eq. (3).

Using Eq. (47) to substitute for $v(z)$ in Eq. (45) and carrying out the integration in Eq. (44), we obtain for the optical depth profile

$$\tau(z) = \frac{14\dot{M}\sigma_T}{\pi r_0^2 m_p}\left(\frac{2GM_*}{R_*}\right)^{-1/2}\sqrt{h_c z}. \tag{48}$$

Finally, setting $z = h_c$ and $\tau = \tau_*$, we find that the Thomson optical depth required for Coulomb stopping is given by

$$\tau_* = \frac{14\dot{M}\sigma_T h_c}{\pi r_0^2 m_p}\left(\frac{2GM_*}{R_*}\right)^{-1/2}, \tag{49}$$

which can be rearranged to obtain for the subcritical emission height

$$h_c = \frac{\pi r_0^2 m_p \tau_*}{14\dot{M}\sigma_T}\left(\frac{2GM_*}{R_*}\right)^{1/2}. \tag{50}$$

Substituting for $\dot{M}$ and $r_0$ using Eqs. (15) and (23), respectively, yields the equivalent cgs expression

$$h_c = 1.48 \times 10^5\text{ cm}\left(\frac{\Lambda}{0.1}\right)^{-1}\left(\frac{\tau_*}{20}\right)\left(\frac{M_*}{1.4\,M_\odot}\right)^{19/14}\left(\frac{R_*}{10\text{ km}}\right)^{1/14}$$

$$\times\left(\frac{B_*}{10^{12}\text{ G}}\right)^{-4/7}\left(\frac{L_X}{10^{37}\text{ erg s}^{-1}}\right)^{-5/7}. \tag{51}$$

This result indicates that the emission height in the subcritical sources decreases with increasing luminosity, which is consistent with the behavior observed in the group 2 sources (Staubert et al. 2007). As indicated in Fig. 1, in the subcritical case, a decrease in the luminosity causes the beam pattern to transition from a pure fan configuration to a hybrid pattern that includes a pencil component. At very low luminosities, the shock essentially sits on the stellar surface, and the emission occurs via the pencil component only (Burnard et al. 1991; Nelson et al. 1993).

## 3.3. Transition from Coulomb stopping to gas shock

Equation (51) gives the height of the emission zone in the subcritical case, based on the assumption that the final deceleration to rest at the stellar surface occurs via Coulomb interactions. We can estimate the minimum luminosity (or accretion rate) such that Coulomb interactions are capable of stopping the flow by requiring that $h_c < H$, where $H$ is the altitude of the radiation-dominated shock. If this condition is violated, then the incident velocity of the gas entering the Coulomb deceleration region becomes essentially the full free-fall velocity, $v_{ff}$, rather than the reduced post-shock velocity, $v_{ps} = v_{ff}/7$. The associated drop in the density causes the Thomson depth $\tau$ to fall below the value $\tau_* \sim 20$ required for the gas to be effectively stopped via Coulomb interactions. It is not completely clear what happens in this case, but we expect that the final phase of deceleration will occur via passage through a gas-mediated shock near the stellar surface (Langer & Rappaport 1982).

By combining Eqs. (14), (15) and (50), we can show that the condition $h_c < H$ implies that

$$L_X > \frac{2^{1/4}\pi m_p r_0}{\sigma_T}\left(\frac{\tau_* c}{7}\right)^{1/2}\left(\frac{GM_*}{R_*}\right)^{5/4}. \tag{52}$$

Substituting for $r_0$ using Eq. (23) and rearranging, we obtain
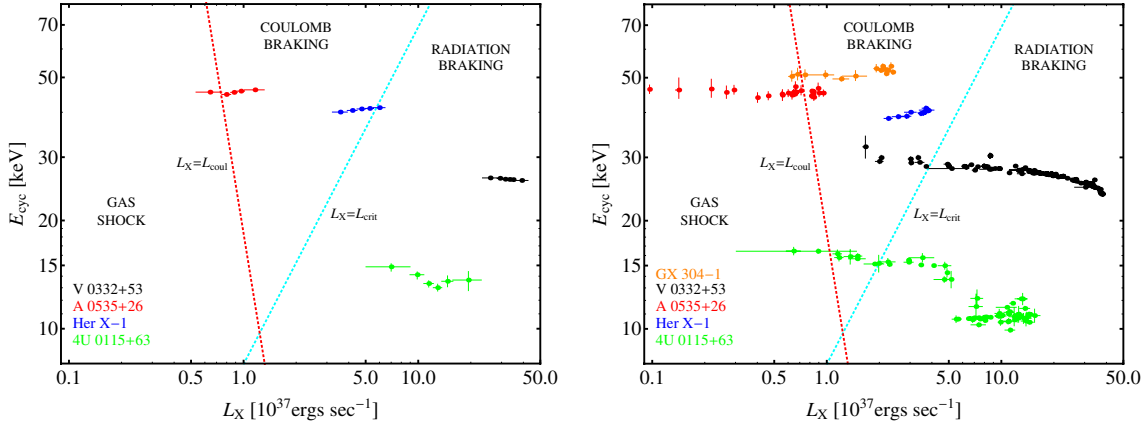
$$L_X > L_{coul}, \tag{53}$$

**Fig. 2.** Variability of the cyclotron line energy with luminosity for different sources. The blue dashed line represents the critical luminosity, plotted by setting $L_X = L_{crit}$ and $E_{cyc} = E_*$, where $L_{crit}$ is evaluated using Eq. (55). The red dashed line represents the Coulomb stopping luminosity, plotted by setting $L_X = L_{coul}$ and $E_{cyc} = E_*$, where $L_{coul}$ is evaluated using Eq. (59). *Left*: observations on a pulse-to-pulse timescale. *Right*: observations on longer timescales.

**Table 1.** Source sample characteristics.

| Source | Instrument | Long-term correlation | Pulse-pulse correlation | $\Delta E$ (keV) | Distance (kpc) |
|---|---|---|---|---|---|
| 4U 0115+63 | INTEGRAL/RXTE | cont. dependent[1] | negative[6] | [3−60] | 8.0[7] |
| V0332+53 | INTEGRAL/RXTE | negative[2] | negative[6] | [3−100] | 7.5[8] |
| Her X-1 | RXTE | positive[3] | positive[6] | [5−60] | 6.4[9] |
| A0535+26 | INTEGRAL/RXTE | no[4] | positive[6] | [3−50] | 2.0[10] |
| GX 304-1 | RXTE/Suzaku | positive[5] | – | [3−100] | 2.4[11] |

**References.** [1] Müller et al. (2011); [2] Tsygankov et al. (2010); [3] Staubert et al. (2007); [4] Caballero et al. (2007); [5] Yamamoto et al. (2011); [6] Klochkov et al. (2011); [7] Negueruela & Okazaki (2001); [8] Negueruela et al. (1999); [9] Reynolds et al. (1997); [10] Steele et al. (1998); [11] Parkes et al. (1980).

**Notes.** Our analysis is based on a combination of published data (references given) and reprocessed observational data for a number of cyclotron line sources (Col. 1) as observed by different X-ray observatories (Col. 2), listed here. The cyclotron line sources have been observed to show different types of correlation, or no correlation, of their cyclotron line energies with changes in the X-ray luminosity.

where

$$L_{coul} = 1.17 \times 10^{37} \text{ erg s}^{-1} \left(\frac{\Lambda}{0.1}\right)^{-7/12} \left(\frac{\tau_*}{20}\right)^{7/12} \left(\frac{M_*}{1.4\,M_\odot}\right)^{11/8}$$

$$\times \left(\frac{R_*}{10 \text{ km}}\right)^{-13/24} \left(\frac{B_*}{10^{12} \text{ G}}\right)^{-1/3}. \tag{54}$$

For luminosities $L_X \lesssim L_{coul}$, we expect that the characteristic emission height settles down onto the stellar surface. For very low luminosities, $L_X \lesssim 10^{34-35}$ erg s$^{-1}$, the radiation-dominated shock and the Coulomb atmosphere both dissipate, and the matter strikes the stellar surface after passing through a gas-mediated shock (Langer & Rappaport 1982), as indicated in Fig. 1.

## 4. Applications

Our final result for the critical luminosity as a function of the surface magnetic field strength $B_*$ is given by Eq. (32), which can be rewritten as

$$L_{crit} = 1.28 \times 10^{37} \text{ erg s}^{-1} \left(\frac{\Lambda}{0.1}\right)^{-7/5} w^{-28/15}$$

$$\times \left(\frac{M_*}{1.4\,M_\odot}\right)^{29/30} \left(\frac{R_*}{10 \text{ km}}\right)^{1/10} \left(\frac{E_*}{10 \text{ keV}}\right)^{16/15}, \tag{55}$$

where

$$E_* = 11.58 \text{ keV} \left(\frac{B_*}{10^{12} \text{ G}}\right) \tag{56}$$

denotes the surface value of the CRSF energy. This relation is indicated by the dashed blue line in Fig. 2. Sources to the right of this line are radiating supercritically, and consequently radiation pressure accomplishes the deceleration all the way down to the stellar surface. For sources to the left of this line, the final deceleration occurs via Coulomb interactions.

It is now interesting to compute the critical luminosity for a number of sources and to compare it with the observed variability of $E_{cyc}$ as a function of $L_X$ for subcritical and supercritical cases. We have selected for this study the sources for which the behavior of the cyclotron line energy with luminosity has been studied sufficiently well, including both the variations on long timescales (days to months) and short timescales ("pulse-to-pulse"). Our source sample is listed in Table 1, where we also summarize the reported $E_{cyc}-L_X$ behavior (positive/negative correlation or no dependence) for each source. The two panels in Fig. 2 depict the variability of $E_{cyc}$ with luminosity both on "pulse-to-pulse" (left) and longer (right) timescales for all of the sources considered here. The corresponding references for the data are given in Table 1. The data for the longer-term variability are based on studies of the phase-averaged emission conducted either during outbursts of the transient sources
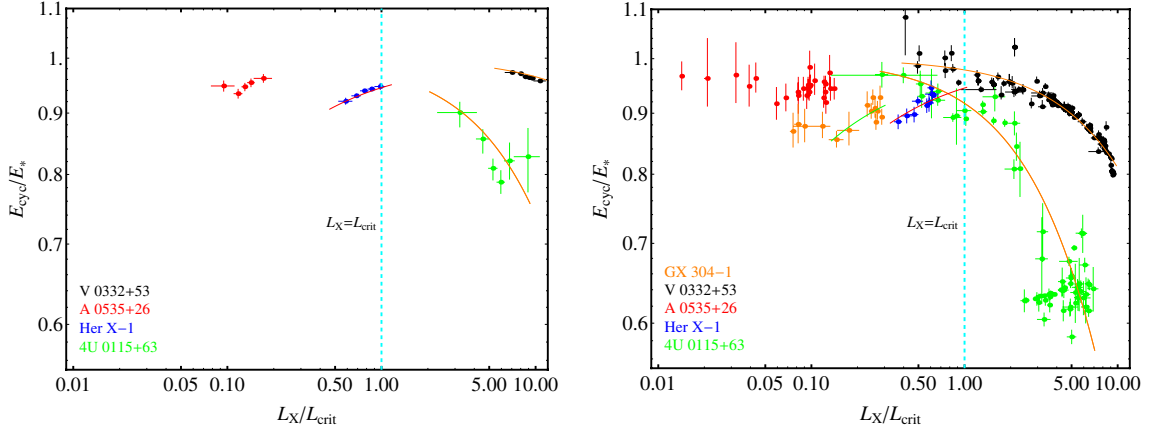
**Fig. 3.** Same as Fig. 2 except with the $x$-axis rescaled as $L_X/L_{crit}$ and the $y$-axis rescaled as $E_{cyc}/E_*$. The values of $E_*$ and $L_{crit}$ used for each source are listed in Table 2. The solid curves associated with each group of data represent the theoretical predictions for the variation of the CRSF energy $E_{cyc}$ as a function of $L_X$ for each source, computed using Eq. (58), with the emission height $h$ evaluated using Eq. (40) for the supercritical sources and Eq. (51) for the subcritical sources.

**Table 2.** Theoretical parameters for each source, based on analysis of the pulse-to-pulse variability and the longer-term variability.

| Source | Long-term $\xi$ | Long-term $E_*$ [keV] | Long-term $L_{crit}$ [$10^{37}$ erg s$^{-1}$] | Pulse-pulse $\xi$ | Pulse-pulse $E_*$ [keV] | Pulse-pulse $L_{crit}$ [$10^{37}$ erg s$^{-1}$] |
|---|---|---|---|---|---|---|
| 4U 0115+63 | $5.72 \times 10^{-2}$ | 17.0 | 2.24 | $2.14 \times 10^{-2}$ | 16.5 | 2.17 |
| V 0332+53 | $7.86 \times 10^{-3}$ | 29.7 | 4.06 | $1.43 \times 10^{-3}$ | 27.0 | 3.67 |
| Her X-1 | – | 43.5 | 6.11 | – | 43.5 | 6.11 |
| A 0535+26 | – | 48.0 | 6.78 | – | 48.0 | 6.78 |
| GX 304-1 | – | 58.0 | 8.30 | – | – | – |

**Notes.** The parameter $\xi$ is relevant only for the two supercritical sources, 4U 0115+63 and V 0332+53 (see Sect. 3.1).

(Tsygankov et al. 2007, 2010), or following the long-term variation of the emission from the persistent sources (Staubert et al. 2007). For the pulse-to-pulse variability we refer to the results of Klochkov et al. (2011) who have shown that for a set of pulsars the cyclotron line energy varies with the amplitude of individual pulses. This amplitude most probably reflects the instantaneous mass accretion rate.

The luminosities for A 0535+26, 4 U0115+63 and Her X-1 were calculated by integrating the flux of each source over a nearly identical energy range $\Delta E$ (see Table 1). For V 0332+53 (Tsygankov et al. 2010) and GX 304-1 (Yamamoto et al. 2011) published values for $L_X$ and $E_{cyc}$ were taken, where the luminosity has been calculated over a slightly larger energy range [3–100] keV. The luminosities were computed using the source distances listed in Table 1. It should be noted that uncertainties in the distances will create additional uncertainties in our computed luminosities, which have not been considered here. However, the typical effective uncertainties of ∼10% in the calculated luminosities do not strongly affect our results.

One can see that the sign of the correlation between the cyclotron line energy and the luminosity, when detected, is consistent between the long-term and pulse-to-pulse studies. This suggests that both are reflecting the same underlying physics. It is clear that the variation of $E_{cyc}$ with $L_X$ for sources on each side of the critical line $L_X = L_{crit}$ is qualitatively consistent with the theoretical predictions, i.e., the correlation between $E_{cyc}$ and $L_X$ is negative for the supercritical sources, and positive for the subcritical ones, reflecting the positive variation of the emission height $h = h_s$ (Eq. (40)) with increasing $L_X$ for the former sources and the negative variation of the emission height $h = h_c$

(Eq. (51)) for the latter sources. In the next section, we explore the variation of $E_{cyc}$ as a function of $L_X$ in more detail.

### 4.1. Variation of $E_{cyc}$ with $L_X$

The observed value of $E_{cyc}$ is connected with the local field strength $B$ at the emission altitude $h$ via Eq. (26), where $B$ has the dipole dependence

$$\frac{B(R)}{B_*} = \left(\frac{R}{R_*}\right)^{-3}, \qquad R = R_* + h. \tag{57}$$

The corresponding variation of $E_{cyc}$ as a function of the emission height $h$ is therefore given by

$$\frac{E_{cyc}}{E_*} = \left(\frac{R_* + h}{R_*}\right)^{-3}, \tag{58}$$

where $E_*$ is the surface value for the cyclotron energy, computed using Eq. (56). Note that we have neglected the variation of the gravitational redshift factor, which is reasonable given the level of approximation employed here (Staubert et al. 2007). In applying Eq. (58) to the supercritical and subcritical cases, we set $h = h_s$ (Eq. (40)) and $h = h_c$ (Eq. (51)), respectively. Hence Eq. (58) can be used to develop theoretical predictions for the variation of $E_{cyc}$ as a function of $L_X$ for supercritical and subcritical sources.

In Fig. 3 we replot the Fig. 2 data based on a rescaling of the vertical and horizontal axes using the parameters $E_*$ and $L_{crit}$, respectively, which are related to each other via Eq. (55). The value of $L_{crit}$ used for each source is listed in Table 2, along with

the corresponding value for the surface cyclotron energy $E_*$ obtained by comparing the theoretical variation of $E_{cyc}$ with the observed variation for each source. In computing $L_{crit}$, we assume for all sources the same canonical neutron star mass and radius values $M_* = 1.4\,M_\odot$ and $R_* = 10$ km, and we set $\Lambda = 0.1$ and $w = 1$ based on the theoretical considerations discussed above. The vertical dashed line marked $L_X = L_{crit}$ separates the sources into their sub- and supercritical luminosity states. It should be noted that, as $M_*$ and $R_*$ are also input parameters for $L_{crit}$, the exact positioning of the source data on the $x$-axis is driven also by the assumed canonical mass and radius values, which might in fact differ between the individual sources.

Figure 3 also includes curves representing the expected theoretical variation of the CRSF energy $E_{cyc}$ as a function of the luminosity $L_X$, computed using Eq. (58) with either $h = h_s$ (Eq. (40)) for the supercritical sources or $h = h_c$ (Eq. (51)) for the subcritical ones. We again adopt the canonical values $M_* = 1.4\,M_\odot$, $R_* = 10$ km, $\Lambda = 0.1$, and $w = 1$, and we set the Coulomb stopping optical depth using $\tau_* = 20$. The values of $E_*$ and $\xi$ are varied for each source so as to improve the agreement with the data (see Table 2). The parameter $\xi$ is only relevant for the supercritical sources. The values of $\xi$ reported in Table 2 for V 0332+53 and 4U 0115+63 are in the range $\xi \sim 10^{-2}$–$10^{-3}$, as expected for marginally trapped accretion columns (Becker 1998). Based on the results depicted in Fig. 3, we conclude that the agreement between the observed variation of $E_{cyc}$ and that predicted by the theoretical models developed here is reasonably close for both the supercritical and subcritical sources.

A special case is 4U 0115+63. This source was previously observed to show an anticorrelation (e.g. Tsygankov et al. 2007 and references therein). The right panels of our Figs. 2 and 3 (observations on longer timescales) include the results for $E_{cyc}$ and $L_X$ obtained by Tsygankov et al. (2007). However, recent studies have shown that the presence of the anticorrelation depends on the choice of the continuum model (Müller et al. 2011).

### 4.2. Comparison of $L_X$ with $L_{coul}$

It is also interesting to compare the observed luminosities with the minimum value, $L_{coul}$, required for Coulomb stopping to decelerate the flow to rest at the stellar surface, given by Eq. (54). By combining Eqs. (54) and (56), we find that $L_{coul}$ is related to $E_*$ via

$$L_{coul} = 1.23 \times 10^{37} \text{ erg s}^{-1} \left(\frac{\Lambda}{0.1}\right)^{-7/12} \left(\frac{\tau_*}{20}\right)^{7/12} \left(\frac{M_*}{1.4\,M_\odot}\right)^{11/8}$$

$$\times \left(\frac{R_*}{10 \text{ km}}\right)^{-13/24} \left(\frac{E_*}{10 \text{ keV}}\right)^{-1/3}. \tag{59}$$

This relation is indicated by the dashed red line in Fig. 2. For sources to the left of this line, we expect that the effect of Coulomb interactions is reduced, and the final stopping occurs via passage through a discontinuous, gas-mediated shock (Langer & Rappaport 1982). Hence we anticipate that the emission region approaches the stellar surface as $L_X$ is reduced below $L_{coul}$. This interpretation is consistent with the observational data plotted in Figs. 2 and 3, which indicate that $E_{cyc}$ approaches a constant value in the limit $L_X/L_{coul} \ll 1$.

Following our hypothesis, sources in their supercritical state ($L_X/L_{crit} \gtrsim 1$) should display a negative correlation between the luminosity and the cyclotron energy while sources in the subcritical state ($L_X/L_{crit} \lesssim 1$) should display the reverse behavior. V 0332+53 and Her X-1 in their super- and subcritical luminosity states nicely fit into that hypothesis on both long and very

short timescales. In particular, we note that the model parameters listed in Table 2 for Her X-1 are the same for both the long-term and pulse-to-pulse data. Hence the model developed here for the variation of $E_{cyc}$ as a function of $L_X$ provides a robust connection with the data across the entire range of luminosity variation for this source, which implies that the underlying physical mechanism of variation is the same for the long-term and pulse-to-pulse variations.

The subcritical source A 0535+26 shows no significant trend on long timescales (Fig. 2, right), perhaps due to the fact that the luminosity is always close to or below the Coulomb stopping limit, $L_{coul}$, which suggests that we should expect little variation of $E_{cyc}$ with $L_X$. On pulse-to-pulse timescales, A 0535+26 shows some suggestion of a positive correlation (Fig. 2, left), as expected for a subcritical source. The positive correlation suggested by the short-timescale data may reflect the fact that the luminosity is somewhat higher than $L_{coul}$, which places it in the subcritical regime according to our theory. However, we note that our model for the variation of $E_{cyc}$ with $L_X$ does not work well for A 0535+26, unless we choose an unreasonably large value for $E_*$ relative to the observational data. We believe this reflects the inapplicability of our model in very low-luminosity sources with $L_X \lesssim L_{coul}$. For GX 304-1, only an indication of a positive $E_{cyc}$–$L_X$ correlation, consistent with its subcritical state, can be seen, as also reported by Yamamoto et al. (2011). No pulse-to-pulse spectra are yet available for GX 304-1.

## 5. Conclusions

We have examined the hypothesis that observed bimodal variability of the CRSF energy $E_{cyc}$ with luminosity $L_X$ in accretion-powered X-ray pulsars reflects the dominant mode of accretion, as proposed by Staubert et al. (2007) and Klochkov et al. (2011). In particular, we have derived an expression for the critical luminosity $L_{crit}$ such that the dynamics in the supercritical sources is determined by the radiation pressure, and the dynamics in the subcritical sources is determined by a combination of radiation pressure and either Coulomb interactions or gas pressure. The detailed formula for $L_{crit}$ is given by Eq. (32), but essentially we find that for typical neutron star parameters, $L_{crit} \sim 1.5 \times 10^{37} B_{12}^{16/15}$ erg s$^{-1}$, where $B_{12}$ is the surface magnetic field strength in units of $10^{12}$ G.

The formula for the critical luminosity was evaluated for 5 sources, based on the maximum value for the CRSF centroid energy for each source, $E_*$, which is treated as a variable parameter in our approach. The results obtained for $E_*$ are close to the maximum observed values for the CRSF energy. The results depicted in Fig. 2 confirm that $L_X > L_{crit}$ in the group 1 sources and $L_X < L_{crit}$ in the group 2 sources. The situation is less clear for highly variable sources with luminosity $L_X$ that crosses over the line $L_X = L_{crit}$, such as V 0332+53 and 4U 0115+63. These two sources display a negative correlation between $E_{cyc}$ and $L_X$ in the supercritical regime, as expected, but the trend does not reverse as predicted by our model when $L_X < L_{crit}$. This suggests that these sources may actually always remain supercritical, despite the fact that they cross the vertical line in Fig. 3. This behavior can be accommodated within our model by slightly changing the parameters $\Lambda$ and $w$ in Eq. (55). Or, alternatively, the behavior of these sources could indicate that their mass and radius values deviate from the canonical values assumed here.

We have developed simple physical models describing the quantitative variation of $E_{cyc}$ with $L_X$ in the supercritical and subcritical sources, given by Eq. (58), with the emission height $h$ set using $h = h_s$ (Eq. (40)) for the supercritical sources (group 1),

and $h = h_c$ (Eq. (51)) for the subcritical sources (group 2). In Fig. 3 the formulas we derived for $E_{cyc}$ as a function of $L_X$ were compared with the data for the supercritical and subcritical sources. The agreement between the theoretical predictions and the data suggests that our fundamental model for the physical processes operating in these systems is essentially correct. It is important to note that our formulas for the emission heights $h_c$ and $h_s$ are not equipped to handle the trans-critical case with $L_X \sim L_{crit}$, and therefore further work is required in order to treat sources such as V 0332+53 and 4U 0115+63.

Although the observational picture is still not complete, especially for sources with highly variable luminosities, nonetheless we believe that the emerging bimodal paradigm for the variability of the CRSF energy with luminosity in XRBPs supports the hypothesis that we are seeing direct evidence for two different accretion regimes, depending on whether the luminosity is above or below the corresponding value of $L_{crit}$ for the given surface magnetic field strength $B_*$. The agreement between the theoretical predictions and the observational data is rather surprising given the level of approximation employed here. We therefore believe that these ideas can provide a useful framework for future detailed modeling of XRBPs with variable luminosities, as well as motivation for further observations.

## Appendix A: Effective velocity

The characteristic emission height in the supercritical sources treated in Sect. 3.1 is estimated by comparing the vertical transport time for the radiation with the mean escape time for the photons to diffuse out through the walls of the accretion column. This requires a determination of the "effective velocity", $v_{eff}$, which is defined as the net photon transport velocity in the vertical direction, taking into account the competing effects of advection and diffusion. The former process tends to drag photons downward toward the stellar surface, and the latter process tends to transport photons in the opposite direction, upward through the accretion column. The relationship between the effective velocity $v_{eff}$ and the flow velocity $v$ is expressed by the dimensionless parameter $\xi$, defined by

$$\xi \equiv \frac{v_{eff}}{v}. \tag{A.1}$$

In "trapped" regions of the flow, vertical advection and diffusion are nearly balanced, and consequently $v_{eff} \ll v$ and $\xi \ll 1$ (Becker 1998). Trapping tends to occur in the lower, hydrostatic region of the accretion column in the supercritical sources. In this situation, the photons tend to "hover" in a small altitude range until they escape through the walls of the accretion column. Hence this effect reduces the size of the emission region in the supercritical sources treated in Sect. 3.1.

The gas enters the top of the accretion column moving supersonically, but it must come to rest at the stellar surface, and therefore the flow passes through a sonic point somewhere in the column. The sonic point is located in the middle of the radiation-dominated shock, where the flow begins to decelerate from the incident free-fall velocity $v_{ff}$ (Eq. (3)). Hence the sonic point represents the top of the hydrostatic sinking region, where the radiation tends to escape, and we will therefore estimate the value of $\xi$ using conditions there.

In order to determine the flow velocity at the sonic point, it is useful to consider the conservation of mass and momentum in the hydrostatic region of the column. We have

$$J \equiv \rho v = \text{const.}, \qquad I \equiv P_r + \rho v^2 = \text{const.}, \tag{A.2}$$

where $J$ and $I$ denote the fluxes of mass and momentum, respectively. These two fluxes are conserved in the roughly cylindrical, hydrostatic portion of the accretion column.

We can use Eqs. (A.2) to obtain a relationship between the flow velocity $v$ and the radiation Mach number, $\mathcal{M}$, defined by

$$\mathcal{M} \equiv \frac{v}{a}, \tag{A.3}$$

where $a$ denotes the radiation sound speed, given by

$$a = \sqrt{\frac{\gamma P_r}{\rho}}, \qquad \gamma = \frac{4}{3}. \tag{A.4}$$

The result obtained is

$$\frac{I}{J} = v\left(1 + \frac{1}{\gamma \mathcal{M}^2}\right) = \frac{7}{4} v_c, \tag{A.5}$$

where $v_c$ denotes the flow velocity at the radiation sonic point, where $\mathcal{M} = 1$.

The value of $\xi$ can be estimated by examining the vertical propagating of the photons in a radiation-dominated accretion column described by the exact dynamical solution obtained by Basko & Sunyaev (1976) and Becker (1998). This solution assumes a cylindrical geometry in the hydrostatic lower region of the accretion column. The total radiation energy flux in the vertical direction is given by

$$E_r = 4P_r v + \frac{c}{n_e \sigma_\parallel} \frac{dP_r}{dz}, \tag{A.6}$$

where $P_r$ is the radiation pressure, and the first and second terms on the right-hand side represent advection and diffusion, respectively. We define $v_{eff}$ by writing

$$4P_r v_{eff} \equiv E_r, \tag{A.7}$$

so that $v_{eff}$ represents the "effective" bulk velocity that would yield the correct energy flux.

By combining Eqs. (A.6) and (A.7), we obtain

$$v_{eff} = v + \frac{c}{4 n_e \sigma_\parallel P_r} \frac{dP_r}{dz}, \tag{A.8}$$

or, equivalently,

$$\xi = \frac{v_{eff}}{v} = 1 + \frac{c m_p}{4 \sigma_\parallel J P_r} \frac{dP_r}{dz}, \tag{A.9}$$

where we have eliminated the electron number density using the relation $J = n_e m_p v$. The pressure $P_r$ can be expressed in terms of the flow velocity $v$ by using Eqs. (A.2) to write

$$P_r(z) = I - J v(z). \tag{A.10}$$

Using this relation to substitute for the pressure $P_r$ in Eq. (A.9) yields

$$\xi = 1 - \frac{c m_p}{4 \sigma_\parallel (I - Jv)} \frac{dv}{dz}. \tag{A.11}$$

The exact solution for the flow velocity profile $v(z)$ in a cylindrical accretion column is given by (Basko & Sunyaev 1976; Becker 1998)

$$v(z) = v_c \left( \frac{14}{7 + 2\epsilon_c} \right) \left[ 1 - \left( \frac{14}{7 - 2\epsilon_c} \right)^{-z/z_{st}} \right], \tag{A.12}$$

where

$$\epsilon_c = \frac{3 m_p^2 c^2}{8 r_0^2 J^2 \sigma_\perp \sigma_\parallel} \tag{A.13}$$

denotes the value of the dimensionless total energy flux $(E_r + \rho v^3/2)/(Jv_c^2)$ at the sonic point, and

$$z_{st} = r_0 \left( \frac{8\epsilon_c \sigma_\perp}{3\sigma_\parallel} \right)^{1/2} \left( \frac{2}{7 + 2\epsilon_c} \right) \ln \left( \frac{14}{7 - 2\epsilon_c} \right) \tag{A.14}$$

is the altitude of the sonic point above the stellar surface.

Combining Eqs. (A.11)–(A.14), we obtain after some algebra

$$\xi = 1 - \left( 1 - \frac{4v}{7v_c} \right)^{-1} \left[ 1 - \left( \frac{7 + 2\epsilon_c}{14} \right) \frac{v}{v_c} \right]. \tag{A.15}$$

In particular, at the sonic point ($z = z_{st}$), we have $v = v_c$, and therefore our result for $\xi$ reduces to

$$\xi \bigg|_{z=z_{st}} = \frac{2\epsilon_c - 1}{6}. \tag{A.16}$$

The dimensionless energy flux is related to the incident Mach number of the flow, $\mathcal{M}_\infty$, via (Becker 1998)

$$\epsilon_c = \frac{1}{2} + \frac{3}{\mathcal{M}_\infty^2}. \tag{A.17}$$

Combining Eqs. (A.16) and (A.17) yields for the value of $\xi$ at the radiation sonic point

$$\xi \bigg|_{z=z_{st}} = \frac{1}{\mathcal{M}_\infty^2}. \tag{A.18}$$

We use this relation in Sect. 3.1, where we estimate the height of the emission region in the supercritical sources.

## Appendix B: Coulomb stopping depth

In the subcritical sources treated in Sect. 3.2, radiation pressure is insufficient to decelerate the flow to rest at the stellar surface. In this regime, the final deceleration likely occurs via Coulomb interactions between the infalling plasma and the mound of dense gas that has built up just above the stellar surface. We can estimate the vertical extent of this region, and therefore obtain an approximation of the characteristic emission altitude in the subcritical sources, by computing the Thomson optical depth, $\tau$, measured from the stellar surface, and setting it equal to the value required to stop the flow, denoted by $\tau_*$. Nelson et al. (1993) carried out a detailed calculation of $\tau_*$, and the final result is presented in their equation Eq. (3.34). In this section we summarize the derivation.

In a magnetized pulsar accretion column, the Coulomb stopping of the gas occurs via coupling between infalling protons and stationary electrons in the mound. The corresponding rate of change of the proton kinetic energy,

$$E_p = \frac{1}{2} m_p v^2, \tag{B.1}$$

is given by Eq. (3.31) from Nelson et al. (1993), which states that

$$\frac{dE_p}{dz} = \frac{4\pi n_e e^4}{m_e v^2} \ln \Lambda_c, \tag{B.2}$$

where $\ln \Lambda_c$ is the Coulomb logarithm and $v$ is the velocity of the protons. Note that the right-hand side of Eq. (B.2) is positive in our sign convention since the value of $E_p$ decreases with decreasing altitude.

Using Eq. (B.1) to substitute for $v$ yields the equivalent form

$$\frac{dE_p^2}{dz} = \frac{m_p}{m_e} 4\pi n_e e^4 \ln \Lambda_c. \tag{B.3}$$

We can transform from the altitude $dz$ to the Thomson depth $d\tau$ using

$$d\tau = n_e \sigma_T dz, \tag{B.4}$$

which yields

$$\frac{dE_p^2}{d\tau} = \frac{m_p}{m_e} \frac{4\pi e^4}{\sigma_T} \ln \Lambda_c. \tag{B.5}$$

Treating the Coulomb logarithm as a constant and integrating with respect to $\tau$, we obtain the solution

$$E_p(\tau) = E_0 \left( 1 - \frac{\tau}{\tau_*} \right)^{1/2}, \tag{B.6}$$

where the stopping depth, $\tau_*$, is defined by

$$\tau_* = \frac{m_e}{m_p} \frac{\sigma_T E_0^2}{4\pi e^4 \ln \Lambda_c}, \tag{B.7}$$

and the incident proton kinetic energy, $E_0$, is equal to the free-fall value,

$$E_0 = \frac{1}{2} m_p v_{ff}^2. \tag{B.8}$$

Substituting for the Thomson cross section, $\sigma_T$, in Eq. (B.7) using

$$\sigma_T = \frac{8\pi e^4}{3 c^4 m_e^2}, \tag{B.9}$$

yields the equivalent result

$$\tau_* = \frac{1}{6 \ln \Lambda_c} \frac{m_p}{m_e} \frac{v_{ff}^4}{c^4}. \tag{B.10}$$

In magnetized pulsar accretion columns, with discrete Landau levels, the Coulomb logarithm is given by Eq. (3.32) from Nelson et al. (1993), which states that

$$\ln \Lambda_c = \ln (2 n_{max}), \tag{B.11}$$

where the maximum excited Landau level, $n_{max}$, is given by

$$n_{max} = \frac{m_e v_{ff}^2}{2 E_{cyc}}. \tag{B.12}$$

Combining Eqs. (B.10) and (B.11) and substituting for $v_{ff}$ using Eq. (3) gives the final result,

$$\tau_* = 51.4 \left(\frac{M_*}{1.4 \, M_\odot}\right)^2 \left(\frac{R_*}{10 \text{ km}}\right)^{-2} \frac{1}{\ln{(2 n_{max})}}, \tag{B.13}$$

in agreement with Eq. (3.34) from Nelson et al. (1993). For typical X-ray pulsar parameters, we obtain $\tau_* \sim 20$, and this is the value utilized in computing the characteristic emission height in the subcritical sources in Sect. 3.2.

## References

Araya-Góchez, R. A., & Harding, A. K. 2000, ApJ, 544, 1067
Arons, J., Klein, R. I., & Lea, S. M. 1987, ApJ, 312, 666
Basko, M. M., & Sunyaev, R. A. 1976, MNRAS, 175, 395
Becker, P. A. 1998, ApJ, 498, 790
Becker, P. A., & Wolff, M. T. 2007, ApJ, 654, 435
Blum, S., & Kraus, U. 2000, ApJ, 529, 968
Burnard, D., Arons, J., & Klein, R. 1991, ApJ, 367, 575
Caballero, I., Kretschmar, P., Santangelo, A., et al. 2007, A&A, 465, L21
Davidson, K. 1973, Nature Phys. Sci., 246, 1
Ferrigno, C., Becker, P. A., Segreto, A., Mineo, T., & Santangelo, A. 2009, A&A, 498, 825
Frank, J., King, A. R., & Raine, D. J. 2002, Accretion Power in Astrophysics (Cambridge: Cambridge Univ. Press)
Giacconi, R., Gursky, H., Kellogg, E., et al. 1971, ApJ, 167, L67
Harding, A. K., Kirk, J. G., Galloway, D. J., Meszaros, P., et al. 1984, ApJ, 278, 369
Imamura, J. N., Durisen, R. H., Lamb, D. Q., & Weast, G. J. 1987, ApJ, 313, 298
Isenberg, M., Lamb, D. Q., & Wang, J. C. 1998, ApJ, 493, 154
Klochkov, D., Staubert, R., Santangelo, A., et al. 2011, A&A, 532, A126
Mihara, T., Makishima, K., & Nagase, F. 2004, ApJ, 610, 390
Mowlavi, N., Kreykenbohm, I., Shaw, S. E., et al. 2006, A&A, 451, 187
Müller, S., Obst, M., Kreykenbohm, I., et al. 2011, The X-ray Universe 2011, Presentations of the Conference held in Berlin, Germany
Negueruela, I., & Okazaki, A. T. 2001, A&A, 369, 108
Negueruela, I., Roche, P., Fabregat, J., & Coe, M. J. 1999, MNRAS, 307, 695
Nelson, R., Salpeter, E., & Wassermann, I. 1993, ApJ, 418, 874
Lamb, F. K., Pethick, C. J., & Pines, D. 1973, ApJ, 184, 271
Langer, S. H., & Rappaport, S. 1982, ApJ, 257, 733
Parkes, G. E., Murdin, P. G., & Mason, K. O. 1980, MNRAS, 190, 537
Reynolds, A. P., Quaintrell, H., Still, M. D., et al. 1997, MNRAS, 288, 43
Shakura, N. I., & Sunyaev, R. A. 1973, A&A, 24, 337
Staubert, R., Shakura, N. I., Postnov, K., et al. 2007, A&A, 465, L25
Steele, I. A., Negueruela, I., Coe, M. J., & Roche, P. 1998, MNRAS, 297, L5
Tananbaum, H., Gursky, H., Kellogg, E. M., et al. 1972, ApJ, 174, L143
Trümper, J., Pietsch, W., Reppin, C., et al. 1978, ApJ, 219, L105
Tsygankov, S. S., Lutovinov, A. A., Churazov, E. M., & Sunyaev, R. A. 2007, Astron. Lett., 33, 368
Tsygankov, S. S., Lutovinov, A. A., & Serber, A. V. 2010, MNRAS, 401, 1628
Vasco, D., Klochkov, D., & Staubert, R. 2011, A&A, 532, A99
Wang, Y.-M., & Frank, J. 1981, A&A, 93, 25
Yamamoto, T., Sugizaki, M., Mihara, T., et al. 2011, PASJ, 63, 751

# Appendix G

# Long-term change in the cyclotron line energy in Hercules X-1

**Astronomy & Astrophysics**

# Long-term change in the cyclotron line energy in Hercules X-1

R. Staubert[1], D. Klochkov[1], J. Wilms[2], K. Postnov[3], N. I. Shakura[3], R. E. Rothschild[4], F. Fürst[5], and F. A. Harrison[5]

[1] Institut für Astronomie und Astrophysik, Universität Tübingen, Sand 1, 72076 Tübingen, Germany
e-mail: staubert@astro.uni-tuebingen.de
[2] Dr. Remeis Sternwarte, Astronomisches Institut der Universität Erlangen-Nürnberg, Sternwartstr. 7, 96049 Bamberg, Germany
[3] Moscow M.V. Lomonosov State University, Sternberg Astronomical Institute, 119992 Moscow, Russia
[4] Center for Astrophysics and Space Sciences, University of California at San Diego, La Jolla, CA 92093-0424, USA
[5] Cahill Center for Astronomy and Astrophysics, California Institute of Technology, Pasadena, CA 91125, USA

## ABSTRACT

*Aims.* We investigate the long-term evolution of the cyclotron resonance scattering feature (CRSF) in the spectrum of the binary X-ray pulsar Her X-1 and present evidence of a true long-term decrease in the centroid energy $E_{cyc}$ of the cyclotron line in the pulse phase averaged spectra from 1996 to 2012.

*Methods.* Our results are based on repeated observations of Her X-1 by those X-ray observatories capable of measuring clearly beyond the cyclotron line energy of ~40 keV; these are RXTE, INTEGRAL, *Suzaku*, and NuSTAR. We consider results based on our own successful observing proposals as well as results from the literature.

*Results.* The historical evolution of the pulse phase averaged CRSF centroid energy $E_{cyc}$ since its discovery in 1976 is characterized by an initial value around 35 keV, an abrupt jump upwards to beyond ~40 keV between 1990 and 1994, and an apparent decay thereafter. Much of this decay, however, was found to be due to an artifact, namely a correlation between $E_{cyc}$ and the X-ray luminosity $L_x$ discovered in 2007. In observations after 2006, however, we now find a statistically significant true decrease in the cyclotron line energy. At the same time, the dependence of $E_{cyc}$ on X-ray luminosity is still valid with an increase of ~5% in energy for a factor of two increase in luminosity. We also report on the first evidence of a weak dependence of $E_{cyc}$ on phase of the 35 d precessional period, which manifests itself not only in the modulation of the X-ray flux, but also in the systematic variation in the shape of the 1.24 s pulse profile. One of our motivations for repeatedly observing Her X-1, namely the suspicion that the cyclotron line energy may be gradually decreasing after its strong upward jump in the early 1990s, is finally confirmed. A decrease in $E_{cyc}$ by 4.2 keV over the 16 years from 1996 to 2012 can either be modeled by a linear decay, or by a slow decay until 2006 followed by a more abrupt decrease thereafter.

*Conclusions.* The observed timescale for the decrease in $E_{cyc}$ of a few decades is too short for a decay of the global magnetic field. We speculate that the physical reason could be connected to a geometric displacement of the cyclotron resonant scattering region in the polar field or to a true physical change in the magnetic field configuration at the polar cap by the continued accretion. In the second scenario, the upward jump in $E_{cyc}$ observed around 1991 may have been due to a relatively fast event in which the polar magnetic field rearranged itself after releasing part of the accumulated material to larger areas of the neutron star surface.

**Key words.** radiation mechanisms: non-thermal – binaries: eclipsing – pulsars: individual: Her X-1 – accretion, accretion disks – magnetic fields – X-rays: binaries

## 1. Introduction

The accreting binary X-ray pulsar Her X-1 shows strong variability on several different timescales: the 1.24 s spin period of the neutron star, the 1.7-day binary period, the 35-day period, and the 1.65-day period of the pre-eclipse dips. The 35-day ON-OFF modulation can be understood as due to the precession of a warped accretion disk. Because of the high inclination ($i > 80°$) of the binary we see the disk nearly edge-on. The precessing warped disk therefore covers the central X-ray source during a substantial portion of the 35-day period. Furthermore, a hot X-ray heated accretion disk corona reduces the X-ray signal (energy independently) by Compton scattering whenever it intercepts our line of sight to the neutron star. As a result the X-ray source is covered twice during a 35-day cycle. Another 35 d modulation is present in the systematic variation of the shape of the 1.24 s pulse profile. It has been suggested (Trümper et al. 1986) that the reason for this is free precession of the neutron star, leading to a systematic change in our viewing angle to the X-ray emitting regions. By comparing the variation in flux (the

turn-ons) and the variations in pulse shape, Staubert et al. (2009) had concluded, that if precession of the NS exists a strong interaction between the NS and the accretion disk is required, allowing a synchronization of the two clocks to nearly the same frequency through a closed loop physical feed-back (for which there is independent evidence). Further analysis of the variations in pulse profiles (Staubert et al. 2013), however, has shown that the histories of the turn-ons and of the variations in pulse shape are identical, with correlated variations even on short timescales (~300 d).

It is believed that the X-ray spectrum emerges from the hot regions around the magnetic poles where the accreted material is channeled by the ~$10^{12}$ G magnetic field down to the surface of the NS. The height of the accretion mound is thought to be a few hundred meters. If the magnetic and spin axes of the neutron star are not aligned, the view of a terrestrial observer is modulated at the rotation frequency of the star.

The X-ray spectrum of Her X-1 is characterized by a power law continuum with exponential cut-off and an apparent

line-like feature. The continuum is believed to be due to thermal bremsstrahlung radiation from the $\sim 10^8$ K hot plasma modified by Comptonization (Becker & Wolff 2007; Becker et al. 2012). The line feature was discovered in 1976 in a balloon observation (Trümper et al. 1978). This feature is now generally accepted as an absorption feature around 40 keV due to resonant scattering of photons off electrons on quantized energy levels (Landau levels) in the Terragauss magnetic field at the polar cap of the neutron star. The feature is therefore often referred to as a cyclotron resonant scattering feature (CRSF). The energy spacing between the Landau levels is given by $E_{cyc} = \hbar e B / m_e c = 11.6 \, \mathrm{keV} \, B_{12}$, where $B_{12} = B/10^{12}$ G, providing a direct method of measuring the magnetic field strength at the site of the emission of the X-ray spectrum. The observed line energy is subject to gravitational redshift $z$ at the location where the line is formed, such that the magnetic field may be estimated by $B_{12} = (1 + z) \, E_{obs}/11.6 \, \mathrm{keV}$, with $E_{obs}$ being the observed cyclotron line energy. The discovery of the cyclotron feature in the spectrum of Her X-1 provided the first ever direct measurement of the magnetic field strength of a neutron star, in the sense that no other model assumptions are needed. Originally considered an exception, cyclotron features are now known to be rather common in accreting X-ray pulsars, with $\sim 20$ binary pulsars now being confirmed cyclotron line sources, with several objects showing multiple lines (up to four harmonics in 4U 0115+63). Reviews are given by e.g., Coburn et al. (2002), Staubert (2003), Heindl et al. (2004), Terada et al. (2007), Wilms (2012), Caballero & Wilms (2012). Theoretical calculations of cyclotron line spectra have been performed either analytically (Ventura et al. 1979; Nagel 1981; Nishimura 2008) or making use of Monte Carlo techniques (Araya & Harding 1999; Araya-Góchez & Harding 2000; Schönherr et al. 2007).

Here we present new results (from the last five years) on the energy of the cyclotron resonance scattering feature $E_{cyc}$ in the pulse averaged X-ray spectrum of Her X-1, combined with the historical long-term evolution. We present the first statistically significant evidence of a true long-term decrease in $E_{cyc}$ and first evidence of a weak dependence of $E_{cyc}$ on phase of the 35 d cycle. We speculate about the physics behind both the long-term decrease and the previously observed fast upward jump as being connected to changes in the configuration of the magnetic field structure at the responsible polar cap of the accreting neutron star. A preliminary report was published earlier by Staubert (2013).

## 2. Data base and method of analysis

Her X-1 is probably the best observed accreting binary X-ray pulsar. Its X-ray spectrum, including the CRSF, has been measured by many instruments since the discovery of the CRSF in 1976 (Trümper et al. 1978). The data base behind previously reported results are summarized in corresponding tables of the following publications: Gruber et al. (2001), Coburn et al. (2002), Staubert et al. (2007, 2009, 2013), Klochkov et al. (2008a, 2011), Vasco et al. (2011, 2013). Details about more recent observations (proposed by our group during the last five years) by RXTE, INTEGRAL, *Suzaku*, and NuSTAR are given in Tables 1 and 2. Of particular importance is the observation by NuSTAR in September 2012 which provided the most accurate value for the CRSF energy measured to date (Fürst et al. 2013). For the investigation of the long-term evolution of the cyclotron line energy, *Main-On* state observations at 35-day-phases <0.20 were used, in order to avoid interference with a dependence on 35 d phase (see Sect. 5). The spectral analysis was performed using the standard software appropriate for

**Table 1.** Details of recent observations of Her X-1 by INTEGRAL, RXTE, *Suzaku*, and NuSTAR.

| Observatory | Date of observation | Center MJD | Obs ID | Expos. [ks] |
|---|---|---|---|---|
| INTEGRAL | 2007 Sep. 03–08 | 54 348.0 | Rev. 597/598 | 414.72 |
| RXTE | 2009 Feb. 04–05 | 54 866.6 | P 80015 | 22.19 |
| INTEGRAL | 2010 Jul. 10–18 | 55 390.0 | Rev. 945–947 | 621.03 |
| *Suzaku* | 2010 Sep. 22 | 55 462.0 | 405058010/20 | 41.66 |
| *Suzaku* | 2010 Sep. 29 | 55 468.0 | 405058030/40 | 45.66 |
| INTEGRAL | 2011 Jun. 25–27 | 55 738.3 | Rev. 1062 | 95.9 |
| INTEGRAL | 2011 Jul. 03–05 | 55 744.5 | Rev. 1069 | 107.8 |
| INTEGRAL | 2012 Apr. 1–4 | 56 019.5 | Rev. 1156 | 42.6 |
| *Suzaku* | 2012 Sep. 19–25 | 56 192.2 | 4070510-10, 20, 30 | $\sim$70 |
| NuSTAR | 2012 Sep. 19–25 | 56 192.2 | 3000200600-2, 3, 5, 7 | 72.9 |

the respective satellites (see the publications cited above), with the addition of non-standard corrections based on our deeper analysis of the calibration of Imager on Board the INTEGRAL Satellite (IBIS, Ubertini et al. 2003), and the use of RECORN models (Rothschild et al. 2011) for RXTE. For the spectral model we have chosen the `highecut`[1] model which is based on a power law continuum with exponential cut-off, and the CRSF is modeled by a multiplicative absorption line with a Gaussian optical depth profile. Details of the fitting procedure can be found in the papers cited above.

## 3. Variation of the cyclotron line energy $E_{cyc}$

Variability in the energy of the CRSF in Her X-1 is found with respect to the following variables:

- Variation with X-ray luminosity (both on long and on short timescales).
- Variation with phase of the 1.24 s pulsation.
- Variation with phase of the 35 d precessional period.
- Variation with time, that is a true long-term decay.

The dependence on pulse phase, which is described in detail by Vasco et al. (2013), will only be discussed here to the extent necessary to understand the connection to the 35 d phase dependence.

## 4. Variation of $E_{cyc}$ with luminosity

For Her X-1, the dependence of the centroid energy of the phase averaged cyclotron line on X-ray flux was discovered by Staubert et al. (2007) while analyzing a uniform set of observations from RXTE. The original aim of the analysis at that time had been to investigate a possible decrease in the phase averaged cyclotron line energy with time during the first decade of RXTE observations. Instead, the dependence on X-ray flux was discovered and shown that the apparent decrease in the measured values of the line energy (see Sect. 6) was largely an artifact due to this flux dependence. The correlation was found to be positive, that is the cyclotron line energy $E_{cyc}$ increases with increasing X-ray luminosity $L_x$.

Figure 1 reproduces the original correlation graph of Staubert et al. (2007) with new data points added (see Table 2). The first three new data points (INTEGRAL 05 and

---

[1] http://heasarc.nasa.gov/xanadu/xspec/manual/XSmodelHighecut.html

**Table 2.** Recent cyclotron line energy measurements during *Main-Ons* of Her X-1 by INTEGRAL, RXTE, *Suzaku*, and NuSTAR.

| Satellite | Observation year/month | 35 d cycle | Center [MJD] | 35 d phase | observed $E_{cyc}$ [keV] | max. Flux [ASM cts/s][1] | Flux normalized $E_{cyc}$ [keV][3] | References |
|---|---|---|---|---|---|---|---|---|
| RXTE | 2009 Feb. | 388 | 54 866.60 | 0.11 | 37.76 ± 0.70 | 5.94 ± 0.50 | 38.14 ± 0.71 | this work |
| *Suzaku* | 2005 Oct. | 353 | 53 648.00 | 0.11 | 38.70 ± 1.00 | 5.03 ± 0.20 | 39.47 ± 1.02 | Enoto et al. (2008)[2] |
| | 2006 Mar. | 358 | 53 824.20 | 0.19 | 38.20 ± 1.00 | 4.70 ± 0.35 | 39.12 ± 1.02 | Enoto et al. (2008)[2] |
| | 2010 Sep. | 405 | 55 462.00 | 0.07 | 37.83 ± 0.22 | 7.56 ± 0.23 | 37.50 ± 0.22 | this work |
| | 2010 Sep. | 405 | 55 468.00 | 0.25 | 36.50 ± 1.05 | 7.56 ± 0.23 | 35.17 ± 1.04 | this work |
| | 2012 Sep. | 426 | 56 192.23 | 0.09 | 37.03 ± 0.50 | 6.60 ± 0.50 | 37.12 ± 0.50 | this work |
| INTEGRAL | 2010 July | 403 | 55 390.00 | 0.05 | 37.50 ± 0.30 | 6.67 ± 0.20 | 37.56 ± 0.30 | this work |
| | 2011 June | 413 | 55 738.26 | 0.08 | 37.34 ± 0.28 | 6.03 ± 0.20 | 37.68 ± 0.28 | this work |
| | 2007 July/Aug. | 373 | 54 348.00 | 0.25 | 36.50 ± 0.60 | 4.50 ± 0.48 | 37.51 ± 0.62 | this work |
| | 2011 July | 413 | 55 744.50 | 0.25 | 38.53 ± 0.78 | 7.00 ± 0.20 | 38.44 ± 0.78 | this work |
| | 2012 Aug. | 421 | 56 019.50 | 0.09 | 38.97 ± 0.38 | 5.03 ± 0.20 | 39.74 ± 0.39 | this work |
| NuSTAR | 2012 Sep. | 426 | 56 192.20 | 0.09 | 37.33 ± 0.17 | 6.60 ± 0.20 | 37.42 ± 0.17 | Fürst et al. (2013) |

**Notes.** Uncertainties are at the 68% level. 35 d cycle numbering and 35 d phase is according to Staubert et al. (1983, 2013). [1] The maximum *Main-On* flux was determined using the monitoring data of RXTE/ASM and *Swift*/BAT (since 2012 from BAT only); the conversion is: (2–10 keV ASM-cts/s) = 89 × (15–50 keV BAT-cts cm$^{-2}$ s$^{-1}$). [2] The two *Suzaku* data points from 2005 and 2006 are from Enoto et al. (2008), adjusted to describing the cyclotron line by a Gaussian line profile (see text). [3] These values refer to this work: normalization to an ASM flux of 6.8 (ASM-cts/s) using the $E_{cyc}$/flux relationship (slope of 0.44 keV/ASM-cts/s) of the two-variable fit to the 1996–2012 data set (see Table 4).
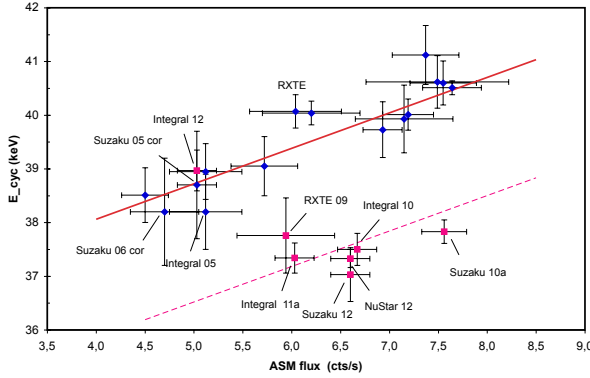


**Fig. 1.** Positive correlation between the cyclotron line energy and the maximum X-ray flux of the corresponding 35 day cycle as measured by RXTE/ASM (see Fig. 2 of Staubert et al. 2007) with eight added points: INTEGRAL 2005 (Klochkov et al. 2008a), *Suzaku* of 2005 and 2006 (Enoto et al. 2008), RXTE 2009, INTEGRAL 2010, *Suzaku* 2010 and 2012, and NuSTAR 2012. The *Suzaku* points of 2005/2006 have been corrected upward by 2.8 keV, to account for the difference arising because the Lorentzian profile was used in the analysis by Enoto et al. (2008), while for all others the Gaussian profile was used. The blue rhombs are values observed until 2006, the red dots are from after 2006. The solid red line is a linear fit to data until 2006 with the original slope of 0.66 keV/(ASM cts/s), as found by Staubert et al. (2007). The dotted red line is the best fit to the data after 2006 with the slope fixed to the same value.

*Suzaku* 05/06) fit very well into the previous data set (and do not change the formal correlation – see the solid red line), but most of the values from 2006–2012 are significantly lower. As we will show below, it is these data which clearly establish a decrease in the cyclotron line energy with time. After 2006 the flux dependence is less obvious. However, the data points (except the one from INTEGRAL 2012) are consistent with the originally measured slope (0.66 keV/ASM-cts/s) with generally lower $E_{cyc}$ values. The dotted red line is a fit through the data after 2006 with the same slope as the solid red line. We note that *flux* refers to the maximum *Main-On* flux as determined using the RXTE/ASM and/or the *Swift*/BAT monitoring data (since 2012

from BAT only); the conversion is: (2–10 keV ASM-cts/s) = 89 × (15–50 keV BAT-cts cm$^{-2}$ s$^{-1}$). The INTEGRAL 2012 point does clearly not follow this behavior, as will be more obvious below. We have invested a considerable effort to check the calibration of the INTEGRAL/ISGRI detector (INTEGRAL Soft Gamma-Ray Imager, Lebrun et al. 2003) for the time of observation and the data analysis procedure. The ISGRI response was closely examined by us for each of our Her X-1 observations. When necessary, the ARFs (Auxilliary Response Files) were checked (using the nearest Crab observations) and the energy scale was individually controlled by making use of observed instrumental background lines with known energy. Finally, spectra were generated using data from SPI (Spectrometer onboard INTEGRAL, Vedrenne et al. 2003): the resulting $E_{cyc}$ values were always consistent with those of the ISGRI analysis. Since we have found no errors, we keep this point in our data base, but will exclude it from some of the analysis discussed below.

## 5. Variation of $E_{cyc}$ with precessional phase

In order to investigate whether the cyclotron line energy has any dependence on phase of the 35 d precession, we had successfully scheduled a few *Main-On* observations at late 35 d phases. In addition to the full coverage of the *Main-On* of cycle No. 232 (a singular event!), we so far have four more measurements: from INTEGRAL in July/August 2007 and July 2011, as well as from *Suzaku* in September 2011 (all at 35 d phases 0.25, see Table 2) and from INTEGRAL in July 2005 at phase 0.24 ($E_{cyc}$ = (37.3 ± 1.2) keV and (5.12 ± 0.37) ASM-cts/s). As we will show below, the cyclotron line energy changes with time. So, for a comparison of values measured at different times, they must be normalized to a common reference time. We are therefore making use of the results presented in Sect. 6 and compare $E_{cyc}$ values which are normalized to the reference time of MJD 53500 (using the slope of fit 4 of Table 4): (37.11 ± 0.61) keV, (40.15 ± 0.81) keV, (36.92 ± 1.09) keV, and (37.36 ± 1.20) keV, respectively. Three out of these four values are indeed quite low in comparison to all other time normalized values, and gives an indication that $E_{cyc}$ may indeed decrease at late 35 d phases. However, because of the lower fluxes at late 35 d phases, the uncertainties are fairly large for all of these measurements.
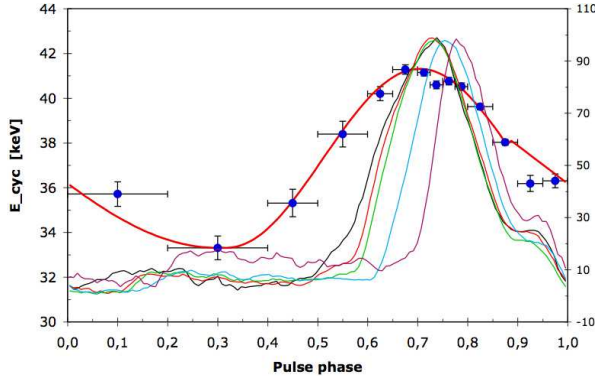
**Fig. 2.** Mean dependence of cyclotron line energy on pulse phase for the *Main-On* of 35 d cycle 323, as observed by RXTE/PCA in 2002 November. The solid red line represents a best fit function (a combination of two cosine components). Normalized pulse profiles of the 30–45 keV range are shown for five different 35 d phases: 0.048 (black), 0.116 (red), 0.166 (green), 0.21 (blue) and 0.24 (purple). The main pulse is progressively moving to the right. The right hand scale is normalized flux (0–100) for the pulse profiles.
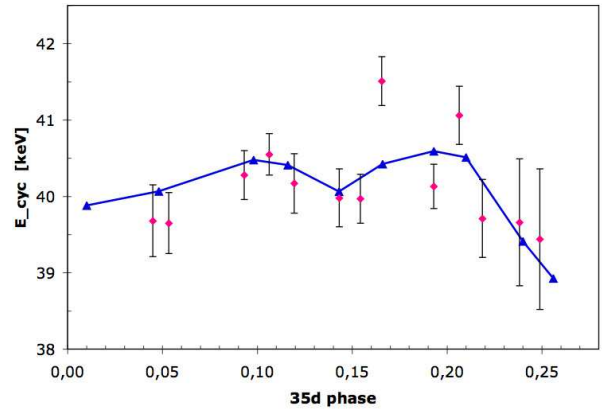


**Fig. 3.** Centroid pulse phase averaged cyclotron line energies at different 35 d phases of *Main-On* cycle 323. The data points with uncertainties are direct measurements for ten small integration intervals. The blue triangles connected by the solid blue line are values which are calculated by folding observed pulse profiles in the 30–45 keV range with template ($E_{cyc}$ vs. pulse phase)-profiles for the same 35 d phases (see text for a detailed description).

A more indirect, but perhaps more reliable method is the following: There are two well established observational facts with regard to pulse profiles and cyclotron line energies in Her X-1, both demonstrated in Fig. 2:

1. $E_{cyc}$ varies strongly with pulse phase (by up to ~25%) (Voges et al. 1982; Soong et al. 1990; Vasco et al. 2013). The shape of the ($E_{cyc}$ vs. pulse phase)-profile, is not dependent on 35 d phase (Vasco et al. 2013).
2. The main peak of the pulse profile moves to later pulse phases with increasing 35 d phase (Staubert et al. 2009). This is also true for the 30–45 keV profiles – the energy range which includes the CRSF (these profiles are shown in Fig. 2).

The combination of these two observational facts inevitably leads to a modulation of $E_{cyc}$ with 35 d phase: with progressing 35 d phase, more and more photons are found at later pulse phases (in the main peak of the pulse) where the cyclotron line energy is decreasing. This means that the phase averaged cyclotron line energy must decrease with progressing 35 d phase (the above mentioned effect was first considered by Klochkov et al. 2008b). In order to quantitatively test this, we have performed a formal folding of 30–45 keV pulse profiles (for 10 different 35 d phases) with template ($E_{cyc}$ vs. pulse phase) profiles for these 35 d phases. The template profiles were constructed by inter- and extrapolation of the four individual profiles at different 35 d phases as given in Figs. 3 and 4 of Vasco et al. (2013) (taking into account that both the maximum value and the peak-to-peak amplitude are slightly 35 d phase dependent). By folding the pulse profile with the corresponding $E_{cyc}$ profile, the expected pulse phase averaged $E_{cyc}$ value can be calculated.

In Fig. 3 these calculated values are shown as blue triangles (connected by the solid blue line): a slow increase up to phase ~0.19 is followed by a somewhat sharper decay. For comparison, we show the directly measured phase averaged $E_{cyc}$ values (data points with uncertainties) for 13 small integration intervals covering the *Main-On* of cycle 323 (MJD 52 599/Nov 2002). The directly measured values have relatively large uncertainties, but are overall consistent with the calculated modulation, and also with regard to the mean absolute value.

## 6. Variation of $E_{cyc}$ with time – long-term variation

In Fig. 4 (an update of Fig. 1 of Staubert et al. 2007) we display observed values of the pulse phase averaged centroid cyclotron line energy as a function of time, covering the complete history of observations since the discovery of the line in 1976. We combine historical data, as taken from the compilation by Gruber et al. (2001, their Tables 2 and 3) for the time before the RXTE era, published values from observations with RXTE and INTEGRAL (Klochkov et al. 2006; Staubert et al. 2007; Klochkov et al. 2008a) and with *Suzaku* (Enoto et al. 2008), as well as recent values as given in Table 2 (see also Staubert 2013; Fürst et al. 2013). For the analysis of the long-term variation of $E_{cyc}$ we exclude values with 35 d phases >0.20 in order to avoid contamination due to a possible third variable, the 35 d phase (a dependence, if any, is very weak for small phases; see Fig. 3).

Two features are apparent from Fig. 4: firstly, we confirm the apparent difference in the mean cyclotron line energy before and after 1991, first pointed out by Gruber et al. (2001). Taking the measured values of $E_{cyc}$ and their stated uncertainties at face value, the mean cyclotron line energies $\langle E_c \rangle$ from all measurements before 1991 is 34.9 ± 0.3 keV, the corresponding value for all measurements between 1991 and 2006 is 40.3 ± 0.1 keV (40.2 ± 0.1 keV for RXTE results only, showing that the very high value measured by *BATSE* is not decisive). However, a comparison of measurements from different instruments is difficult because of systematic uncertainties due to calibration and analysis techniques. Nevertheless, we believe that the large difference of ~5 keV between the mean values and the good internal consistency within the two groups (5 different instruments before 1991 and four after 1991) most likely indicate real physics.

As already mentioned in Sect. 4, the first observations with RXTE in 1996 and 1997 showed lower $E_{cyc}$ values than those found from *CGRO*/BATSE and *Beppo*/SAX, leading to the idea of a possible decay with time. This idea had then served successfully as an important argument to ask for more observations of Her X-1. In a series of RXTE observations until 2005 the apparent decrease seemed to continue until this date. At this time we were determined to publish a paper claiming evidence of a decay of the phase averaged cyclotron line
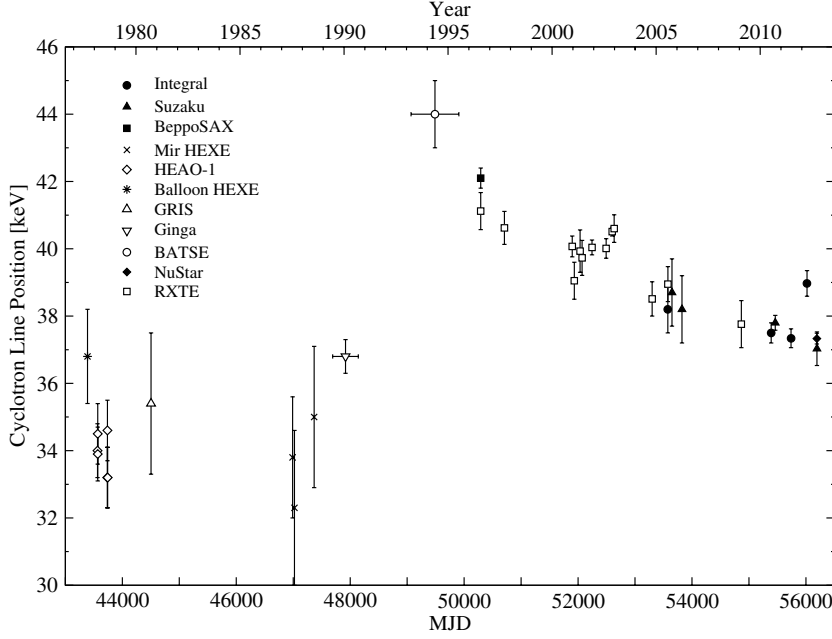
**Fig. 4.** Centroid energy of the phase averaged cyclotron resonance line feature in Her X-1 since its discovery. Data from before 1997 were originally compiled by Gruber et al. (2001), where the original references can be found. The data after 1997 are from observations by RXTE, INTEGRAL (Klochkov et al. 2006, 2008a; Staubert et al. 2007) and *Suzaku* (Enoto et al. 2008), plus recent values as given in Table 2. Here only values measured at 35d phases <0.20 are shown.

energy $E_{cyc}$. However, working with a uniform set of RXTE data between 1996 and 2005, we discovered that there was a dependence of $E_{cyc}$ on X-ray flux (Staubert et al. 2007), degrading the apparent decrease with time largely to an artifact: nature seemed to have conspired such that later measurements were (on average) taken when the flux happened to be low (Her X-1 is known for varying its flux within a factor of two, on timescales of a few 35 d cycles). When the cyclotron line energy was normalized to a common flux value, the time dependence vanished.

In the following we will demonstrate in a systematic way that today we have clear evidence for a reduction in the phase averaged cyclotron line energy $E_{cyc}$ with time over the last 20 years. Both dependencies – on flux and on time – seem to be always present (they may, however, change their relative importance with time). Using a procedure of fitting with two variables simultaneously, the two dependencies can be separated and the formal correlation minimized. With the inclusion of new measurements (2005–2012), we are now able to present the first statistically significant evidence of a true long-term decay of the phase averaged cyclotron line energy.

### 6.1. Normalizing $E_{cyc}$ using the originally discovered flux dependence

Before introducing fits with two variables (flux and time), we repeat here the procedure applied in Staubert (2013), that neglects any time dependence and normalizes $E_{cyc}$ by flux only, using the originally determined linear dependence with a slope of 0.66 keV/(ASM-cts/s) (Staubert et al. 2007). The normalization is done to the common reference flux of 6.80 ASM-cts/s. The results were shown in Fig. 2 (right) of Staubert (2013) (and, slightly updated, in Fig. 13 of Fürst et al. 2013), showing the flux normalized cyclotron line energy as a function of time (1996–2012). These figures demonstrate that there is a significant decrease in $E_{cyc}$ at least after 2006 (>MJD 54 500). Based on a repeated analysis we give the following additional information.

(1) The normalized $E_{cyc}$ values between 1996 and 2006 (MJD 50 000–54 000) are consistent with a constant (based

on $\chi^2$/d.o.f. = 0.77), supporting the neglect of a time dependence for this decade. The weighted mean is (40.06 ± 0.09) keV. However, even during this time period there is a slight downward trend with a slope of $(-2.5 \pm 1.4) \times 10^{-4}$ keV d$^{-1}$. In order to test whether this downward trend is really a true time dependence and not an artifact due to the neglect of e.g., a more complicated flux dependence, a quadratic term was added when doing the flux normalization: this does not improve the fit and does not remove the downward trend.

(2) The weighted mean of the normalized $E_{cyc}$ values for 2006–2012 is (37.69 ± 0.10) keV (with a high $\chi^2$/d.o.f. of 6.6, mainly due to the INTEGRAL 2012 point).

(3) The difference between these two mean values is highly significant (>17 standard deviations), demonstrating the decrease in $E_{cyc}$ with time.

### 6.2. Normalizing $E_{cyc}$ using fits to the 1996–2006 data with two variables

From Fig. 1, it is already evident that most of the $E_{cyc}$ values measured after 2006 are significantly lower than those from before. In order to separate the dependence on time and the dependence on X-ray flux, we have performed fits to the 1996–2006 data with two variables – X-ray flux and time. We use the function

$$E_{cyc}(calc) = E_0 + a \times (F - F_0) + b \times (T - T_0) \qquad (1)$$

with $F$ being the X-ray flux (the maximum flux of the respective 35 d cycle) in units of ASM-cts/s, as observed by RXTE/ASM (and/or *Swift*/BAT), with $F_0 = 6.80$ ASM-cts/s, and $T$ being time in MJD with $T_0 = 53\,000$ – the relationship between ASM and BAT is the following: (2–10 keV ASM-cts/s) = 89 * (15–50 keV BAT-cts cm$^{-2}$ s$^{-1}$).

In Table 3 we summarize results of fits to the 1996–2006 data set with successive numbers of free parameters. Assuming no dependence at all ($a = b = 0.0$), as well as dependence only on time ($a = 0$) leads to unacceptable fits with $\chi^2$/d.o.f. of 3.4 and 2.9, respectively. Allowing simultaneous dependence on flux
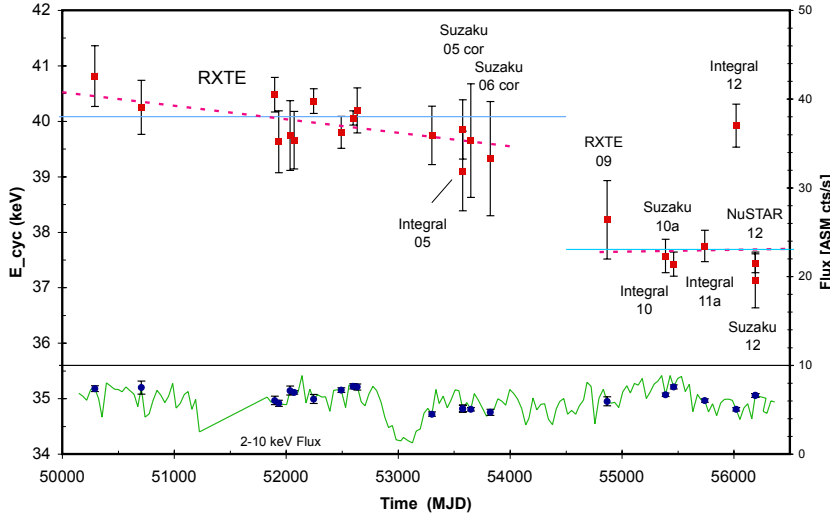
**Fig. 5.** *Upper panel*, left scale: Her X-1 pulse phase averaged cyclotron line energies $E_{\rm cyc}$ normalized to a reference ASM count rate of 6.8 cts/s using a flux dependence of 0.54 keV/ASM-cts/s. A break in mean $E_{\rm cyc}$ after MJD 54 000 (>2006) is apparent. *Lower panel*, right scale: 2–10 keV X-ray flux (of 35 d maximum) from monitoring by RXTE/ASM (from *Swift*/BAT after MJD 56 000). Blue data points with uncertainties are those fluxes which are used to correlate with $E_{\rm cyc}$, the green curve connects measurements of each 35 d cycle.

**Table 3.** Details of fits with formula (1) to $E_{\rm cyc}$ values observed between 1996 and 2006.

| Param. fitted | $E_0$ [keV] | $a$ [keV/ ASM-cts/s] | $b$ [$10^{-4}$ keV/d] | $\chi^2$ | d.o.f. |
|---|---|---|---|---|---|
| $E_0$ | $40.15 \pm 0.09$ | 0.00 | 0.00 | 47.6 | 14 |
| $E_0, a$ | $40.08 \pm 0.09$ | $0.58 \pm 0.10$ | 0.00 | 10.9 | 13 |
| $E_0, b$ | $39.88 \pm 0.12$ | 0.00 | $-4.60 \pm 1.43$ | 37.3 | 13 |
| $E_0, a, b$ | $39.88 \pm 0.12$ | $0.54 \pm 0.10$ | $-2.91 \pm 1.47$ | 7.0 | 12 |

**Notes.** The reference time is $T_0 = 53\,000$.

and on time leads to a good fit ($\chi^2$/d.o.f. = 0.6), representing a description of these data with a satisfactory separation of flux and time dependence. It is again verified, that the flux dependence is the dominating effect, as clearly seen when the F-test is applied[2].

Allowing a simultaneous flux and time dependence, reduces the flux dependence slightly (as compared to neglecting the time dependence). If we now use the flux dependence of 0.54 keV/ (ASM-cts/s) for the normalization of the complete data set (1996–2012), we arrive at Fig. 5. We note the following features:

1) The mean cyclotron line energies before and after 54 500 (~2007) are $40.1 \pm 0.1$ and $37.6 \pm 0.1$, respectively. The difference is significant to >17 standard deviations (similar to the result of Sect. 6.1, where the flux normalization was done with the original slope of 0.66 keV/(ASM-cts/s)).

2) As noted before, there is a small downward trend between 1996 and 2006. Again, an added quadratic term for the flux normalization is not significant.

3) Because of the lack of measurements in 2007 and 2008 (at 35 d phases <0.20), we cannot distinguish between a fairly abrupt drop within this period and a smooth change from the 2004–2006 period to the 2009–2012 period (possibly with a somewhat stronger decay than between 1996 and 2006).

4) The lower panel of Fig. 5 shows the 2–10 keV X-ray flux (the maximum flux of each 35 d cycle) from monitoring by

---

[2] The respective improvements in $\chi^2$, when one additional free parameter is added, yields chance probabilities of 1.7% and <$10^{-10}$, respectively, for an improvement by chance, when as the third free parameter the time dependence or the flux dependence is added.

RXTE/ASM and *Swift*/BAT. The typical variation of the flux by a factor of ~2 (as also evident from Fig. 1) is apparent. The mean flux, averaged over several 35 d cycles, is constant.

### 6.3. Normalizing $E_{\rm cyc}$ using fits to the 1996–2012 data with two variables

We finally turn to fits with two variables (flux and time) to the data set of 1996–2012. For these fits we exclude the data point measured in April 2012 by INTEGRAL since, as noted before, this value is not consistent with measurements by both *Suzaku* and NuSTAR about six months later.

As discussed in Sect. 4, we have invested a strong effort to check the calibration of the INTEGRAL/IBIS detector for the time of observation and the subsequent data analysis procedure. We have not found any errors, so we keep this point in our data base (and show it in all plots), but exclude it from the fits to be discussed now (but even if this data point is included, the general conclusion about the long-term decrease in the cyclotron line energy is not changed). As before, the bilinear function (formula (1)) is applied. The results of these fits with increasing numbers of free parameters are summarized in Table 4, the fits are numbered 1 through 4. Using the flux dependence found in the final (simultaneous) fit (fit 4) for normalizing the observed $E_{\rm cyc}$ values to the reference flux of 6.8 (ASM-cts/s), the remaining linear time dependence is shown in Fig. 6. The bilinear fit number 4 is acceptable with a $\chi^2 = 20.4$ for 18 d.o.f.

From Fig. 6 we see that the INTEGRAL12 point is far (~$6\sigma$) from the best fit (the dashed line). If we now repeat the bilinear fit including this point, the linear time dependence is not changed significantly (from $(-7.22 \pm 0.39) \times 10^{-4}$ to $(-6.91 \pm 0.39) \times 10^{-4}$ keV d$^{-1}$), which means that the conclusions about the decay of $E_{\rm cyc}$ with time are not changed.

We note that a further improvement of the fit can be achieved by introducing a quadratic term in the time dependence (again for INTEGRAL12 excluded): the flux dependence is unchanged, the linear time term is now $(-6.59 \pm 0.49) \times 10^{-4}$ keV d$^{-1}$ and the quadratic time term is $(-6.88 \pm 3.18) \times 10^{-8}$ keV d$^{-2}$ (both with a reference time MJD 53 500), and a $\chi^2 = 15.7$ for 17 d.o.f. However, the improvement is only marginally significant with an $F$-value of 5.1, corresponding to a probability of 3.7% for an improvement by chance.
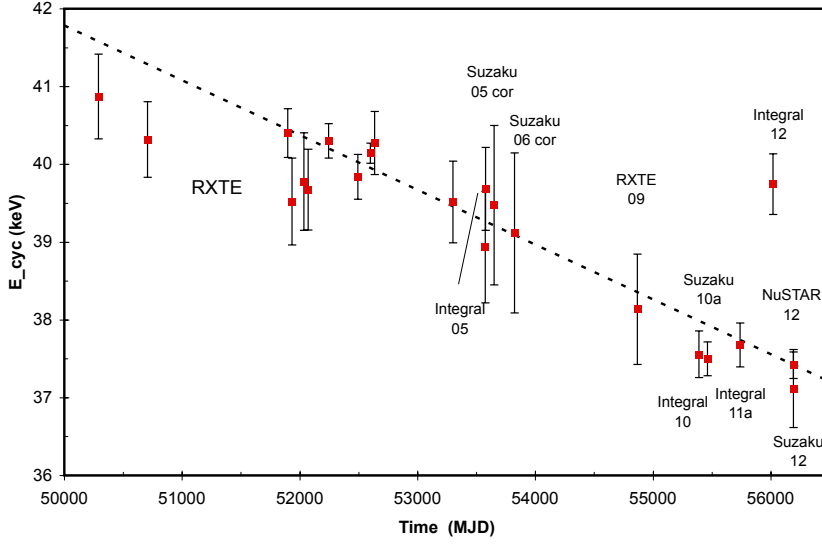
**Fig. 6.** Her X-1 pulse phase averaged cyclotron line energies $E_{cyc}$ normalized to a reference ASM count rate of 6.8 cts/s using a flux dependence of 0.44 keV/ASM-cts/s. The data are now consistent with a linear decline of $E_{cyc}$ with time with a slope of $-7.22\times10^{-4}$ keV d$^{-1}$.

**Table 4.** Details of fits with formula (1) to $E_{cyc}$ values observed between 1996 and 2012 (excluding INTEGRAL12).

| Fit No. | Param. fitted | $E_0$ [keV] | $a$ [keV/ASM-cts/s] | $b$ [$10^{-4}$ keV/d] | $\chi^2$ | d.o.f. | $F$-values | Chance probab. |
|---|---|---|---|---|---|---|---|---|
| 1 | $E_0$ | $39.12 \pm 0.07$ | 0.00 | 0.00 | 430 | 20 | | |
| 2 | $E_0, a$ | $39.08 \pm 0.07$ | $0.74 \pm 0.09$ | 0.00 | 357 | 19 | $F(1–2) = 3.86$ | 0.06 |
| 3 | $E_0, b$ | $39.29 \pm 0.07$ | 0.00 | $-7.59 \pm 0.39$ | 45.0 | 19 | $F(1–3) = 163$ | $9 \times 10^{-11}$ |
| 4 | $E_0, a, b$ | $39.25 \pm 0.07$ | $0.44 \pm 0.09$ | $-7.22 \pm 0.39$ | 20.4 | 18 | $F(3–4) = 131$ | $5 \times 10^{-5}$ |

**Notes.** The reference flux is $F_0 = 6.8$ (ASM-cts/s) and the reference time is $T_0$ = MJD 53 500. The $F$-values are calculated according to the following formula: $F = \Delta(\chi^2)/\chi_2^2 \times$ d.o.f.(2). The last column gives the F-test probability that the improvement in $\chi^2$ (by adding one additional free parameter) is just by chance.

Referring to Table 4 and Fig. 6 we note the following results:

1) Clearly, fit 1 is not acceptable ($\chi^2 = 430$ for 20 d.o.f.): $E_{cyc}$ is not constant.
2) Introducing a linear flux dependence (neglecting any time dependence (fit 2)), improves the $\chi^2$ significantly and finds a flux dependence of $0.74 \pm 0.09$ keV/(ASM-cts/s), which is (within uncertainties) consistent with the value found for the previous fit over the shorter time range (Table 3). However, a flux dependence alone is not sufficient. In addition, when a quadratic term for the flux normalization is introduced, assuming no time dependence, the fit is not acceptable ($\chi^2 = 313$, compare the corresponding values of Table 4).
3) Introducing a linear time dependence (neglecting any flux dependence (fit 3)), improves the $\chi^2$ dramatically. The $F$-value corresponds to a formal probability of $<10^{-10}$ for the improvement to be just by chance.
4) Adding now the linear flux dependence (fit 4), $\chi^2$ is further reduced significantly, meaning that the flux dependence is definitely needed in addition to the time dependence (the $F$-value corresponds to a chance probability of $\sim 5 \times 10^{-5}$). The slope describing the flux dependence is somewhat reduced as compared to fit 2, but is now very close to the corresponding dependence found in fitting the <2006 data (see Table 3).
5) We note that now the time dependence is the more dominant variation, while for the <2006 data set it was the flux dependence. This is consistent with a ~4 keV reduction in $E_{cyc}$ over the covered time range (1996–2012), while the increase

is only ~3 keV over the flux range provided by nature (a factor of ~2 in flux). A reduction in importance of the flux dependence, when adding the data after 2006, can already be expected from Fig. 1: the >2006 data are consistent with no flux dependence at all (even though they are formally consistent with the same slope as the <2006 data).
6) An even better fit can be achieved by introducing a quadratic term in the time dependence ($E_{cyc}/dt^2 = (-6.88 \pm 3.18) \times 10^{-8}$ keV d$^{-2}$), albeit marginally significant (3.7% chance probability). The negative second derivative means that the decrease in $E_{cyc}$ accelerates with time. We note, that one might rather expect the opposite, e.g., a kind of exponential decay.
7) It is not understood why the measurement of INTEGRAL in 2012 is so different from the nearby (<six months) observations by *Suzaku* and NuSTAR. We find no errors in our analysis. However, this one data point does not in any way change the general conclusion.

## 7. Summary of observational results

Here we summarize our observational results:

1. The main result of this research is that we finally can establish a long-term decay of the pulse phase averaged cyclotron line energy $E_{cyc}$ over time. The time range covered here is 16 years (1996 to 2012). The reduction is highly significant and can be well described by a linear decay with a change by $(7.2 \pm 0.4) \times 10^{-4}$ keV d$^{-1}$ (0.26 keV yr$^{-1}$

or 4.2 keV over 16 yrs). The data are, however, also consistent with two other models: First (see Fig. 5), a somewhat slower decay ($\sim 3 \times 10^{-4}$ keV d$^{-1}$) until 2006 and then a more sudden drop between 2006 and 2009, with a possible constant value ($\sim 37.7$ keV) thereafter. Alternatively, even an acceleration of the decay of $E_{cyc}$ over time is possible, since the fit with a quadratic term in the time dependence is formally the best one.

2. The flux dependence of $E_{cyc}$ is confirmed with a value between 0.44 and 0.54 keV/ASM-cts/s (with a typical uncertainty of 0.1), corresponding to a $\sim 5\%$ increase for a factor of two increase in flux. This value is slightly lower than the value ($0.66 \pm 0.10$) from the original discovery (Staubert et al. 2007) (at that time, a time dependence was neglected). It is not excluded that there is a variation with time of this flux dependence, but this is difficult to judge since the fluxes observed after 2006 only cover a very small range.

3. One observation, the one from INTEGRAL in April 2012, does not fit into the overall picture and is inconsistent with values measured by *Suzaku* and NuSTAR six months later. Since we find no errors in our analysis, we can only speculate that it is due to real physics – that is a fluctuation on a timescale of a few months.

4. From the analysis of pulse profiles and pulse phase resolved spectroscopy (see Sect. 5), both as a function of 35 d phase, we find evidence of a variation of $E_{cyc}$ with this precessional phase: while there is very little (if any) variation until 35 d phase 0.2, there may be a decrease at later phases. If it is indeed so, that the pulse phase dependence of $E_{cyc}$ does not change with 35 d phase (Vasco et al. 2013), then this effect is inevitable. The fully covered *Main-On* of cycle 232 (Fig. 3) and the few dedicated observations at late 35 d phases support this finding. This new result adds another piece to the puzzle on the question about the physical nature of the 35 d modulation – precession of the accretion disk (plus?) precession of the neutron star? – and the mechanism of generating the varying pulse profiles and the varying spectra – continua and CRSF (see Sect. 8 and discussions in Staubert et al. 2009, 2013; Vasco et al. 2013).

## 8. Discussion

### 8.1. Dependence of $E_{cyc}$ on luminosity

A negative correlation between the pulse phase averaged cyclotron line energy and the X-ray luminosity (a decrease in $E_{cyc}$ with increasing $L_x$), had first been noted by Mihara (1995) in observations of a few high luminosity transient sources (4U 0115+63, Cep X-4, and V 0332+53) by *Ginga*. This negative correlation was associated with the high accretion rate during the X-ray outbursts, as due to a change in height of the shock (and emission) region above the surface of the neutron star with changing mass accretion rate, $\dot{M}$. In the model of Burnard et al. (1991), the height of the polar accretion structure is tied to $\dot{M}$. From this model one expects that an increase in accretion rate leads to an increase in the height of the scattering region above the neutron star surface, and therefore to a decrease in magnetic field strength and hence a decrease in $E_{cyc}$. During the 2004/2005 outburst of V 0332+53 a clear anti-correlation of the line position with X-ray flux was observed (Tsygankov et al. 2006). A similar behavior was observed in outbursts of 4U 0115+63 in March/April 1999 and Sep/Oct 2004: both Nakajima et al. (2006) and Tsygankov et al. (2007) had found a general anti-correlation between $E_{cyc}$ and luminosity.

However, Müller et al. (2013b), analyzing data of a different outburst of this source in March/April 2008, observed by RXTE and INTEGRAL, have found that the negative correlation for the fundamental cyclotron line is likely an artifact due to correlations between continuum and line parameters when using the NPEX continuum model.

The first positive correlation was discovered by Staubert et al. (2007) in Her X-1, and secured by a reanalysis of the same RXTE data by Vasco et al. (2011), using the bolometric X-ray flux as reference. This analysis confirmed that the originally used 2–10 keV flux is a good measure of the bolometric luminosity. While the above discussed analysis tests the correlated variability of $E_{cyc}$ and $L_x$ on long timescales (35 d and longer), the pulse-amplitude resolved analysis of Klochkov et al. (2011) does so on short timescales (down to the pulse period of 1.24 s). Selecting pulses with amplitudes in certain ranges and producing mean spectra for each pulse amplitude range, showed that the cyclotron line energy scales positively with the mean pulse amplitude. In addition, it was found that the photon index $\Gamma$ of the underlying power law continuum scales negatively with the pulse amplitude (the absolute value of $\Gamma$ gets smaller, that is the spectrum flattens). The same behavior was seen in data of the transient A 0535+26. A recent pulse phase resolved analysis of A 0535+26 observations by RXTE and INTEGRAL showed that data of one of the two peaks (of the double peak pulse profile) displays the same trend while data of the other peak do not (Müller et al. 2012, 2013a). Applying the same pulse-amplitude resolved technique to data of V 0332+53 and 4U 0115+63, Klochkov et al. (2011) found the same behavior as originally detected in data sets that were selected on much longer timescales: $E_{cyc}$ decreases and $\Gamma$ increases with increasing $L_x$. Finally, we mention that a positive correlation of $E_{cyc}$ with $L_x$ was also found in two more X-ray binary pulsars: in GX 304-1 (Yamamoto et al. 2011; Klochkov et al. 2012) and in NuSTAR observations of Vela X-1 (Fürst et al. 2014). We note, that the still small group of four objects with a positive $E_{cyc}/L_x$ correlation now outnumbers the group of secure sources with the originally discovered opposite behavior.

Our current understanding of the physics behind these correlations assumes that we can distinguish between *two accretion regimes* in the accretion column above the polar cap of the neutron star: *super- and sub-Eddington accretion*. The former is responsible for the first detected negative correlation in high luminosity outbursts of transient X-ray sources (the reference source being V 0332+53): in this case the deceleration of the accreted material is provided by radiation pressure, such that with increasing accretion rate $\dot{M}$, the shock and the scattering region move to larger height above the surface of the neutron star and consequently to weaker $B$-field (Burnard et al. 1991). Sub-Eddington accretion, on the other hand, leads to the opposite behavior. In this regime the deceleration of accreted material is predominantly through Coulomb interactions and an increase in $\dot{M}$ leads to an increase in electron density (due to an increase of the combined hydrostatic and dynamical pressure) resulting in a *squeezing* of the decelerating plasma layer to smaller height and stronger $B$-field (Staubert et al. 2007). More detailed physical considerations have recently been presented by Becker et al. (2012). The persistent sources Her X-1 and Vela X-1 are clearly sub-Eddington sources.

Despite the above discussed doubts about the reality of the negative correlation of the energy $E_{cyc}$ of the fundamental CRSF with $L_x$ in 4U 0115+63 (Müller et al. 2013b), and keeping in mind that Klochkov et al. (2011) had confirmed the correlation using the pulse-amplitude resolved technique (not using the

NPEX function), we would like to note here that we are intrigued by the following plots about 4U 0115+63: Fig. 8 of Nakajima et al. (2006) and Figs. 11 and 12 of Tsygankov et al. (2007). In going to the lowest luminosities, there is an indication for a leveling-off or even a reduction in $E_{cyc}$. Do we possibly see here the transition between the two accretion regimes?

### 8.2. The long-term decay of $E_{cyc}$

With regard to the physical interpretation of the now observed long-term decrease in the cyclotron line energy, we speculate that it could be connected to either unknown effects in the neutron star and its magnetic field, to a geometric displacement of the cyclotron resonant scattering region in the dipole field or to a true physical change in the magnetic field configuration at the polar cap, which evolves due to continued accretion. Apparently, the magnetic field strength at the place of the resonant scattering of photons trying to escape from the accretion mound surface must have changed with time. Putting internal neutron star physics aside, we suggest that it reflects a local phenomenon in the accretion mound: either a geometric displacement of the emission region or a change in the local field configuration, rather than a change in the strength of the underlying global dipole field (here a minimum timescale of a million years is estimated from population studies of rotation-powered pulsars; Bhattacharya et al. 1992; Geppert & Urpin 1994). Our observed timescale, a few tens of years, is extremely short.

The whole issue of accretion onto highly magnetized neutron stars in binary X-ray sources is very complex. Ideas or models with potential relevance to our observations attempting to understand the magnetic field configuration in accreting neutron stars and its evolution over extended periods of continued accretion, can be found in e.g.: Hameury et al. (1983), Konar & Bhattacharya (1997), Brown & Bildsten (1998), Cheng & Zhang (1998), Litwin et al. (2001), Cumming et al. (2001), Melatos & Phinney (2001), Choudhuri & Konar (2002), Payne & Melatos (2004), Payne & Melatos (2007), Wette et al. (2010), Mukherjee & Bhattacharya (2012), Mukherjee et al. (2013a), Mukherjee et al. (2013b). However, as far as we can see, none of them gives the complete picture. Most calculations deal with static solutions that are found under special boundary conditions.

Since the main purpose of this contribution is to report on the discovery of a new observational phenomenon, we refrain from going into any details regarding interpretations of existing models. Instead, we only mention a few areas which we think could have some connection with the observed facts and which may be worthwhile to be explored. Our hope is that the new observational results presented here may boost the motivation for further theoretical studies.

We start by asking whether the observed decrease in $E_{cyc}$ with time could be a simple movement of the resonant scattering region to a larger distance from the neutron star surface, where the field strength is lower. This would be similar to the decrease in $E_{cyc}$ during outbursts in high luminosity transients, except that (being in the sub-Eddington regime of accretion) we would not think of the shock region to rise, but rather the total height of the accretion mound may slowly increase with time, such that also the resonant scattering region is displaced to a higher position. For a dipole field with an $r^{-3}$ dependence of field strength, the observed ~5 keV reduction in $E_{cyc}$ from 1992 to 2012 (0.25 keV per year) would correspond to a change in height of ~400 m (starting from the surface itself). The question here is, whether continued accretion really leads to a growth of

the accretion mound with time – both in terms of geometrical height and of total mass.

With similar uncertainty, it can be asked whether the accreted material could drag the central field lines radially out, possibly enlarging the total hotspot area and thereby diluting the effective field strength in the region where the resonant scattering takes place (Cheng & Zhang 1998; Zhang & Kojima 2006). Or, whether *screening* or *burial* of the magnetic field at the polar caps is possible (Brown & Bildsten 1998; Payne & Melatos 2004; Litwin et al. 2001; Payne & Melatos 2007). It needs to be investigated, how much mass could eventually be stored in the magnetically confined mountains, whether matter is continuously leaking out to larger areas of the neutron star surface (due to plasma pressure exceeding the magnetic pressure) and on what timescales an observational effect can be expected.

Finally, the question of Ohmic dissipation and diffusion of the magnetic field may play a role and physical processes either in the accretion mound or in or below the surface of the neutron star (like hydrodynamic flows) could *bury* or reduce the surface field (Choudhuri & Konar 2002; Patruno 2012). One would need to investigate whether physical parameters like the characteristic length scale and the relevant conductivity $\sigma$ for either the crust or the plasma in the accretion mound could be of the right order of magnitude to allow the magnetic diffusion timescale $\tau = 4\pi R^2 \sigma / c^2$ (Cumming et al. 2001; Ho 2011) to be compatible with the timescale of a few tens of years – as observed for the decrease in the local polar field strength in Her X-1. If magnetic diffusion is indeed relevant, we note that the necessary small length scales and relatively low conductivities would argue for local physics in the hot plasma of the accretion mound, the structure of which is most likely complex because of contributions from higher-order multipoles.

We finally speculate on a possible cyclic behavior of $E_{cyc}$ on timescales of a few tens to hundreds of years. Could it be that the fast rise of the observed $E_{cyc}$ values after 1991 (see Fig. 4) represents a special event in which the magnetic field in the accretion mound has rearranged itself as a result of a sudden radial outflow of material? In models by Brown & Bildsten (1998); Litwin et al. (2001); Payne & Melatos (2004); Payne & Melatos (2007); Mukherjee & Bhattacharya (2012); Mukherjee et al. (2013a) the field configuration is shown to change considerably with increased material, leading to a *ballooning* of the field configuration with diluted field in the symmetry center and increased density of field lines at the circumference of the base of the mound. The estimates of how much mass could be confined by the field vary substantially between the different models. It remains unclear, how important continuous leaking through the outer magnetic boundary may be and what the timescales for semi-catastrophic events might be, in which the field would release (on a short timescale) a substantial fraction of stored material to larger areas of the neutron star surface. For Her X-1 this scenario could mean that we are now in a phase of continuous build-up of the accretion mound with the mass (and the height?) of the mound growing and the observed cyclotron line energy continuously decreasing until another event like the one around 1991 happens again. The mean $E_{cyc}$ value measured before 1991 of ~35 keV may represent a bottom value. So, when the current decay continues steadily, one may expect another event of a rather fast increase in $E_{cyc}$.

In conclusion, we like to urge both observers and model builders to continue to accumulate more observational data as well as more understanding of the physics responsible for the various observed properties of Her X-1 and other objects of similar nature. For model builders a challenge would be to work

towards dynamical computations that might eventually lead to self-consistent solutions of the structure and evolution of magnetized accretion mounds of accreting neutron stars with only a few input parameters.

# References

Araya, R., & Harding, A. 1999, ApJ, 517, 334
Araya-Góchez, R. A., & Harding, A. K. 2000, ApJ, 544, 1067
Becker, P. A., & Wolff, M. T. 2007, ApJ, 654, 435
Becker, P. A., Klochkov, D., Schönherr, G., et al. 2012, A&A, 544, A123
Bhattacharya, D., Wijers, R. A. M. J., Hartman, J. W., & Verbunt, F. 1992, A&A, 254, 198
Brown, E., & Bildsten, L. 1998, ApJ, 496, 915
Burnard, D. J., Arons, J., & Klein, R. I. 1991, ApJ, 367, 575
Caballero, I., & Wilms, J. 2012, Mem. Soc. Astron. It., 83, 230
Cheng, K. S., & Zhang, C. M. 1998, A&A, 337, 441
Choudhuri, A. R., & Konar, S. 2002, MNRAS, 332, 933
Coburn, W., Heindl, W. A., Rothschild, R. E., et al. 2002, ApJ, 580, 394
Cumming, A., Zweibel, E., & Bildsten, L. 2001, ApJ, 557, 958
Enoto, T., Makishima, K., Terada, Y., et al. 2008, PASJ, 60, 57
Fürst, F., Grefenstette, B. W., Staubert, R., et al. 2013, ApJ, 779, 69
Fürst, F., Pottschmidt, K., Wilms, J., et al. 2014, ApJ, 780, 133
Geppert, U., & Urpin, V. 1994, MNRAS, 271, 490
Gruber, D. E., Heindl, W. A., Rothschild, R. E., et al. 2001, ApJ, 562, 499
Hameury, J. M., Bonazzola, S., Heyvaerts, J., & Lasota, J. P. 1983, A&A, 128, 369
Heindl, W. A., Rothschild, R. E., Coburn, W., et al. 2004, in X-ray Timing 2003: Rossi and Beyond, eds. P. Kaaret, F. K. Lamb, & J. H. Swank, AIP Conf. Ser., 714, 323
Ho, W. C. G. 2011, MNRAS, 414, 2567
Klochkov, D. K., Shakura, N. I., Postnov, K. A., et al. 2006, Astron. Lett., 32, 804
Klochkov, D., Staubert, R., Postnov, K., et al. 2008a, A&A, 482, 907
Klochkov, D., Staubert, R., Postnov, K., et al. 2008b, in Proc. 7th INTEGRAL Workshop, Copenhagen, Sep., eds. N. Lund, et al., PoS(INTEGRAL2008)112
Klochkov, D., Staubert, R., Santangelo, A., Rothschild, R. E., & Ferrigno, C. 2011, A&A, 532, A126
Klochkov, D., Doroshenko, V., Santangelo, A., et al. 2012, A&A, 542, L28
Konar, S., & Bhattacharya, D. 1997, MNRAS, 284, 311
Lebrun, F., Leray, J. P., & Lavocat, P., et al. 2003, A&A, 411, L141
Litwin, C., Brown, E. F., & Rosner, R. 2001, ApJ, 553, 788
Melatos, A., & Phinney, E. S. 2001, PASA, 18, 421
Mihara, T. 1995, Ph.D. Thesis, Univ. of Tokyo
Mukherjee, D., & Bhattacharya, D. 2012, MNRAS, 420, 720
Mukherjee, D., Bhattacharya, D., & Mignone, A. 2013a, MNRAS, 430, 1976
Mukherjee, D., Bhattacharya, D., & Mignone, A. 2013b, MNRAS, 435, 718
Müller, D., Klochkov, D., Caballero, I., Staubert, R., & Santangelo, A. 2012, in An INTEGRAL view of the high-energy sky (the first 10 years), Proc. of 9th INTEGRAL Workshop, Paris, 15–19 October, PoS(INTEGRAL 2012)030
Müller, D., Klochkov, D., Caballero, I., & Santangelo, A. 2013a, A&A, 552, A81
Müller, S., Ferrigno, C., Kühnel, M., et al. 2013b, A&A, 551, A6
Nagel, W. 1981, ApJ, 251, 288
Nakajima, M., Mihara, T., Makishima, K., & Niko, H. 2006, ApJ, 646, 1125
Nishimura, O. 2008, ApJ, 672, 1127
Patruno, A. 2012, ApJ, 753, L12
Payne, D., & Melatos, A. 2004, MNRAS, 351, 569
Payne, D. J. B., & Melatos, A. 2007, MNRAS, 376, 609
Rothschild, R. E., Markowitz, A., Rivers, E., et al. 2011, ApJ, 733, 23
Schönherr, G., Wilms, J., Kretschmar, P., et al. 2007, A&A, 472, 353
Soong, Y., Gruber, D. E., Peterson, L. E., & Rothschild, R. E. 1990, ApJ, 348, 634
Staubert, R. 2003, ChJAA, 3, S270
Staubert, R. 2013, in An INTEGRAL view of the high-energy sky (the first 10 years), Proc. 9th INTEGRAL Workshop Paris, 15–19 Oct. 2012, PoS(INTEGRAL 2012)010
Staubert, R., Bezler, M., & Kendziorra, E. 1983, A&A, 117, 215
Staubert, R., Shakura, N. I., Postnov, K., et al. 2007, A&A, 465, L25
Staubert, R., Klochkov, D., Postnov, K., et al. 2009, A&A, 494, 1025
Staubert, R., Klochkov, D., Vasco, D., et al. 2013, A&A, 550, A110
Terada, Y., Mihara, T., Nagase, F., et al. 2007, Adv. Space Res., 40, 1485
Trümper, J., Kahabka, P., Oegelman, H., Pietsch, W., & Voges, W. 1986, ApJ, 300, L63
Trümper, J., Pietsch, W., Reppin, C., et al. 1978, ApJ, 219, L105
Tsygankov, S. S., Lutovinov, A. A., Churazov, E. M., & Sunyaev, R. A. 2006, MNRAS, 371, 19
Tsygankov, S. S., Lutovinov, A. A., Churazov, E. M., & Sunyaev, R. A. 2007, Astron. Lett., 33, 368
Ubertini, P., Lebrun, F., Di Cocco, G., et al. 2003, A&A, 411, L131
Vasco, D., Klochkov, D., & Staubert, R. 2011, A&A, 532, A99
Vasco, D., Staubert, R., Klochkov, D., et al. 2013, A&A, 550, A111
Vedrenne, G., Roques, J.-P., Schönfelder, V., et al. 2003, A&A, 411, L63
Ventura, J., Nagel, W., & Meszaros, P. 1979, ApJ, 233, L125
Voges, W., Pietsch, W., Reppin, C., et al. 1982, ApJ, 263, 803
Wette, K., Vigelius, M., & Melatos, A. 2010, MNRAS, 402, 1099
Wilms, J. 2012, in Proc. 39th COSPAR Sci. Assembly, 14–22 July, Mysore, India, 39, 2159
Yamamoto, T., Sugizaki, M., Mihara, T., et al. 2011, PASJ, 63, 751
Zhang, C. M., & Kojima, Y. 2006, MNRAS, 366, 137